



**HAL**  
open science

# Dynamic modeling and characterization of magnetic hybrid films of polyvinyl butyral/iron oxide nanoparticles (PVB/Fe<sub>2</sub>O<sub>3</sub>) devoted to microactuators

Mayra Llamas-Hernandez

► **To cite this version:**

Mayra Llamas-Hernandez. Dynamic modeling and characterization of magnetic hybrid films of polyvinyl butyral/iron oxide nanoparticles (PVB/Fe<sub>2</sub>O<sub>3</sub>) devoted to microactuators. Automatic. Université Bourgogne Franche-Comté; Universidad autónoma de Nuevo León, 2019. English. NNT : 2019UBFCD034 . tel-02502396

**HAL Id: tel-02502396**

**<https://theses.hal.science/tel-02502396>**

Submitted on 9 Mar 2020

**HAL** is a multi-disciplinary open access archive for the deposit and dissemination of scientific research documents, whether they are published or not. The documents may come from teaching and research institutions in France or abroad, or from public or private research centers.

L'archive ouverte pluridisciplinaire **HAL**, est destinée au dépôt et à la diffusion de documents scientifiques de niveau recherche, publiés ou non, émanant des établissements d'enseignement et de recherche français ou étrangers, des laboratoires publics ou privés.



**THESE DE DOCTORAT DE L'ETABLISSEMENT UNIVERSITE BOURGOGNE FRANCHE-COMTE  
PREPAREE A L'INSTITUTE FEMTO-St**

École doctorale n°37

Sciences Pour l'Ingénieur et Microtechniques (SPIM)

Doctorat en automatique

Par

Mme. LLAMAS HERNANDEZ Mayra Iveth

Modélisation dynamique et caractérisation de films hybrides magnétiques de nanoparticules de polyvinylbutyral/oxyde de fer (PVB/Fe<sub>2</sub>O<sub>3</sub>) pour microactionneurs

Thèse présentée et soutenue à San Nicolás de los Garza, Nuevo León, Mexique, le 31 octobre 2019

Composition du Jury :

M. ORTIZ MENDEZ, Ubaldo	Professeur à l'UANL, San Nicolas de los Garza, N.L., Mexique	Président
M. RAHARIJAONA, Thibaut	MCF HDR à l'AMU, Marseille, France	Rapporteur
M. GARCÍA LOERA, Antonio	Professeur à l'UANL, San Nicolas de los Garza, N.L., Mexique	Rapporteur
M. RAKOTONDRABE, Micky	Professeur des Universités à l'ENIT, Tarbes, France	Directeur de thèse
Mme. LOPEZ WALLE, Beatriz	MCF HDR à l'UANL, San Nicolas de los Garza, N.L., Mexique	Codirecteur de thèse

**Titre :** Modélisation dynamique et caractérisation de films hybrides magnétiques de nanoparticules de polyvinylbutyral/oxyde de fer (PVB/Fe<sub>2</sub>O<sub>3</sub>) pour microactionneurs

**Mots clés :** modélisation, microactionneurs, magnétique, films, matériaux hybrides

**Résumé :** Les polymères hybrides peuvent être définis comme des matériaux ayant une ou plusieurs phases non organiques dispersées dans une matrice polymérique. Les films hybrides magnétiques sont généralement composés de particules magnétisables dispersées dans une matrice polymérique. Le terme film est donné en raison de leur épaisseur inférieure à 1 mm.

Les films hybrides magnétiques sont un sujet intéressant de recherche dans le domaine des technologies des microactionneurs car ils offrent la possibilité d'obtenir des dispositifs magnétiques flexibles avec une manipulation sans contact.

Les modèles mathématiques décrivant les réponses dynamiques des films hybrides magnétiques soumis à des champs magnétiques externes servent de base pour l'obtention de contrôleurs du comportement.

Dans cette étude, des films hybrides magnétiques de polyvinylbutyral avec des nanoparticules d'oxyde de fer (PVB/Fe<sub>2</sub>O<sub>3</sub>) sont évalués. L'objectif général est de proposer un modèle du comportement dynamique de ces films en tant que microactionneurs en cantilever, basé sur les propriétés physiques de ces films.

Alors, des films hybrides magnétiques ont été synthétisés à trois concentrations différentes en poids de fer (% wt Fe): 11%, 14% et 17%. Ceci permet d'obtenir trois concentrations différentes de nanoparticules d'oxyde de fer incorporées dans la matrice de PVB.

Alors, une caractérisation des propriétés physiques (mécaniques et magnétiques) des films de PVB/Fe<sub>2</sub>O<sub>3</sub> ainsi que de leur comportement dynamique comme microactuateur a été réalisée.

Les résultats de la caractérisation magnétique ont montré un comportement superparamagnétique à température ambiante. Or, d'après la caractérisation mécanique, le module d'élasticité des films de PVB/Fe<sub>2</sub>O<sub>3</sub> diminue lorsque la quantité de nanoparticules d'oxyde de fer augmente.

Le champ magnétique utilisé pour la caractérisation dynamique du comportement des microactionneurs est fourni par un électroaimant. Le courant a été appliqué selon deux modalités: mode échelon et mode oscillatoire.

Dans le mode échelon, cette caractérisation a montré un comportement amorti. Un déplacement maximal de 0,95 mm a été observé une fois atteinte la position d'équilibre ; ceci pour le microactionneur contenant 17% wt Fe en appliquant un voltage de 30 V (0,87 kOe). Lors du test en mode oscillatoire, on a observé un comportement dépendant de la fréquence et la présence d'hystérésis. Une longueur de bande inférieure à 5 Hz a été estimée pour tous les microactionneurs.

La validation expérimentale du modèle a été réalisée pour le microactionneur contenant 14% wt Fe, en modifiant le voltage appliqué et les dimensions des microactionneurs. Des erreurs relatives comprises entre 1,46% et 2,66% ont été obtenues en mode échelon en comparant les déplacements expérimentaux et simulés. En mode oscillatoire, le modèle ne suit pas complètement les résultats expérimentaux, sauf pour les fréquences 0,1 Hz et 1 Hz où le déplacement maximal présente une erreur entre 4% et 7%. Cela doit être encore amélioré dans des recherches futures.

**Title :** Dynamic modeling and characterization of magnetic hybrid films of polyvinyl butyral/iron oxide nanoparticles (PVB/Fe<sub>2</sub>O<sub>3</sub>) devoted to microactuators

**Keywords :** modeling, microactuators, magnetic, films, hybrid polymers

**Abstract :** Polymeric hybrid materials can be defined as a material having one or more phases dispersed into a polymeric matrix. Magnetic hybrid films are a kind of polymeric hybrid materials because they are usually composed by magnetizable particles dispersed in a polymeric matrix. The term film is given due to their thickness, which is less than 1 mm.

Magnetic hybrid films are a motivating research topic for microactuator technologies because they provide the possibility to obtain flexible magnetic devices with contactless manipulation. Mathematical models describing the dynamic responses of magnetic hybrid films when subjected to magnetic fields are the basis to obtain positioning and hysteresis controllers.

In this study, magnetic hybrid films of polyvinyl butyral with iron oxide nanoparticles (PVB/Fe<sub>2</sub>O<sub>3</sub>) are evaluated. The overall objective is to propose a model of the dynamic behavior of PVB/Fe<sub>2</sub>O<sub>3</sub> films as cantilever microactuators, based on the physical properties of such films.

Magnetic hybrid films were synthesized at three different concentrations by weight of iron (% wt Fe): 11%, 14% and 17%. This allows to obtain three different concentrations of iron oxide nanoparticles embedded into the PVB matrix.

Results of the magnetic characterization showed a superparamagnetic behavior at room temperature.

From mechanical characterization, it was observed a decrease in the elastic modulus of the

PVB/Fe<sub>2</sub>O<sub>3</sub> films as the iron oxide nanoparticles content increases.

The magnetic field used for the dynamic characterization of the PVB/Fe<sub>2</sub>O<sub>3</sub> films as cantilever microactuators was obtained by an electromagnet. The current was supplied to the electromagnet in two modalities: step mode and oscillatory mode.

Dynamic characterization showed a damped-like behavior in the step mode. A maximum settling displacement of 0.95 mm was observed for the sample with 17%wt Fe when a step voltage of 30 V (0.87 kOe) is applied. In the oscillatory mode test, a hysteretic and frequency-dependent behavior was observed. A bandwidth lower than 5 Hz was estimated for all the samples.

The experimental validation of the model was performed for the sample of 14%wt Fe with voltage and size variations. Relative errors between 1.46% and 2.66% were obtained in the step voltage mode by comparing experimental and simulated settling displacements. In the oscillatory mode, the model does not completely follow the experimental results. The smallest relative errors were obtained by comparing the values of maximum displacement between experimental and simulated results. At the frequencies of 0.1 Hz and 1 Hz, the relative errors are 4% and 7%, respectively. This must to be further improve in future researches.



UANL

UNIVERSIDAD AUTÓNOMA DE NUEVO LEÓN



FACULTAD DE INGENIERÍA MECÁNICA Y ELÉCTRICA

**UNIVERSIDAD AUTÓNOMA DE NUEVO LEÓN**  
**FACULTAD DE INGENIERÍA MECÁNICA Y ELÉCTRICA**



“Dynamic modeling and characterization of magnetic hybrid films of polyvinyl butyral/iron oxide nanoparticles (PVB/Fe<sub>2</sub>O<sub>3</sub>) devoted to microactuators”

**Por**

Mayra Iveth Llamas Hernández

**EN OPCIÓN AL GRADO DE**  
Doctor en ingeniería de materiales

**Octubre de 2019**



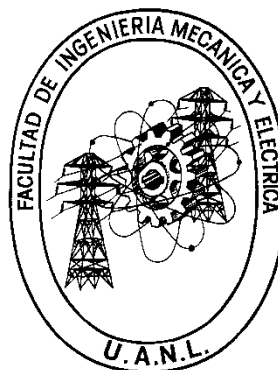
**UANL**

UNIVERSIDAD AUTÓNOMA DE NUEVO LEÓN



FACULTAD DE INGENIERÍA MECÁNICA Y ELÉCTRICA

**UNIVERSIDAD AUTÓNOMA DE NUEVO LEÓN**  
**FACULTAD DE INGENIERÍA MECÁNICA Y ELÉCTRICA**  
**SUBDIRECCIÓN DE ESTUDIOS DE POSGRADO**



“Dynamic modeling and characterization of magnetic hybrid films of polyvinyl butyral/iron oxide nanoparticles (PVB/Fe<sub>2</sub>O<sub>3</sub>) devoted to microactuators”

**Por**

Mayra Iveth Llamas Hernández

**EN OPCIÓN AL GRADO DE**  
Doctor en ingeniería de materiales

**Octubre de 2019**



UANL

UNIVERSIDAD AUTÓNOMA DE NUEVO LEÓN



FACULTAD DE INGENIERÍA MECÁNICA Y ELÉCTRICA

**UNIVERSIDAD AUTÓNOMA DE NUEVO LEÓN**  
**FACULTAD DE INGENIERÍA MECÁNICA Y ELÉCTRICA**  
**SUBDIRECCIÓN DE ESTUDIOS DE POSGRADO**

Los miembros del Comité de Tesis recomendamos que la Tesis "Dynamic modeling and characterization of magnetic hybrid films of polyvinyl butyral/iron oxide nanoparticles (PVB/Fe<sub>2</sub>O<sub>3</sub>) devoted to microactuators" realizada por el alumno(a) Mayra Iveth Llamas Hernández, con número de matrícula 1291614, sea aceptada para su defensa como opción al grado de "Doctorado en Ingeniería de Materiales"

El Comité de Tesis

Dra. Beatriz Cristina López Walle  
Director

Dr. Micky Rakotondrabe  
Revisor

Dr. Ubaldo Ortiz Mendez  
Revisor

Dr. Antonio Francisco García Loera  
Revisor

Dr. Thibaut Raharijaona  
Revisor

Vo. Bo.

Dr. Simón Martínez Martínez  
Subdirector de Estudios de Posgrado



San Nicolás de los Garza, Nuevo León, 15 de octubre de 2019

*To my parents R. Llamas and G. Hernández,  
with their love and encouragement during my studies made this aim possible.*

*To my husband,  
my favorite companion in life and in the world of science.*

*To my son,  
who has become a source of motivation, inspiration and love.*



# ACKNOWLEDGEMENTS

I would like to thank to the Consejo Nacional de Ciencia y Tecnología (CONACYT), the Universidad Autónoma de Nuevo León (UANL) and the Université Bourgogne Franche-Comté (UBFC) for the financial support provided to carry out this research.

I thank to Facultad de Ingeniería Mecánica y Eléctrica and the Femto-St Institute for having given me the opportunity to develop my Ph.D. study in their facilities.

It is a pleasure to express my deep gratitude to my mentors Dra. Beatriz Cristina López Walle and Dr. Micky Rakotondrabe for accepting this collaboration, for their patience and all their treasured guidance during the research and writing of this thesis.

I would like to express my thankfulness to Dr. Francisco Antonio García Loera, Dr. Thibaut Raharijaona and Dr. Ubaldo Ortiz Mendez for accepting to be my reviewers and for all their valuable comments to complement this thesis.

I would also like to show my gratitude to all the professors in Mexico and in France that have shared with me some of their treasured knowledge. Special mention deserves Dr. Martín Edgar Reyes Melo whose contribution has been an important part for the development of this research.

I want to give my thanks to all my friends and colleagues in Mexico and in France for the great moments together along these years.

I also express my profuse thanks to my family for their unconditional love and support.

# Content

1	INTRODUCTION .....	9
1.1	CONTEXT .....	9
1.2	JUSTIFICATION .....	12
1.3	HYPOTHESIS.....	13
1.4	OBJECTIVES .....	13
1.5	THESIS ORGANIZATION .....	14
2	HYBRID MATERIALS, STIMULI- RESPONSIVE POLYMERS AND MICROACTUATION .....	15
2.1	INTRODUCTION.....	15
2.2	SIGNIFICANCE OF POLYMER-BASED MATERIALS IN MICROACTUATION .....	16
2.3	POLYMERIC HYBRID MATERIALS.....	18
2.4	STIMULI-RESPONSIVE POLYMERS .....	21
2.4.1	Chemical stimuli .....	23
2.4.2	Biological stimuli.....	25
2.4.3	Physical stimuli .....	26
2.5	MODELING OF MAGNETOACTIVE POLYMERS FOR THEIR CONTROL AS MICROACTUATORS.....	37
2.5.1	Modeling of the magneto-mechanical properties of magnetoactive polymers 38	
2.5.2	Modeling of polymer-based films as cantilever beam actuators (electroactive approach).....	41
2.6	MAGNETIC HYBRID FILMS FOR MICROACTUATION.....	45
2.6.1	Synthesis methods to obtain magnetoactive polymeric films.....	45
2.6.2	Advantages, limitations and applications of magnetic hybrid films .....	48

2.7	CONCLUSIONS .....	49
3.	SYNTHESIS AND CHARACTERIZATION OF POLYVINYL BUTYRAL WITH IRON OXIDE NANOPARTICLES (PVB/Fe <sub>2</sub> O <sub>3</sub> ) FILMS.....	51
3.1	INTRODUCTION .....	51
3.2	GENERAL ASPECTS OF POLYVINYL BUTYRAL AND IRON OXIDE NANOPARTICLES.....	52
3.2.1	Polyvinyl Butyral (PVB).....	52
3.2.2	Superparamagnetic iron oxide nanoparticles .....	53
3.3	SYNTHESIS OF THE PVB/FE <sub>2</sub> O <sub>3</sub> FILMS.....	54
3.3.1	Used materials.....	55
3.3.2	Synthesis process .....	55
3.3.3	Obtained samples .....	57
3.4	DYNAMIC MECHANICAL ANALYSIS (DMA) .....	58
3.4.1	DMA operation principle .....	58
3.4.2	Sample preparation and measurement conditions.....	60
3.4.3	DMA results .....	61
3.5	MAGNETIC CHARACTERIZATION OF THE PVB/FE <sub>2</sub> O <sub>3</sub> FILMS.....	65
3.5.1	Vibrating Sample Magnetometer (VSM) operation principle .....	66
3.5.2	Sample preparation and measurement conditions.....	67
3.5.3	Results of the magnetic characterization.....	67
3.6	DYNAMIC CHARACTERIZATION (DISPLACEMENT UNDER MAGNETIC FIELD).....	71
3.6.1	The experimental setup and data acquisition techniques .....	71
3.6.2	Sample preparation and measurement conditions.....	75
3.6.3	Results of the step voltage mode.....	79
3.6.4	Results of the periodic voltage mode .....	88
3.6.5	Conclusions.....	102

4	MODELING AND SIMULATION OF THE DYNAMIC DISPLACEMENTS ..	104
4.1	INTRODUCTION .....	104
4.2	THE CONFIGURATION OF THE SYSTEM.....	104
4.3	MODELING OF THE MICROACTUATOR.....	106
4.3.1	The electric circuit block.....	109
4.3.2	The electromagnet block.....	111
4.3.3	Cantilever magnetization block.....	116
4.3.4	Nonlinear static displacement block .....	118
4.3.5	Linear dynamic displacement block.....	127
4.3.6	Summary of equations.....	130
4.4	PARAMETER IDENTIFICATION.....	133
4.4.1	Electrical circuit block .....	133
4.4.2	Magnetic field block .....	134
4.4.3	Cantilever magnetization block.....	134
4.4.4	Nonlinear static displacement block .....	137
4.4.5	Linear dynamic displacement block.....	137
4.5	SIMULATION OF THE MODEL .....	139
4.5.1	Step response validation.....	139
4.5.2	Oscillatory response validation.....	144
4.6	CONCLUDING REMARKS .....	153
5	CONCLUSION AND PERSPECTIVES .....	155
	Appendix 1 .....	174
	Appendix 2.....	177
	Appendix 3.....	180
	Appendix 4.....	187
	Appendix 5.....	189

# List of figures

Figure 1.1. Schematic representation of a cantilever beam microactuator. ....	13
Figure 2.1. Examples of the applications of microactuators. (a) Four-legged small size robot. Legs are made of a polymer that responds to electric stimulus (dielectric polymer) (Adapted from [28]). (b) Magnetic microgripper for micromanipulation based on a polymer with embedded magnetic nanoparticles. This polymer is activated by magnetic fields (adapted from [29]). (c) Biodegradable magnetically driven micro-swimmer for drug delivery. It is made of a polymeric matrix with iron oxide nanoparticles (adapted from [30]). (d) Mechanisms for eyes muscles emulation using dielectric (DE) polymers (adapted from [31][32]).....	16
Figure 2.2. Comparison between a conventional material and a polymer-based material considering their actuation (Adapted from [33]). ....	17
Figure 2.3. Schematic examples of the different approaches to obtain hybrid materials: (a) the building block approach, (b) the <i>in-situ</i> approach. ....	20
Figure 2.4. Popular applications of polymeric hybrid materials and their relationship with stimuli-responsive polymers. ....	20
Figure 2.5. Classification of the stimuli-responsive polymers according to the stimuli they can respond.....	22
Figure 2.6. General methods to obtain stimuli-responsive polymers and their relationship with polymeric hybrid materials. ....	22
Figure 2.7. Representation of a pH-responsive polymer. It is possible to see the transition from a folded state to unfolded state due to changes in pH and cations formation. ....	24
Figure 2.8. Representation of the actuation of an enzyme-responsive polymer. ....	25
Figure 2.9. Phase diagram showing UCST and LCST behavior (temperature versus polymer weight fraction).....	27
Figure 2.10. Actuation mechanism of the thermally induced shape memory effect in SMP. ....	28
Figure 2.11. Schematic representation of a photo-responsive polymer actuation in drug delivery.....	29

Figure 2.12. Classification of magnetoactive polymers according to the used polymeric matrix (adapted from [106]).	32
Figure 2.13. Arrangement of magnetic moments in (a) ferromagnetic materials and (b) ferrimagnetic materials.	32
Figure 2.14. (a) Representation of the domains inside ferromagnetic and ferrimagnetic materials. When they are under an external magnetic field $H$ , they start to move to the direction of the field (b) in order to be parallel to it like in (c).	33
Figure 2.15. Representative hysteretic behavior of ferromagnetic and ferrimagnetic materials.	34
Figure 2.16. Representation of magnetic moments in superparamagnetic nanoparticles.	35
Figure 2.17. Magnetization curve of a superparamagnetic material.	36
Figure 2.18. Scanning Electron Microscope (SEM) images of magnetic particles in a polymeric elastomer: (left) without external magnetic field, (right) particles aligned after applying a magnetic field, adapted from [123].	40
Figure 2.19. (Left) Schematic structure of the PPy trilayer actuator. (Right) Schematic beam model with the load distribution, adapted from [130].	43
Figure 2.20. Assignment for rigid finite elements and spring-damper elements, adapted from [127].	44
Figure 2.21. Different classifications where magnetoactive polymeric films can be found.	45
Figure 2.22. Schematic representation of the film casting process.	46
Figure 2.23. Steps of the dip-coating technique to obtain polymeric films.	47
Figure 2.24. Steps of the spin-coating technique to obtain polymeric films.	48
Figure 3.1. Chemical structure of the PVB.	52
Figure 3.2. Schema of the synthesis process of the PVB/Fe <sub>2</sub> O <sub>3</sub> films.	56
Figure 3.3. Stress response of different kind of materials: (a) applied periodic strain stimulus, (b) pure elastic response, (c) pure viscous response and (d) viscoelastic response.	59
Figure 3.4. Schematic of a DMA in tension mode.	60
Figure 3.5. DMA results at frequency strains of 0.1 Hz and 1 Hz for: (a) pristine PVB, (b) PVB/Fe <sub>2</sub> O <sub>3</sub> _11% wt Fe, (c) PVB/Fe <sub>2</sub> O <sub>3</sub> _14% wt Fe and (d) PVB/Fe <sub>2</sub> O <sub>3</sub> _17% wt Fe.	62

Figure 3.6. Schematic representation of the polymeric chains: (a) entangled polymeric chains and (b) plasticizer effect of iron oxide nanoparticles on the polymeric chains. ...	63
Figure 3.7. Agglomerates of iron oxide nanoparticles into de PVB matrix.....	64
Figure 3.8. Schema of a magnetic sample magnetometer functioning. ....	66
Figure 3.9. Encapsulation of the samples for magnetic measurements. ....	67
Figure 3.10. Magnetization curves of the PVB/Fe <sub>2</sub> O <sub>3</sub> films measured at room temperature (300 K). ....	68
Figure 3.11. Zoomed view around the zero-magnetization point of the magnetization curves for the samples: (a) PVB/Fe <sub>2</sub> O <sub>3</sub> _11%wt Fe, (b) PVB/Fe <sub>2</sub> O <sub>3</sub> _14%wt Fe and (c) PVB/Fe <sub>2</sub> O <sub>3</sub> _17% wt Fe. ....	69
Figure 3.12. Schematic representation of the actuation system. ....	71
Figure 3.13. Schema of the experimental setup and the flow process to acquire the displacement values of the PVB/Fe <sub>2</sub> O <sub>3</sub> films under external magnetic fields. ....	73
Figure 3.14. Laboratory workspace for the displacement measurements: (a) experimental setup, (b) a close-up view of the electromagnet and the film, (c) the laser sensor conditioner and (d) the controller board for the communications with the PC.....	74
Figure 3.15. Position of the gaussmeter probe to take measurements of the magnetic field generated by the electromagnet at 2 mm of distance. ....	74
Figure 3.16. Two different modalities of input voltage: (a) the step voltage mode and ..	77
Figure 3.17. Design of experiments for the dynamic characterization. Experimental conditions for: (a) step voltage mode and (b) periodic voltage mode.....	78
Figure 3.18. Characteristic underdamped response for a step voltage input. ....	79
Figure 3.19. Responses of the microactuators at three different iron oxide nanoparticles concentrations: (a) PVB/Fe <sub>2</sub> O <sub>3</sub> _17%wt Fe, (b) PVB/Fe <sub>2</sub> O <sub>3</sub> _14%wt Fe and (c) PVB/Fe <sub>2</sub> O <sub>3</sub> _11% wt Fe. ....	81
Figure 3.20. Schematic representation of the iron oxide nanoparticles in the PVB matrix of the microactuators: (a) without magnetic field and (b) when an external uniform magnetic field H is applied. ....	82
Figure 3.21. Responses of the PVB/Fe <sub>2</sub> O <sub>3</sub> _14%wt Fe microactuator at two different step voltage inputs: (a) 30 V and (b) 15 V. ....	85

Figure 3.22. Responses of the PVB/Fe <sub>2</sub> O <sub>3</sub> _14%wt Fe microactuator with different dimensions. (a) Size 1: 15 mm in length, 2 mm in width, 0.018 mm in thickness. (b) Size 2: 15 mm in length, 4 mm in width, 0.018 mm in thickness.....	87
Figure 3.23. Recorded data in the periodic mode tests: (a) periodic voltage input, (b) oscillatory response (displacement) of the microactuator, (c) hysteresis loop of the displacement in function of the input voltage. ....	89
Figure 3.24. Response of a dielectric elastomer: (a) the transition and stable regions of the oscillatory displacement, (b) the effects of the transition region in the hysteresis loops [181]. ....	90
Figure 3.25. Experimental responses of the PVB/Fe <sub>2</sub> O <sub>3</sub> microactuators at 0.1 Hz, 1 Hz, 5 Hz and 10 Hz: (a) PVB/Fe <sub>2</sub> O <sub>3</sub> _17%wt Fe, (b) PVB/Fe <sub>2</sub> O <sub>3</sub> _14%wt Fe and (c) PVB/Fe <sub>2</sub> O <sub>3</sub> _11%wt Fe. ....	92
Figure 3.26. 2D simulation of the cantilever beam exposed to different magnetic field gradients. ....	93
Figure 3.27. Oscillatory input voltage and harmonic displacement for the microactuators of the samples: (a) PVB/Fe <sub>2</sub> O <sub>3</sub> _17%wt Fe, (b) PVB/Fe <sub>2</sub> O <sub>3</sub> _14%wt Fe and (c) PVB/Fe <sub>2</sub> O <sub>3</sub> _11%wt Fe. ....	94
Figure 3.28. Experimental responses of the PVB/Fe <sub>2</sub> O <sub>3</sub> microactuators at 20 Hz, 30 Hz, 40 Hz and 50 Hz: (a) PVB/Fe <sub>2</sub> O <sub>3</sub> _17%wt Fe, (b) PVB/Fe <sub>2</sub> O <sub>3</sub> _14%wt Fe and (c) PVB/Fe <sub>2</sub> O <sub>3</sub> _11%wt Fe. ....	96
Figure 3.29. Experimental responses of the PVB/Fe <sub>2</sub> O <sub>3</sub> _14%wt Fe microactuator at 0.1 Hz, 1 Hz, 5 Hz and 10 Hz, applying voltages of: (a) 0-30 V, (b) 0-15 V. ....	98
Figure 3.30. Oscillatory input voltage and harmonic displacement of the PVB/Fe <sub>2</sub> O <sub>3</sub> _14%wt Fe microactuator with voltages of: (a) 0-30 V and (b) 0-15 V. ....	98
Figure 3.31. Experimental responses of the PVB/Fe <sub>2</sub> O <sub>3</sub> _14%wt Fe microactuator at 20 Hz, 30 Hz, 40 Hz and 50 Hz, with voltages of: (a) 0-30 V and (b) 0-15 V. ....	99
Figure 3.32. Experimental responses of the PVB/Fe <sub>2</sub> O <sub>3</sub> _14%wt Fe microactuators at 0.1 Hz, 1 Hz, 5 Hz and 10 Hz; voltage of 0-30 V and dimensions (length, width, thickness) of: (a) 15 mm, 2 mm, 0.018 mm (size 1) and (b) 15 mm, 4 mm, 0.018 mm (size 2). ...	100
Figure 3.33. Oscillatory input voltage and harmonic displacement of the microactuators with dimensions (length, width, thickness) of: (a) 15 mm, 2 mm, 0.018 mm (size 1) and (b) 15 mm, 4 mm, 0.018 mm (size 2). ....	101



Figure 3.34. Experimental responses of the PVB/Fe <sub>2</sub> O <sub>3</sub> _14%wt Fe microactuator at 20 Hz, 30 Hz, 40 Hz and 50 Hz; voltage of 0-30 V and dimensions (length, width, thickness) of: (a) 15 mm, 2 mm, 0.018 mm (size 1), (b) 15 mm, 4 mm, 0.018 mm (size 2). .....	102
Figure 4.1. Representation of the PVB/Fe <sub>2</sub> O <sub>3</sub> cantilever microactuator.....	105
Figure 4.2. Block representation of the whole actuation process. ....	106
Figure 4.3. Block diagram of the model including each sub-block. ....	106
Figure 4.4. Plane sections remain plane before and after deformation. ....	109
Figure 4.5. Representation of the electromagnet as a series RL circuit.....	109
Figure 4.6. Magnetic field contribution of a current loop at a point P on the z-axis. ....	112
Figure 4.7. Schematic representation of a solenoid. ....	113
Figure 4.8. Schematic representation of a multilayer solenoid.....	114
Figure 4.9. Schema of the large deformation (displacement) of the microactuators. ....	119
Figure 4.10. Algorithm to estimate the value of $\Delta$ .....	125
Figure 4.11. Example of a moment diagram for a cantilever beam with an applied force at its free end. ....	127
Figure 4.12. Relation between $\delta D_{dynamic}$ and $\delta D_{static}$ .....	128
Figure 4.13. Relation between $\delta D_{dynamic}$ and $\delta D_{static}$ incorporating the term $g$ (gain). .....	128
Figure 4.14. Example of test results of magnetization (M) versus magnetic field strength (H). The zoomed area shows the approximately linear behavior of this kind of responses at low magnetic fields. ....	136
Figure 4.15. Conditions to evaluate by the model in the step mode. ....	140
Figure 4.16. Example of the simulated responses for each block of the overall model: (a) applied step voltage of 30 V, (b) current flowing through the electromagnet due to the applied voltage, (c) magnetic field dependent of the current, (d) magnetic force in function of the magnetic field, (e) static displacement of the microactuator free end, and (f) dynamic displacement of the microactuator free end. ....	141
Figure 4.17. Validation of the model for: (a) current and (b) magnetic field, by applying a step voltage of 30 V. ....	142
Figure 4.18 Comparison between simulated and experimental dynamic displacements for the microactuator of the sample PVB/Fe <sub>2</sub> O <sub>3</sub> _14%wt Fe tested at the following conditions:	

(a) 30 V of step and size 1, (b) 15 V of step and size 1, and (d) 30 V of step and size 2. .....	144
Figure 4.19. Conditions to evaluate by the model in the periodic voltage mode.....	145
Figure 4.20. Comparison between simulated and experimental dynamic displacements for the PVB/Fe <sub>2</sub> O <sub>3</sub> _14%wt Fe microactuator, tested in the oscillatory voltage mode. The test was carried out for the microactuator of size 1 by applying a voltage of 0-30 V and frequency of: (a) 0.1 Hz, (b) 1 Hz and (c) 5 Hz. ....	147
Figure 4.21. Examples of different kind of magnetic force distributions along the cantilever microactuator.....	149
Figure 4.22. Comparison between simulated and experimental dynamic displacements for the microactuator of the sample PVB/Fe <sub>2</sub> O <sub>3</sub> _14%wt Fe, tested in the oscillatory voltage mode. The tests were carried out for the microactuator of size 1 by applying a sine voltage of 0-15 V and frequencies of: (a) 0.1 Hz, (b) 1 Hz and (c) 5 Hz. ....	150
Figure 4.23. Comparison between simulated and experimental dynamic displacements for the microactuator of the sample PVB/Fe <sub>2</sub> O <sub>3</sub> _14%wt Fe, tested in the oscillatory voltage mode. The tests were carried out for the microactuator of size 2 by applying an amplitude of 0-30 V and frequencies of: (a) 0.1 Hz, (b) 1 Hz and (c) 5 Hz. ....	151
Figure 4.24. Estimated transfer function's bode diagram. ....	152

## Appendix figures

Figure A3. 1. Last block of the overall block-structured model representing the linear dynamics and proposed in chapter 4. ....	180
Figure A3. 2. Interface of the System Identification Toolbox of MATLAB.....	180
Figure A3. 3. Import data in the time domain.....	181
Figure A3. 4. Declaration of input, output, starting time and sampling time. ....	182
Figure A3. 5. Input and output behavior of the dynamic system. The input (u1) corresponds to the static displacement, while the output (y1) is the experimental dynamic displacement.....	182
Figure A3. 6. The model was estimated as a polynomial model. ....	183
Figure A3. 7. Different polynomial model structures. ....	184
Figure A3. 8. Chosen orders of the ARX model.....	184

Figure A3. 9. Agreement between model and experimental responses. ....	185
Figure A3. 10. The model is sent to the workspace of MATLAB. ....	185
Figure A3. 11. Discrete transfer function from the selected polynomial model. ....	186
Figure A3. 12. Obtained continuous time transfer function. ....	186
Figure A4. 1. Interpretation of ARX models. Dynamic system with input $u(t)$ , error $e(t)$ and output $y_t$ . ....	187

# List of tables

Table 2.1. Classification of EAPs and their characteristic examples.....	30
Table 2.2. Modeling of the magneto-mechanical properties of magnetoactive polymers at different scales. ....	38
Table 3.1. Raw materials for the synthesis of PVB/Fe <sub>2</sub> O <sub>3</sub> films.....	55
Table 3.2. PVB and FeCl <sub>2</sub> · 4H <sub>2</sub> O content for the three different samples. ....	57
Table 3.3. Values of elastic modulus (E') and glass transition temperature (Tg), obtained at 0.1 Hz and 1 Hz, for all the samples. ....	62
Table 3.4. Magnetic parameters for the magnetization curves for the three magnetic films concentrations. ....	70
Table 3.5. Magnetic field strength and magnetic flux density in function of current and applied voltage. All these values were taken at 2 mm from the central axis of the electromagnet. ....	75
Table 3.6. Maximum displacement and settling displacement values for the three microactuators with different iron oxide nanoparticles content.....	83
Table 3.7. Peak time and settling time values for the three microactuators with different iron oxide nanoparticles content. ....	84
Table 3.8. Maximum displacement and settling displacement values for the PVB/Fe <sub>2</sub> O <sub>3</sub> _14%wt Fe microactuator at 30 V and 15 V of step voltage.....	86
Table 3.9. Peak time and settling time values for the PVB/Fe <sub>2</sub> O <sub>3</sub> _14%wt Fe microactuator at 30 V and 15 V of step voltage.....	86
Table 3.10. Maximum displacement and settling displacement values for the PVB/Fe <sub>2</sub> O <sub>3</sub> _14%wt Fe microactuator of size 1 and size 2.....	87
Table 3.11. Peak time and settling time values for the PVB/Fe <sub>2</sub> O <sub>3</sub> _14%wt Fe microactuator of size 1 and size 2.....	88
Table 4.1. Comparison between experimental and simulated settling displacements. ..	144
Table 4.2. Comparison between experimental and simulated maximum displacements. ....	152

# CHAPTER 1

## INTRODUCTION

This thesis was accomplished in a dual-degree modality between the consolidated group of Synthesis and Characterization of Materials –Facultad de Ingeniería Mecánica y Eléctrica (FIME), Universidad Autónoma de Nuevo León (UANL), México, and the research group of Methodologies for Automatic Control and for Design of Mechatronic Systems (MACS), department of Automatic Control and Micro-Mechatronic Systems – FEMTO-ST institute, Université Bourgogne Franche-Comté (UBFC), France.

### 1.1 CONTEXT

Research and development of polymeric hybrid materials have been widely discussed in recent times. A polymeric hybrid material is considered as a polymeric matrix (organic phase) having one or more inorganic phases dispersed inside it [1]. The synthesis of these materials allows to exploit the exceptional properties of polymers (toughness, good elongation, processability, lightweight and low cost) and they can be combined with the properties of other materials. This combination of properties makes polymeric hybrid materials suitable for specific applications.

Some polymeric hybrid materials have the ability to change their properties in response to an external stimulus and they can return to their original state on termination of the stimulus; these materials are called stimuli-responsive polymers [2]. There are different

stimuli at which these materials could respond, such as changes in pH, temperature, electric or magnetic fields, among others. Stimuli-responsive polymers that respond to external magnetic fields are called magnetoactive polymers and they are usually formed by magnetic particles dispersed within a polymeric matrix [3].

Magnetoactive polymers have very promising applications as microactuators. An actuator could be considered as a device that transforms energy from an external source into mechanical energy in a controllable manner [4]. The current trend suggests that the miniaturization of these devices should be implemented in applications such as magnetic micromanipulation, biomedical or biomimetics [5].

The use of magnetoactive polymers as microactuators permits to obtain devices with the following advantages [5]:

- Flexibility
- Lightweight and low-density
- Relative low cost of processing
- Optical transparency
- Remote and wireless control
- Operation in many different media including air, vacuum, conducting and non-conducting liquids.

A number of researches have been published on magnetic microactuators technology using magnetoactive polymers, for example as micropumps in peristaltic devices which can aid the blood circulation by venous contraction [6], microactuators for minimally invasive surgery and handling cells [7], microgrippers of manipulating microscale objects [8], for drug delivery applications which enable long-term and targeted drug release [9], microvalves for microfluidic applications [10] or even to emulate the movement of natural muscles due to its high flexibility [11].

Despite the significant applications of microactuators using magnetoactive polymers, there are many interrogations to fully understand and exploit these materials. The prediction of the constitutive nonlinear dynamic responses of magnetoactive polymers when subjected to magnetic fields poses a tremendous challenge [12]. Moreover, magnetoactive polymers shows frequency dependence and hysteretic behavior that must

be also identified [13]. The understanding of all these concepts is necessary due to the high positioning accuracy and precision required for the expected applications [14].

Mathematical models describing the dynamic responses of magnetoactive polymers are the basis to obtain positioning and hysteresis control of these materials. Mathematical models can be based on physical principles involving the properties of the material [15]. This approach allows to visualize the optimal magnetic and mechanical properties configuration from a materials science point of view. In consequence, it is necessary to make a previous analysis of the physical properties of the magnetoactive polymers and their influence on the dynamic response in order to propose an accurate model.

Several models of the dynamic response of magnetoactive polymers based on physical principles have been previously reported [16][17][18][19]. However, many questions are still to be answered. Moreover, there is not a general solution for these models because the dynamic response is dependent on each particular case. Therefore, the modeling of the dynamic response of magnetoactive polymers must be performed by considering the properties of the specific polymeric matrix, the kind of magnetic particles and the coupled magnetic-mechanical properties obtained by the combination of both elements [12][20].

The magnetoactive material used in this thesis was selected following the research line of the group Synthesis and Characterization of Materials, FIME, UANL. In 2013, magnetic hybrid films of polyvinyl butyral (PVB) with iron oxide nanoparticles ( $\text{Fe}_2\text{O}_3$ ) were synthesized and characterized [21]. The term film was given due to their thickness, which is less than 1 mm ( $\sim 18 \mu\text{m}$ ). These magnetic hybrid films behave as magnetoactive polymers and their potential for applications as microactuators was observed. Subsequently, other researches were performed to deepen the understanding of the physical properties of these magnetic hybrid films, specially dielectric and mechanical properties [22][23]. Further, the behavior of a cantilever microactuator of copper with a section of magnetic hybrid film of PVB/ $\text{Fe}_2\text{O}_3$  added to its free end was evaluated [24]. Experiments were conducted by applying different magnetic fields and measuring the displacement of the free end. A mathematical model for the measured responses was proposed. Results showed that PVB/ $\text{Fe}_2\text{O}_3$  films attached to the free end of the copper

cantilever promotes a magnetic response, however, copper reduces flexibility to the microactuator. Based on these results, the possibility of exploring the PVB/Fe<sub>2</sub>O<sub>3</sub> films as cantilever microactuators without any other added element was posed. Moreover, developing a control of this kind of microactuator would be advantageous to exploit potential applications where precise positioning is required.

## 1.2 JUSTIFICATION

As seen in the context described in the last section, there is a great potential to use magnetoactive polymers as microactuators. However, there are still many challenges to be assessed to understand and predict the behavior of these materials when they are subjected to external magnetic fields. The understanding and prediction of these materials is necessary to obtain the positioning and hysteresis control that the application as microactuator demands.

The understanding of the behavior of these materials can be obtained by the analysis of both their physical properties (magnetic-mechanical) and their influence on the behavior when the material is under magnetic fields. The prediction of the behavior of these materials can be estimated by mathematical models. Mathematical models with a physical approach involve the physical properties of magnetoactive polymers [12][20]. By giving a physical approach, it is possible to visualize the optimal properties configuration from materials science point of view. This may permit to modify the synthesis processes and methods in order to achieve the required properties.

Based on the previously mentioned, this study is focused on the modeling of the dynamic response of microactuators composed by magnetic hybrid films of polyvinyl butyral (PVB) with iron oxide nanoparticles (Fe<sub>2</sub>O<sub>3</sub>). These films behave as a magnetoactive polymer and their potential as microactuator was evaluated in cantilever beam configuration, according to Figure 1.1.



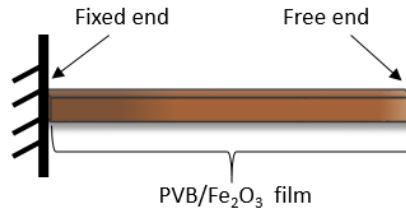


Figure 1.1. Schematic representation of a cantilever beam microactuator.

The dual-degree modality of this thesis was established to take advantage of the experience of each institution in their research fields: on the one hand, to continue with the well-defined research line on magnetoactive polymers as well as with the experience on characterization and the relation structure-properties of materials (FIME, UANL, México); on the other hand, the experience on microdevices, dynamic characterization and modeling (FEMTO-ST, UBFC, France). It is also expected that the model works as a starting point to establish a control of the behavior of the material for its application as microactuator.

Considering all above, the hypothesis and objectives of the research project were established, and they are described in next sections.

### 1.3 HYPOTHESIS

The dynamic behavior of PVB/Fe<sub>2</sub>O<sub>3</sub> films as microactuators can be predicted by a model that relates the physical properties of the films (magnetic and mechanical) with their dynamic response (displacement) when subjected to external magnetic stimulus.

### 1.4 OBJECTIVES

The main objective of the project is to model the dynamic behavior of a *polymer-based hybrid films* consisting of a polymer matrix of polyvinyl butyral (PVB) with iron oxide nanoparticles (Fe<sub>2</sub>O<sub>3</sub>), functioning as cantilever microactuator.

To achieve the main objective, four goals are proposed:

- 1 To perform the characterization of the physical (magnetic and mechanical) properties of the films.
- 2 To carry out experimental studies of the response (displacement) produced by a magnetic field in PVB/Fe<sub>2</sub>O<sub>3</sub> films as cantilever microactuators.
- 3 To relate the properties (mechanical-magnetic) of the PVB/Fe<sub>2</sub>O<sub>3</sub> films with the displacement of the material as a function of an external magnetic field.
- 4 To get a dynamic model for the behavior of the film and to validate it.

## 1.5 THESIS ORGANIZATION

This thesis is divided in five chapters:

The **first chapter** corresponds to the context and justification of the problematic, as well as the hypothesis and objectives of the thesis.

The **second chapter** deals in detail with the different kinds of stimuli responsive polymers and the significance to apply this kind of polymers as microactuators, given more attention to polymers that respond to magnetic fields (magnetoactive polymers). The importance to understand and predict the behavior of magnetoactive polymers is also explained. Moreover, a survey on the modeling of microactuators is presented.

The **third chapter** explains thoroughly the synthesis process to obtain the magnetic hybrid films of PVB/Fe<sub>2</sub>O<sub>3</sub>. The methods followed to perform the characterization of the physical properties and the dynamic behavior under static and oscillatory magnetic fields are also described. In addition, the results of the obtained results are discussed in this chapter.

The **fourth chapter** deals with the followed method to obtain the model describing the dynamic behavior of PVB/Fe<sub>2</sub>O<sub>3</sub> films as cantilever microactuators. The validation of the model is also performed in this section.

The **fifth chapter** corresponds to the general conclusions and future perspectives according to the results and analysis of this research.

# CHAPTER 2

## HYBRID MATERIALS, STIMULI-RESPONSIVE POLYMERS AND MICROACTUATION

### 2.1 INTRODUCTION

Polymeric hybrid materials and stimuli-responsive polymers are considered as good candidates for microactuators. However, these materials remain under study for two main reasons: the physical properties must be well understood to establish their influence on the response and a control of the response is required to obtain an optimal performance. It is considered that a good control design starts from predictive models of the responses. Thus, the modeling of these polymers is also an important research subject. In this chapter, the significance to use polymer-based materials as microactuators is presented in section 2.2. The concept and generalities of polymeric hybrid materials and stimuli-responsive polymers are exposed in sections 2.3 and 2.4, respectively. A special emphasis is given to polymers that respond to magnetic stimuli (magnetoactive polymers) which are the target of this thesis. The importance to understand and predict the behavior of magnetoactive polymers by modeling is explained in section 2.5. Finally, section 2.6 shows the

advantages to use magnetoactive polymeric films on microactuation along with their limitations.

## 2.2 SIGNIFICANCE OF POLYMER-BASED MATERIALS IN MICROACTUATION

Actuators are fundamental components of many industrial and natural processes. An actuator is, basically, a converter that transforms any kind of energy source into a mechanical energy [4]. Examples of actuators are motors, valves, relays, pumps, grippers, and so on. Recent trends suggest the miniaturization of actuators for the development of smaller systems, especially for industrial or medical applications.

Microactuators are actuators that can produce small force and motion at microscales (from 1 millimeter upper to 0.1 micrometer lower limits) [25][26]. They are used for applications like small-size robots or micromanipulation. In other cases, when microactuators are made of biodegradable or biocompatible materials, they can be used in applications such as artificial muscles or microrobots for drug delivery [27]. Figure 2.1 shows some examples of the mentioned applications.

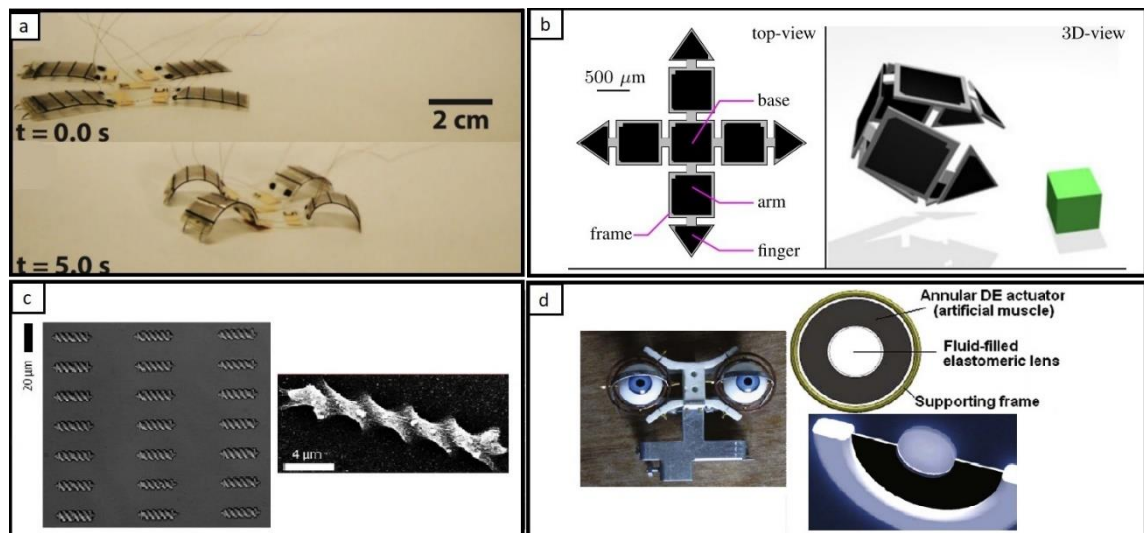


Figure 2.1. Examples of the applications of microactuators. (a) Four-legged small size robot. Legs are made of a polymer that responds to electric stimulus (dielectric polymer) (Adapted from [28]). (b) Magnetic microgripper for micromanipulation based on a polymer with embedded magnetic nanoparticles. This polymer is activated by magnetic fields (adapted from [29]). (c) Biodegradable magnetically driven micro-swimmer for drug

delivery. It is made of a polymeric matrix with iron oxide nanoparticles (adapted from [30]). (d) Mechanisms for eyes muscles emulation using dielectric (DE) polymers (adapted from [31][32]).

We can observe from all the examples in Figure 2.1 that actuation at micrometric scales requires, among others, the ability to respond to certain stimulus, flexibility and lightweight. In this way, conventional materials used for actuating tasks (e.g. metals and their alloys, or ceramics) may be replaced by polymer-based materials in order to obtain more efficient actuation at such scales. Otherwise, the rigidity of conventional materials causes the need of articulations driven by motors or pneumatic systems. In consequence, the systems become bulky and several subcomponents such as screws, nuts or gearbox at very small scales would be needed. Moreover, the several joints of subcomponents may produce friction or clearance, which makes difficult to obtain accurate positioning or fast response times [33]. Figure 2.2 shows schematically the difference to use a conventional material and a polymer-based material for a polyarticulated arm. It is shown in figure that the use of polymer-based materials avoids the need of additional components to perform the same actuation.

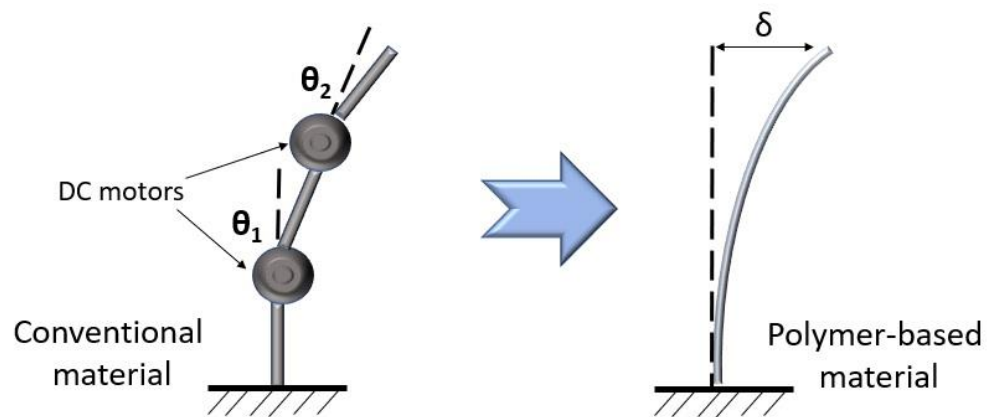


Figure 2.2. Comparison between a conventional material and a polymer-based material considering their actuation (Adapted from [33]).

There are many efforts focused on the development of polymer-based materials to be used as microactuators. Polymeric hybrid materials and stimuli responsive polymers are considered as good candidates for these applications. They correspond to two different

research areas. However, it is possible to obtain new materials by combining characteristics and properties of both. Next sections of this chapter give a frame of the efforts focused on these topics.

### 2.3 POLYMERIC HYBRID MATERIALS

Polymeric hybrid materials are materials composed of an organic matrix (a polymer) with one or more inorganic components [1]. The importance of these materials lies in the exceptional properties that can be achieved from the synergy of the properties of each individual component.

The final properties of hybrid materials depend mostly on the interface interactions between organic and inorganic components. Interface interactions can be weak, for example van der Waals or hydrogen bonding. Weak interactions are preferred when a dynamic behavior is needed, for example when some mobility of a component is necessary for the final application [34]. However, interactions may be also very strong, such as ionic or covalent bonding. Strong interactions avoid agglomerations or phase separation between components and they markedly influence the final mechanical, electrical or thermal properties.

The inorganic components added into the polymeric matrix to form a hybrid material commonly show a morphology of particles, whiskers or fibers. Basically, there are two different approaches to obtain a hybrid material. These two approaches are: the building block approach and the *in-situ* formation of inorganic components [35].

In the building block approach, the inorganic building blocks completely conserve (or at least partially) their molecular integrity throughout the formation of the hybrid material. One example of this approach is the addition of nanoparticles with attached reactive groups. These reactive groups enhance the interactions between inorganic building blocks and the polymeric matrix. Figure 2.3(a) shows the schematic representation of this approach.

In the *in-situ* formation of inorganic components approach, the hybrid material is obtained by the chemical transformation of a precursor material. In this case, the properties of the final material are totally different from the original precursor. The main advantage of this approach is the use of low temperatures and pressure to process some ceramics (e.g. oxides) [36]. The most common way for the *in-situ* formation is the synthesis by the sol-gel method. This method starts from a colloidal suspension of a solid material called *sol*, which can be the precursor of the inorganic component with a polymer (or monomer). Then, a precursor hybrid material is formed (called *gel*) as the product of some chemical reactions occurring in the suspension. The final hybrid material is obtained after solvent evaporation [37] and, in some cases, after post-chemical treatments. One example of the *in-situ* formation of nanoparticles into a polymer is schematically shown in Figure 2.3(b).

Polymeric hybrid materials could be applied in bulk, as films, or shaped in any form [34]. Polymeric hybrid materials are used as sensors[38][39], microactuators [40] [41][42], mechanical reinforcements for building, automotive or aircraft fields [43][44][45][46], absorbent materials to remove pollutants in water or other media [47][48], scaffolds for tissue engineering [49], among many others.

Mostly, polymeric hybrid materials used for sensors and microactuators are obtained by the incorporation of stimuli-sensitive inorganic components into the polymeric matrix. This results in a special kind of polymeric hybrid material called stimuli-responsive polymer. Figure 2.4 shows some relevant applications of polymeric hybrid materials and their relationship with the stimuli-responsive polymers. The route concerning this thesis is highlighted in green.

It is important to clarify that stimuli-responsive polymers correspond to another research field and they could be obtained by other methods. Generalities concerning stimuli-responsive polymers are described in section 2.4

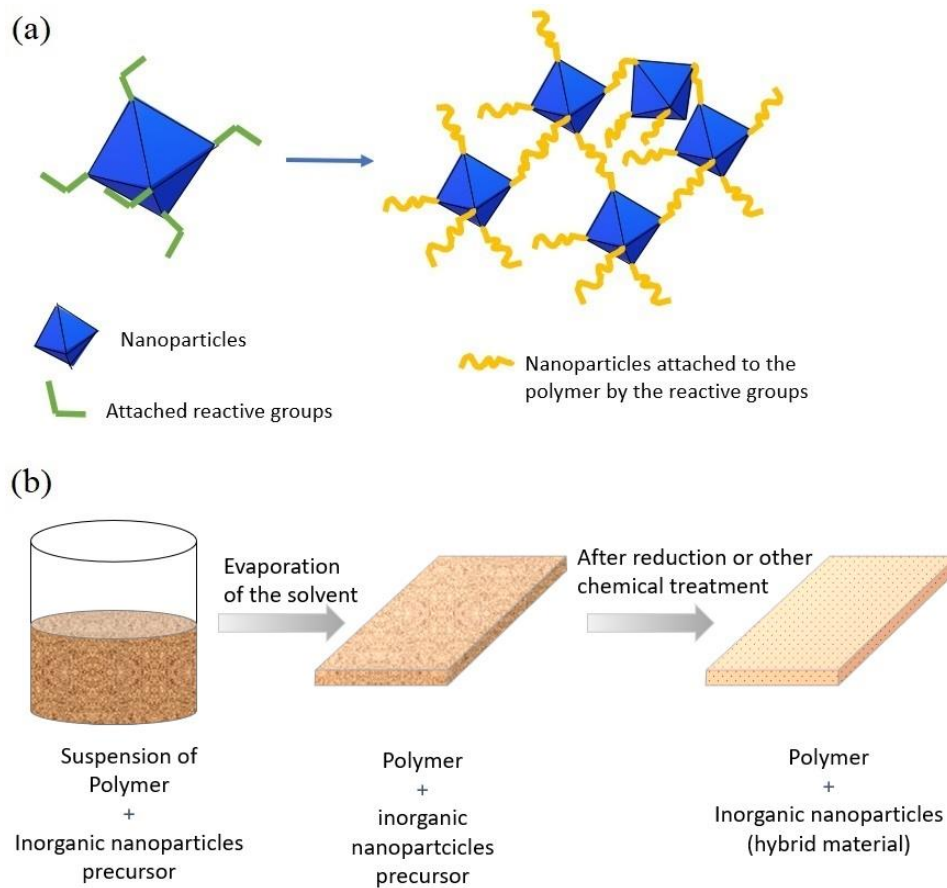


Figure 2.3. Schematic examples of the different approaches to obtain hybrid materials: (a) the building block approach, (b) the *in-situ* approach.

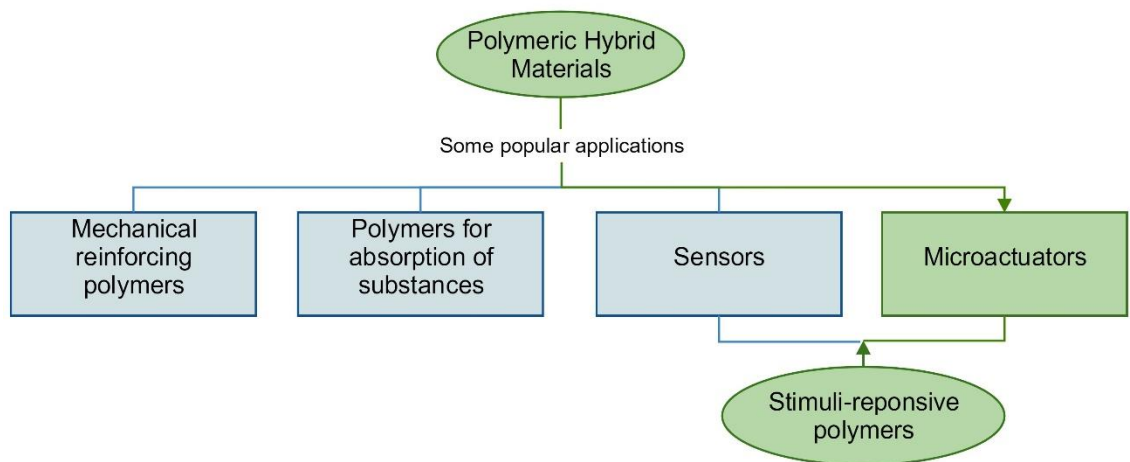


Figure 2.4. Popular applications of polymeric hybrid materials and their relationship with stimuli-responsive polymers.



## 2.4 STIMULI-RESPONSIVE POLYMERS

There is a wide research line focused on stimuli-responsive polymers. This kind of polymers can be also found in literature as smart polymers, active polymers or soft active materials [50].

Stimuli-responsive polymers have the ability to change some chemical or physical aspects such as their shape, solubility, permeability, mechanical/optical/electrical or magnetic properties when subjected to a variation of environmental conditions. These variations can be: changes in pH, temperature, light, magnetic or electric field, and so forth [51]. The change of properties of a stimuli-responsive polymer could be reversible: it returns to its initial state when the external stimulus is removed.

Stimuli at which polymers respond can be classified into three categories: biological, chemical and physical stimuli [52][53]. Biological stimuli correspond to changes of some biological substances, such as enzymes, glucose or other metabolites. Chemical stimuli are related to changes in pH and some ionic or redox reactions. Physical stimuli could be variations in temperature, light, electric or magnetic fields. These three categories are summarized in the diagram of Figure 2.5. Moreover, there are some polymers with the ability to respond to more than one stimulus.

Synthesis of stimuli-responsive polymers can be generally achieved by two methods. One method is conducted by the addition of stimuli-sensitive functional groups along the polymer backbone [50][54]. The second method involves the incorporation of some stimuli-sensitive inorganic components within the polymeric matrix, thus obtaining polymeric hybrid materials [1][55][56][57]. Figure 2.6 shows the two methods to obtain stimuli-responsive polymers and their relationship with polymeric hybrid materials. The route concerning this thesis is colored in green.

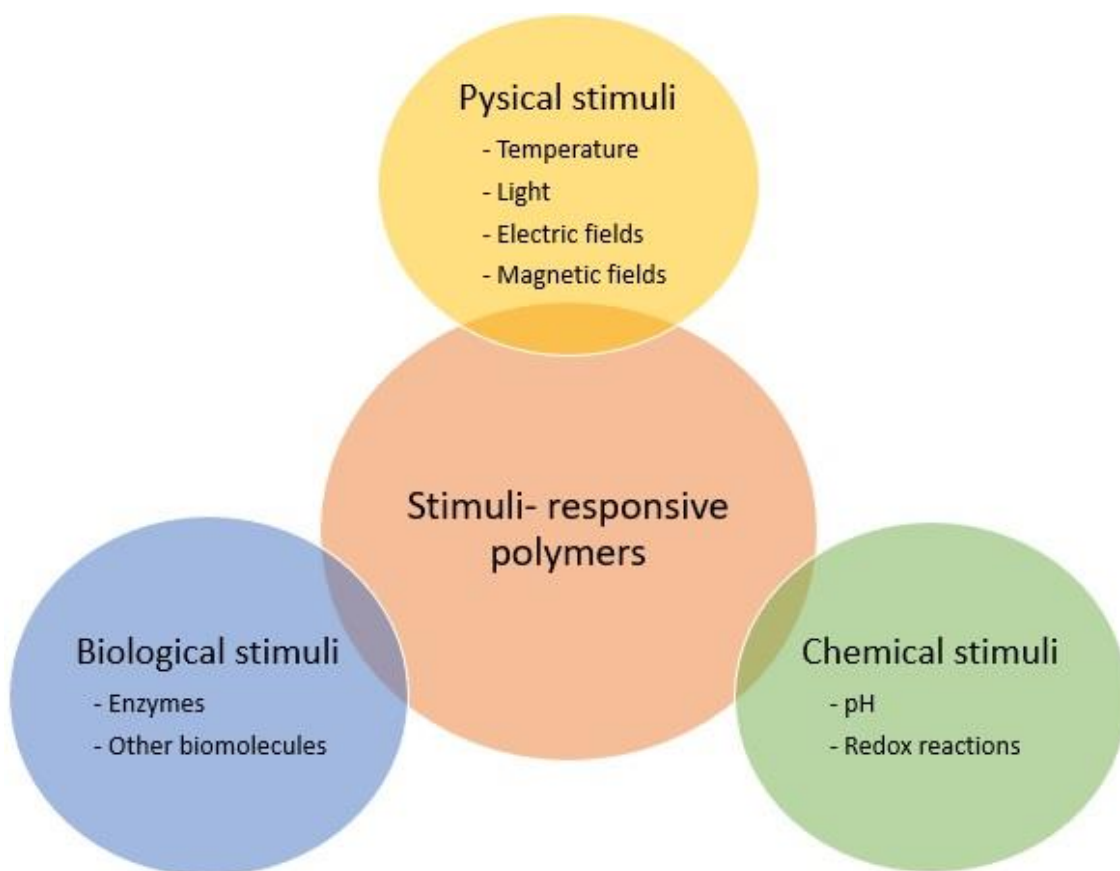


Figure 2.5. Classification of the stimuli-responsive polymers according to the stimuli they can respond.

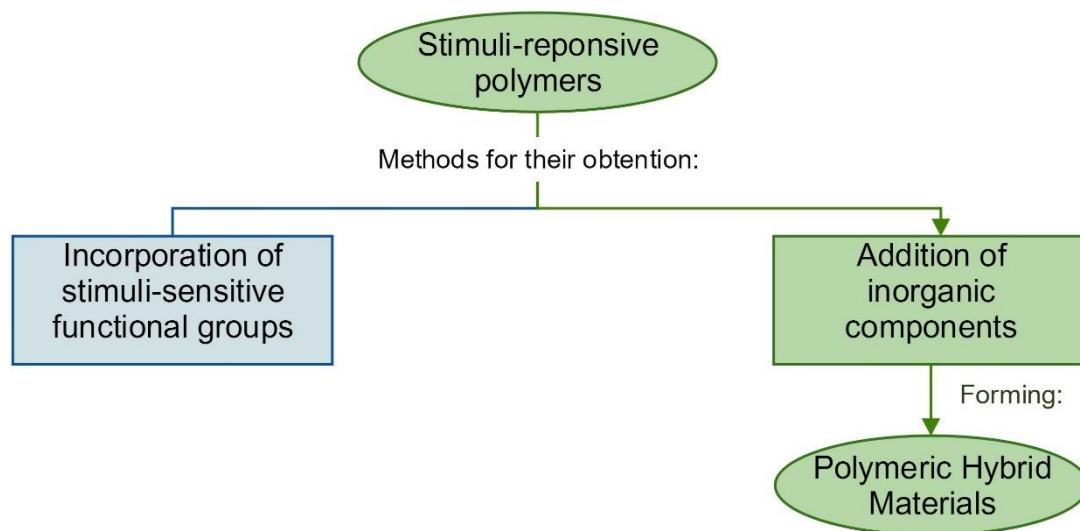


Figure 2.6. General methods to obtain stimuli-responsive polymers and their relationship with polymeric hybrid materials.

A brief description of the activation mechanism for the different stimuli-responsive polymers is presented in next sections. Representative examples of applications of this kind of polymers are also given. More emphasis will be addressed to the polymers that respond to magnetic fields (magnetoactive polymers) which are the polymers of main interest for this research.

## **2.4.1 Chemical stimuli**

### *2.4.1.1 pH-responsive polymers*

pH-responsive polymers accept or release protons in function of pH changes. They have acidic or basic groups in their structure linked to the polymer backbone such as carboxy or amino groups [58]. As pH-responsive polymers work in aqueous media, they can be defined as polyelectrolytes. A polyelectrolyte is a macromolecule that can dissociate to give polymeric ions when dissolved in water or other ionizing solvents [59]. A change of pH promotes the ionization of the acidic or basic groups and generates anions or cations. These anions or cations cause an extension of the polymeric chains due to electrostatic repulsion [60]. Figure 2.7 shows a schematic example of a pH-responsive polymer. In this figure, the formation of cations after a change in pH is represented. Also, the transition from a folded state to an expanded state due to electrostatic repulsion is also shown.

pH responsive polymers are considered to be used in pharmaceutical applications such as on-demand drug delivery [61][62]. This application can be achieved due to detectable changes in pH by comparing a healthy and an unhealthy biological system, for example the human body.

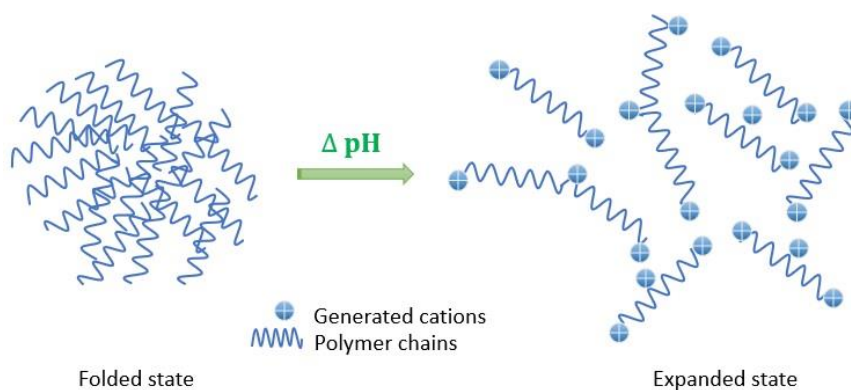


Figure 2.7. Representation of a pH-responsive polymer. It is possible to see the transition from a folded state to unfolded state due to changes in pH and cations formation.

#### 2.4.1.2 Redox-responsive polymers

Redox-responsive polymers respond to oxidation or reduction stimulus. Hence, redox-responsive polymers are divided into two categories: polymers sensitive to oxidation and polymers sensitive to reduction [63].

The principal method to obtain redox-responsive polymers is by the addition of redox-sensitive units to the polymer backbone. These units may be disulfides or acid labile groups. Examples of redox-responsive polymers are disulfide groups attached to polyethylene glycol (PEG) polypropylene sulfide (PPS) copolymer [64], acid labile groups embedded to polyanhydrides [65] or poly lactic/glycolic acid (PLGA) [66], among others.

The most common applications of redox-responsive polymers use the redox stimuli from biological systems. These polymers respond by breaking the interactions between reactive groups and the polymeric backbone due to differences in redox states of biological fluids. This promotes a disassembly of the polymer [63]. Applications involve carrier and delivery of drugs [67][68][69], proteins [70] or nucleic acids [71][72].

## 2.4.2 Biological stimuli

### 2.4.2.1 Enzyme-responsive polymers

Enzymes are catalysts for biochemical reactions within cells [73]. Enzyme-responsive polymers are polymers that respond to enzyme dysregulations. These responses are caused by the incorporation of elements capable of recognize enzymes. Common recognition elements include amino acid sequences attached to the polymer [74].

Generally, enzyme-responsive polymers are studied to be used in biomedical applications like drug delivery [73][75][76][77], biosensing [57] [77][2] or as scaffolds in tissue engineering [78][79]. The mechanism of actuation for these applications strongly depends on the abnormally regulation of enzymes within a biological system. Enzyme dysregulation is usually a response of pathological disorders, such as cancer, cardiovascular disease, inflammations, etc. [74]. Therefore, enzyme-responsive polymers react to these enzyme changes by degradation or swelling. Figure 2.8 shows a representation of the actuation mechanism of an enzyme-responsive polymer.

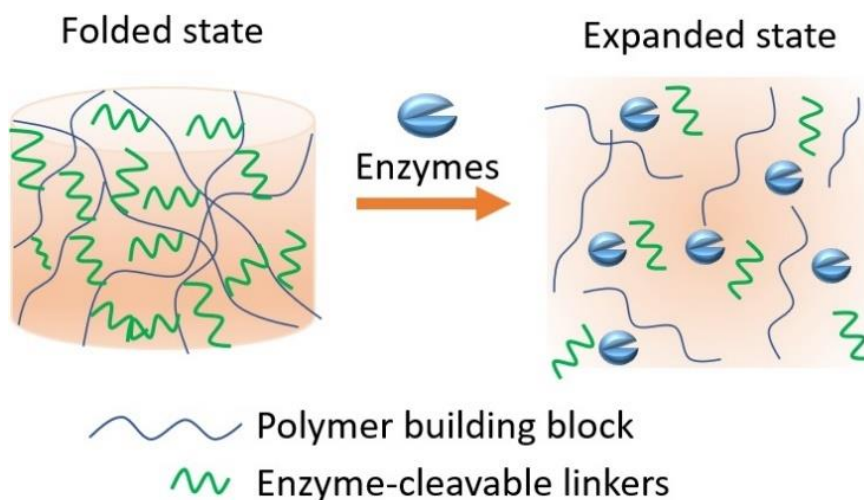


Figure 2.8. Representation of the actuation of an enzyme-responsive polymer.

#### *2.4.2.2 Different biomolecules-responsive polymers*

Biomolecules-responsive polymers include all polymers that are sensitive to changes of specific biomolecules, such as glucose, DNA and some proteins [80]. These polymers respond to stimuli by the same actuation mechanism of the enzyme-responsive polymers. In consequence, they could also be utilized in biomedical applications acting as drug carriers or detectors of diseases.

The detection of the biomolecular stimuli is achieved by attaching responsive units to the polymer to be used. For example, in this category, glucose sensitive polymers are the most investigated to control insulin dose for diabetics in response to glucose levels [81]. For this application, glucose oxidase (GOx) is commonly added as the glucose sensing unit to the backbone of some polymers or hydrogels [82].

### **2.4.3 Physical stimuli**

#### *2.4.3.1 Thermo-responsive polymers*

Thermo-responsive polymers are sensitive to changes in temperature and they modify their microstructural features in function of these changes. According to the literature, there are three types of thermo-responsive polymers [83]:

- Lower Critical Solution Temperature (LCST)
- Upper Critical Solution Temperature (UCST)
- Shape memory polymers (SMPs)

LCST and UCST polymers operate in aqueous media. They adjust their structure when their solubility becomes different due to variations in temperature. LCST polymers are monophasic at lower temperatures and biphasic above a certain temperature. Examples of LCST polymers are poly(N-isopropylacrylamide)s (PNIPAAms) [84] or poly(2-oxazoline)s (POxs) [85]. Meanwhile, UCST polymers show the opposite behavior: they are monophasic at certain temperature and biphasic below a critical temperature. Polyacrylamide (PAAm) [86] or polyacrylic acid (PAAc) [87] are examples of UCST

polymers. These changes of phase correspond to a macroscopical behavior of swelling or deswelling. Figure 2.9 is a phase diagram showing a representation of the swelling and deswelling of polymers with UCST and LCST behavior.

The sensitivity to changes in temperature of UCST and LCST polymers allows their well manipulation for on-demand drug delivery applications, by the fact that the human body temperature is always set in the same range (35°C-37°C). It is well known that any alteration of the human body temperature corresponds to a disease signal. Hence, there is no need to consider any other condition of organs, tissues or cells. This entails a great advantage over other stimuli-responsive polymers for these applications [83].

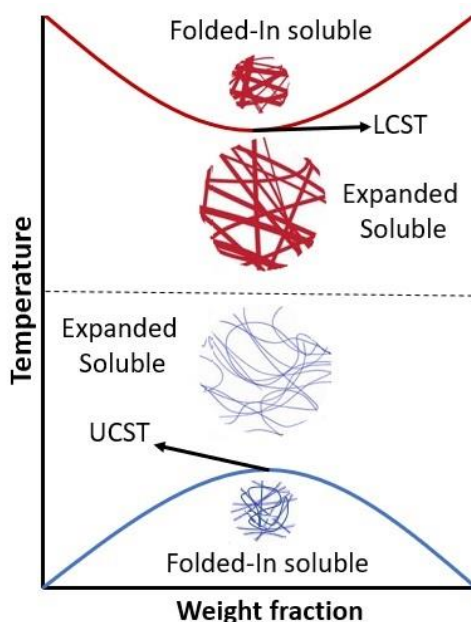


Figure 2.9. Phase diagram showing UCST and LCST behavior (temperature versus polymer weight fraction).

On the other hand, shape memory polymers (SMPs) exhibit a change of shape due to a variation of temperature and they generally actuate in a non-liquid media. SMPs are formed by soft segments (amorphous segments) and hard segments (crystalline segments). The changes in shape are caused by microstructural changes of these segments. They are commonly based on copolymers of polyurethanes and polyetheresters [88].

The actuation mechanism of SMPs starts by having a permanent shape A that could be deformed and fixed into a temporary shape B. After application of the thermal stimulus, the polymer could recover its initial permanent shape A. Figure 2.10 shows schematically this activation mechanism. In addition to temperature variations, there are some SMPs able to respond to changes in light, electric or magnetic fields and other stimuli.

Applications of SMPs are in medical devices [89][90][91], soft robotics [92][27], smart electronic devices [93], among others.

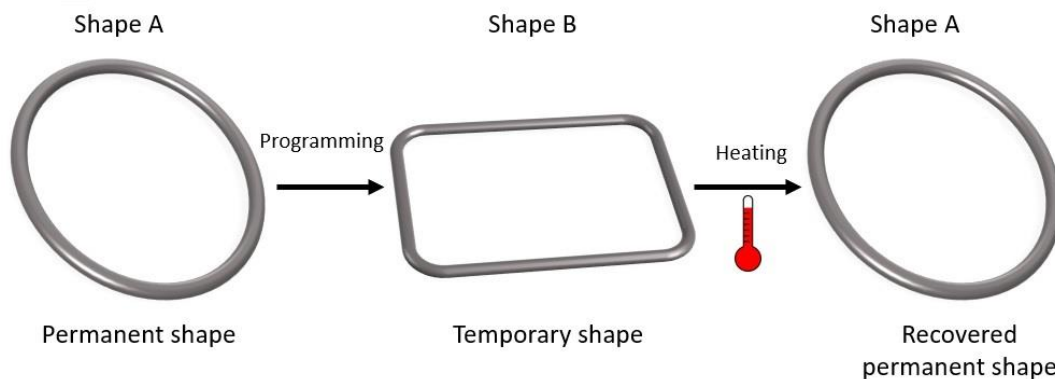


Figure 2.10. Actuation mechanism of the thermally induced shape memory effect in SMP.

#### 2.4.3.2 Photo-responsive polymers

Photo-responsive polymers respond to electromagnetic waves by changing their properties such as viscosity, conductivity, solubility, morphology, and so on [94]. The photo-response is obtained by attaching photo-sensitive groups such as O-nitrobenzyl or hyperbranched polyglycerols to the polymer backbone. The response of these polymers strongly depends on their photon energy absorbance capacity. This photon energy absorbance capacity is related to the energy band-gap of the corresponding photosensitive group [95].

The major advantage of photo-sensitive polymers is that they could be stimulated remotely and the modulation of wavelength, intensity or irradiation time of the electromagnetic transmitter could be relatively easy [94][96][97]. However, the light of the environment should be highly controlled to avoid interferences, which can be difficult in some cases.



Moreover, the scarce light penetration inside bodies should be considered for biological applications [98].

The most popular application of photo-responsive polymers is in drug delivery. In this case, polymers change their morphology in function of incident electromagnetic waves which produces swelling or degradation. After that, the content inside the polymer can be released [97], as schematically shown in Figure 2.11.

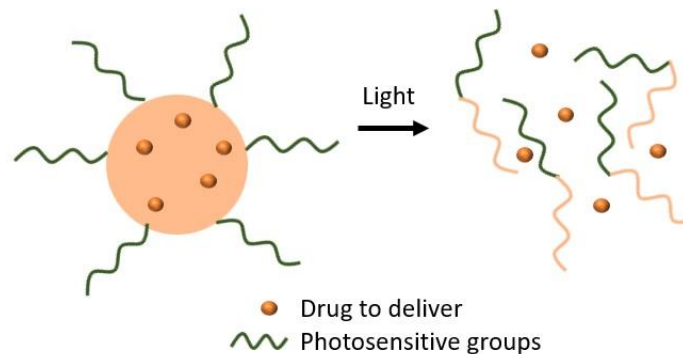


Figure 2.11. Schematic representation of a photo-responsive polymer actuation in drug delivery.

#### 2.4.3.3 Electro-responsive polymers (electroactive polymers)

Electroactive polymers can be stimulated to bend, stretch or contract by using electrical excitation [99]. The electroactive behavior of these materials is achieved by chemical modifications of the polymeric structure or by the incorporation of elements able to promote such behavior, e.g. the incorporation of particles sensitive to electrical stimuli. Because of their ability to emulate some biological operations, the most attractive applications for these polymers are in biomimetics as artificial muscles or as actuators in biological inspired robotics [100].

Electroactive polymers can be divided into two categories according to their activation mechanism:

- Electronic electroactive polymers (eEAPs)
- Ionic electroactive polymers (iEAPs).

Electronic electroactive polymers (eEAPs) are mainly driven by electric field or coulomb forces. They could be: dielectric, piezoelectric, electrostrictive or ferroelectric polymers, as well as liquid crystal elastomers. The main advantage of these polymers is their ability to operate in air and not only in aqueous media, compared with other stimuli-responsive polymers. Moreover, they can hold the induced deformation or displacement while they are activated under DC voltage. In addition, they show a rapid response time of milliseconds [100]. These advantages make eEAPs good candidates for robotic applications [99][101]. However, the reported limitation of these polymers are the required activation fields considered as high (more than 100 V/ $\mu\text{m}$ ) [70] [71].

Meanwhile, ionic electroactive polymers (iEAPs) are driven by transportation or diffusion of ions. Therefore, the activation of iEAPs consists of two electrodes and one electrolyte. Differently to eEAPs, the activation voltage of iEAPs is considered as low. iEAPs could be activated by applying 1-5 V and they can achieve higher strains in comparison with eEAPs. One of the limitations of these materials is that they must operate in a wet state or solid electrolyte. Moreover, they show slower response times by comparing with eEAPs. Slower response times in iEAPs are related to the ion transportation needed for their activation (which is a transportation of mass). Examples of iEAPs are ionic polymer gels, ionic polymer-metal composites or conducting polymers [100][101].

Table 2.1 shows the general classification of the electroactive polymers (EAPs), including examples of each category.

Table 2.1. Classification of EAPs and their characteristic examples.

<b>Electronic EAP</b>	<b>Ionic EAP</b>
Dielectric EAP	Ionic polymer gels
Electrostrictive EAP	Conductive polymers
Ferroelectric polymers	Ionic polymer metallic composites
Liquid crystal elastomers	

#### 2.4.3.4 Magneto-responsive polymers (Magnetoactive polymers)

Magnetoactive polymers respond to changes in magnetic fields. They are hybrid materials composed by magnetizable particles embedded in a polymeric matrix [102]. In these materials the magnetic and mechanical properties are coupled each other [20].

First reported classifications of magnetoactive polymers handle two main categories based on the kind of polymeric matrix. These two categories are: ferrogels (also called magnetoactive polymer gels) and magnetoactive elastomers (also called magnetorheological elastomers). However, some researches in magnetoactive polymers based on other kind of polymeric matrixes, such as thermoplastic or thermosetting, have also been reported [102][103][104].

A ferrogel is formed by a cross-linked polymer network containing a ferrofluid, which is a colloidal dispersion of monodomain magnetic particles [13]. Magnetoactive elastomers are composed of high elastic polymeric elastomers with micromagnetic particles [105].

In 2017, Musaddique *et al.* reported magnetoactive polymers based on thermoplastic or thermosetting polymers as a third category in the classification of magnetoactive polymers. This third category was called magnetic plastics [106]. For this thesis, the classification of magnetoactive polymers will be treated according to the diagram shown in Figure 2.12 (adapted from [106]).

As polymers are in general diamagnetic materials, the actuation mechanism of magnetoactive polymers occurs when an external magnetic field produces a force to the embedded magnetic particles, producing a response of the whole material. This bulk response is mainly attributed to the interfacial interactions between magnetic particles and the polymer [107]. Magnetoactive polymers exhibit two different types of response in presence of an external magnetic field which are: the response by magnetic moments or torques, and the response by magnetic induced normal forces [108].

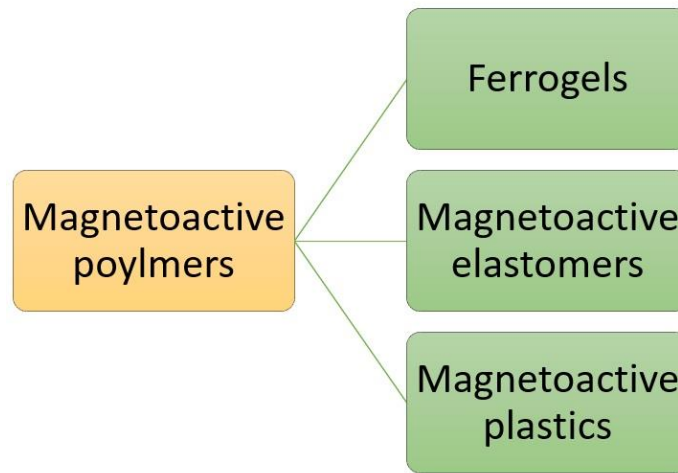


Figure 2.12. Classification of magnetoactive polymers according to the used polymeric matrix (adapted from [106]).

Usually, embedded magnetic particles are ferromagnetic or ferrimagnetic materials, such as iron, nickel, cobalt and some iron oxides. These particles exhibit similar behavior although they are different in structure. In a ferromagnetic material the adjacent magnetic moments are parallel, and their magnitude is uniform, as schematically shown in Figure 2.13a. In a ferrimagnetic material adjacent magnetic moments are antiparallel, however, net magnetic moment results from the difference between their unequal magnitudes, as illustrated in Figure 2.13b [109].

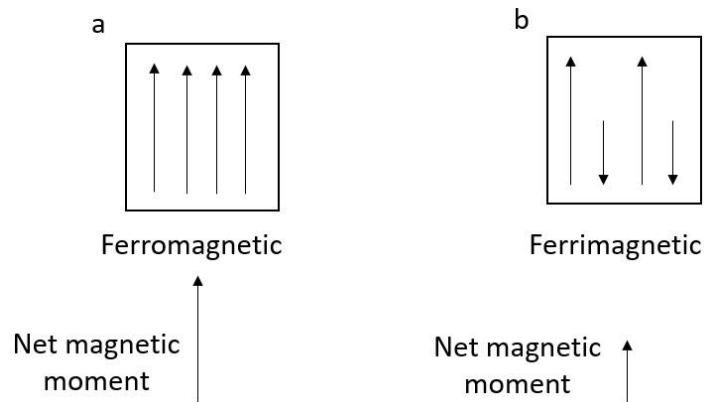


Figure 2.13. Arrangement of magnetic moments in (a) ferromagnetic materials and (b) ferrimagnetic materials.

Ferromagnetic and ferrimagnetic materials in bulk present regions called Weiss domains or magnetic domains at temperatures lower than their Curie temperature. Such domains are small regions (from 20 nanometer to some micrometers [110]) within magnetic moments or net magnetic moments are aligned to the same direction as shown in Figure 2.14a. However, if an external magnetic field ( $H$ ) is applied, magnetic moments start to move to the direction of the field (Figure 2.14b). This process is called magnetization ( $M$ ) [111][112].

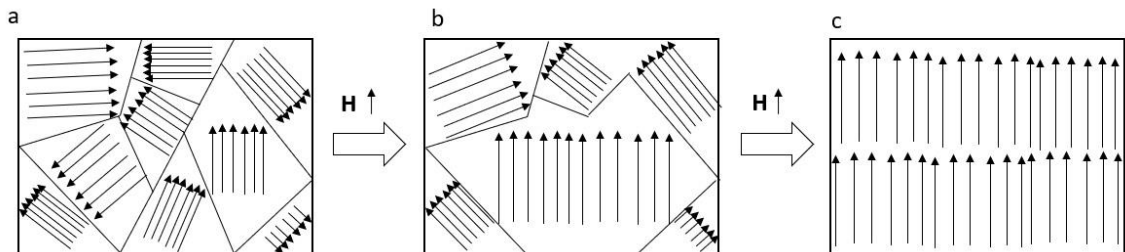


Figure 2.14. (a) Representation of the domains inside ferromagnetic and ferrimagnetic materials. When they are under an external magnetic field  $H$ , they start to move to the direction of the field (b) in order to be parallel to it like in (c).

Ferromagnetic and ferrimagnetic materials reach their saturation magnetization ( $M_s$ ) when almost all their magnetic moments are aligned parallel to the external magnetic field ( $H$ ), as shown in Figure 2.14c. However, when the external magnetic field is removed, these materials do not relax back to zero; instead, they retain some degree of magnetization (remanent magnetization). Thus, the external magnetic field must be reversed ( $-H$ ) to drive the magnetization to zero again. The negative magnetic field required to drive magnetization to zero is called the coercive force ( $H_c$ ). When the material is repeatedly magnetized in the positive and negative direction, the graph of magnetization ( $M$ ) versus magnetic field ( $H$ ) describes the hysteric curve shown in Figure 2.15. The dash line shown in this figure represents the magnetization obtained when the material is magnetized for the first time [111][112].

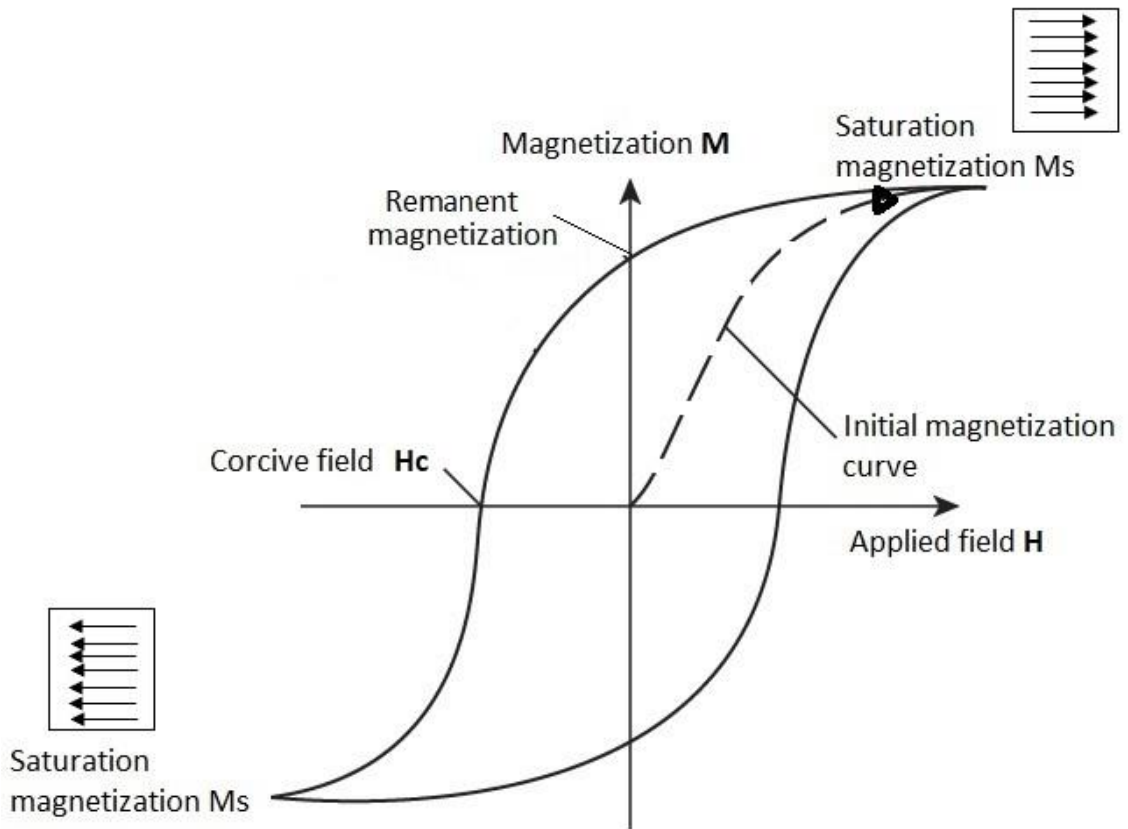


Figure 2.15. Representative hysteretic behavior of ferromagnetic and ferrimagnetic materials.

The magnetic response of ferromagnetic and ferrimagnetic materials show size-related effects [110]. If such materials are presented in separated nanoparticles instead of bulk, they will show a different magnetic behavior.

Magnetic nanoparticles are considered as single-domains due to their sizes (usually less than 20 nm). Magnetic moments in nanoparticles are randomly oriented in the absence of an external magnetic field. When an external magnetic field is applied, the magnetic moments of the nanoparticles exhibit spin rotation and tend to have an orientation parallel to the field [113]. The single-domain condition permits the magnetic moments to move freely with the external magnetic field, as shown in Figure 2.16. Moreover, if the external magnetic field is removed, the single-domain condition of magnetic nanoparticles allows to recover their zero magnetization without hysteretic losses. This magnetic behavior is called superparamagnetism [112][113]. Figure 2.17 shows the characteristic magnetization curve of a superparamagnetic material.

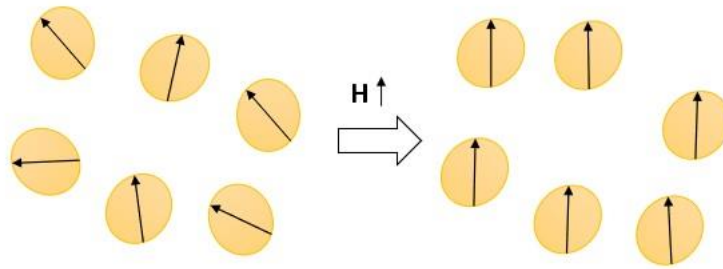


Figure 2.16. Representation of magnetic moments in superparamagnetic nanoparticles.

Magnetoactive polymers could exhibit different kinds of actuation such as deflection, contraction/elongation and coiling [107]. The kind of actuation strongly depends on the initial orientation of the magnetic dipoles of the nanoparticles, the position and orientation of the external magnetic field, the nature of the polymeric matrix and the resultant magneto-mechanical properties [114].

It is important to pay close attention to the selection of the polymeric matrix and the magnetic component to be used in order to obtain a magnetoactive polymer suitable for its final purpose [106]. For example, magnetic components in bulk with ferromagnetic behavior (as the one shown in Figure 2.15) are a good option for applications when high saturation magnetization and remanent magnetization are needed. However, these magnetic materials tend to agglomerate in low viscous polymers due to magnetic dipole interactions (magnetic attraction). In this case, polymers with high viscosity or viscosity increasing agents should be used [115].

Nonetheless, superparamagnetic nanoparticles are good for applications in robotics because of their negligible remanent magnetization and their low magnetic attraction. Therefore, nanoparticles can be dispersed relatively easy into the polymeric matrix. However, magnetic nanoparticles tend to form agglomerates to reduce the energy associated with the high surface area to volume ratio of the nano-sized particle [116]. The dispersion of magnetic nanoparticles into the polymeric matrix must be improved during the synthesis process.

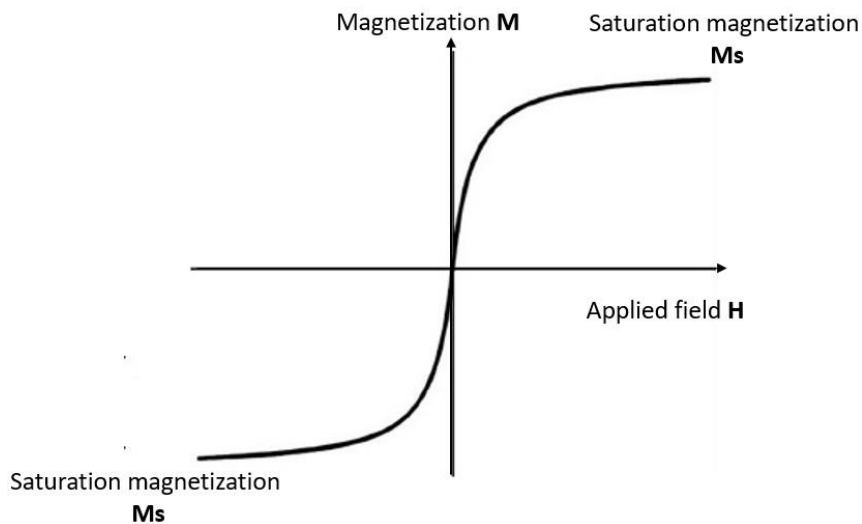


Figure 2.17. Magnetization curve of a superparamagnetic material.

When magnetic particles are randomly dispersed into the polymeric matrix, the obtained mechanical and magnetic properties are usually non-directional. This kind of materials are called isotropic magnetoactive polymers. In some cases, magnetic particles could be aligned by applying strong magnetic fields during the synthesis process. By this process, magnetic dipoles get an easy axis to rotate by applying an external magnetic field. In this case, mechanical properties depend strongly on the orientation of the magnetic field and the particles alignment. These materials are called anisotropic magnetoactive materials [117][114].

In general, magnetoactive polymers exhibit a great potential for large strain actuators because of the large quantity of particles usually added and the large interfacial area between particles and the polymeric matrix [102]. They could be applied for bearings and vibration absorbance [118][119], soft robotic microactuators [29], in medicine [30], among others.

Physical properties of polymeric matrixes and magnetic components in their neat state are different compared to the physical properties obtained from the synergy of both in a



magnetoactive polymer. Because of that, the physical properties of the whole system (polymer/magnetic component) should be characterized in order to understand its behavior before any further application [106]. The prediction of the response of these materials has become an important requirement to obtain the positioning control that applications as microactuators demand. The prediction of the response of these materials can be estimated by modeling.

## 2.5 MODELING OF MAGNETOACTIVE POLYMERS FOR THEIR CONTROL AS MICROACTUATORS

Magnetoactive polymers show many advantages for their application as microactuators. Such advantages are among others their ability to operate without the need of external wires or any physical contact (wireless control), their possibility to operate in different environments (air or liquid) or their large strains. However, as previously mentioned, the preliminary understanding of the physical properties of these materials and their relationship with the dynamic response is fundamental in order to obtain controllable microactuators.

Models of magnetoactive polymers reported in the literature are generally focused on two main purposes:

- to understand their magneto-mechanical properties.
- to understand their dynamic response (actuation) when subjected to magnetic fields.

A broader view of models focused on the magneto-mechanical properties of magnetoactive polymers is described in section 2.5.1 The literature review was focused on the reported models for magnetoactive polymers using thermoplastic matrixes (magnetoactive plastics), which is the kind of polymeric matrix concerning this thesis. However, a lack of information about the modeling of these materials was notorious. In consequence, the review is centered on the modeling of magneto-mechanical properties of magnetoactive elastomers and ferrogels. This information will be useful as a reference point in the analysis of the magnetoactive plastic used in this thesis.

The dynamic response (actuation) of magnetoactive plastics is different in comparison with the response of ferrogels or magnetoactive elastomers, mainly due to the different mechanical properties of the polymeric matrixes. It was found in the literature that the way in which magnetoactive plastics as cantilever microactuators respond is similar to that of some electroactive polymers. Because of that, a review of the modeling of electroactive polymeric films as cantilever microactuators is presented in section 2.5.2 This will also serve as a reference point for the analysis of the topic corresponding to this thesis.

### 2.5.1 Modeling of the magneto-mechanical properties of magnetoactive polymers

Models focused on the magneto-mechanical properties of magnetoactive polymers deal generally with internal interactions and how they affect the mechanical and magnetic behavior. This approach of modeling may be divided based on the length scales [120], as shown in Table 2.2. Examples of modeling at all the mentioned scales are presented below.

Table 2.2. Modeling of the magneto-mechanical properties of magnetoactive polymers at different scales.

<b>Length scale</b>	<b>Model</b>
<b>Nano/micro</b>	Single-particle
<b>Micro</b>	Particle-particle interactions Interactions of magnetic particles with polymeric chains
<b>Meso</b>	Magneto-mechanical properties of the whole system
<b>Macro</b>	Dynamic response (actuation) of the whole material when subjected to a magnetic field

For example at nano/micro scale, a model that describes the mechanism of magnetic deformation surrounding a single particle in magnetoactive elastomers was reported [121]. The model was focused on the deformation caused by the alignment of the particle with an applied magnetic field. The alignment of the particle was supposed to be a rearrangement of its entire mass and not only the alignment of its internal magnetic

moment vector. The alignment of the entire mass of the particle was considered to occur only in low viscous polymeric matrixes. It was theoretically shown that the whole polymeric matrix does not rotate, except in the vicinity of the magnetic rotative particle. Thus, this behavior causes mechanical deformation and mechanical stresses in the vicinity of the particle. The authors suggest that the sum of the magnetic-field-induced internal stresses over single particles may lead the effect of magnetodeformation.

Models at microscale are focused on interactions between particles (of sizes in the order of micrometers) in magnetoactive elastomers. These particle-particle interactions are mainly caused by their magnetic moments and their approach due to attraction forces, particularly in low viscous polymeric matrixes. An example of this kind of models was reported in [122]. This analysis shown that particle interactions can be weak but also strong enough to form clusters, depending on the applied magnetic field. A mathematical expression describing these interactions was proposed. However, this kind of interactions is not applicable for magnetoactive polymers with particles at the nanoscale (nanoparticles) that use more rigid polymeric matrixes, including thermoplastics or thermosets. In this case, nanoparticle interactions are considered to be very small because of the particle size [116] and the high viscosity of the polymers limits their approximation.

As example of modeling at mesoscales, the relationship between the viscoelastic properties of the polymeric matrix and the magnetization of the magnetic particles was studied in [123]. It was observed that particles (typically of 3 to 5 microns) rearrange forming chains when they are under magnetic fields, as shown in Figure 2.18. A model was proposed by assuming spherical morphology of the particles and considering them as dipoles interacting each other in the chain conformation. The results were capable of examining mechanical and magnetic properties of the magnetoactive elastomers. However, some error coefficients were used to fit the analysis with experimental values. The study conclude that particle interactions decrease with particle volume content. Based on the previous analysis, another model of liquid silicone caoutchouc with dispersed carbonyl iron (2-4 micrometers) was reported [124]. The grouping and ungrouping of the particles by applying and removing the magnetic field, respectively, was modeled. The conclusion was that the field-induced growth of chains in weak-to-moderate fields

enhances the magnetic susceptibility of the material while at stronger fields the magnetic susceptibility goes down due to magnetic saturation.

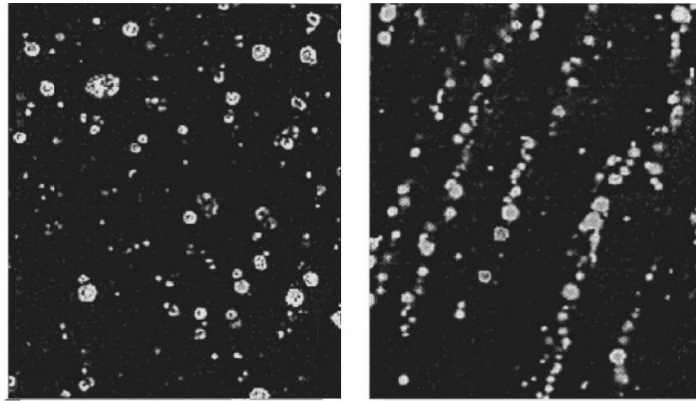


Figure 2.18. Scanning Electron Microscope (SEM) images of magnetic particles in a polymeric elastomer: (left) without external magnetic field, (right) particles aligned after applying a magnetic field, adapted from [123].

Furthermore, a three-dimensional magneto-viscoelastic model was proposed [125]. The objective was to model the change of the viscoelastic properties of the polymeric matrix by applying a magnetic field and considering the nanoparticles content. The model of the viscoelastic properties was performed using fractional derivative methods. Then, a mechanism of particle-matrix interaction was added to the model and the dependence of the viscoelastic changes due to magnetic fields was introduced by Helmholtz free energy theory. Finally, a correction factor was added. The model was experimentally proved having a 4% of error.

For modeling at macroscales, a model of the dynamic response of a hydrogel with magnetic nanoparticles was proposed [18]. The model was formed on the thermodynamic second law. The chemical potential of the surrounding liquid environment, the applied magnetic field and the deformation resulting in swelling or deswelling were introduced to the model. The model was established for control purposes in a future application as drug delivery.

Moreover, the dynamic response of a sphere and a cylinder made of a magnetoactive elastomer was modeled. The modeling was accomplished considering the magneto-mechanical properties of the material. The use of classical Maxwell equations was

proposed for the modeling of the magnetic field distribution and mechanical equilibrium equations were used in order to predict the axial deformation of the sphere and the cylinder when subjected to magnetic fields [120].

The dynamic response of a membrane (200 nm in thickness) of polyamide with iron oxide ( $\text{Fe}_3\text{O}_4$ ) nanoparticles was modeled. The model describes the magnitude of the particle displacements within the polymeric matrix in function of the nanoparticle size, the magnetic field strength and the nanoparticles volume content. The sample was placed in a coupled magnetic field between two different coils. Nanoparticle sizes showed a greater influence on the deformation of the polymeric matrix than the nanoparticle volume content [108].

Besides, a model for the response of a cantilever actuator made of a magnetoactive elastomer was developed by Maxwell stress tensors for the magnetic part and kinematic theories for the response. A comparison with finite element simulations using COMSOL Multiphysics was performed, resulting in good agreement with the analytical model [126].

Although magnetoactive plastics may show different responses than those mentioned here, the presented examples of models can serve as reference for the understanding and the analysis of these magnetoactive plastics. The adaptation could be performed by considering the specific properties of thermosets or thermoplastic matrixes such as their elastic modulus, viscosity or thermal transition temperature ( $T_g$ ). The characterization of the coupled magneto-mechanical properties of the obtained magnetoactive plastic is also important for modeling purposes.

### **2.5.2 Modeling of polymer-based films as cantilever beam actuators (electroactive approach)**

This review is focused on the reported models of some electroactive polymeric films as cantilever beam actuators. This approach was considered in order to take advantage of the similarities between electroactive polymers and magnetoactive plastics in response to magnetic fields as cantilever microactuator. These similarities include their damping

vibrations and nonlinear responses as well as their response at periodic stimuli showing hysteresis. Some models of electroactive polymers also involve the concept of electrical dipoles, which could be taken analogously to the magnetic dipoles in the magnetoactive plastics.

Models of electroactive polymers are usually categorized as black box, white box and gray box models. Black box models are mathematical models that approximate data during experiments (empirical). They are relatively simple because physical analysis of phenomena is not included. However, black box models have limited applications because their development is focused on a specific test and testing every possible input is difficult or time-consuming. White box models predict the behavior of a system by describing all the involved physical and chemical phenomena. White box models predict behaviors quite accurately, but they are complex. Therefore, they are not suitable for real time control of actuators. Finally, gray box models are based on well understood physical theories combined with other parameters that could be experimentally estimated [127][128][129]. This review will be focused on gray box models.

A model describing the displacement of a cantilever microactuator based on an electroactive polymer was presented in [130]. This microactuator is a trilayer cantilever formed by an ionic-electroactive polymer composed by polypyrrole (PPy) and polyvinylidene fluoride (PVDF), as shown in Figure 2.19. The model is based on nonlinear Euler-Bernoulli equations for large beam deflections under continuous distributed loads. An effective elastic modulus of the whole microactuator was estimated. The load was analogous to the internal transportation of ions in and out to the layers. A model of the displacement for the free end of the cantilever microactuator was therefore obtained.

A different approach to model the displacement of a trilayer polypyrrole (PPy)-polyvinylidene fluoride (PVDF) cantilever microactuator was presented in [131]. The model was carried out in two steps: first, the equations of motion of the actuator were obtained; second, the dynamic parameters of the model were identified, including the stiffness of the materials and the damping coefficient for each joint. Results model the

displacement of the free end of the microactuator. The model showed good agreement with the experimental values.

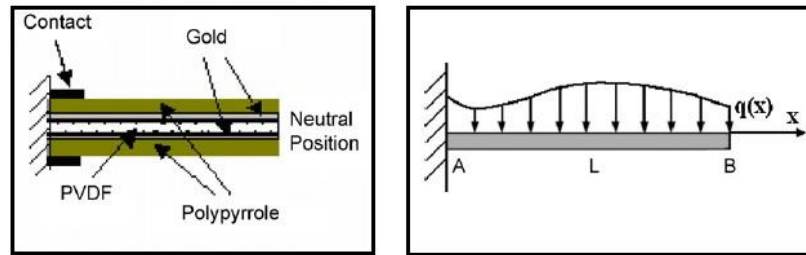


Figure 2.19. (Left) Schematic structure of the PPy trilayer actuator. (Right) Schematic beam model with the load distribution, adapted from [130].

The classical beam theory was also applied to model the displacement of the free end of a bimorph IPMC cantilever microactuator [128]. The microactuator was made of polypyrrole and a commercial polymer called Kapton. Gold electrodes were used to promote the ionic diffusion. The elastic modulus of the gold electrodes was neglected. Results showed an error of 5% when the thickness of the electrodes is one thousand times thinner than Kapton. If the electrodes were thicker than the mentioned relation, the error could be bigger [132].

Due to the characteristic viscoelasticity of polymeric matrixes, these microactuators usually demonstrate frequency-dependent responses. In consequence, some researches have proposed models involving the viscoelastic properties of polymers in order to get a better prediction. For example, for the trilayer PPy and PVDF, another approach for modeling the displacement of the PPy-PVDF microactuator free end was developed in [133]. This model is based on the combination between the electrical behavior and the mechanical properties of the electroactive polymer. The mechanical part is focused on the modeling of the viscoelastic behavior of the polymers by a Kelvin-Voigt model approach. The elastic modulus of each individual material was introduced instead of an equivalent modulus. The proposed model was able to predict the curvature of the cantilever microactuator.

A model based on the Euler-Bernoulli theory for cantilever beams was adapted to include viscoelastic parameters [134]. This model was discretized and linearized to be time-

dependent in order to model the transient vibrating response at a step input of force. Moreover, the hysteretic response by applying a periodic triangle input of force was modeled. The model showed well accuracy for microactuators with low hysteresis. However, the model loose its accuracy as the hysteresis increases.

An electromechanical model of an ionic electroactive polymer was reported in [127]. The model was obtained by the rigid finite element method which discretizes elements in small sections. The discretized sections are named rigid parts. These rigid parts represent the inertial elements along the cantilever microactuator (see Figure 2.20). Each rigid part is joined to the other by a spring-damper system. Accurate results were obtained for the displacement of each discrete point along the cantilever length.

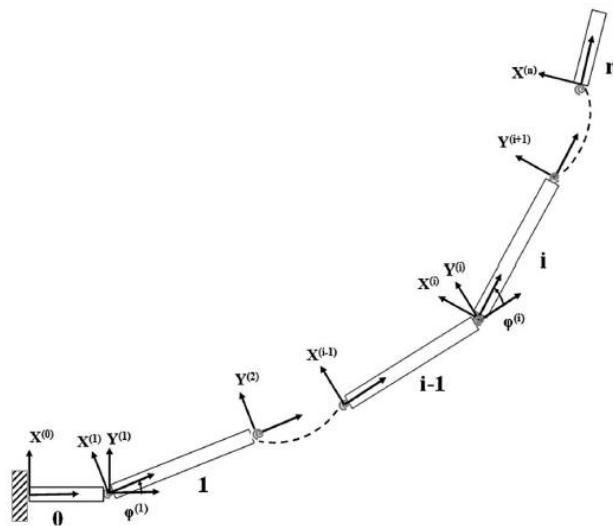


Figure 2.20. Assignment for rigid finite elements and spring-damper elements, adapted from [127].

Another important factor to be considered in the modeling of polymer-based films as cantilever microactuators is the geometry. From the mechanics point of view, the moment area of inertia influences the displacement of cantilever beams. Therefore, for rectangular cantilever microactuators, width and thickness have an effect on the final displacement. The length of the microactuator is also important. These geometrical aspects (specially thickness) depend strongly on the synthesis process to obtain the polymeric films.



Generalities and methods to obtain magnetoactive polymeric films (or magnetic hybrid films) for their application as cantilever microactuators is described in the next section.

## 2.6 MAGNETIC HYBRID FILMS FOR MICROACTUATION

Magnetic hybrid films are a kind of magnetoactive polymer with overall thickness less than 1 millimeter (quasi-2D systems) [98]. Such films are composed of a polymeric matrix with magnetizable materials embedded inside. Usually, magnetizable materials are magnetic metals (e.g. nickel particles) or iron oxides.

Magnetoactive polymeric films are considered as hybrid materials because they are formed by inorganic components embedded in organic materials. In addition, they can be considered as stimuli-responsive polymers because they respond to external magnetic fields. Figure 2.21 shows the classifications where magnetoactive polymeric films can be found.

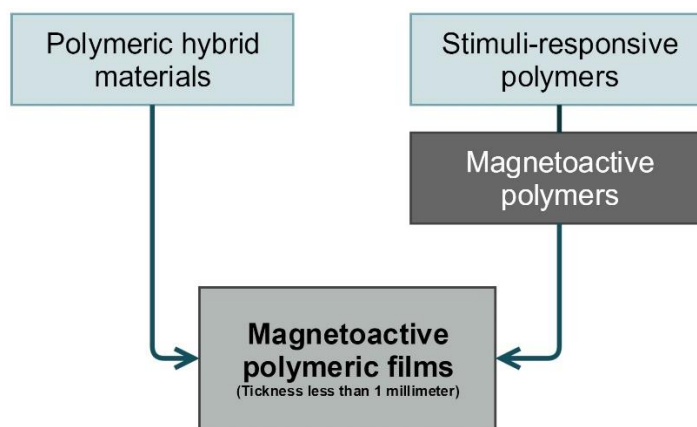


Figure 2.21. Different classifications where magnetoactive polymeric films can be found.

### 2.6.1 Synthesis methods to obtain magnetoactive polymeric films

As magnetoactive polymeric films are considered as hybrid materials, they are commonly synthesized following one of the approaches described in section 2.2. These approaches are: the building block approach and the *in-situ* formation of the components. Some synthesis methods of both approaches utilize solvents to promote chemical reactions.

These solvents must to be dried to obtain the final material. The formation of the film shape depends greatly on the way that the dissolved material is deposited to dry the solvent. For example, films can be obtained from pouring a dissolved material on a substrate, then the solvents and remanent water are dried until the formation of the film. This technique is called film casting.

There are many reports in the literature that apply the film casting technique to form magnetoactive polymeric films. For example, polyimide with iron oxide nanoparticles ( $\gamma$ - $\text{Fe}_2\text{O}_3$ ) was synthesized *in-situ* and the formation of the films was conducted by casting the diluted material onto glass substrates. After solvent evaporation, the films were removed from the glass substrate by immersing them in deionized water [135]. Moreover, films of cellulose with  $\text{Fe}_3\text{O}_4$  nanoparticles were prepared by film casting in glass substrates and poly(methyl methacrylate) plates [136]. Other examples for the formation of magnetoactive polymeric films by film casting are: films preparation of poly(vinyl chloride) with  $\text{Fe}_3\text{O}_4$  nanoparticles [137] or films preparation of poly(vinyl alcohol) with  $\text{Fe}_3\text{O}_4$  nanoparticles [138]. A schematic representation of the film casting technique is shown in Figure 2.22.

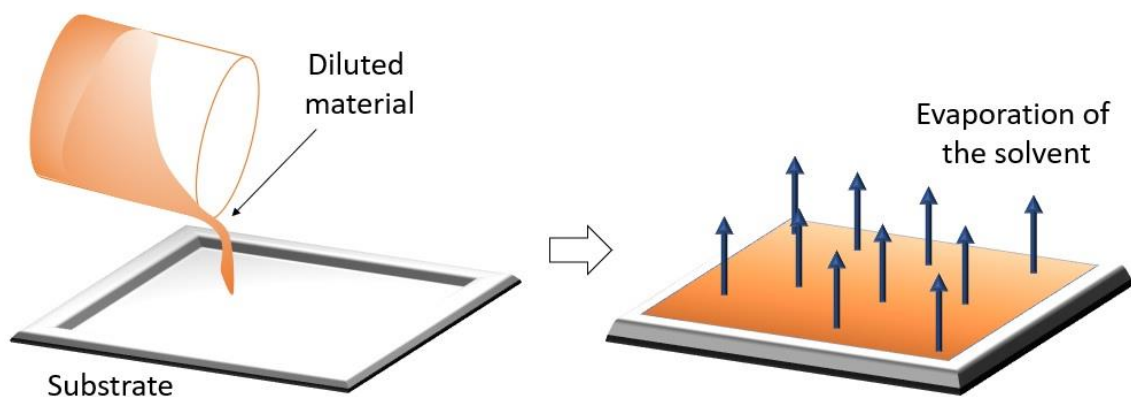


Figure 2.22. Schematic representation of the film casting process.

The dip-coating and spin-coating techniques are also conventional ways to promote the formation of polymeric films. Dip-coating consists of immersing a substrate of glass or silicon into the diluted material and pull it up. The result of this process is a thin layer

deposited on the substrate. After evaporation of the solvent, the polymeric film is obtained [98]. This process is shown in Figure 2.23. The thickness of the deposited layer is dependent on the withdrawing velocity [139]. Surface roughness and wettability of the substrate are very important to obtain defect free and smooth film surfaces [98]. Examples of magnetoactive films obtained by this technique are: polyester films with  $\text{Fe}_3\text{O}_4$ -silica [140], polyisobutylene-block-poly(ethylene oxide) with a ferrimagnetic material called holmium iron garnet ( $\text{Ho}_3\text{Fe}_5\text{O}_{12}$ ) [141].

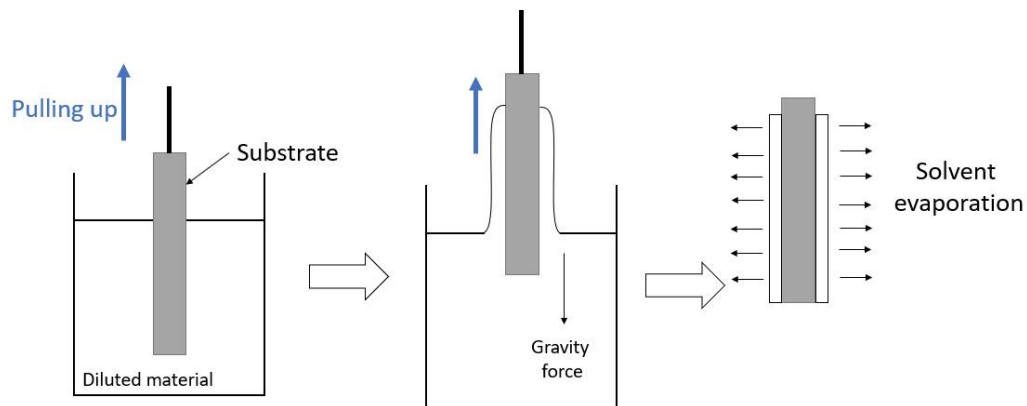


Figure 2.23. Steps of the dip-coating technique to obtain polymeric films.

On the other hand, the spin-coating technique consists of applying a drop or small quantity of diluted material on the center of a substrate. The substrate starts to spin to a certain velocity spreading the liquid to the outside by centrifugal forces (as shown in Figure 2.24). The thickness is controlled by varying the concentration and viscosity of the polymer solution, as well as the spin velocity [98]. Films of polydimethylsiloxane doped with NdFeB magnetic powder were reported using this procedure, obtaining a thickness of 15-35  $\mu\text{m}$  [142].

Films of  $\text{NiFe}_2\text{O}_4$ -PVDF- $\text{BaTiO}_3$  were obtained by mixing dried powders of the three components and pressing them in a hot plate. The temperature of the plate must be above the glass transition temperature of the polymer. The magnetic films were obtained after cooling at room temperature [143]. A similar procedure was followed to obtain PVDF with other iron oxides [144].

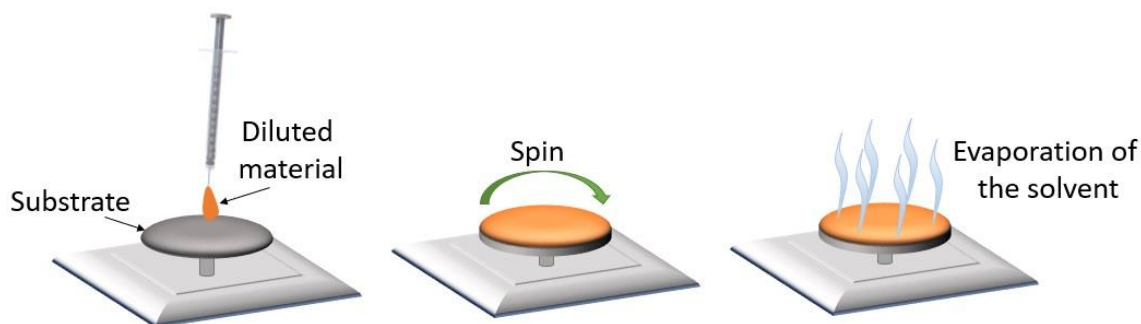


Figure 2.24. Steps of the spin-coating technique to obtain polymeric films.

In this research, the used procedure to obtain the magnetic hybrid films was the film casting technique. Details of the synthesis process followed to obtain the magnetic hybrid films for this research are described in chapter 3.

### 2.6.2 Advantages, limitations and applications of magnetic hybrid films

Magnetic hybrid films present the same advantages than magnetoactive bulk materials. These advantages are the possibility of non-contact control, which permits to obtain devices with freedom of actuation or manipulation. Also, there is no need to use additional materials for their actuation like electrodes, if compared with electroactive polymers. Moreover, they can operate in different media, such as air, vacuum, conducting and non-conducting liquids [11]. An additional advantage of magnetic hybrid films (quasi-2D system) over 3D bulk materials is their higher flexibility due to their geometry and large surface area/thickness ratio [98].

In spite of the above-mentioned advantages, the challenge to obtain better dispersion of magnetic particles into the polymeric matrix, a better control of particles size distributions and uniform thicknesses of magnetic hybrid films remain under research. Furthermore, bubbles could appear during the film formation, which interfere with the continuity of the matrix. Bubbles also could avoid the formation and growth of magnetic particles during the synthesis process [106].

For the application as microactuators of magnetic hybrid films, it is necessary to consider the decrement of the external magnetic field in function of the distance. Also, external

magnetic fields can be affected by the environment, thus the environment at which the microactuator will operate shall be considered before any application [98]. Moreover, the magnitude of forces and torques produced by magnetic hybrid films decreases considerably as nanoparticle sizes also decrease. In consequence, for the application of magnetic hybrid films as microactuators is necessary to obtain materials that allow bigger forces and torques.

Magnetic hybrid films are useful to many technologies and applications. They are used for packaging, coating, recording tapes, sensors and microactuators applications [145]. Magnetic hybrid films are used as microactuators in soft robotics [146], biomedical applications such as artificial muscles [145] or magnetic manipulation [29][147].

## 2.7 CONCLUSIONS

- Polymer-based materials are considered as a good option for applications such as microactuators due to the recent trend of devices miniaturization.
- Polymers used for applications as microactuators are generally stimuli-responsive, because they respond to an external stimulus and recover their original state by removing the stimulus.
- Some stimuli-responsive polymers can be obtained by embedding inorganic components (such as particles, fibers or sheets) into polymeric matrixes. This kind of polymers are called polymeric hybrid materials. Thus, it is possible to obtain stimuli-responsive polymers being also polymeric hybrid materials.
- Within the classification of stimuli-responsive polymers that respond to physical stimuli, magnetoactive polymers stand out from the others due to their possibility to be non-contact controlled and their ability to operate in different environments.
- Modeling magnetoactive polymers using thermoplastics as matrix (magnetoactive plastics) is not yet fully explored in the literature, neither to model the magneto-mechanical coupling properties nor to model the operation as microactuators in a cantilever configuration. This thesis will contribute in this research area.

- The synthesis process and the film formation process of magnetic hybrid films are of great importance to avoid undesired defects for their application as microactuators.

# CHAPTER 3

## SYNTHESIS AND CHARACTERIZATION OF POLYVINYL BUTYRAL WITH IRON OXIDE NANOPARTICLES (PVB/Fe<sub>2</sub>O<sub>3</sub>) FILMS

### 3.1 INTRODUCTION

This chapter deals with the experimental techniques adopted to synthesize and characterize the magnetic hybrid films composed of polyvinyl butyral (PVB) with iron oxide nanoparticles (Fe<sub>2</sub>O<sub>3</sub>) used in this research. The analysis of the obtained results is also presented. Section 3.2 describes the general aspects of both components (polyvinyl butyral and iron oxide nanoparticles). Furthermore, the followed procedure to synthesize the magnetic hybrid films of PVB/Fe<sub>2</sub>O<sub>3</sub> is shown in section 3.3. The characterization of PVB/Fe<sub>2</sub>O<sub>3</sub> films was performed to analyze their mechanical and magnetic properties (section 3.4 and 3.5, respectively) and their dynamic response when they are submitted to an external magnetic field (section 3.6).

## 3.2 GENERAL ASPECTS OF POLYVINYL BUTYRAL AND IRON OXIDE NANOPARTICLES

### 3.2.1 Polyvinyl Butyral (PVB)

Polyvinyl butyral (PVB) is an amorphous copolymer consisting of vinyl butyral, vinyl alcohol and vinyl acetate units. It is obtained by the condensation of polyvinyl alcohol with *n*-butyraldehyde by using an acid catalyst. The percentage content of each monomer is not consistent; however, typical values are approximately 75-82% of vinyl butyral, 17-22% of vinyl alcohol and 1-3% of vinyl acetate. So, chemical composition can change depending on the polymerization process. The final properties of the obtained PVB can be adjusted by varying the percentage of each monomer [148][149][150]. Figure 3.1 shows the schematic representation of the PVB structure.

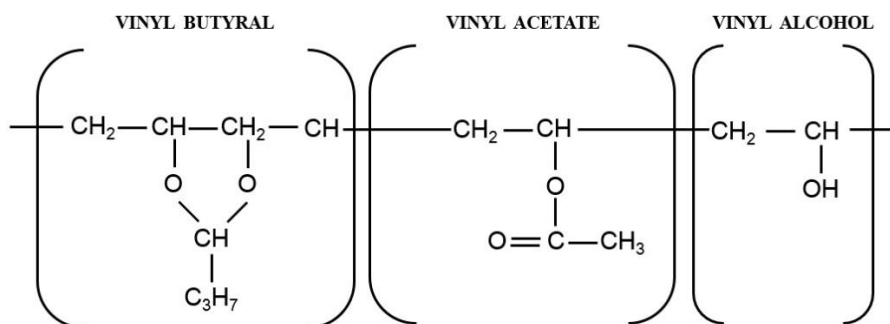


Figure 3.1. Chemical structure of the PVB.

The vinyl butyral units are hydrophobic and they are responsible of the good processability, elasticity, toughness and compatibility with other polymers. The hydrophilic vinyl alcohol units provide high adhesion to inorganic materials [149][150].

The mechanical behavior of PVB is highly nonlinear and time-dependent [151]. PVB is extensively used for laminated glass due to its film forming abilities and transparency. Laminated glass is basically a film of PVB placed between two glass layers. It is a kind of safety glass that avoids the risk of fragmentation during an impact [152][153]. It is used



mainly for automotive, aerospace or architectural applications [148]. Moreover, PVB shows a great potential in packaging due to its mechanical and gas barrier properties, its biodegradability at low butyral contents and relative low cost. Additionally, it is completely non-toxic [152][153].

In this thesis, the PVB was selected as polymeric matrix due to the above-mentioned properties. These properties permit the obtention of thin and very flexible films useful in the research of new electronics or mechatronics devices [154]. Also, good interactions between the OH groups of the hydrophilic part (vinyl alcohol) of the PVB and iron oxide nanoparticles have been previously reported [154][155]. These interactions may allow a good dispersion of the iron oxide nanoparticles into the PVB matrix.

### **3.2.2 Superparamagnetic iron oxide nanoparticles**

Iron oxides are chemical compounds formed by iron (Fe) and oxygen (O). There is a variety of different iron oxides; however, at ambient conditions the most common are: hematite ( $\alpha$ -Fe<sub>2</sub>O<sub>3</sub>), magnetite (Fe<sub>3</sub>O<sub>4</sub>) and maghemite ( $\gamma$ -Fe<sub>2</sub>O<sub>3</sub>) [156][157].

Hematite ( $\alpha$ -Fe<sub>2</sub>O<sub>3</sub>) is the oldest known of the iron oxides. It is extremely stable at ambient conditions and often it is the end-product of the transformation of other iron oxides. It is weakly ferromagnetic at room temperature and its magnetic saturation is very poor (0.3 A·m<sup>2</sup>/kg). It usually exhibits a rhombohedral crystalline structure. Magnetite (Fe<sub>3</sub>O<sub>4</sub>) shows the strongest magnetism of any transition metal oxide. It is ferromagnetic at room temperature and its saturation magnetization in bulk is about 92-100 A·m<sup>2</sup>/kg. It exhibits a cubic crystalline structure. Finally, maghemite ( $\gamma$ -Fe<sub>2</sub>O<sub>3</sub>) could be considered as a product of the aging of magnetite. It is ferrimagnetic at room temperature and its saturation magnetization is about 60-80 A·m<sup>2</sup>/kg. It exhibits a cubic crystalline structure [156].

Although magnetite presents the highest magnetic properties in comparison with the others, it is not very stable and it is sensitive to oxidation: magnetite transforms into maghemite in the presence of oxygen [158]. Consequently, maghemite ( $\gamma$ -Fe<sub>2</sub>O<sub>3</sub>) is useful because of its chemical and physical stability at ambient conditions [156].

Iron oxide nanoparticles are considered to be particles with a diameter between 1 and 100 nanometers [157]. Their magnetic properties are size-dependent. Maghemite and magnetite becomes superparamagnetic below 15 nanometers, approximately [159].

Technological applications for superparamagnetic iron oxide nanoparticles are magnetic storage media, magnetic inks for printing and ferrofluids, among others. Superparamagnetic iron oxide nanoparticles are also studied for biomedical applications because of their biocompatibility and low toxicity for the human body [156].

There are several chemical methods to synthesize superparamagnetic iron oxide nanoparticles. However, the most common, and probably the simplest and most efficient, is the chemical coprecipitation technique of iron salts [158].

The combination of polymers and iron oxide nanoparticles has many advantages such as the dispersion stability of these ones, *i.e.* polymers avoid the aggregation or coalescence of the iron oxide nanoparticles. This dispersion stability is achieved due to the viscoelasticity of the polymers. Additionally, when the iron oxide nanoparticles have the right size, it is possible to obtain hybrid materials with superparamagnetic properties useful for many applications [156][160]. The next section describes the synthesis process of the magnetic hybrid films studied in this research.

### 3.3 SYNTHESIS OF THE PVB/Fe<sub>2</sub>O<sub>3</sub> FILMS

The method used to synthesize the magnetic hybrid films of polyvinyl butyral with iron oxide nanoparticles (PVB/Fe<sub>2</sub>O<sub>3</sub>) is based on the procedure developed by Puente-Córdova [21]. This method involves the *in-situ* formation of the iron oxide nanoparticles into the polymeric matrix by using an iron salt as precursor.

### 3.2.3 Used materials

A summary of the used materials, their molecular weight and suppliers is shown in Table 3.1. In this case, polyvinyl butyral (commercial name *PVB BM-5Z*) was used as polymeric matrix, iron (II) chloride tetrahydrate ( $\text{FeCl}_2 \cdot 4\text{H}_2\text{O}$ ) was used as precursor salt in the formation of the iron oxide nanoparticles and tetrahydrofuran (THF) was used as common solvent of the PVB and the  $\text{FeCl}_2 \cdot 4\text{H}_2\text{O}$ . Finally, sodium hydroxide (NaOH) and hydrogen peroxide ( $\text{H}_2\text{O}_2$ ) were utilized to promote the formation of the iron oxide nanoparticles.

Table 3.1. Raw materials for the synthesis of PVB/ $\text{Fe}_2\text{O}_3$  films.

Material	Molecular weight (g/mol)	Supplier
PVB BM-5Z	53 000	Sekisui Chemical
$\text{FeCl}_2 \cdot 4\text{H}_2\text{O}$	198.81	Sigma-Aldrich
THF	72.11	Fisher Scientific
NaOH	40	Fermont
$\text{H}_2\text{O}_2$	34	Zuum

### 3.2.4 Synthesis process

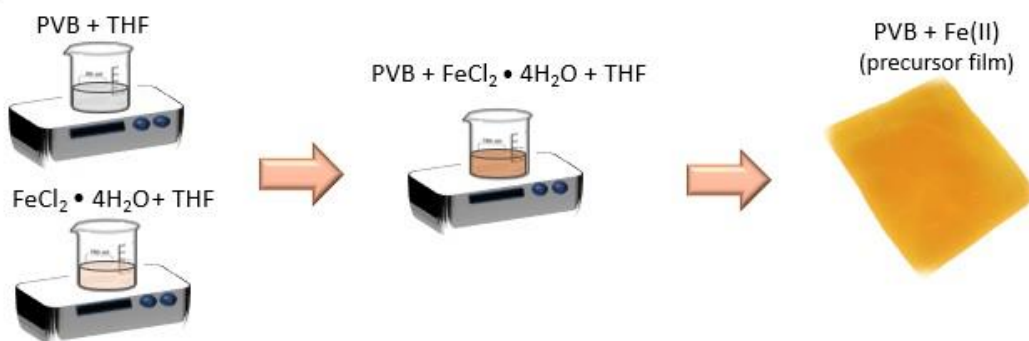
The synthesis process was performed in two main stages. The aim of the first stage is to obtain a precursor hybrid material by dispersing the precursor salt ions into the PVB matrix. In the second stage the precursor hybrid material is subjected to a thermochemical treatment to obtain the magnetic hybrid films of PVB/ $\text{Fe}_2\text{O}_3$ . These films were obtained at three different concentrations of iron oxide nanoparticles into the PVB matrix. Figure 3.2 is a schema of the two stages of the synthesis process.

For the first stage, a solution of PVB in 20 ml of THF was prepared. At the same time, the  $\text{FeCl}_2 \cdot 4\text{H}_2\text{O}$  precursor salt was dissolved in 15 ml of the same solvent (THF). Both solutions were stirred at 700 rpm for 60 minutes at 45°C. Upon completion of the time, the solution of  $\text{FeCl}_2 \cdot 4\text{H}_2\text{O}$ -THF was poured in the solution of PVB-THF and stirred at 700 rpm for other 60 minutes at 45°C. After that, the formation of the films was carried

out by casting the dissolved material onto a non-sticking surface. The films were dried for 24 hours to eliminate the presence of solvent by natural convection. At the end of this process, the films of a precursor hybrid material of PVB-Fe(II) were obtained.

In the second stage, the PVB-Fe(II) films were submerged in an aqueous solution of NaOH 6.7 M at 55°C. A color change was notorious during this process, from yellow to dark brown. Then, 30 ml of hydrogen peroxide ( $H_2O_2$ ) were added causing another color change, from dark brown to copper red. This change can be related to the presence of iron oxide in the material. Finally, the material was washed with unionized water many times to eliminate impurities. Magnetic hybrid films of PVB/ $Fe_2O_3$  with a thickness of 0.018 mm were obtained at the end of this process.

### Stage 1



### Stage 2

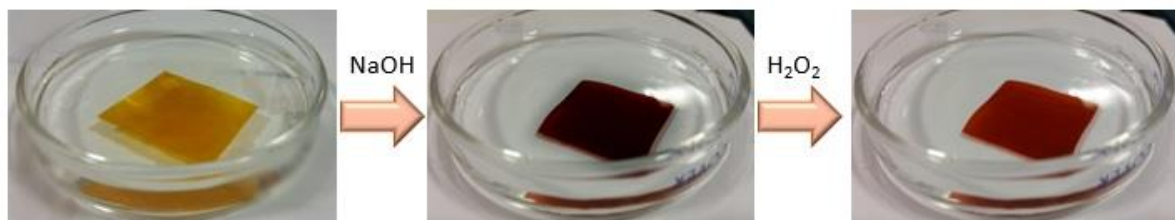


Figure 3.2. Schema of the synthesis process of the PVB/ $Fe_2O_3$  films.

### 3.3.3 Obtained samples

The magnetic hybrid films were obtained at three different precursor salt ( $\text{FeCl}_2 \cdot 4\text{H}_2\text{O}$ ) concentrations. This allow to obtain three different content of iron oxide nanoparticles embedded into the PVB matrix.

Precursor salt ( $\text{FeCl}_2 \cdot 4\text{H}_2\text{O}$ ) concentrations of 40%, 50% and 60% by weight (wt) with respect to the PVB were utilized for this study. These concentrations contribute approximately with 11%, 14% and 17% by weight of iron (Fe), respectively, in the PVB matrix.

Table 3.2 summarizes the specific quantities of PVB and  $\text{FeCl}_2 \cdot 4\text{H}_2\text{O}$  used in the synthesis for each concentration. The identification of the samples along this text will be in function of the iron content which is the relevant element in the formation of the iron oxide nanoparticles. All the samples were prepared following the method described in section 3.3.2.

Table 3.2. PVB and  $\text{FeCl}_2 \cdot 4\text{H}_2\text{O}$  content for the three different samples.

<b>Sample number</b>	<b>Sample ID</b>	<b>PVB content (g)</b>	<b><math>\text{FeCl}_2 \cdot 4\text{H}_2\text{O}</math> content (g)</b>
1	PVB/ $\text{Fe}_2\text{O}_3$ _11% wt Fe	1.92	1.28
2	PVB/ $\text{Fe}_2\text{O}_3$ _14% wt Fe	1.6	1.6
3	PVB/ $\text{Fe}_2\text{O}_3$ _17% wt Fe	1.28	1.92

The characterization of each sample was performed to know the mechanical and magnetic properties of the material, as well as the dynamic response of the material under different external magnetic fields. The characterization techniques and their results are described in the next sections.

### 3.4 DYNAMIC MECHANICAL ANALYSIS (DMA)

The frequency-dependent viscoelastic properties of the PVB/Fe<sub>2</sub>O<sub>3</sub> magnetic hybrid films were tested by dynamic mechanical analysis (DMA). DMA provides useful information about the mechanical behavior of polymers at the molecular level, and so, for the hybrid materials. Moreover, DMA is a convenient method to detect thermal transitions. This information is useful to know the conditions at which the studied materials can operate for specific applications.

#### 3.4.1 DMA operation principle

Dynamic Mechanical Analysis (DMA) is a technique in which a periodic strain is applied to a sample material at a certain frequency and amplitude. The periodic strain is commonly a sine signal. The applied strain generates a periodic stress as response. The stress response is measured in function of time or temperature. Hence, some physical properties can be approximated by measuring the stress amplitude or the lag between the stress and strain waves [161].

For ideally elastic materials that obey the Hooke's law, the stress response is proportional to the applied strain. When a periodic strain is applied, there is no delay in the stress response. Thus, the strain and the stress signals will be in phase [162][163]. Figure 3.3a represents a periodic strain applied to a sample of material. The corresponding stress response for an ideally elastic material is shown in Figure 3.3b.

If the same periodic strain is applied to a pure viscous material that follows the Newton's law of viscosity (Newtonian fluid), the stress response will be proportional to the strain and it will present a phase shift angle of  $\pi/2$  radians with respect to the applied strain [162][163], as shown in Figure 3.3c.

A viscoelastic material responds in a combined manner between elastic and viscous behaviors. The response for viscoelastic materials exhibit a phase shift angle ( $\delta$ ) between

zero and  $\pi/2$  radians with respect to the applied stimulus [162][163]. Figure 3.3d presents a characteristic stress response for a viscoelastic material when the cyclic is applied.

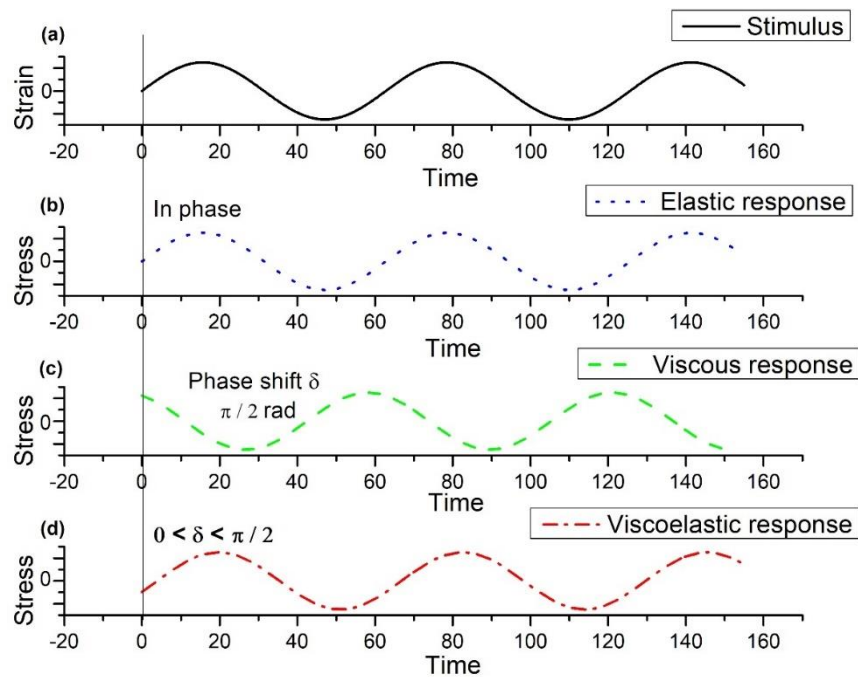


Figure 3.3. Stress response of different kind of materials: (a) applied periodic strain stimulus, (b) pure elastic response, (c) pure viscous response and (d) viscoelastic response.

DMA results consist of three main parameters: the elastic modulus (or dynamic storage modulus,  $E'$ ), the viscous modulus (or dynamic loss modulus,  $E''$ ) and the damping coefficient ( $\tan \delta$ ) which corresponds to the relation of the viscous modulus and the elastic modulus ( $\tan \delta = E''/E'$ ) [164].

The elastic modulus ( $E'$ ) is associated with the material stiffness and it is related to the young's modulus ( $E$ ) for a tensile test. Also, the elastic modulus ( $E'$ ) determines the elastically stored and released energy (reversible strain). The viscous modulus ( $E''$ ) is associated with the loss of energy due to internal friction.

DMA is sensitive to molecular motion, relaxation processes and other structural information [164][165]. Thermal transitions can be determined by drastic changes on

these parameters. An example of a thermal transition can be the glass transition temperature ( $T_g$ ) or other phase/structure changes in the polymer [165].

Different test modalities are available depending on the strain axis. These test modalities can be tension, compression or bending tests. However, it is reported that the dynamic properties of polymeric films of thickness less than 1 millimeter (thin films) can only be measured with accuracy in tension [165].

In this thesis, dynamic mechanical analysis was performed in tension mode. The tension test consists of a mobile clamp used to apply the periodic deformation to a sample of a known geometry. The force transmitted to the fixed clamp and the stress generated as response are measured simultaneously. Figure 3.4 shows schematically the main parts of a DMA in a tension test.

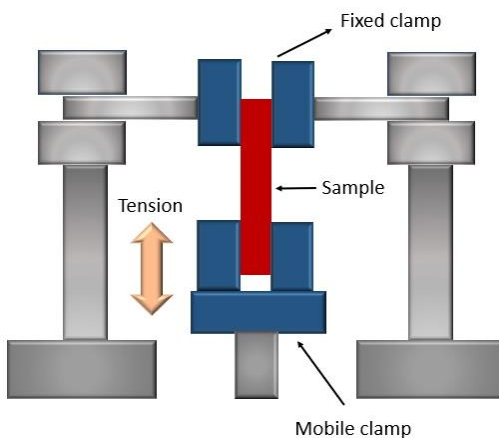


Figure 3.4. Schematic of a DMA in tension mode.

Details of the PVB/ $\text{Fe}_2\text{O}_3$  films results are explained below.

### 3.4.2 Sample preparation and measurement conditions

Dynamic mechanical analysis was conducted for the samples PVB/ $\text{Fe}_2\text{O}_3$ \_11% wt Fe, PVB/ $\text{Fe}_2\text{O}_3$ \_14% wt Fe and PVB/ $\text{Fe}_2\text{O}_3$ \_17% wt Fe. Tests were aimed to study the effect



of the iron oxide nanoparticles on the mechanical properties of the PVB matrix. An additional sample of pristine PVB was added as reference of the original properties.

Tests were carried out on a DMA 8000 Perkin Elmer. Specimens of rectangular geometry were cut with a width of 4 mm, a thickness of 0.018 mm and a gauge length of 10 mm. The specimens were tested in uniaxial tension at frequencies of 0.1 Hz and 1 Hz. The strain amplitude was set at 0.1 mm. The temperature of analysis was conducted from room temperature (about 25°C) to 150°C with a heating rate of 2°C/min.

The recorded parameters were the storage modulus ( $E'$ ) and  $\tan \delta$  ( $\tan \delta = E''/E'$ ). Thermal information of the material (specifically, glass transition temperature values) was also obtained.

### 3.4.3 DMA results

In this section the obtained DMA results for the elastic modulus ( $E'$ ) and  $\tan \delta$  in function of temperature are analyzed. Figure 3.5a shows the results for a pristine sample of PVB used as reference, while Figure 3.5b, c and d shows, respectively, the results for the samples PVB/Fe<sub>2</sub>O<sub>3</sub>\_11% wt Fe, PVB/Fe<sub>2</sub>O<sub>3</sub>\_14% wt Fe and PVB/Fe<sub>2</sub>O<sub>3</sub>\_17% wt Fe. The plots of the tests performed at 0.1 Hz ( $E'$  and  $\tan \delta$ ) are presented in solid lines, while the squared lines correspond to the tests taken at 1 Hz.

According to the results shown in Figure 3.5, the elastic modulus of pristine PVB has been modified by the addition of iron oxide nanoparticles. At room temperature ( $\sim 25^\circ\text{C}$ ), the elastic modulus of the pristine PVB is the highest in comparison with the three samples of PVB/Fe<sub>2</sub>O<sub>3</sub> (see Table 3.3). Also, at this temperature, a decrease in the elastic modulus is observed as the content of iron oxide nanoparticles increases. This decrease may be attributed to poor interfacial interactions between the iron oxide nanoparticles and the PVB matrix [166]. As previously mentioned in section 3.2.1, PVB is formed by three different groups which are vinyl butyral, vinyl acetate and vinyl alcohol. The interfacial interactions between the iron oxide nanoparticles and the PVB matrix are mainly formed by the *OH* groups of the vinyl alcohol and some hydroxyl groups present on the surface

of the iron oxide nanoparticles [155]. However, vinyl alcohol is only present in a nominal concentration of 17%-22% in relation to the other groups. Therefore, interfacial interactions become harder as the iron oxide nanoparticles content increases. Poor interfacial interactions could produce a plasticizer effect on the polymeric matrix.

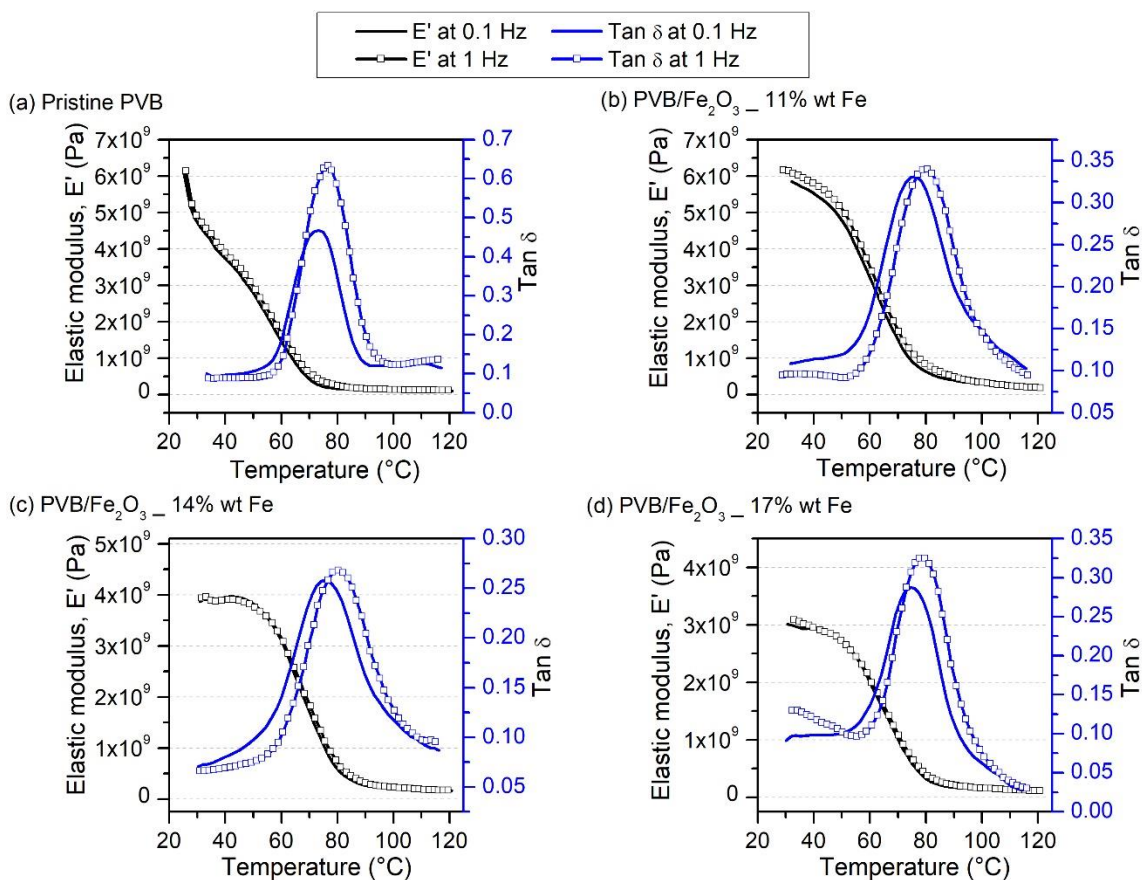


Figure 3.5. DMA results at frequency strains of 0.1 Hz and 1 Hz for: (a) pristine PVB, (b) PVB/Fe<sub>2</sub>O<sub>3</sub>\_11% wt Fe, (c) PVB/Fe<sub>2</sub>O<sub>3</sub>\_14% wt Fe and (d) PVB/Fe<sub>2</sub>O<sub>3</sub>\_17% wt Fe.

Table 3.3. Values of elastic modulus ( $E'$ ) and glass transition temperature ( $T_g$ ), obtained at 0.1 Hz and 1 Hz, for all the samples.

Sample ID	0.1 Hz			1 Hz		
	$E'$	$E'$	$T_g$	$E'$	$E'$	$T_g$
	(at ~25°C)	(at 120°C)	(°C)	(at ~25°C)	(at 120°C)	(°C)
<b>Pristine PVB</b>	$6.08 \times 10^9$	$9.10 \times 10^7$	70.8	$6.13 \times 10^9$	$1.16 \times 10^8$	74.7
<b>PVB/Fe<sub>2</sub>O<sub>3</sub>_11%wt Fe</b>	$5.85 \times 10^9$	$9.90 \times 10^7$	79.1	$6.12 \times 10^9$	$1.83 \times 10^8$	83.3
<b>PVB/Fe<sub>2</sub>O<sub>3</sub>_14%wt Fe</b>	$3.90 \times 10^9$	$1.60 \times 10^8$	78.8	$4.00 \times 10^9$	$1.70 \times 10^8$	83.2
<b>PVB/Fe<sub>2</sub>O<sub>3</sub>_17%wt Fe</b>	$3.00 \times 10^9$	$1.09 \times 10^8$	76.9	$3.10 \times 10^9$	$1.14 \times 10^8$	80.6

In polymers, repetitive groups are connected to form long chains. These chains intermingle with each other to become entangled, as shown in Figure 3.6a. The plasticizer effect is produced by voids or free space created by the non-interaction between the iron oxide nanoparticles and the polymeric chains. This free space promotes the disentanglement of polymeric chains (see Figure 3.6b) and their motion becomes easier. Thus, stiffness and elastic modulus decrease [167].

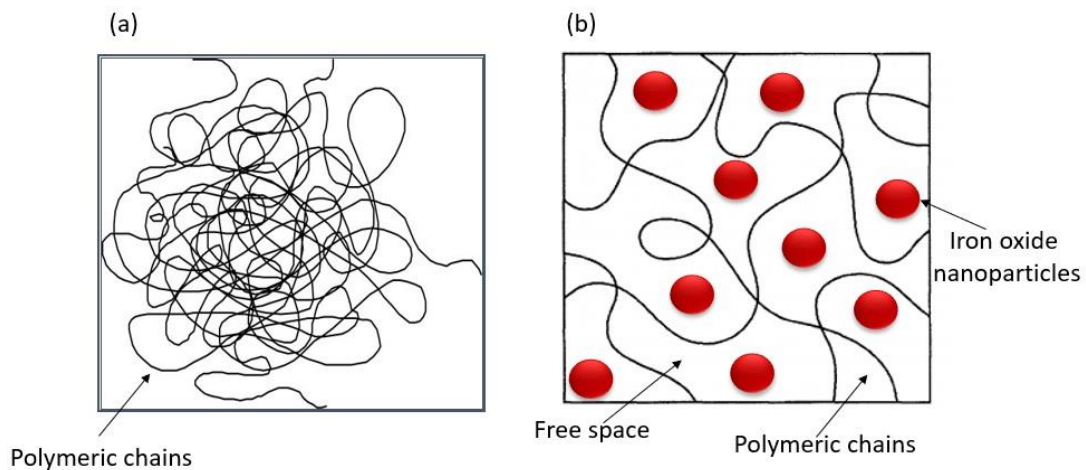


Figure 3.6. Schematic representation of the polymeric chains: (a) entangled polymeric chains and (b) plasticizer effect of iron oxide nanoparticles on the polymeric chains.

Another possibility of poor interactions between the PVB matrix and the iron oxide nanoparticles could be the formation of agglomerates with the increase of the iron content. Agglomerations reduce the interfacial area between the iron oxide nanoparticles and the PVB matrix, as shown in Figure 3.7. This behavior causes a decrement in the stiffness of the material and the elastic modulus also decreases [168]. Previous characterization studies of PVB with iron oxide nanoparticles have reported an increment in the agglomerates as the precursor salt content (or iron content) increases [169]. The decrement of the elastic modulus of PVB at room temperature with the addition of other concentrations of iron oxide nanoparticles has been also reported [154]. The use of coaters or other agents to prevent agglomerations of iron oxide nanoparticles remains under study [170].

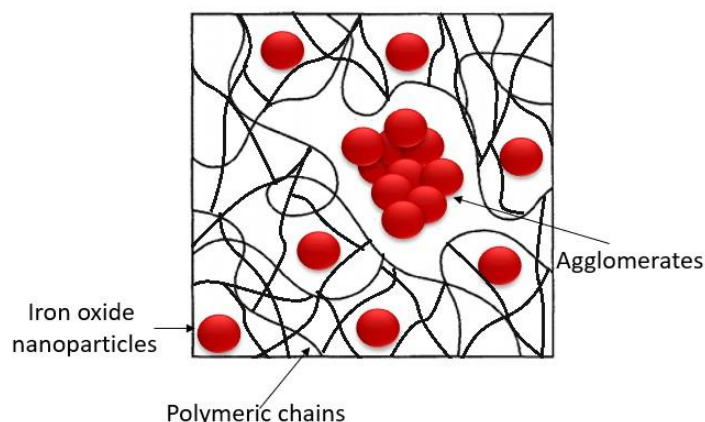


Figure 3.7. Agglomerates of iron oxide nanoparticles into de PVB matrix.

The elastic modulus of all the samples exhibits a region of sudden decay at a certain temperature. This region is characteristic of polymers and represents the mechanical manifestation of its main relaxation due to temperature. As the temperature increases, the polymer changes from a glassy state (apparently solid state) to a rubbery state as consequence of the motion and disentanglement of the polymeric chains. This region is called the glass transition region [171].

For pristine PVB, the glass transition region begins almost at room temperature. However, for the PVB/Fe<sub>2</sub>O<sub>3</sub> samples this region starts at higher temperatures. This behavior may be associated to two phenomena: (a) an increment of the physical interfacial interactions caused by the mobility of the polymeric chains at this temperature, (b) the iron oxide nanoparticles restrict the movement of the polymeric chains avoiding their disentanglement [154]. These two possibilities can also explain the elastic behavior at temperatures above the glass transition region. For example, at 120°C PVB/Fe<sub>2</sub>O<sub>3</sub> samples also exhibit higher values of elastic modulus in comparison to pristine PVB (as shown in Table 3.3).

The glass transition temperature ( $T_g$ ) of each sample can be estimated from the plots of  $\tan \delta$ . In these plots, the highest rate of decrease of the elastic modulus is presented as a peak. The temperature at which this peak is observed corresponds to the estimation of the  $T_g$ . It is observed that the glass transition temperature increases with the addition of iron oxide nanoparticles (see Table 3.3). However, for the sample with the highest content of

nanoparticles (PVB/Fe<sub>2</sub>O<sub>3</sub>\_17% wt Fe) the T<sub>g</sub> starts to decrease. These results suggest the presence of a threshold value of the iron oxide nanoparticles content in relation to the PVB matrix to increase the T<sub>g</sub>.

In addition, the elastic modulus and  $\tan \delta$  are affected by frequency. The elastic modulus of each sample is incremented as the deformation frequency increases from 0.1 Hz to 1 Hz. The peak of  $\tan \delta$  also shifts to higher temperatures, as observed in Table 3.3. Both, the augment of the elastic modulus and the shift of  $\tan \delta$  peak depend on polymeric chains motions (or molecular motions). Polymeric chain motions are frequency-dependent. If a polymeric material is subjected to a constant stress or very low frequency of stress, its elastic modulus will decrease over the time. This decrement is caused by the rearrangement of the polymeric chains in order to minimize the localized stress. This rearrangement may produce a disentanglement of the polymeric chains. However, if the stress is applied for short times (or higher frequency) the time is not enough to experiment such rearrangement to minimize the stress. This gives as a result higher elastic modulus at higher frequencies [172].

Results in this section showed that mechanical and thermal properties of PVB can be modified by the addition of iron oxide nanoparticles. Also, such properties are sensitive to variations of the added content of precursor salt during the synthesis process. These properties shall be considered for the analysis of the dynamic response of the magnetic hybrid films when subjected to external magnetic fields.

### 3.5 MAGNETIC CHARACTERIZATION OF THE PVB/Fe<sub>2</sub>O<sub>3</sub> FILMS

The magnetic behavior of the PVB/Fe<sub>2</sub>O<sub>3</sub> films was characterized in a Vibrating Sample Magnetometer (VSM) model MPMS SQUID produced by Quantum Design. Tests were conducted on each sample showed in Table 3.2.

### 3.5.1 Vibrating Sample Magnetometer (VSM) operation principle

A Vibrating Sample Magnetometer (VSM) is used to study the magnetic properties of magnetic materials. A VSM operates following the Faraday's law of induction, which indicates that a changing magnetic field will induce an electric current in a coiled wire [173]. A VSM works by placing a sample in a constant and uniform external magnetic field at a controlled temperature, as shown in Figure 3.8. The external magnetic field induces magnetization in the sample. The magnetization in the sample is produced by the alignment of its individual magnetic dipoles with the external magnetic field [112]. Then, the magnetized sample begins to vibrate. In consequence, perturbations are introduced to the external magnetic field. In turn, the introduced perturbations generate variations in the magnetic flux. These variations are detected by coils that are placed near the vibrating sample. The detector coils generate a difference in current according to Faraday's law of induction [174][175].

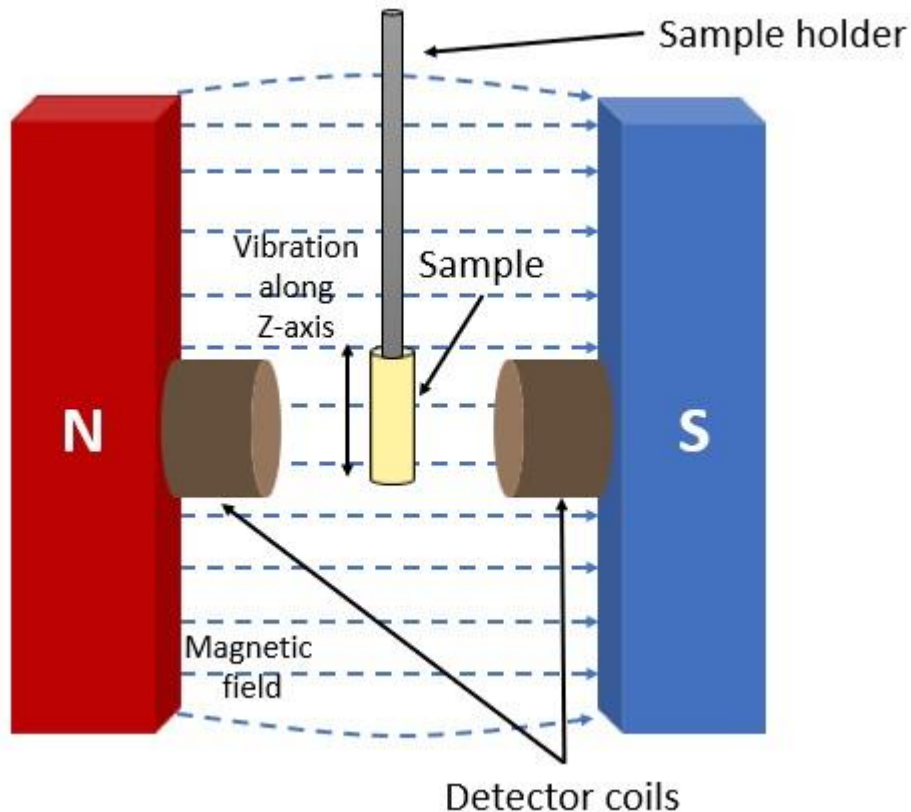


Figure 3.8. Schema of a magnetic sample magnetometer functioning.

As the magnetization in the vibrating sample increases, the induced current by the detector coils also increase. Therefore, the differences in current are translated by a computer as variations in the magnetization of the sample [174][175].

### 3.5.2 Sample preparation and measurement conditions

The samples used to perform the magnetic measurements in the vibrating sample magnetometer are sections of the PVB/Fe<sub>2</sub>O<sub>3</sub> films. The sections were cut from films of each concentration presented in Table 3.2. Samples were encapsulated in order to have a better fixation during the analysis, as shown in Figure 3.9.

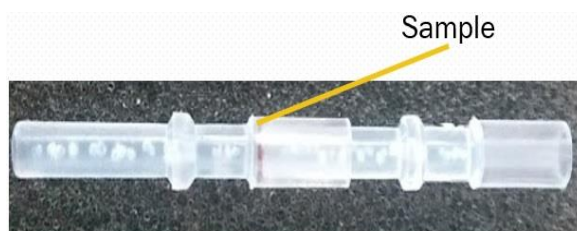


Figure 3.9. Encapsulation of the samples for magnetic measurements.

VSM measurements of magnetization ( $M$ ) in function of an applied magnetic field ( $H$ ) were recorded at room temperature ( $\sim 300$  K). The applied magnetic field was varied from  $-70$  to  $70$  kOe, at a rate of  $12$  kOe per second.

### 3.5.3 Results of the magnetic characterization

Figure 3.10 shows the magnetization curves of the PVB/Fe<sub>2</sub>O<sub>3</sub> films measured for the samples of 11% wt, 14% wt and 17% wt of iron. The magnetization ( $M$ ) as response of an applied magnetic field ( $H$ ) is plotted. Remanent magnetization ( $M_r$ ) and coercive field ( $H_c$ ) are imperceptible in such graph. This kind of curve is characteristic of superparamagnetic materials. Magnetic moments in superparamagnetic materials are able to be ordered and magnetized when an external magnetic field is applied, and they can return to zero magnetization when removing the external magnetic field without showing

remanent magnetization [112][113]. Superparamagnetic behavior is directly associated with the presence of single domain magnetic nanoparticles with sizes less than 15 nm [9][112]. So, these results suggest the presence of nanoparticles sizes less than 15 nm in all the synthesized films. Consequently, the presence of iron oxide nanoparticles synthesized *in-situ* in the PVB matrix can be confirmed. These results agree with previous results of PVB/Fe<sub>2</sub>O<sub>3</sub> films. They have reported iron oxide nanoparticles embedded in the PVB matrix; these ones with an average size about 8 nm [21][169].

Additionally, magnetization values also increase considerably with the increase of the iron concentration. This can be related with an augment of the iron oxide nanoparticles content. The saturation magnetization is not reached at this magnetic field sweep for any sample. Hence, magnetic field values higher than 70 kOe or below -70 kOe are necessary to reach the saturation magnetization. The maximum measured magnetization corresponds to 6.19 emu/g (-6.19 emu/g) for the sample PVB/Fe<sub>2</sub>O<sub>3</sub>\_17% wt Fe, 3.56 emu/g (-3.56 emu/g) for the sample PVB/Fe<sub>2</sub>O<sub>3</sub>\_14%wt Fe and 1.29 emu/g (-1.29 emu/g) for the sample PVB/Fe<sub>2</sub>O<sub>3</sub>\_11% wt Fe, as shown in Table 3.4. These values are obtained by applying 70 kOe (or -70kOe) of magnetic field.

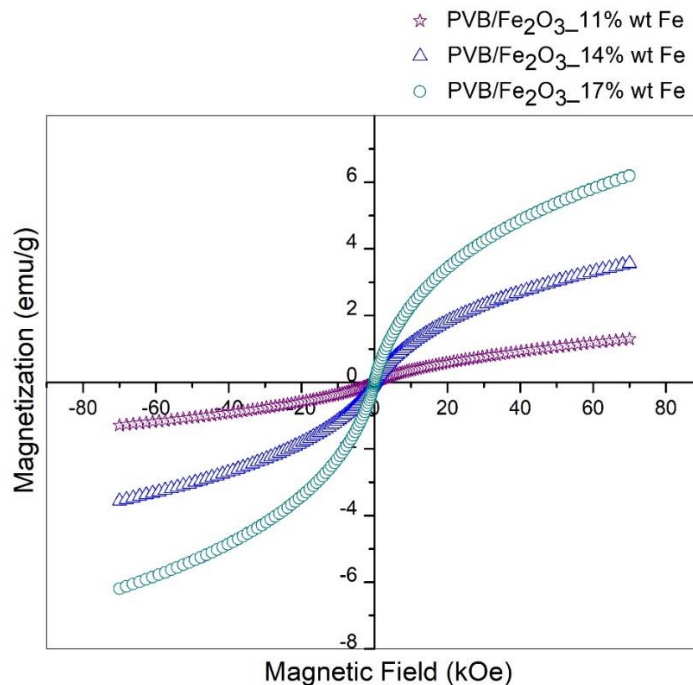


Figure 3.10. Magnetization curves of the PVB/Fe<sub>2</sub>O<sub>3</sub> films measured at room temperature (300 K).



Figure 3.11 shows a zoomed view of the magnetization curves for the three samples in Figure 3.10. All values were taken from -0.4 kOe to 0.4 kOe of the applied magnetic field, in order to be positioned near to the zero-magnetization point. A very narrow hysteresis was observed at such magnification. The values of remanent magnetization and coercive field are extremely low for the three samples. The remanent magnetization ( $M_r$ ) and the coercive field ( $H_c$ ) values obtained for all the samples are shown in Table 3.4.

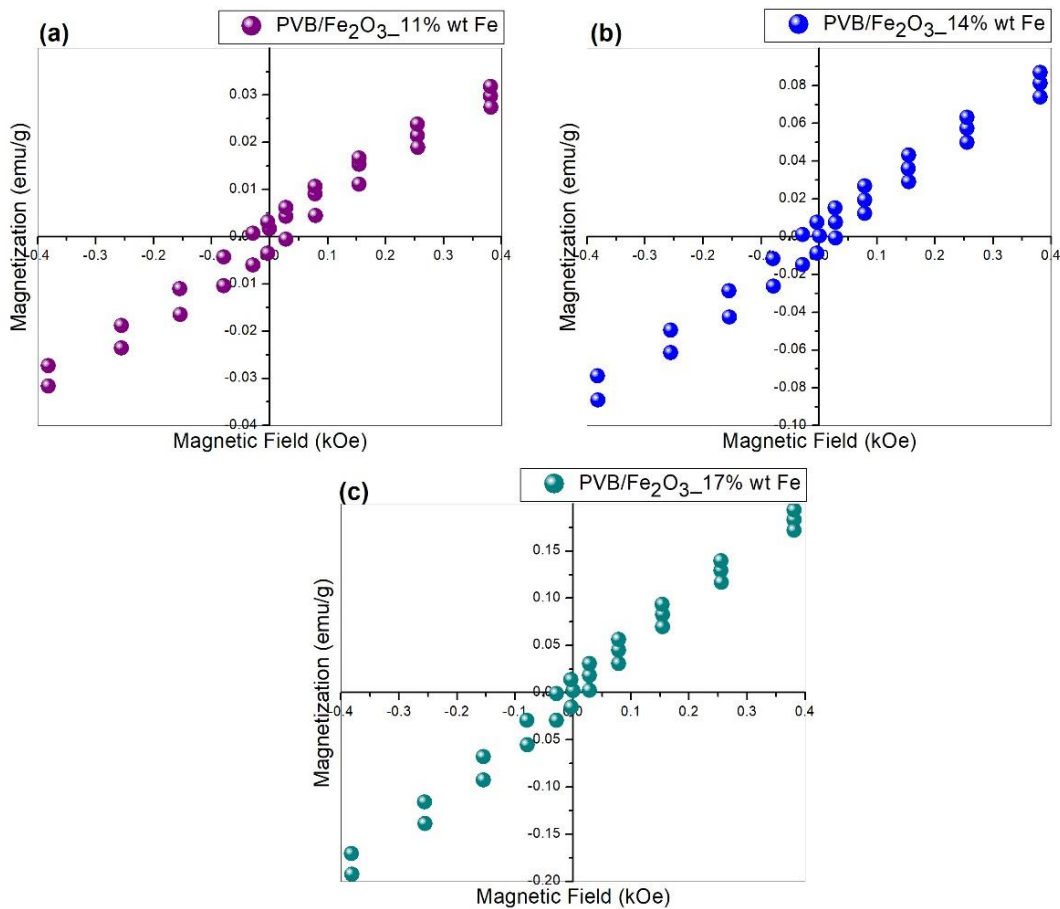


Figure 3.11. Zoomed view around the zero-magnetization point of the magnetization curves for the samples: (a) PVB/Fe<sub>2</sub>O<sub>3</sub>\_11% wt Fe, (b) PVB/Fe<sub>2</sub>O<sub>3</sub>\_14% wt Fe and (c) PVB/Fe<sub>2</sub>O<sub>3</sub>\_17% wt Fe.

Superparamagnetic materials exhibit a remanent magnetization to saturation magnetization ratio much smaller than 0.01 ( $M_r/M_s \ll 0.01$ ) [176]. The  $M_r/M_s$  ratio can be estimated by taking the maximum measured magnetization value as  $M_s$ . Table 3.4

shows the obtained Mr/Ms ratio of the three samples, which accomplish with this characteristic ratio of superparamagnetic materials.

Table 3.4. Magnetic parameters for the magnetization curves for the three magnetic films concentrations.

<b>Sample ID</b>	<b>Maximum measured magnetization Ms (emu/g)</b>	<b>Remanent magnetization Mr (emu/g)</b>	<b>Coercive field (kOe)</b>	<b>Mr/Ms</b>
PVB/Fe <sub>2</sub> O <sub>3</sub> _11%wt Fe	1.29	0.0031	0.0283	0.0023
PVB/Fe <sub>2</sub> O <sub>3</sub> _14%wt Fe	3.56	0.0077	0.0286	0.0022
PVB/Fe <sub>2</sub> O <sub>3</sub> _17%wt Fe	6.19	0.0135	0.0287	0.0022

In addition, it is possible to observe in Table 3.4 that the remanent magnetization and the coercive field increase with the iron oxide nanoparticles concentration. The increment of those values is attributed to the possible formation of agglomerates. The agglomerations of nanoparticles could behave as multidomains particles. Consequently, hysteresis, remanent magnetization and coercive field start to increase. These agglomerates could be caused by the precursor salt concentration used during the *in-situ* synthesis of the nanoparticles in the PVB matrix; as the precursor salt content increases, its dispersion becomes more difficult. The increment of agglomerations due to the increase of the precursor salt content was reported previously for the same concentrations [169].

The magnetic characterization suggests that it is possible to obtain magnetic hybrid films of PVB with superparamagnetic iron oxide nanoparticles at the iron concentrations used in this work and by following the synthesis process described before. Iron oxide nanoparticles present sizes below 15 nm, according to the exhibited behavior and previous analysis. As the precursor salt increases, its dispersion in the PVB matrix is more difficult; this can promote the formation of agglomerates. It is considered that the presence of agglomerates varies the magnetic properties of the samples.

### 3.6 DYNAMIC CHARACTERIZATION (DISPLACEMENT UNDER MAGNETIC FIELD)

The dynamic characterization of PVB/Fe<sub>2</sub>O<sub>3</sub> films was aimed to evaluate their magnetic actuation properties and thus the possibility to use them as microactuators. The configuration of the microactuator used in this study is depicted in Figure 3.12. It consists of a PVB/Fe<sub>2</sub>O<sub>3</sub> film with a cantilever configuration; one fixed end and one free end. An electromagnet generating a controlled magnetic field was placed below the free end of the cantilever structure. The magnetic field produces a bending (displacement of the free end) of the film due to magnetic forces of attraction. Experimental measurements of the displacement were taken on the free end of the cantilever at different conditions.

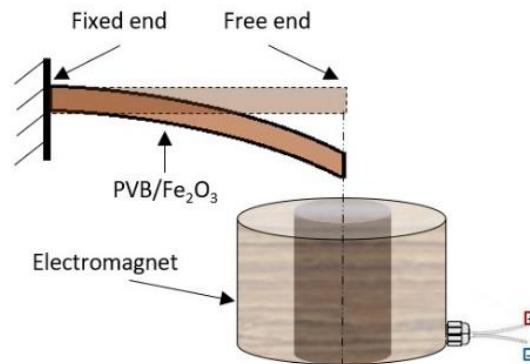


Figure 3.12. Schematic representation of the actuation system.

#### 3.6.1 The experimental setup and data acquisition techniques

The experimental setup to test the displacement of the PVB/Fe<sub>2</sub>O<sub>3</sub> films as cantilever microactuator in response to magnetic fields is shown in Figure 3.13. The flow of the data acquisition process is indicated by arrows.

The equipment used to perform the displacement measurements was composed of a personal computer (PC), a ds1103 controller board supplied by dSPACE, a voltage amplifier of BOP 100-2M model by KEPCO, an electromagnet of 739-3258 model purchased from RS components, a laser sensor of LK G152 model and a conditioner of the laser sensor signal of LK G3001P model (both acquired from Keyence).

The steps involved in the automatic data acquisition process are listed below:

1. The PC sends a driving voltage signal to the controller board. The voltage signal is generated using the MATLAB/Simulink<sup>®</sup> program.
2. The controller board is the interface between the PC and the other components. Therefore, the controller board converts the digital signal from the PC into an analog voltage signal. In this way, the analog voltage signal can be sent to the amplifier.
3. The amplifier receives the signal from the controller board. Voltage and current are then amplified and sent to the electromagnet.
4. A current starts to flow through the electromagnet, generating a magnetic field.
5. The PVB/Fe<sub>2</sub>O<sub>3</sub> film experiments a displacement due to magnetic forces of attraction.
6. The laser sensor detects the displacement at the free end of the cantilever structure.
7. The conditioner for the laser sensor collects the displacement measurements and send them to the controller board.
8. The controller board converts the analog signal received from the laser sensor conditioner into a digital signal. This digital signal is transmitted to the PC.
9. The PC receives all the information and saves the acquired data.

Figure 3.14 shows the laboratory workspace with the main components used to execute the experimental displacement measurements.

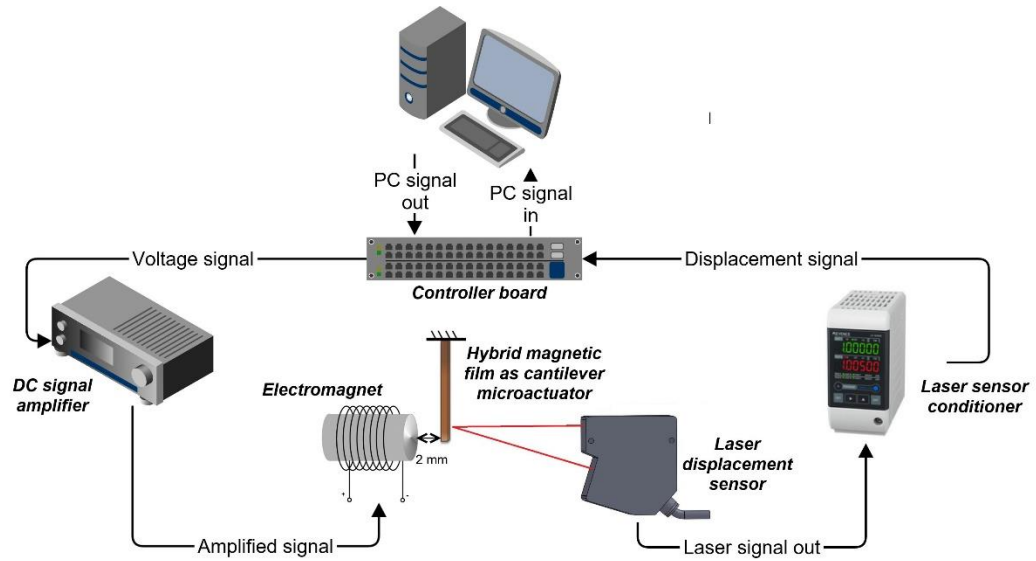


Figure 3.13. Schema of the experimental setup and the flow process to acquire the displacement values of the PVB/Fe<sub>2</sub>O<sub>3</sub> films under external magnetic fields.

The central axis of the electromagnet was placed at 2 millimeters from the free end of the cantilever microactuator, as shown in Figure 3.13. In order to know the magnetic field strength (H) and the magnetic flux density (B) produced by the electromagnet at such position, additional measurements were taken. For these measurements, a gaussmeter GM08 by Hirst Magnetic Instruments Ltd was used. The sensor probe of the gaussmeter was placed at 2 millimeters from the electromagnet (same position of the free end of the microactuator), as shown in Figure 3.15. Table 3.5 summarizes the results of the generated magnetic field and the current flowing through the electromagnet in function of different voltage values.

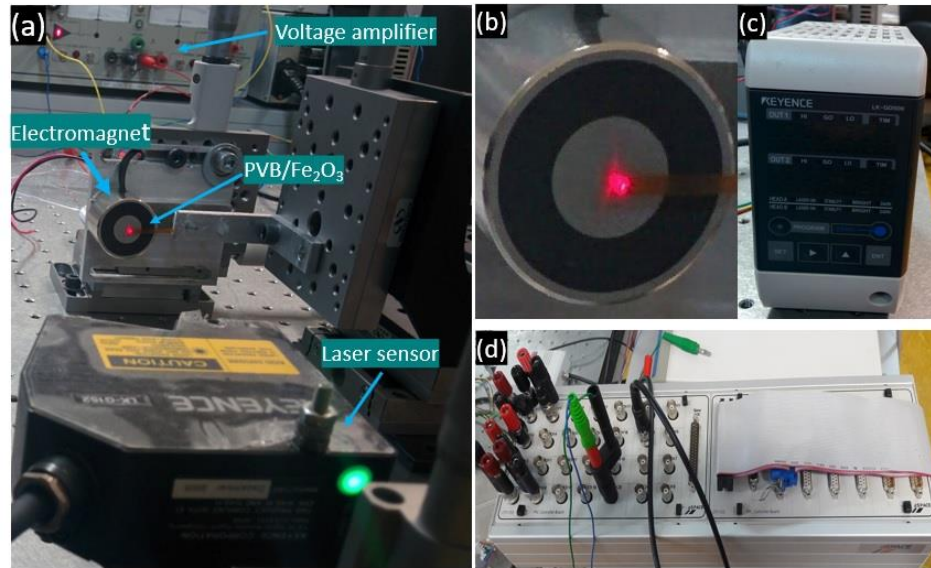


Figure 3.14. Laboratory workspace for the displacement measurements: (a) experimental setup, (b) a close-up view of the electromagnet and the film, (c) the laser sensor conditioner and (d) the controller board for the communications with the PC.

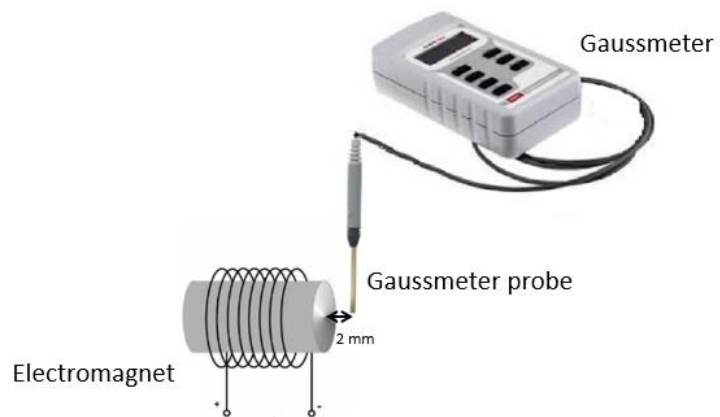


Figure 3.15. Position of the gaussmeter probe to take measurements of the magnetic field generated by the electromagnet at 2 mm of distance.

Table 3.5. Magnetic field strength and magnetic flux density in function of current and applied voltage. All these values were taken at 2 mm from the central axis of the electromagnet.

Voltage	Current	Magnetic field strength (kOe)	Magnetic flux density (T)
1	0.02	0.03	0.003
3	0.07	0.09	0.009
6	0.15	0.18	0.018
9	0.22	0.27	0.027
12	0.29	0.36	0.036
15	0.37	0.45	0.045
18	0.44	0.54	0.054
21	0.51	0.62	0.062
24	0.59	0.71	0.071
27	0.66	0.79	0.079
30	0.73	0.87	0.087

A description about the sample preparation and measurement conditions for dynamic characterization is detailed in the next section.

### 3.6.2 Sample preparation and measurement conditions

As previously mentioned, the displacement measurements were performed in a cantilever structure configuration. The used samples were rectangular sections taken from the PVB/Fe<sub>2</sub>O<sub>3</sub> films. The effect of varying three parameters on the behavior of the PVB/Fe<sub>2</sub>O<sub>3</sub> films as cantilever microactuators was evaluated. These three parameters were the iron oxide nanoparticles content, the voltage supplied to the electromagnet (input voltage) and the dimensions of the microactuator. In addition, tests were performed using two modalities of input voltage: the step voltage mode for the step response and the periodic voltage mode for oscillatory analysis.

In the step voltage mode, a sudden change of voltage from zero to a specific value is applied to the electromagnet as shown in Figure 3.16a. The electromagnet generates a magnetic field in function of the applied voltage. In consequence, a sudden displacement of the microactuator is promoted. From a practical standpoint, sudden stimuli are very common in the operation of microactuators. Hence, it is important to know the response of the PVB/Fe<sub>2</sub>O<sub>3</sub> films to this kind of stimulus. The experimental conditions to evaluate the responses in the step voltage mode are listed below and summarized in Figure 3.17a.

- *Condition 1:* studies are carried out with various iron oxide nanoparticles concentrations but the same cantilever dimensions and input voltage.

In this case, measurements were conducted for the microactuators of the samples PVB/Fe<sub>2</sub>O<sub>3</sub>\_17%wt Fe, PVB/Fe<sub>2</sub>O<sub>3</sub>\_14%wt Fe and PVB/Fe<sub>2</sub>O<sub>3</sub>\_11%wt Fe. These samples correspond to the three different concentrations of iron oxide nanoparticles used in this study. Rectangular sections of 15 mm in length, 2 mm in width and 0.018 mm in thickness were taken. The step voltage was 30 V.

- *Condition 2:* studies are carried out with various voltages but constant iron oxide nanoparticles concentration and cantilever dimensions.

These measurements were performed on the microactuator of the sample PVB/Fe<sub>2</sub>O<sub>3</sub>\_14%wt Fe. The cantilever dimensions were 15 mm in length, 2 mm in width and 0.018 mm in thickness. Two different step voltages were used: 15 V and 30 V.

- *Condition 3:* studies are carried out with different cantilever dimensions but constant iron oxide nanoparticles concentration and input voltage.

The microactuator of the sample PVB/Fe<sub>2</sub>O<sub>3</sub>\_14%wt Fe was used. Two different cantilever dimensions were taken. The cantilever dimensions were 15 mm in length, 2 mm in width and 0.018 mm in thickness for the first microactuator (size 1), and 15 mm in length, 4 mm in width and 0.018 mm in thickness for the second microactuator (size 2). Both microactuators were tested using a step voltage of 30 V.



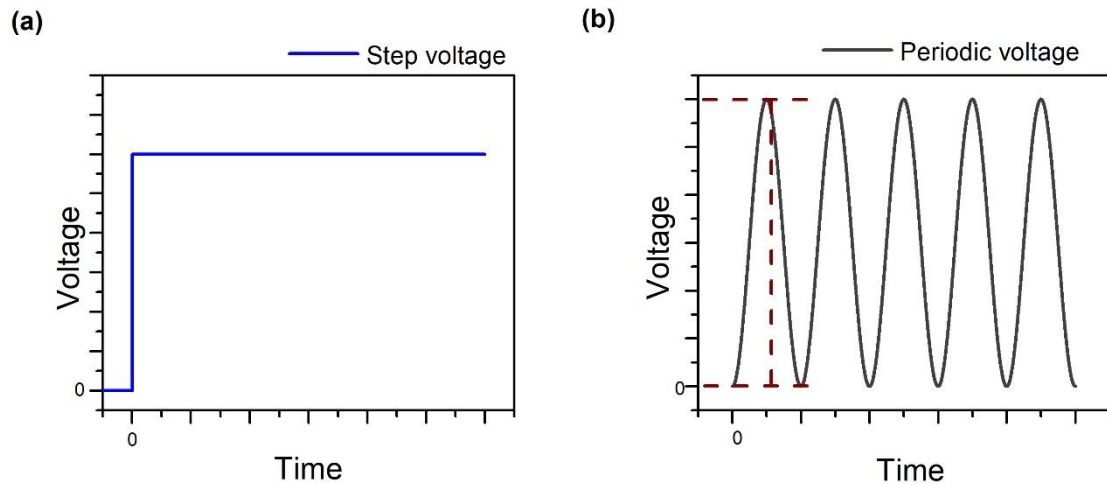
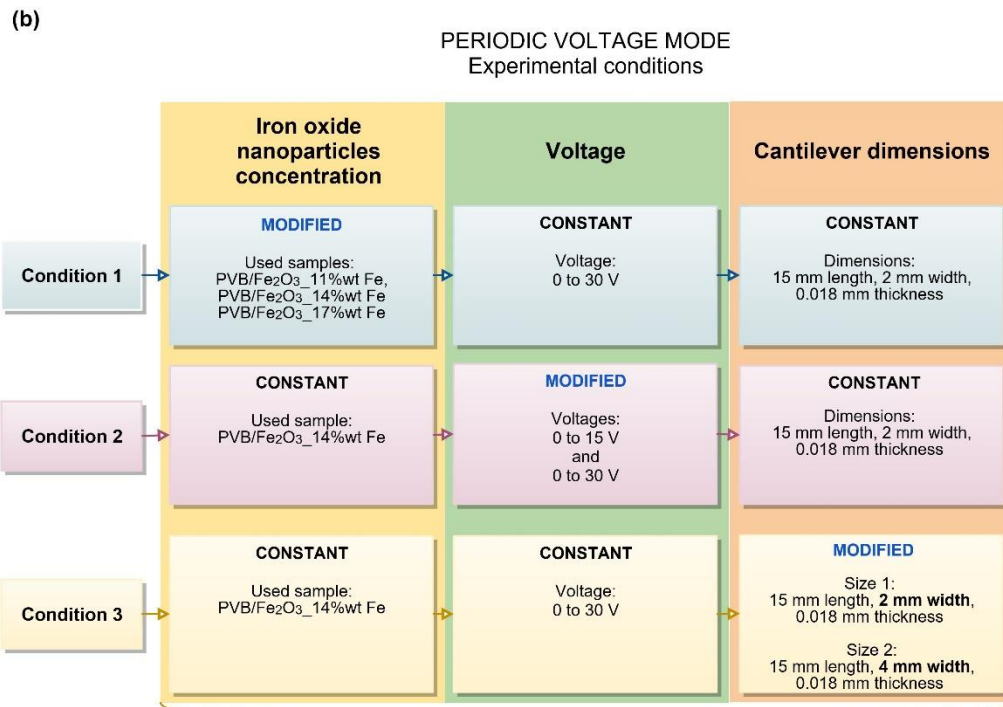
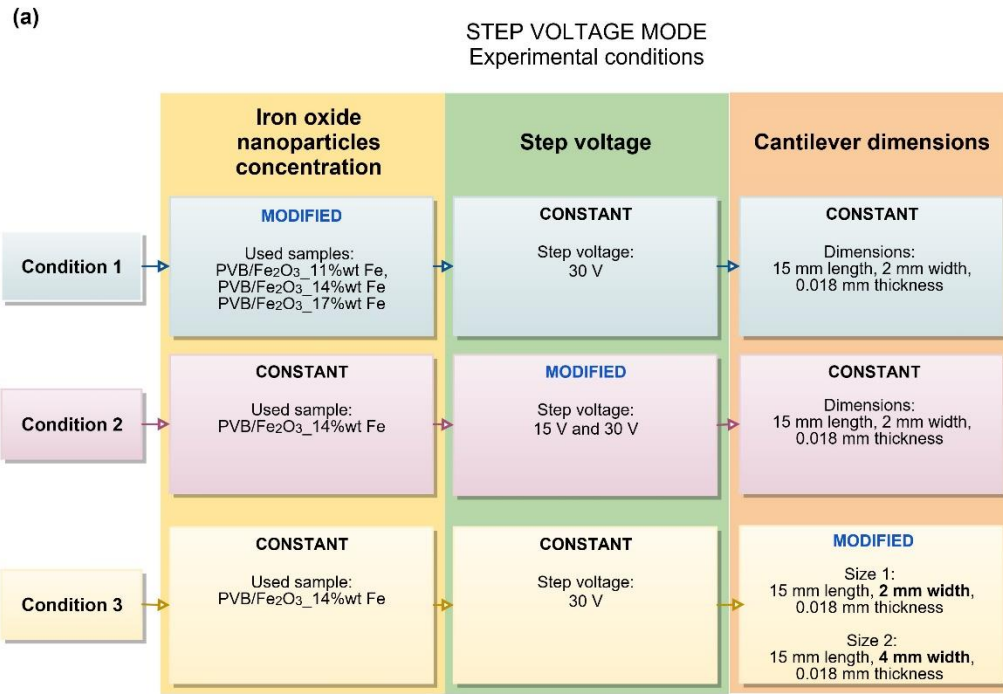


Figure 3.16. Two different modalities of input voltage: (a) the step voltage mode and (b) the periodic voltage mode.

In the periodic voltage mode, a sine voltage of known amplitude and frequency is applied to the electromagnet, as shown in Figure 3.16b. This voltage produces a periodic magnetic field. The microactuators experiment an oscillatory displacement in response of the applied magnetic field. Periodic tests are useful to know how quickly they respond to a changing stimulus (bandwidth). This kind of test is also useful to evaluate the presence of hysteretic losses.

The experimental conditions to measure the response of the microactuators in the periodic voltage mode are shown in Figure 3.17b. The three experimental conditions of the periodic voltage mode were almost the same as those of the step voltage mode. However, amplitude and frequency must be added due to the periodic nature of the input. All the experiments were performed at relatively low frequencies (0.1, 1, 5 and 10 Hz) and at higher frequencies (20, 30, 40 and 50 Hz).



All the conditions were tested at relatively low and high frequencies.  
Low frequency: 0.1, 1, 5 and 10 Hz  
High frequency: 20, 30, 40 and 50 Hz

Figure 3.17. Design of experiments for the dynamic characterization. Experimental conditions for: (a) step voltage mode and (b) periodic voltage mode.

Experimental measurements for each condition in Figure 3.17 was taken at least three times. The potential error for the displacement measurements is mainly attributed to the laser sensor capabilities. Thus, the relative error of the experimental displacement measurements may be 0.05%. The obtained results for both, step and periodic voltage modes, are presented in next sections.

### 3.6.3 Results of the step voltage mode

The essential points from the step responses that are going to be discussed are:

- maximum displacement that the microactuator can achieve (peak)
- time to reach the maximum displacement (peak time)
- settling displacement (steady-state response)
- time required to reach the settling displacement (settling time)

Figure 3.18 shows a characteristic underdamped response at an applied step input. It is possible to observe that the maximum displacement corresponds to the maximum peak in the graph. The time required to reach the maximum displacement is called the peak time. The settling displacement (steady-state response) is achieved when the oscillation amplitudes show variations within a tolerance of  $\pm 2\%$  from a reference value. The time to reach the settling displacement is called the settling time.

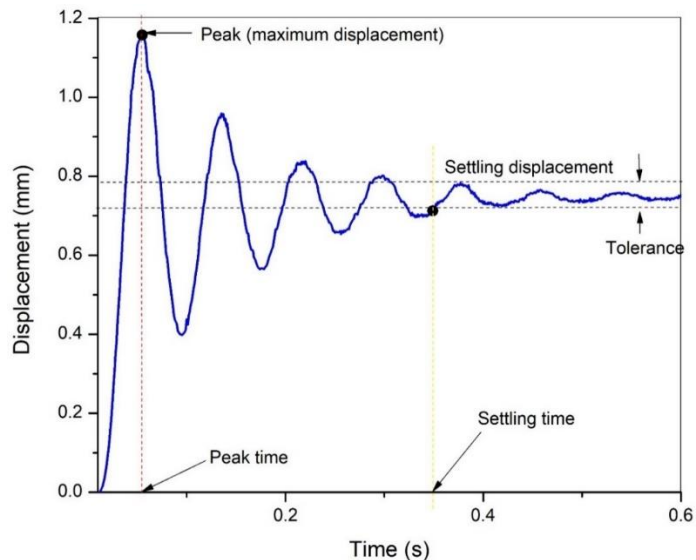


Figure 3.18. Characteristic underdamped response for a step voltage input.

The discussion of the dynamic responses of the microactuators in the step voltage mode are based on the points mentioned above. Samples were tested for each condition showed in Figure 3.17a.

*3.6.3.1 Condition 1: studies are carried out with various iron oxide nanoparticles concentrations but the same cantilever dimensions and input voltage*

A step voltage of 30 V was applied. This voltage generates a magnetic field of 0.87 kOe at a distance of 2 mm from the electromagnet. Figure 3.19 shows the responses (displacement versus time) for the microactuators of the three different iron oxide nanoparticles concentrations: (a) PVB/Fe<sub>2</sub>O<sub>3</sub>\_17% wt Fe, (b) PVB/Fe<sub>2</sub>O<sub>3</sub>\_14% wt Fe and (c) PVB/Fe<sub>2</sub>O<sub>3</sub>\_11% wt Fe. The cantilever dimensions are 15 mm in length, 2 mm in width and 0.018 mm in thickness for the three microactuators tested under this condition.

The three different microactuators exhibit a displacement in response to the magnetic field generated by the electromagnet. Since polymers are diamagnetic in nature, the displacement response is considered a consequence of the iron oxide nanoparticles embedded in the PVB matrix. According to magnetometry results, these iron oxide nanoparticles are superparamagnetic, *i.e.* they have randomly oriented magnetic moments that can be aligned and magnetized with an external magnetic field. Thus, the magnetized iron oxide nanoparticles generate magnetic forces of attraction in the magnetic field direction. These forces are transmitted to the surrounding polymer through its contact surface with the iron oxide nanoparticles. The polymer deforms and this deformation promotes a macroscopical displacement of the whole cantilever. Figure 3.20 shows the schematic representation of the iron oxide nanoparticles inside the PVB before and after applying a uniform magnetic field.

Moreover, all the responses shown in Figure 3.19 exhibit strong oscillations until a steady state is reached. This behavior is characteristic of underdamped systems. It is considered that the underdamped responses of the microactuators are caused by the cantilever structure itself and the internal properties of the material. This will be analyzed along this thesis.

The damping behavior of the microactuators can be appreciated in Figure 3.19. The microactuator of the sample PVB/Fe<sub>2</sub>O<sub>3</sub>\_11%wt Fe shows the weakest oscillations. Stronger oscillations are shown by the PVB/Fe<sub>2</sub>O<sub>3</sub>\_14%wt Fe microactuator. For the microactuator of the sample PVB/Fe<sub>2</sub>O<sub>3</sub>\_17%wt Fe, the oscillations seem to be smoother than the oscillations of the PVB/Fe<sub>2</sub>O<sub>3</sub>\_14%wt Fe sample and the peaks are a little bit rounded. It is considered that the more rounded the shape, the more damping present [177].

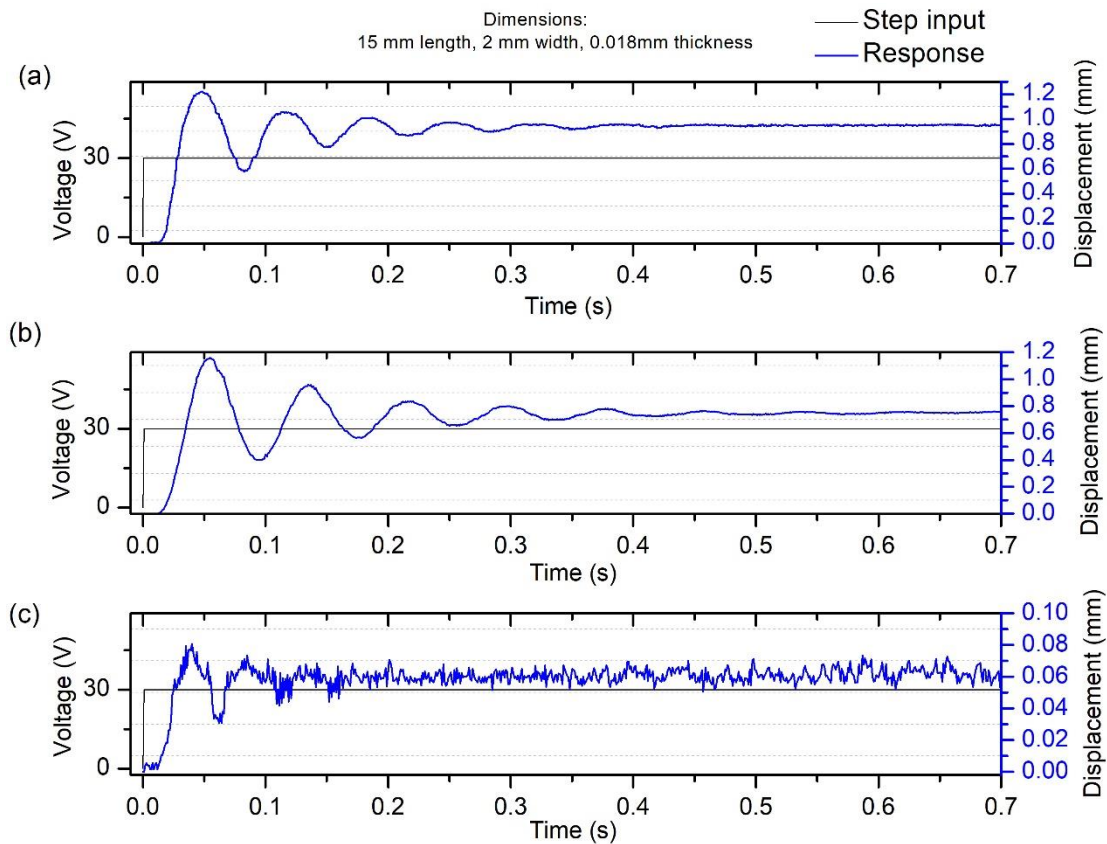


Figure 3.19. Responses of the microactuators at three different iron oxide nanoparticles concentrations: (a) PVB/Fe<sub>2</sub>O<sub>3</sub>\_17%wt Fe, (b) PVB/Fe<sub>2</sub>O<sub>3</sub>\_14%wt Fe and (c) PVB/Fe<sub>2</sub>O<sub>3</sub>\_11%wt Fe.

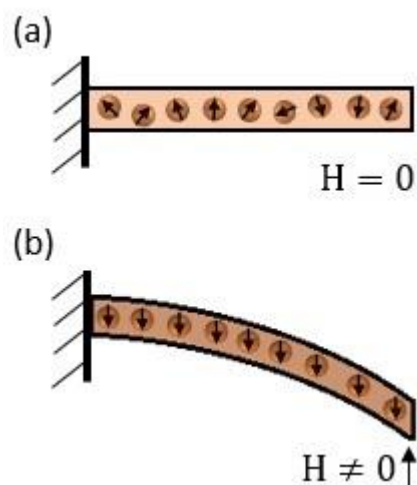


Figure 3.20. Schematic representation of the iron oxide nanoparticles in the PVB matrix of the microactuators: (a) without magnetic field and (b) when an external uniform magnetic field  $H$  is applied.

The values of maximum displacement (peak) and settling displacement for the three microactuator are summarized in Table 3.6. The maximum peak increases when increasing the iron oxide nanoparticles content in the PVB matrix. The same situation occurs with the settling displacement. According to the magnetometry results shown in section 3.5.3, the magnetization increases by increasing the iron oxide nanoparticles concentration. Therefore, by increasing the magnetization, bigger magnetic forces of attraction are present. The bigger the magnetic forces of attraction, the larger the displacement.

It should be noted that a huge difference in the displacement values is presented for the microactuator of the sample PVB/Fe<sub>2</sub>O<sub>3</sub>\_11%wt Fe compared with the two others (PVB/Fe<sub>2</sub>O<sub>3</sub>\_14%wt Fe and PVB/Fe<sub>2</sub>O<sub>3</sub>\_17%wt Fe). For example, the percentage difference between the maximum displacement of the PVB/Fe<sub>2</sub>O<sub>3</sub>\_11%wt Fe and the PVB/Fe<sub>2</sub>O<sub>3</sub>\_14%wt Fe microactuators is 173.82%, while the percentage difference between the PVB/Fe<sub>2</sub>O<sub>3</sub>\_14%wt Fe and the PVB/Fe<sub>2</sub>O<sub>3</sub>\_17%wt Fe microactuators corresponds to 5.46%. These results suggest the presence of a threshold value of the iron oxide nanoparticles content in relation to the PVB matrix. By exceeding this threshold, the magnetic forces generated by the iron oxide nanoparticles at the applied magnetic field should be strong enough to move the diamagnetic mass fraction of PVB. Thus, the

displacement of the cantilever microactuator would be drastically enhanced at the conditions of this study. However, this should be corroborated by further investigations.

Table 3.6. Maximum displacement and settling displacement values for the three microactuators with different iron oxide nanoparticles content.

	<b>PVB/Fe<sub>2</sub>O<sub>3</sub>_11%wt Fe</b>	<b>PVB/Fe<sub>2</sub>O<sub>3</sub>_14%wt Fe</b>	<b>PVB/Fe<sub>2</sub>O<sub>3</sub>_17%wt Fe</b>	<b>Unit</b>
<b>Peak (maximum displacement)</b>	0.081	1.157	1.222	mm
<b>Settling displacement</b>	0.061	0.753	0.951	mm

Table 3.7 presents the time to reach the maximum displacement and the time taken for the settling displacement for each microactuator. The microactuator of the sample PVB/Fe<sub>2</sub>O<sub>3</sub>\_11% wt Fe shows the shortest time to reach the maximum displacement (0.040 s) by comparing with the others. The relatively short times shown by the PVB/Fe<sub>2</sub>O<sub>3</sub>\_11% wt Fe microactuator may be due to its small displacement. An increase in the maximum displacement to 0.55 s was observed for the microactuator of sample PVB/Fe<sub>2</sub>O<sub>3</sub>\_14% wt Fe. This increase may be attributed to the increment in the maximum displacement value, comparing with the PVB/Fe<sub>2</sub>O<sub>3</sub>\_11% wt Fe microactuator. However, for the microactuator of the sample PVB/Fe<sub>2</sub>O<sub>3</sub>\_17% wt Fe the time to reach the maximum displacement is 0.048s. This time is shorter in comparison with the PVB/Fe<sub>2</sub>O<sub>3</sub>\_14% wt Fe microactuator. In this case, although PVB/Fe<sub>2</sub>O<sub>3</sub>\_17% wt Fe microactuator presents the highest value of maximum displacement, it takes less time to achieve it because of the greater amount of iron oxide nanoparticles. In consequence, this microactuator experiments the highest magnetization.

The shortest settling time was presented for the PVB/Fe<sub>2</sub>O<sub>3</sub>\_11% wt Fe microactuator. Since this sample contains the largest amount of polymer in comparison with the others (as shown in Table 3.2), the damping property is better. In this case, damping is considered to be ascribed to viscoelastic properties of the polymeric matrix [178]. For the microactuator of the sample PVB/Fe<sub>2</sub>O<sub>3</sub>\_14% wt Fe the settling time increases to 0.512 s, probably due to a decrease in the polymeric content that diminishes the damping property. However, the microactuator of the sample PVB/Fe<sub>2</sub>O<sub>3</sub>\_17% wt Fe shows higher damper properties in comparison with the PVB/Fe<sub>2</sub>O<sub>3</sub>\_14% wt Fe microactuator. The settling time

of the PVB/Fe<sub>2</sub>O<sub>3</sub>\_17%wt Fe microactuator diminishes to 0.442 s. This behavior is attributed to a combination between magnetic damping and the damping caused by the polymer. Magnetic damping occurs since the PVB/Fe<sub>2</sub>O<sub>3</sub>\_17%wt Fe microactuator contains the largest amount of iron oxide nanoparticles, the PVB content decreases and the distance between the nanoparticles becomes much smaller. In this sample, the magnetized iron oxide nanoparticles promote magnetic repulsive forces due to the proximity between them. The repulsive forces between particles produce energy losses, thus, damping is presented [179].

Table 3.7. Peak time and settling time values for the three microactuators with different iron oxide nanoparticles content.

	PVB/Fe <sub>2</sub> O <sub>3</sub> _11%wt Fe	PVB/Fe <sub>2</sub> O <sub>3</sub> _14%wt Fe	PVB/Fe <sub>2</sub> O <sub>3</sub> _17%wt Fe	Unit
<b>Peak time</b>	0.040	0.055	0.048	s
<b>Settling time</b>	0.250	0.512	0.422	s

*3.6.3.2 Condition 2: studies are carried out with various voltages but constant iron oxide nanoparticles concentration and cantilever dimensions*

The responses of displacement versus time for the PVB/Fe<sub>2</sub>O<sub>3</sub>\_14%wt Fe microactuator at two different step voltages supplied to the electromagnet are shown in Figure 3.21. The applied step voltages are 30 V (Figure 3.21a) and 15 V (Figure 3.21b). The electromagnet generates a magnetic field of 0.87 kOe for the step of 30 V, and 0.45 kOe for the step of 15 V. The magnetic field strength values were measured at 2 mm of distance from the central axis of the electromagnet. The cantilever dimensions are 15 mm in length, 2 mm in width and 0.018 mm in thickness, in both cases.

Table 3.8 shows the recorded values of maximum displacement and settling displacement. As expected, the values of maximum displacement and settling displacement (1.157 mm and 0.753 mm, respectively) are higher when the applied step voltage is 30 V (0.87 kOe), compared to those obtained (0.270 mm and 0.174 mm, respectively) for an input step voltage of 15 V (0.45 kOe). These responses are related to the generated magnetic field.



Stronger magnetic fields produce stronger magnetic forces of attraction in the microactuator, resulting in larger displacements.

Table 3.9 shows that the acquired values of peak time and settling time are very similar for both applied step voltages. All the transient responses are relatively in phase because the microactuators have the same dimensions and same iron oxide nanoparticles content. However, slightly shorter times are observed when a step of 15 V is applied. These shorter times are related to the shorter displacement recorded in this case.

From the above-mentioned analysis, it is possible to conclude that by applying different values of step voltage to the electromagnet, the displacement of the PVB/Fe<sub>2</sub>O<sub>3</sub>\_14% wt Fe microactuator is affected in function of the magnetic field. The displacement of the microactuator is directly proportional to the applied step voltage to the electromagnet. However, the changes in magnetic field do not affect the transient behavior, which was only slightly modified. The study of the displacement responses in a wider range of applied step voltages is of interest on further investigations.

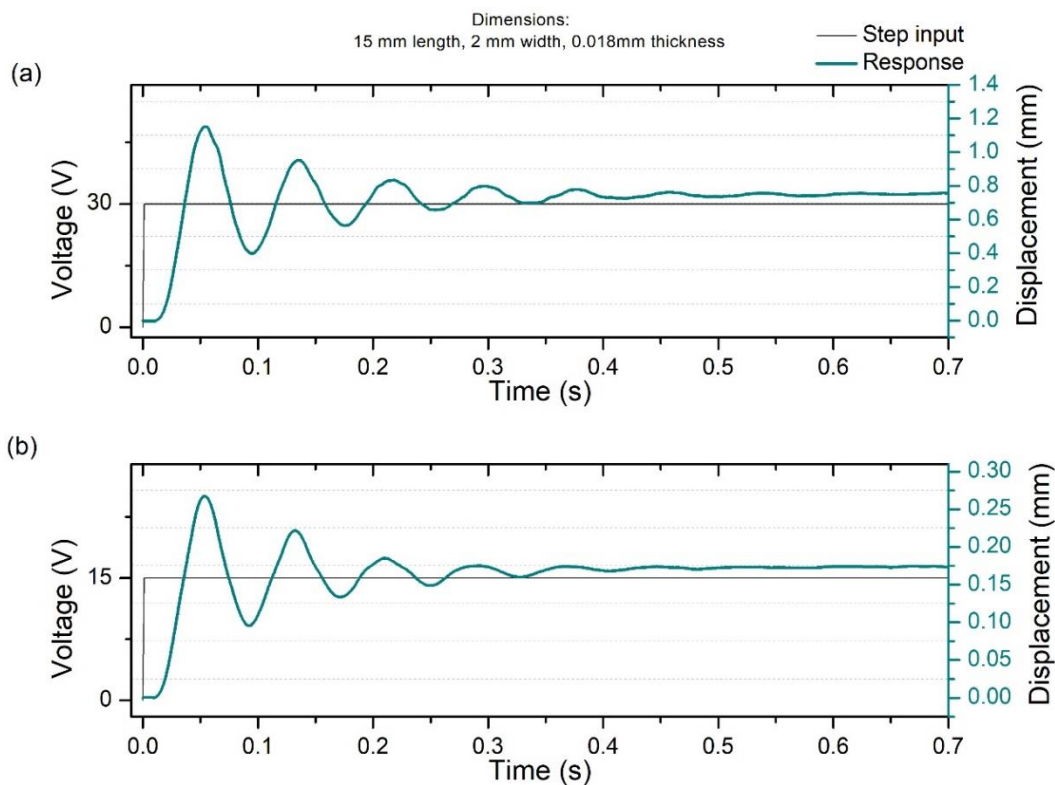


Figure 3.21. Responses of the PVB/Fe<sub>2</sub>O<sub>3</sub>\_14% wt Fe microactuator at two different step voltage inputs: (a) 30 V and (b) 15 V.

Table 3.8. Maximum displacement and settling displacement values for the PVB/Fe<sub>2</sub>O<sub>3</sub>\_14%wt Fe microactuator at 30 V and 15 V of step voltage.

	<b>30 V</b>	<b>15 V</b>	<b>Unit</b>
<b>Peak (maximum displacement)</b>	1.157	0.27	mm
<b>Settling displacement</b>	0.753	0.174	mm

Table 3.9. Peak time and settling time values for the PVB/Fe<sub>2</sub>O<sub>3</sub>\_14%wt Fe microactuator at 30 V and 15 V of step voltage.

	<b>30 V</b>	<b>15 V</b>	<b>Unit</b>
<b>Peak time</b>	0.055	0.053	s
<b>Settling time</b>	0.512	0.491	s

3.6.3.3 *Condition 3: studies are carried out with different cantilever dimensions but constant iron oxide nanoparticles concentration and input voltage*

Figure 3.22 shows the response for the microactuator of the sample PVB/Fe<sub>2</sub>O<sub>3</sub>\_14%wt Fe at two different sizes. The microactuator of size 1 has dimensions of 15 mm in length, 2 mm in width and 0.018 mm in thickness, while the microactuator of size 2 has dimensions of 15 mm in length, 4 mm in width and 0.018 mm in thickness. By comparing the dimensions of the microactuator of size 1 with the one of size 2, it is possible to observe that only the width was changed from 2 mm to 4 mm. This change result in an increment of the microactuator cross-section area from 0.036 mm<sup>2</sup> to 0.072 mm<sup>2</sup>. The step responses of the microactuator of size 1 and size 2 are shown, respectively, in Figure 3.22a and Figure 3.22b. A step of 30 V was applied to the electromagnet in both cases. The electromagnet generates a magnetic field of 0.87 kOe at 2 mm of distance from its central axis.

The values of maximum displacement and settling displacement for the two sizes of microactuator are summarized in Table 3.10. It is possible to observe that by increasing the cross section of the microactuator, the displacement values decrease. Since the same

magnetic field was supplied to the free end of both microactuators, the decrement of the displacement is related to an increment of the stiffness. It has been reported that the stiffness increases with an increase in the cantilever cross-sectional moment of inertia [180].

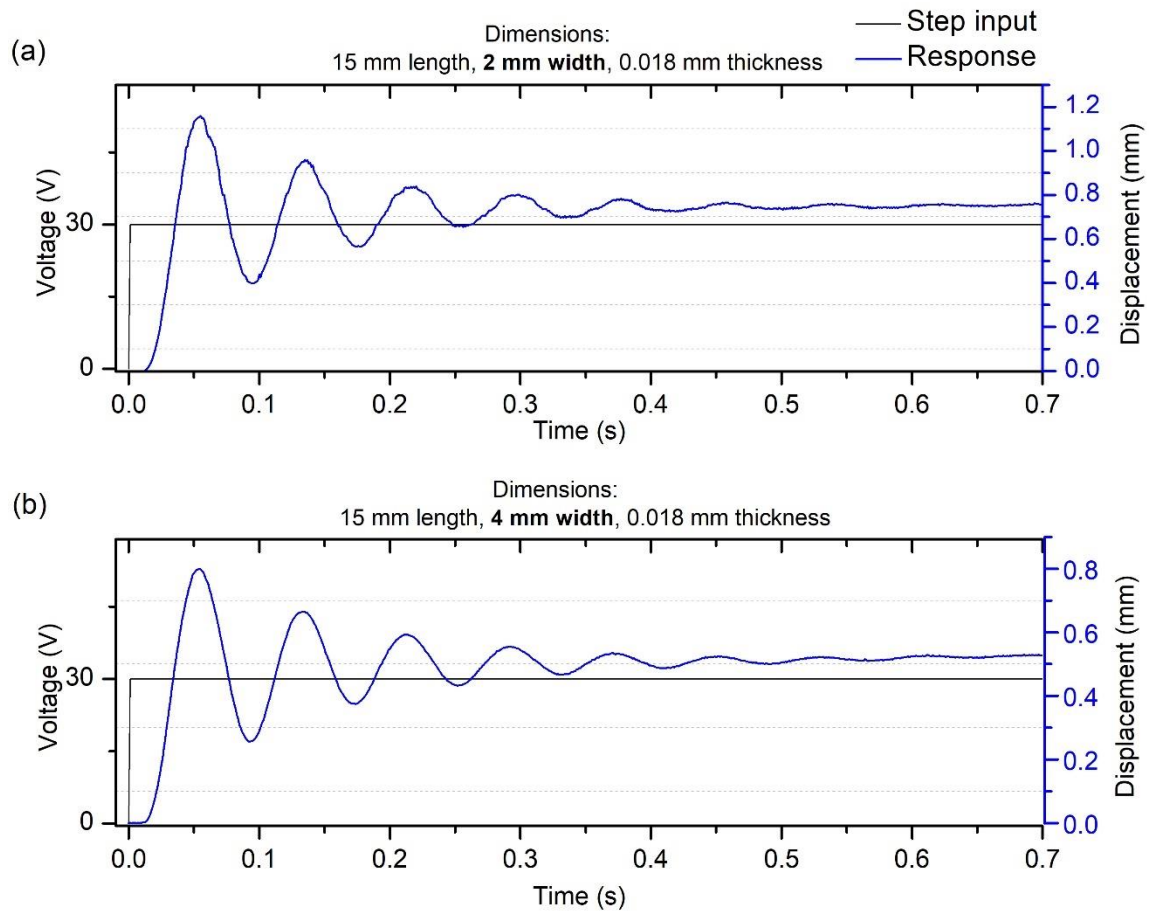


Figure 3.22. Responses of the PVB/Fe<sub>2</sub>O<sub>3</sub>\_14% wt Fe microactuator with different dimensions. (a) Size 1: 15 mm in length, 2 mm in width, 0.018 mm in thickness. (b) Size 2: 15 mm in length, 4 mm in width, 0.018 mm in thickness.

Table 3.10. Maximum displacement and settling displacement values for the PVB/Fe<sub>2</sub>O<sub>3</sub>\_14% wt Fe microactuator of size 1 and size 2.

	Size 1	Size 2	Unit
Peak (maximum displacement)	1.157	0.799	mm
Settling displacement	0.753	0.525	mm

Table 3.11 shows the values of peak time and settling time of both samples. It is possible to observe that the settling time is longer for the sample of size 2. This behavior is attributed also to the inertia moment due to the higher mass and the higher cross-sectional area in comparison with the sample of size 2.

Table 3.11. Peak time and settling time values for the PVB/Fe<sub>2</sub>O<sub>3</sub>\_14%wt Fe microactuator of size 1 and size 2.

	Size 1	Size 2	Unit
<b>Time to peak</b>	0.055	0.054	s
<b>Settling time</b>	0.512	0.581	s

Therefore, by increasing the cross-section of the microactuator, the cross-sectional moment of inertia also increases. As the cross-sectional moment of inertia increases, an increment of the stiffness is presented. The increased stiffness leads augmented values of settling time and shorter displacements in the cantilever microactuator.

The results for the input in periodic voltage mode are described in the next sections.

### 3.6.4 Results of the periodic voltage mode

Tests were performed by supplying a periodic voltage with a given amplitude and frequency to the electromagnet. The electromagnet generates a harmonic magnetic field. Thus, an oscillatory displacement of the PVB/Fe<sub>2</sub>O<sub>3</sub> microactuators was obtained in response. The oscillatory displacement of the cantilever microactuators was measured and plotted in function of the applied voltage. These plots were obtained in order to evaluate their input-output characteristics, specifically the nonlinearity and the possible presence of hysteresis. Figure 3.23 shows an example of the recorded data. In this example, a sine voltage from 0 to 30 V is applied with a frequency of 1 Hz (Figure 3.23a). The displacement response of the microactuator in function of the time is acquired (Figure

3.23b). Finally, the presence of hysteretic behavior is evaluated by plotting the displacement response in function of the applied voltage, as shown in Figure 3.23c.

The recorded hysteresis loops show a transition region and a stable region similar to the behavior of dielectric elastomers (see Figure 3.24). Largest restructuring of the magnetic dipoles in the nanoparticles occur during the first cycles. Since a maximum peak (overshoot) is achieved, minor restructuring is produced, stabilizing the hysteresis [26, 27]. The recorded hysteresis data in this work corresponds only to the monotonous behavior (stable region).

For the concerning experiments of this study, the cyclic responses of the cantilever microactuators were acquired after stabilization. Then, the stable hysteresis loops were normalized to zero. Test were carried out for all the conditions previously shown in Figure 3.17b. The discussion of the results for each condition is presented in the next sections.

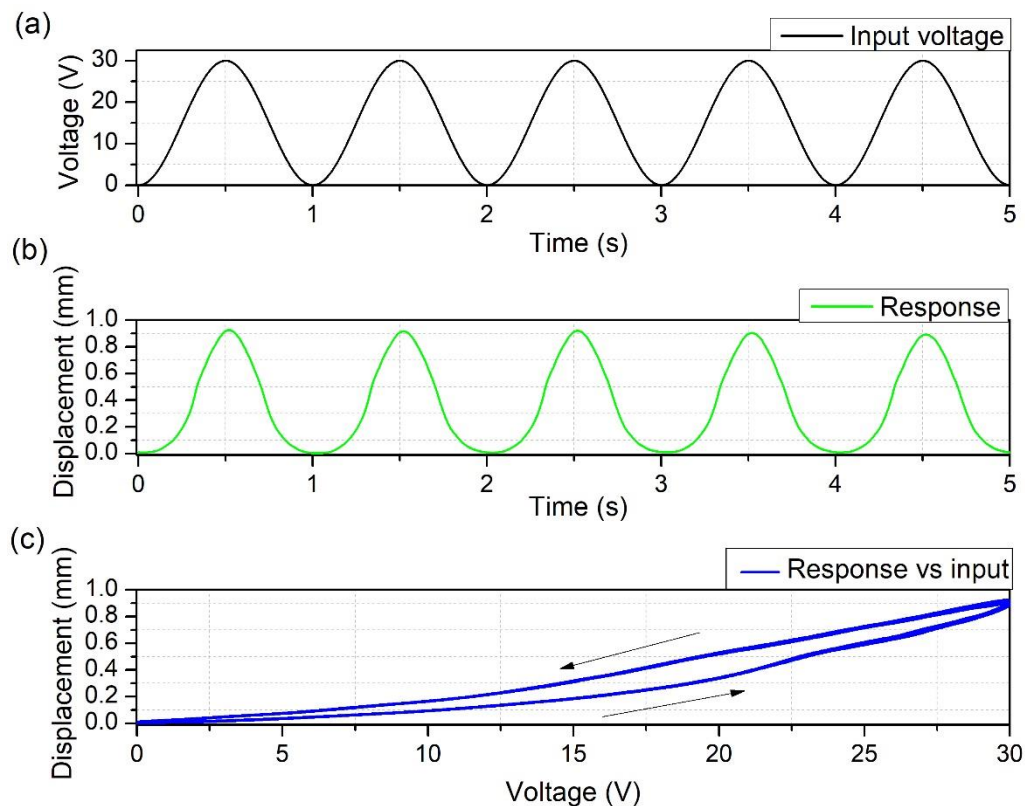


Figure 3.23. Recorded data in the periodic mode tests: (a) periodic voltage input, (b) oscillatory response (displacement) of the microactuator, (c) hysteresis loop of the displacement in function of the input voltage.

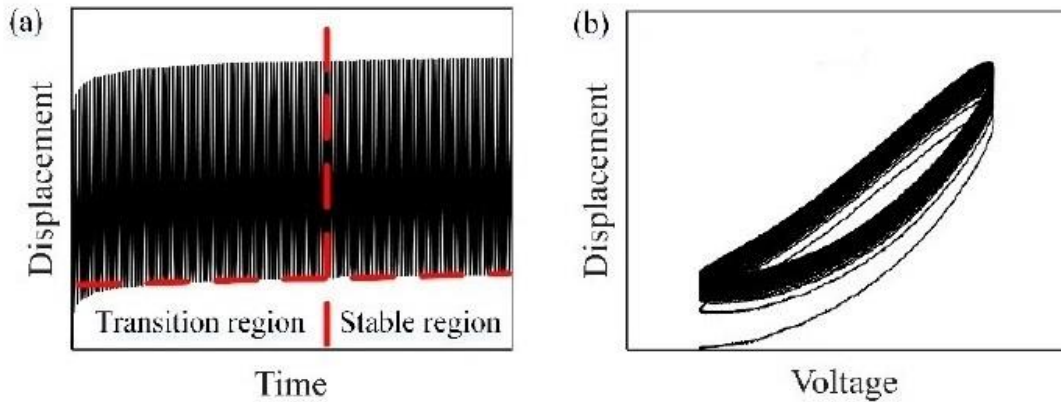


Figure 3.24. Response of a dielectric elastomer: (a) the transition and stable regions of the oscillatory displacement, (b) the effects of the transition region in the hysteresis loops [181].

3.6.4.1 *Condition 1: studies are carried out with various iron oxide nanoparticles concentrations but the same cantilever dimensions and input voltage*

Tests were conducted on each microactuator of different iron oxide nanoparticles concentration: PVB/Fe<sub>2</sub>O<sub>3</sub>\_17%wt Fe, PVB/Fe<sub>2</sub>O<sub>3</sub>\_14%wt Fe and PVB/Fe<sub>2</sub>O<sub>3</sub>\_11%wt Fe. A sine voltage was supplied to the electromagnet from 0 to 30 V. The electromagnet generates an oscillatory magnetic field from 0 to 0.87 kOe at 2 mm from its central axis. The frequency of oscillations was varied from relatively low frequencies (0.1 Hz, 1 Hz, 5 Hz and 10 Hz) to higher frequencies (20 Hz, 30 Hz, 40 Hz and 50 Hz). The dimensions of the microactuator were constant: 15 mm in length, 2 mm in width and 0.018 mm in thickness.

Figure 3.25 shows the curves of displacement versus voltage of the microactuators at relatively low frequencies (0.1 Hz, 1 Hz, 5 Hz and 10 Hz). Hysteresis loops are observed, meaning the presence of energy dissipation phenomena during the cyclic process. The hysteresis increases as the frequency also increases for all the samples, which represents a strong frequency-dependent behavior. Moreover, nonlinear dependence between the response and the input voltage was observed for all the samples.

The frequency-dependence in the response of the microactuators is attributed mainly to the relaxation times of both the viscoelastic polymeric matrix and the magnetic dipoles of the iron oxide nanoparticles. The relaxation time of the viscoelastic part is associated with internal molecular motions. Since the PVB is a thermoplastic polymer, its relaxation time is expected to be greater than 1 second [182][183]. On the other hand, the relaxation time of the magnetic dipoles after removing the external magnetic field is less than 1 second [184]. Therefore, times greater than 1 second should be enough to complete the relaxation process. This phenomenon can be observed for all the samples at the lowest frequency (0.1 Hz) shown in Figure 3.25. In this case, there is more time to carry out the relaxation, obtaining very small hysteresis [185]. As the frequency increases, the energy dissipation also increases, causing bigger hysteresis loops.

The maximum displacements reached at 0.1 Hz are 1.090 mm, 0.797 mm and 0.053 mm for PVB/Fe<sub>2</sub>O<sub>3</sub>\_17% wt Fe, PVB/Fe<sub>2</sub>O<sub>3</sub>\_14% wt Fe and PVB/Fe<sub>2</sub>O<sub>3</sub>\_11% wt Fe microactuators, respectively. The maximum displacement increases with the iron oxide nanoparticles content, as shown previously in the step voltage mode results. At 1 Hz, the maximum displacements decrease for all the samples, being 0.930 mm for PVB/Fe<sub>2</sub>O<sub>3</sub>\_17% wt Fe, 0.729 mm for PVB/Fe<sub>2</sub>O<sub>3</sub>\_14% wt Fe and 0.044 mm for PVB/Fe<sub>2</sub>O<sub>3</sub>\_11% wt Fe. The decrement in the maximum displacements at 1 Hz, compared to 0.1 Hz, is attributed to the greater amount of energy dissipated by the microactuators at such frequency (bigger hysteresis loop). When the microactuator is excited at relatively low frequencies, the material has more time to relax and the displacement is higher [117] [186].

Additionally, it was observed that the slope of the responses dramatically changes at a certain value of voltage (e.g., the direction of the displacement curve changes about 15 V for PVB/Fe<sub>2</sub>O<sub>3</sub>\_11% wt Fe, see Figure 3.25c). This trend is related to the geometry of the microactuator and the spatial distribution of the magnetic field. Figure 3.26 shows a 2-D simulation of an electromagnet and its magnetic field gradients. When the microactuator is distant of the electromagnet (around its rest or original position), the magnetic field gradient is small and the produced displacements are small. On the contrary, as the microactuator is closer to the electromagnet, the magnetic field gradient is higher, causing

larger displacements. A particular magnetic field value should be determinant to obtain this drastic modification [35]. These changes in slope are symmetric when the voltage is increasing and decreasing for all the samples at 0.1 Hz and 1 Hz.

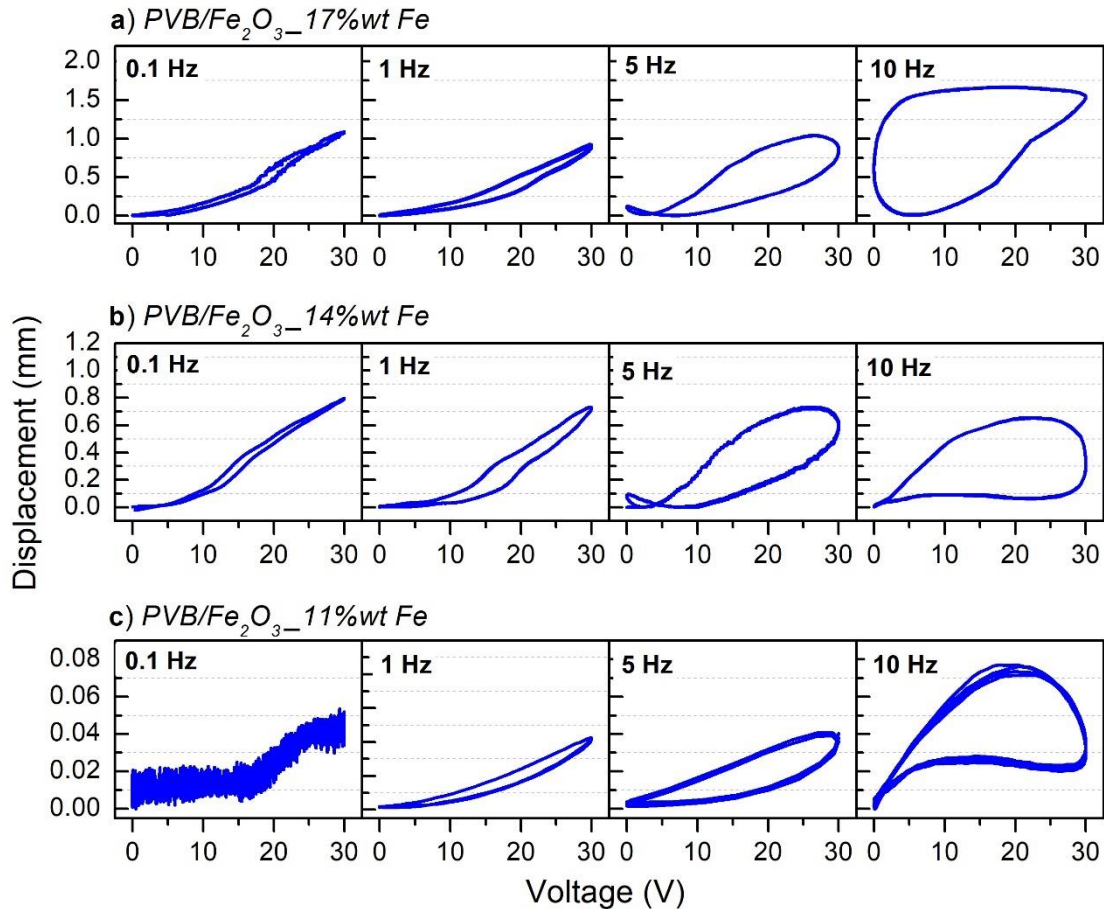


Figure 3.25. Experimental responses of the PVB/Fe<sub>2</sub>O<sub>3</sub> microactuators at 0.1 Hz, 1 Hz, 5 Hz and 10 Hz: (a) PVB/Fe<sub>2</sub>O<sub>3</sub>\_17% wt Fe, (b) PVB/Fe<sub>2</sub>O<sub>3</sub>\_14% wt Fe and (c) PVB/Fe<sub>2</sub>O<sub>3</sub>\_11% wt Fe.

Unusual behavior is found for 5 Hz and 10 Hz of oscillatory voltages applied to the electromagnet. At these frequencies the hysteresis loops become larger. The reversing response at 5 Hz starts to be more rounded for all the samples in comparison with the responses at lower frequencies. It can be noticed that the maximum displacement takes place when the input voltage begins to decrease. It indicates a phase-lag effect with respect to the oscillatory input voltage [186][187][188]. Similar behavior has been observed for dielectric electroactive polymers and it is attributed to the electrical charging and discharging dynamics [187]. In an analogous way, this behavior could be attributed to the



magnetization and demagnetization dynamics of the iron oxide nanoparticles. This should be further analyzed.

More complex hysteretic phenomena were presented at a frequency of 10 Hz for the three different microactuators. The biggest hysteresis loop was shown for the microactuator of the sample with more iron oxide nanoparticles concentration. This may indicate that the energy dissipation at this frequency is predominantly due to the rearrangement of the magnetic dipoles. Based on the showed behavior, it is possible to say that the microactuator is more convenient at low frequencies ( $< 5$  Hz).

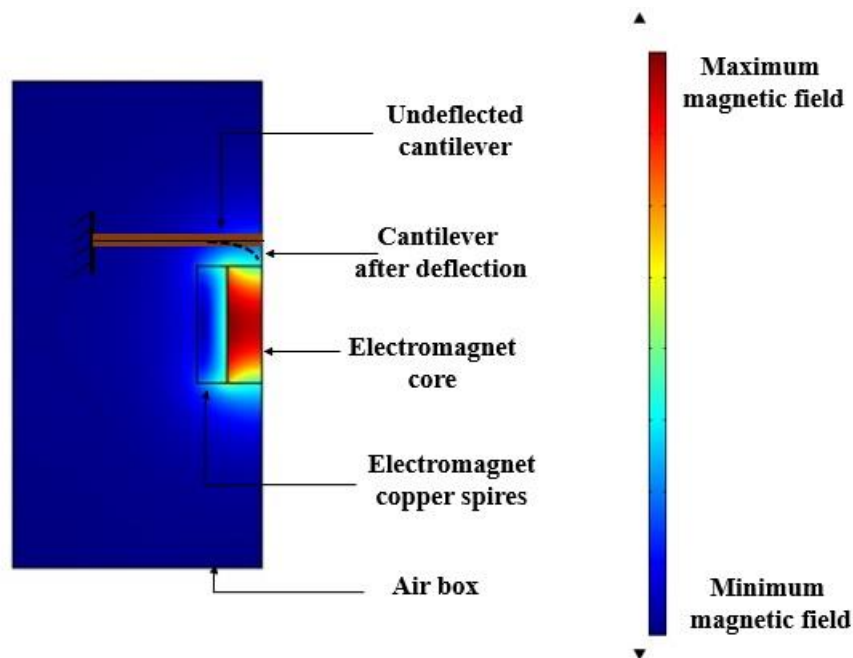


Figure 3.26. 2D simulation of the cantilever beam exposed to different magnetic field gradients.

Figure 3.27 presents the curves of voltage versus time and displacement versus time of the three microactuators in order to show the frequency at which additional oscillations start to appear. These additional oscillations were observed in the response of the PVB/Fe<sub>2</sub>O<sub>3</sub>\_17% wt Fe microactuator when an oscillatory voltage with a frequency of 5 Hz is applied. A similar behavior was observed for the microactuators of PVB/Fe<sub>2</sub>O<sub>3</sub>\_14% wt Fe at the same frequency. The microactuator of the sample PVB/Fe<sub>2</sub>O<sub>3</sub>\_11% wt Fe starts to exhibit these vibrations at a frequency 10 Hz. This behavior is promoted by higher order internal vibrations in the cantilever system [187].

Internal vibrations are associated with the approaching to the resonance region of the system [189]. This indicates that the resonance region of the PVB/Fe<sub>2</sub>O<sub>3</sub>\_17%wt Fe and the PVB/Fe<sub>2</sub>O<sub>3</sub>\_14%wt Fe microactuators can be observable at about 5 Hz, while the resonance region of the and PVB/Fe<sub>2</sub>O<sub>3</sub>\_11%wt Fe microactuator samples starts about 10 Hz.

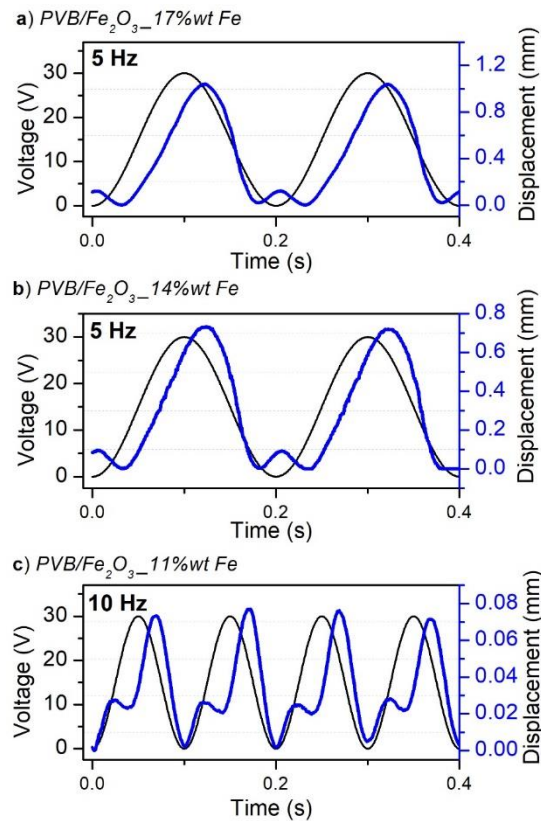


Figure 3.27. Oscillatory input voltage and harmonic displacement for the microactuators of the samples: (a) PVB/Fe<sub>2</sub>O<sub>3</sub>\_17% wt Fe, (b) PVB/Fe<sub>2</sub>O<sub>3</sub>\_14%wt Fe and (c) PVB/Fe<sub>2</sub>O<sub>3</sub>\_11% wt Fe.

As the frequency increases, the behavior starts to be quasi-elliptical and out-of-phase with the excitation input. This behavior could be appreciated in Figure 3.28, which shows the responses at higher frequencies (20 Hz, 30 Hz, 40 Hz and 50 Hz) for the three different microactuators. This indicates the presence of an asymmetry threshold frequency that has been surpassed at a frequency of 20 Hz. Similar behavior has been observed for another magnetoactive polymer in [189].

At 30 Hz and 40 Hz, it is possible to observe that the microactuator of the sample PVB/Fe<sub>2</sub>O<sub>3</sub>\_14% wt Fe shows more displacement, compared to the other microactuators. This could be attributed to two reasons: the lowest nanoparticles concentration of the PVB/Fe<sub>2</sub>O<sub>3</sub>\_11% wt Fe microactuator and the less elasticity of the PVB/Fe<sub>2</sub>O<sub>3</sub>\_17% wt Fe microactuator. On the one hand, the low concentration of iron oxide nanoparticles for the PVB/Fe<sub>2</sub>O<sub>3</sub>\_11% wt Fe microactuator may be not enough to react fast and propitiate the displacement of the polymeric matrix fraction at those frequencies. On the other hand, the PVB/Fe<sub>2</sub>O<sub>3</sub>\_17% wt Fe microactuator presents the lowest elasticity at room temperature (according to DMA results), which suggests that this microactuator is more viscous than elastic. The more viscous the material, the longer the delay of deformation in function of the applied stimuli [117].

When the magnetic field alternates at 50 Hz, the displacement becomes the smallest for all the samples and the hysteresis loops tend to disappear. This indicates that the time is not sufficient to permit higher displacements. In consequence, there is not enough time for the formation of the hysteresis loop [117].

The above results suggest that to avoid energy losses (hysteretic behavior), the actuator should operate at frequencies lower than 5 Hz. The microactuator experiments different gradients of magnetic field as it bends. This has a strong influence on the response. Moreover, the phase-lag effect seems to appear at frequencies about 5 Hz, which induces a low bandwidth for the microactuator. The low bandwidth may be due to the high length of the cantilever. Further researches with shorter lengths should be analyzed. Asymmetric hysteresis loops were found at 5 Hz to 10 Hz, which are attributed to the presence of higher order internal vibrations. The presence of internal vibrations is associated with the proximity to the resonance region of the system. At 50 Hz the displacement and the hysteresis decrease drastically for each sample with different iron oxide nanoparticles concentration.

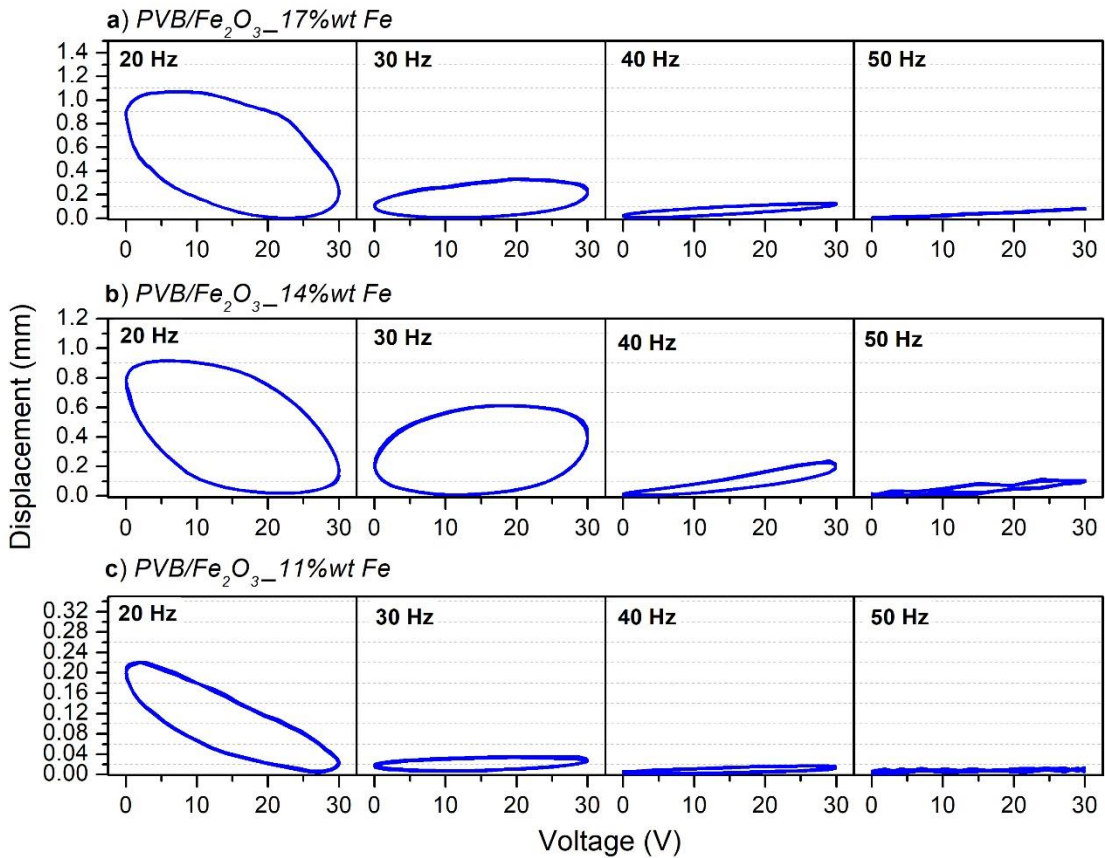


Figure 3.28. Experimental responses of the PVB/Fe<sub>2</sub>O<sub>3</sub> microactuators at 20 Hz, 30 Hz, 40 Hz and 50 Hz: (a) PVB/Fe<sub>2</sub>O<sub>3</sub>\_17% wt Fe, (b) PVB/Fe<sub>2</sub>O<sub>3</sub>\_14% wt Fe and (c) PVB/Fe<sub>2</sub>O<sub>3</sub>\_11% wt Fe.

#### 3.6.4.2 Condition 2: studies are carried out with various voltages but constant iron oxide nanoparticles concentration and cantilever dimensions

The PVB/Fe<sub>2</sub>O<sub>3</sub>\_14%wt Fe microactuator was tested at two different voltages. The tested voltages were from 0 to 30 V, to promote a magnetic field from 0 to 0.87 kOe, and from 0 to 15 V, to generate a magnetic field from 0 to 0.45 kOe. The magnetic field values were measured at a distance of 2 mm from the central axis of the electromagnet. The cantilever dimensions were constant, corresponding to 15 mm in length, 2 mm in width and 0.018 mm in thickness.

Figure 3.29 shows the responses of displacement versus voltage for the voltages of 0-30 V (Figure 3.29a) and 0-15 V (Figure 3.29b) at relatively low frequencies (0.1 Hz, 1 Hz, 5

Hz and 10 Hz). The hysteresis loops are larger as the frequency increases. This behavior is similar to that showed in the last section. The maximum displacement obtained with the voltage of 0-30V is 0.797 mm at 0.1 Hz; while, the maximum displacement obtained with the voltage of 0-15 V is 0.176 mm at 0.1 Hz. The hysteresis loops seem to be rounded at 5 Hz, in both cases. The rounded appearance is attributed to the magnetization and demagnetization dynamics of the iron oxide nanoparticles, as explained before. The hysteresis loops at 10 Hz show similar behavior between them. However, it is observed that with the voltage of 0-15 V, the microactuator reverse faster (the slope of the curve is more inclined). This fast reverse can be produced by a less magnetic force of attraction exerted on the cantilever compared to the case when a voltage of 0-30V is applied.

The response associated to the presence of internal vibrations starts at a frequency of 5 Hz. Figure 3.30 shows the harmonic displacement in function of time when periodic voltages of 0-30 V (Figure 3.30a) and 0-15 V (Figure 3.30b) are applied. As explained before, internal vibrations are related to the proximity to the resonance region of the system. Since the samples have the same nanoparticles concentration and the same cantilever dimensions, internal vibrations start to appear at the same frequency (5 Hz). At this frequency, the voltage amplitude does not have a large effect on the qualitative behavior of the samples. However, the responses are quantitatively different.

Figure 3.31 shows the responses of displacement versus voltage at higher frequencies (20 Hz, 30 Hz, 40 Hz and 50 Hz). The asymmetric threshold is surpassed after 10 Hz and the shapes of the hysteresis loops start to be quasi-elliptical. Also, it is possible to observe the drastic decrease in the hysteresis loops at 50 Hz, in both cases.

According to the presented results, it is possible to conclude that, as expected, by applying different voltage amplitudes to the electromagnet, the displacement of the sample will be different. However, the qualitative response is not strongly affected. Moreover, the start of the resonance region is the same in both cases because the iron oxide nanoparticles content and the dimensions do not change. Additional voltage amplitudes could be tested in future to corroborate these results.

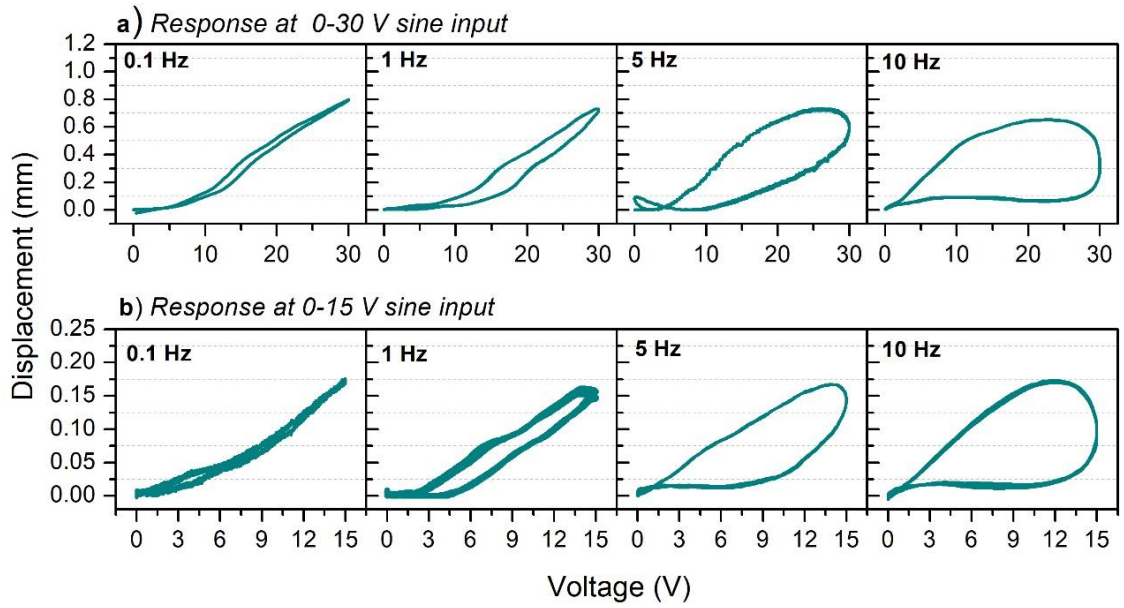


Figure 3.29. Experimental responses of the PVB/Fe<sub>2</sub>O<sub>3</sub>\_14%wt Fe microactuator at 0.1 Hz, 1 Hz, 5 Hz and 10 Hz, applying voltages of: (a) 0-30 V, (b) 0-15 V.

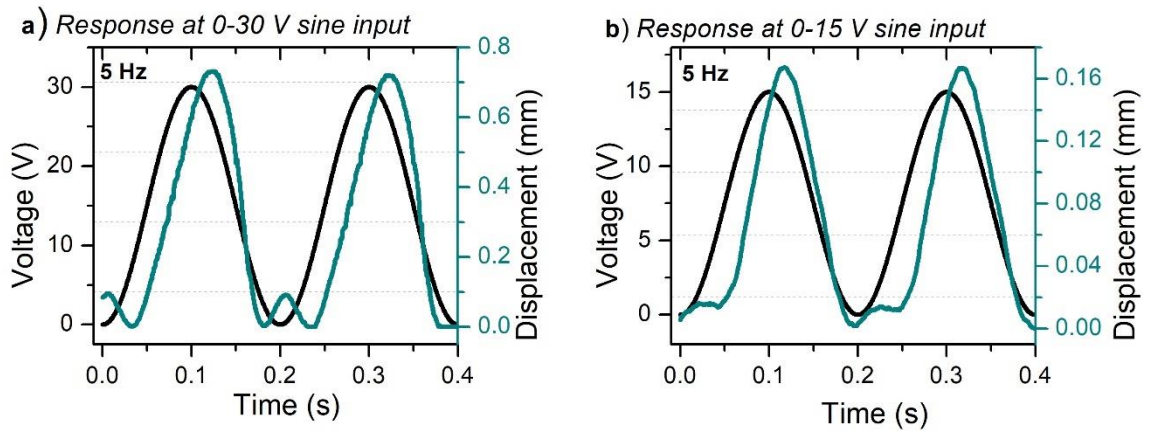


Figure 3.30. Oscillatory input voltage and harmonic displacement of the PVB/Fe<sub>2</sub>O<sub>3</sub>\_14%wt Fe microactuator with voltages of: (a) 0-30 V and (b) 0-15 V.

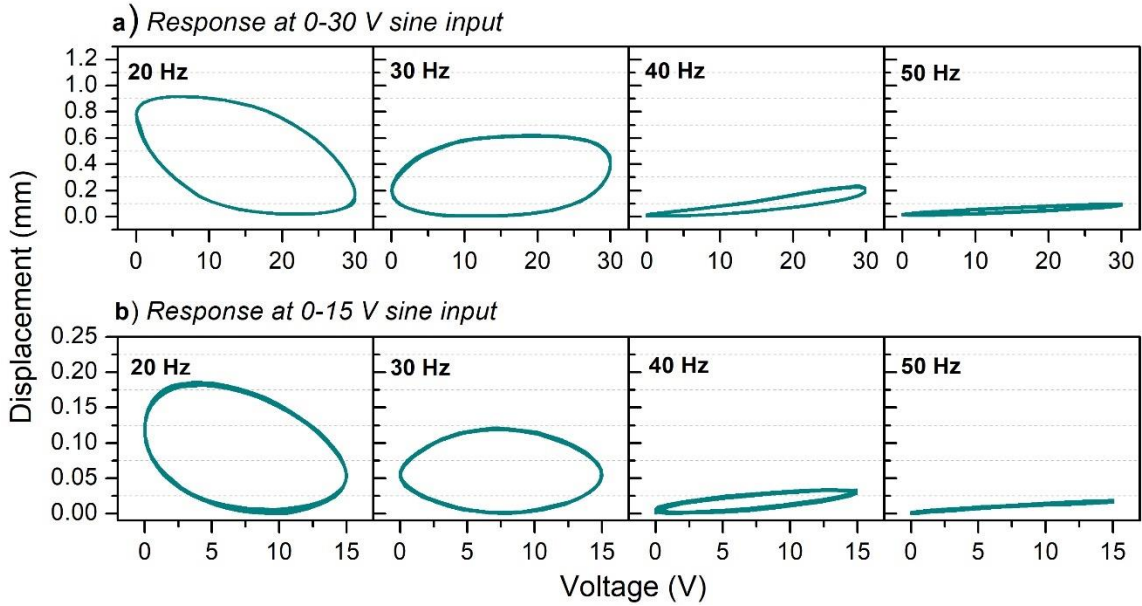


Figure 3.31. Experimental responses of the PVB/Fe<sub>2</sub>O<sub>3</sub>\_14% wt Fe microactuator at 20 Hz, 30 Hz, 40 Hz and 50 Hz, with voltages of: (a) 0-30 V and (b) 0-15 V.

3.6.4.3 Condition 3: studies are carried out with different cantilever dimensions but constant iron oxide nanoparticles concentration and input voltage

Figure 3.32 shows the results for two different cantilever dimensions of the PVB/Fe<sub>2</sub>O<sub>3</sub>\_14% wt Fe microactuator at relatively low frequencies (0.1 Hz, 1 Hz, 5 Hz and 10 Hz). Figure 3.32a shows the results of the cantilever dimensions of 15 mm in length, 2 mm in width and 0.018 mm in thickness (size 1). Figure 3.32b presents the results for the microactuator of 15 mm in length, 4 mm in width and 0.018 mm in thickness (size 2). Tests were performed for a constant voltage of 0-30 V. The electromagnet generates a magnetic field from 0 to 0.87 kOe at 2 mm of distance from its central axis.

The maximum displacements are lower for the microactuator of size 2, compared to the microactuator of size 1. This is attributed to the increase in stiffness at increasing the cross section of the cantilever, as explained in section 3.6.3.3. The maximum displacement is 0.797 mm at 0.1 Hz for the microactuator of size 1 and 0.487 mm for the microactuator of size 2 at the same frequency. The asymmetric behavior is observed at 5 Hz and 10 Hz, in both cases.

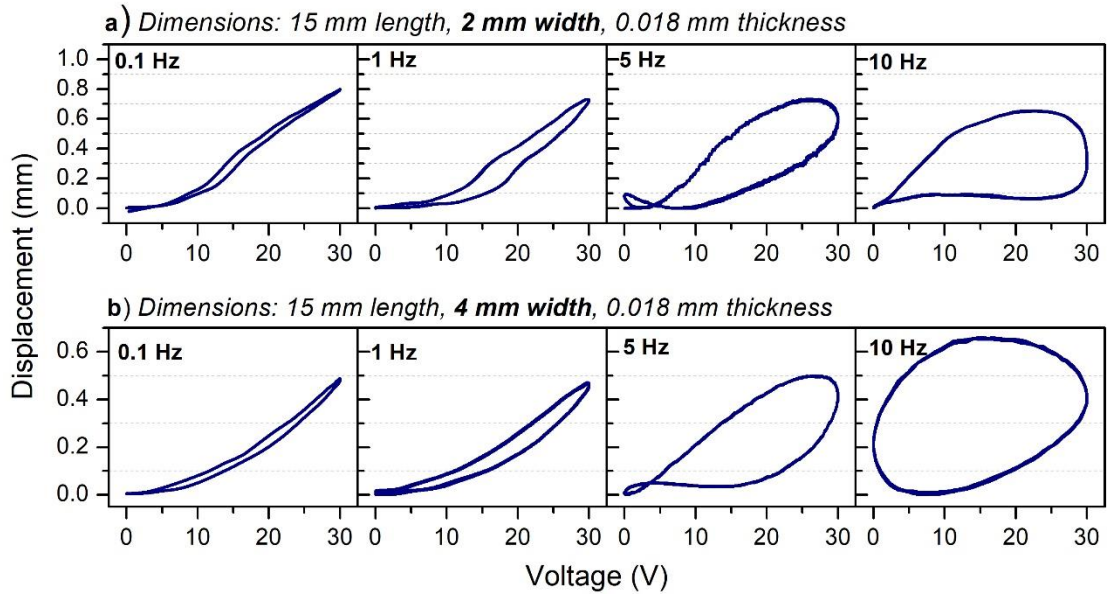
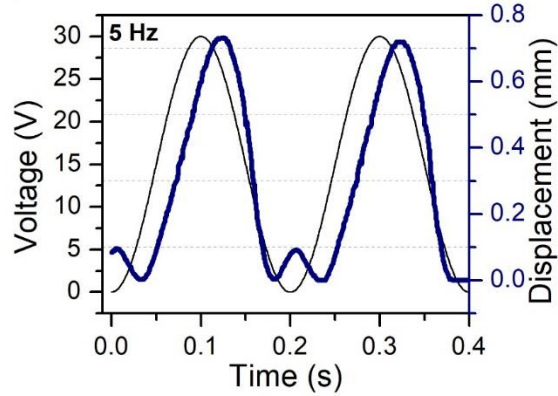


Figure 3.32. Experimental responses of the PVB/Fe<sub>2</sub>O<sub>3</sub>\_14%wt Fe microactuators at 0.1 Hz, 1 Hz, 5 Hz and 10 Hz; voltage of 0-30 V and dimensions (length, width, thickness) of: (a) 15 mm, 2 mm, 0.018 mm (size 1) and (b) 15 mm, 4 mm, 0.018 mm (size 2).

Figure 3.33 shows the displacement versus time for both microactuators at 5 Hz. The oscillatory voltage of 0-30 V is also shown as reference on each graph. The internal vibrations are presented at 5 Hz for both cases. The internal vibrations are related to the resonance region of the system, as mentioned previously.



a) Dimensions: 15 mm length, 2 mm width, 0.018 mm thickness



b) Dimensions: 15 mm length, 4 mm width, 0.018 mm thickness

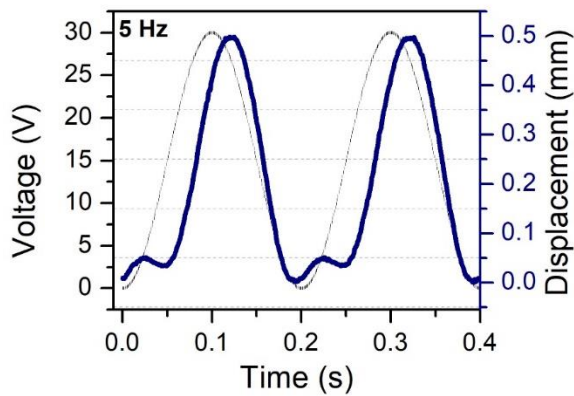


Figure 3.33. Oscillatory input voltage and harmonic displacement of the microactuators with dimensions (length, width, thickness) of: (a) 15 mm, 2 mm, 0.018 mm (size 1) and (b) 15 mm, 4 mm, 0.018 mm (size 2).

At higher frequencies (20 Hz, 30 Hz, 40 Hz and 50 Hz) the asymmetric threshold has been surpassed and the behavior starts to be quasi-elliptical, similar to the obtained results for conditions 1 and 2. This behavior can be observed in Figure 3.34. The hysteresis starts to decrease and the displacement diminishes considerably at 50 Hz.

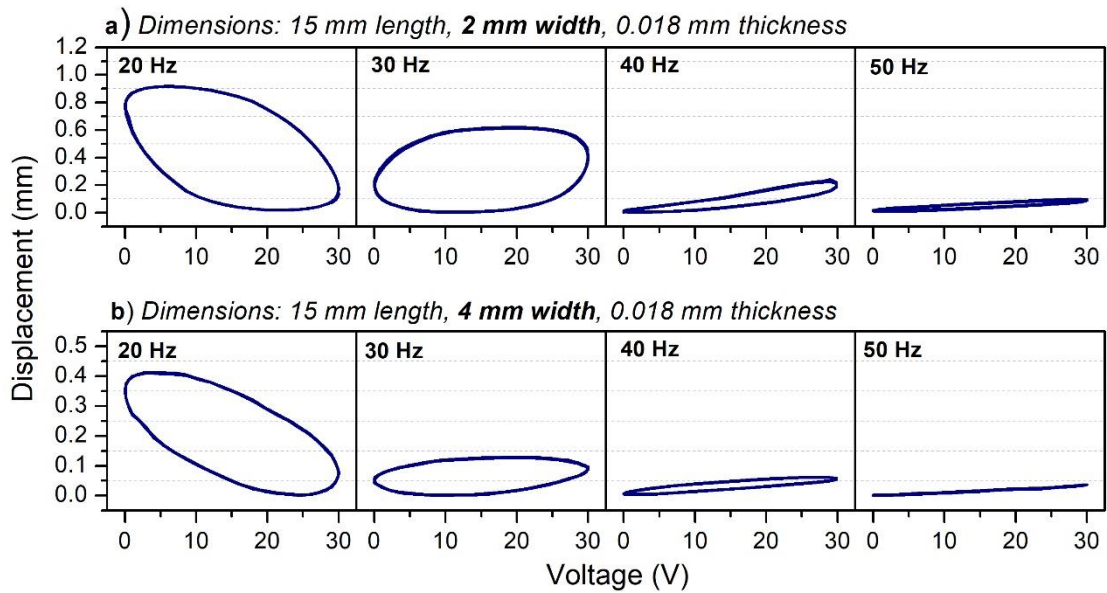


Figure 3.34. Experimental responses of the PVB/Fe<sub>2</sub>O<sub>3</sub>\_14% wt Fe microactuator at 20 Hz, 30 Hz, 40 Hz and 50 Hz; voltage of 0-30 V and dimensions (length, width, thickness) of: (a) 15 mm, 2 mm, 0.018 mm (size 1), (b) 15 mm, 4 mm, 0.018 mm (size 2).

Once having the dynamic responses of the microactuators obtained along the dynamic characterization. The model of such responses will be described in the next chapter.

### 3.6.5 Conclusions

- Films of polyvinyl butyral with iron oxide nanoparticles (PVB/Fe<sub>2</sub>O<sub>3</sub>) were synthesized at nominal concentrations of 11% wt, 14% wt and 17% wt of iron (Fe).
- The PVB/Fe<sub>2</sub>O<sub>3</sub> films exhibit superparamagnetic behavior according to the results of the magnetic characterization. Superparamagnetic behavior indicates the presence of magnetic nanoparticles (size under 15 nm) embedded in the polymeric matrix. These results are coincident with previous researches.
- The characterization of the PVB/Fe<sub>2</sub>O<sub>3</sub> films as cantilever microactuator was performed in two modalities: the step voltage mode and the periodic voltage mode.
- All the responses in the step voltage mode showed underdamped behavior, proper of this kind of cantilever configuration.

- The displacement of the cantilever microactuator increases as the iron oxide nanoparticles content increases.
- The maximum settling displacement obtained in the step voltage mode was 0.951 mm at a step voltage of 30 V (0.87 kOe of magnetic field). This response was obtained for the microactuator of the sample with the highest content of iron oxide nanoparticles (PVB/Fe<sub>2</sub>O<sub>3</sub>\_17% wt Fe).
- The displacement of the cantilever microactuator is proportional to the applied step voltage. However, the transient response will not be modified by changing the step voltage value. This is only applicable when the iron oxide nanoparticles concentration and the microactuator dimensions are constant.
- By increasing the cross section of the cantilever microactuator, the displacement decreases for the same applied step voltage (same magnetic field strength). This is related to the increment in the cross-sectional moment of inertia, which increases the stiffness.
- The cantilever microactuator tested in the periodic voltage mode showed rate-dependent and nonlinear behavior.
- The rate-dependence is attributed to the relaxation times of the polymeric matrix and the iron oxide nanoparticles.
- For all the cases, low bandwidth was observed. According to the results, the use of the microactuator should be at frequencies under 5 Hz.
- Asymmetric hysteresis loops were observed only at 5 Hz and 10 Hz for all the cases. This suggest the presence of an asymmetric threshold frequency.
- Internal vibrations were presented in the same region of the asymmetric threshold frequency (5 Hz and 10 Hz). This behavior is associated to the resonance region of the cantilever microactuator.

# CHAPTER 4

## MODELING AND SIMULATION OF THE DYNAMIC DISPLACEMENTS

### 4.1 INTRODUCTION

In this chapter, a model for the dynamic displacements of the cantilever microactuators formed by magnetic films of polyvinyl butyral with iron oxide nanoparticles (PVB/Fe<sub>2</sub>O<sub>3</sub>) is proposed. The model involves coupled differential equations based on physical principles. The remainder of this chapter is arranged in the following manner: the configuration of the system and the recognition of the fundamental parameters involved in the response of the microactuator are presented in section 4.2; the model formulation is provided in section 4.3; the identification of parameters in the model is deduced in section 4.4; the numerical validation is shown in section 4.5; some concluding remarks are stated in section 4.6.

### 4.2 THE CONFIGURATION OF THE SYSTEM

The PVB/Fe<sub>2</sub>O<sub>3</sub> microactuator is configured in a cantilever structure with one-end fixed and the other end free. This configuration is shown in Figure 4.1. It corresponds to the same configuration used for the experimental measurements presented in chapter 3.

The overall actuation process consists of different actions:

An externally-applied voltage ( $u$ ) creates a current ( $i$ ) flowing through an electromagnet. Due to this current, a magnetic field ( $B$ ) is generated. Magnetic dipoles inside the PVB/Fe<sub>2</sub>O<sub>3</sub> microactuator tends to align with the magnetic field producing the magnetization of the microactuator. This magnetization creates a resultant magnetic force ( $F$ ) in the direction of the electromagnet. Hence, the microactuator responds with a deformation. This deformation consequently leads to a displacement which is more evident at the free end of the cantilever microactuator (point  $D$  in Figure 4.1). At rest state, this point is originally situated at a distance  $z$  from the center of the electromagnet.

The proposed model will be focused on the response of the displacement at the free end of the cantilever microactuator when an external voltage is applied to the electromagnet. This displacement will be treated as  $\delta_D^{dynamic}$  along this text.

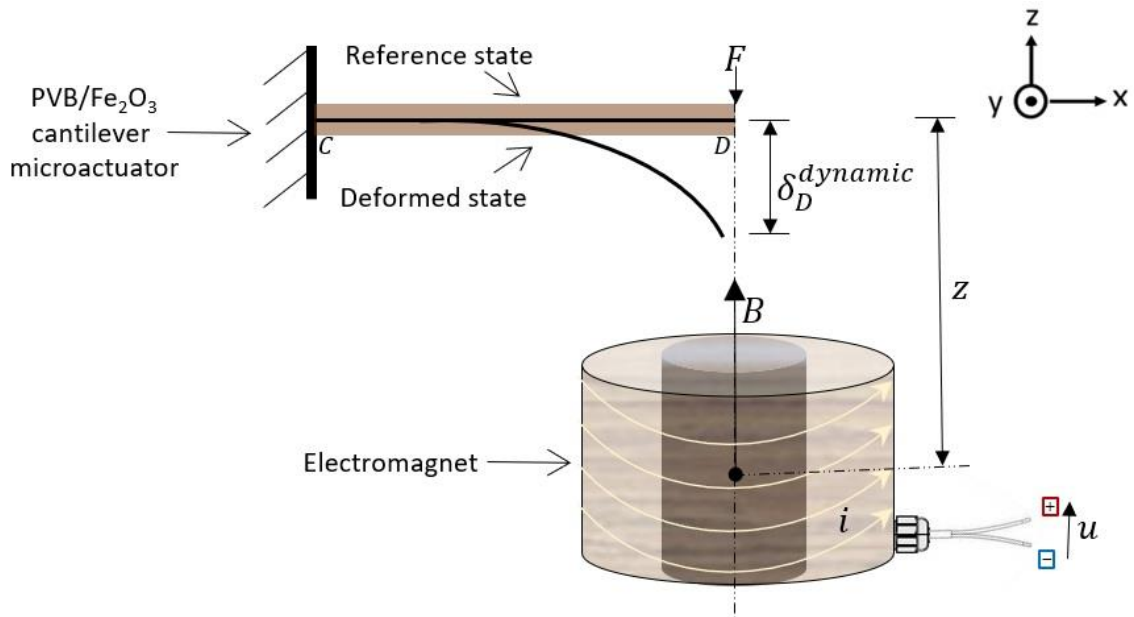


Figure 4.1. Representation of the PVB/Fe<sub>2</sub>O<sub>3</sub> cantilever microactuator.

### 4.3 MODELING OF THE MICROACTUATOR

Based on Figure 4.1, the displacement at the free end of the microactuator ( $\delta_D^{dynamic}$ ) is a function of the voltage ( $u$ ), which is the input of the whole actuation process (see Figure 4.2). However, as described before, intermediate actions occur between the application of the input voltage and the microactuator response. Thus, a block-based model is proposed where the overall actuation process is divided into five smaller procedures (sub-blocks). Each one of these sub-blocks is solved independently. Figure 4.3 shows this block diagram.

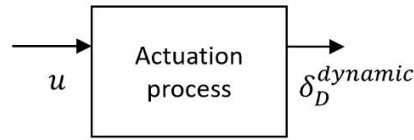


Figure 4.2. Block representation of the whole actuation process.

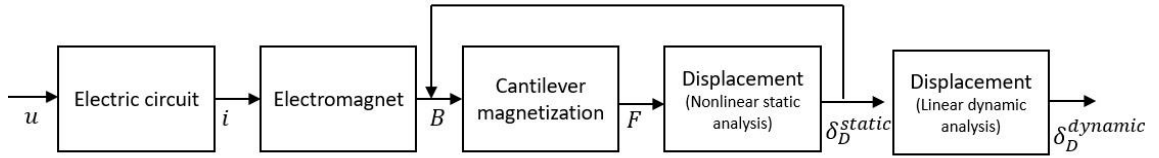


Figure 4.3. Block diagram of the model including each sub-block.

The description and the equations stating the output in function of the input of each block are established below.

- The *electric circuit* block is focused on obtaining an equation to calculate the current ( $i$ ) in function of the input voltage ( $u$ ) along time ( $t$ ), as shown in equation (1).

$$i = i(t) = f_1(u(t)) \quad (1)$$

- In the *electromagnet* block, the equation describing the magnetic field ( $B$ ) generated by the electromagnet due to a flowing current ( $i$ ) along time is obtained.

This magnetic field is also dependent on the distance ( $z$ ). Equation (2) represents the equation to be sought for.

$$B = B(t) = f_2(i(t), z(t)) \quad (2)$$

- The block corresponding to the *magnetization* of the cantilever microactuator deals with the magnetic force ( $F$ ) created by the magnetic field ( $B$ ), as defined in equation (3).

$$F = F(t) = f_3(B(t)) \quad (3)$$

Due to the non-linearities observed in the experimental results and its complexity to be mathematically modeled, we propose to apply here the Hammerstein structure [190] which consists of a nonlinear static block followed by a linear dynamics one. In our case, the nonlinear static block yields a static displacement ( $\delta_D^{static}$ ) while the linear dynamics block output corresponds to the final output ( $\delta_D^{dynamic}$ ) of the microactuator.

- The block of *displacement* related to a *nonlinear static analysis* (equation (4)) describes the static displacement (or steady-state) of the microactuator in function of the magnetic force.

$$\delta_D^{static} = \delta_D^{static}(t) = f_4(F(t)) \quad (4)$$

As the microactuator receives a different magnitude of the magnetic field depending on its position, a feedback loop between the static displacement ( $\delta_D^{static}$ ) of the microactuator and the magnetic field ( $B$ ) is considered in the block diagram of Figure 4.3. The value of  $z$  will always be updated in time following equation (5), where  $z(t = 0)$  is the initial position and  $\delta_D^{static}(t - dt)$  corresponds to the static displacement taken at the instant previous to the current calculus.

$$z = z(t) = z(t = 0) - \delta_D^{static}(t - dt) \quad (5)$$

- The block of *displacement* related to *linear dynamic analysis* describes the dynamic displacement of the microactuator. The dynamic analysis considers the transient regime and thus the oscillations in the time-domain response of the microactuator. This is achieved by taking the nonlinear static displacement as input of the block, as shown in equation (6).

$$\delta_D^{dynamic} = \delta_D^{dynamic}(t) = f_5(\delta_D^{static}(t)) \quad (6)$$

Some assumptions are made in order to reduce the number of parameters in the model:

- Assumptions relative to the magnetic field:

- As the distance between the free end of the microactuator and the electromagnet is small relative to the electromagnet dimensions, the magnetic field is assumed to be uniform and parallel to the z-axis. Only the magnetic field on the z-axis will be considered for the model.
- The interesting magnetic force is on the z-axis Thus, only the displacement on the z-axis is considered.

- Assumptions relative to the magnetic material:

- Dispersion and size distribution of the magnetic nanoparticles into the polymeric matrix are homogeneous.

- Assumptions relative to the beam deflections:

- The material is isotropic and obeys Hooke's law (elastic material).
- The microactuator cross section is constant along its length.
- The microactuator remains symmetrical during its displacement (neither twisting nor torsion).
- Plane sections remain plane: plane sections remain perpendicular to the neutral axis before and after deformation, as shown in Figure 4.4.



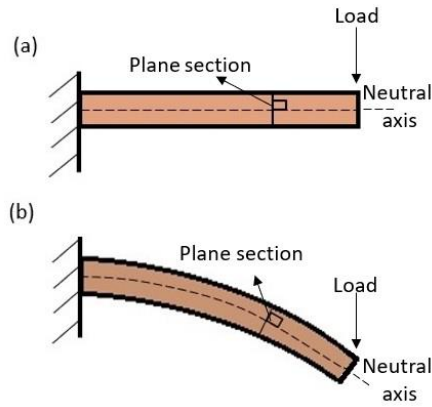


Figure 4.4. Plane sections remain plane before and after deformation.

The derivation of the equations for each block are described in next sections.

### 4.3.1 The electric circuit block

To obtain the equation for the current  $i$  flowing through the electromagnet due to an applied voltage  $u$ , a series resistance-inductance circuit (RL circuit) was considered. It is composed by a resistor of resistance value ( $R$ ) and an inductor of inductance value ( $L$ ) connected in series with the voltage source. Figure 4.5 shows a schematic representation for this kind of circuits.

In our case, the RL circuit corresponds to the electromagnet. The values of inductance ( $L$ ) and resistance ( $R$ ) of the electromagnet are constants and they can be obtained directly from experiments, by measurement with a multimeter or through database from the fabricant.

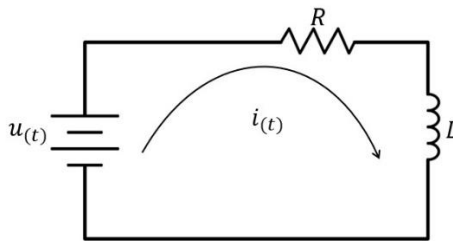


Figure 4.5. Representation of the electromagnet as a series RL circuit.

In order to solve the RL circuit for the current, the Kirchhoff Voltage Law (KVL) [191] can be applied. Analysis by KVL leaves:

$$u - u_R - u_L = 0 \quad (7)$$

Where:

$u$  is the input voltage in function of time  $u(t)$

$u_R$  is the resistance voltage in function of time  $u_R(t)$

$u_L$  is the inductance voltage in function of time  $u_L(t)$ .

By Ohm's law:

$$u_R = Ri \quad (8)$$

Where:

$R$  is the resistance of the electromagnet, which is a constant obtained by measurements with a multimeter.

Also:

$$u_L = L \frac{di}{dt} \quad (9)$$

Where:

$L$  is the inductance of the coil, which is a constant obtained experimentally.

Equation (7) can be rewritten as:

$$u = Ri + L \frac{di}{dt} \quad (10)$$

The solution for the current ( $i$ ) in Equation (10) at the needed boundary conditions will be the equation that describes the current flowing through the electromagnet along time.

### 4.3.2 The electromagnet block

The equation of the magnetic field ( $B$ ) supplied by the electromagnet at any point  $z$  along its central axis can be deduced from the Biot-Savart law [109]. As previously mentioned, this magnetic field depends on the electrical current ( $i$ ), the distance or position ( $z$ ) and the time ( $t$ ).

The electromagnet used in this study shows a solenoid configuration, which is formed by copper wire coiled along a cylindrical core. When a current is flowing through the electromagnet, several current loops are formed due to the coiled wire.

The simplest case to start the analysis by the Biot-Savart law is considering the presence of only one current loop, as shown in Figure 4.6. In this case, the equation to calculate the magnetic field  $B_{loop}$  supplied at a point  $P$  in the central axis of the loop could be calculated as:

$$B_{loop} = \frac{\mu_r \mu_0 r_e^2 i}{2(z^2 + r_e^2)^{3/2}} \quad (11)$$

Where:

$\mu_r$  is the relative magnetic permeability of the core

$\mu_0$  is the magnetic permeability of air

$r_e$  is the radius of the loop

$z$  is the distance from the center of the loop (considered as origin) at any point  $P$  on the  $z$ -axis.

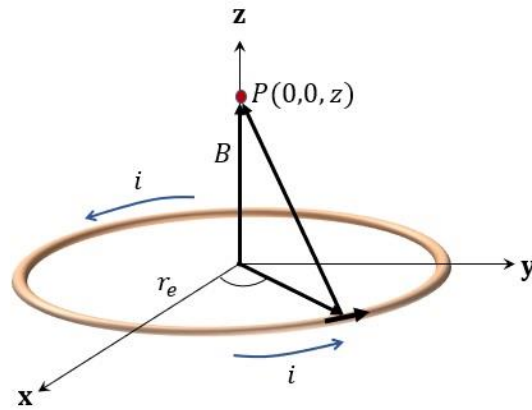


Figure 4.6. Magnetic field contribution of a current loop at a point P on the z-axis.

Equation (11) is useful as starting point to obtain an equation of the magnetic field contribution of several current loops stacked together (as in a solenoid) at any point along the z-axis.

Figure 4.7 shows a schematic representation of a solenoid. By taking randomly a cross section of tightly packed loops located at  $z'$  with a thickness  $dz'$  (as represented in this figure), the magnetic field contribution at a point P for the subset of loops  $dz'$  will be:

$$dB_s = \frac{\mu_r \mu_0 r_e^2}{2[(z - z')^2 + r_e^2]^{3/2}} di \quad (12)$$

Where:

$z - z'$  corresponds to the distance between the position of the packed loops located at  $z'$  and the point P located at  $z$ .

$di$  represents the current flowing through the packed loops.

The amount of current flowing through these packed loops is proportional to the thickness  $dz'$  and it can be calculated by:

$$di = \frac{N}{l_e} idz' \quad (13)$$

Where:

$N$  is the number of turns of the solenoid

$l_e$  is the length of the solenoid

$dz'$  is the thickness of the subset of loops.

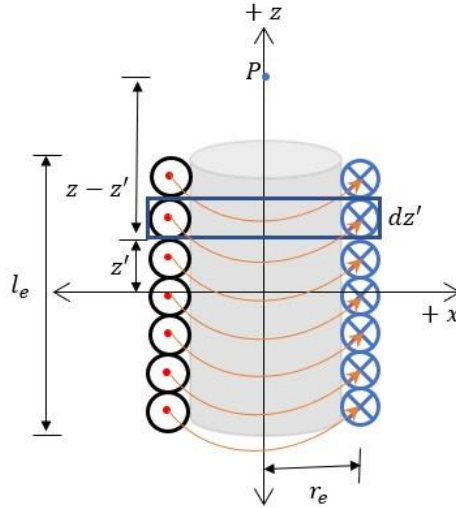


Figure 4.7. Schematic representation of a solenoid.

Substituting equation (13) into equation (12):

$$dB_s = \frac{\mu_r \mu_0 r_e^2}{2[(z - z')^2 + r_e^2]^{3/2}} \frac{N}{l_e} idz' \quad (14)$$

It is necessary to integrate over the entire length of the solenoid, taking the middle point of the solenoid as the origin reference:

$$B_s = \frac{\mu_r \mu_0 Ni r_e^2}{2l_e} \int_{-l_e/2}^{l_e/2} \frac{dz'}{[(z - z')^2 + r_e^2]^{3/2}} \quad (15)$$

The integration of equation (15) gives:

$$B_s = \frac{\mu_r \mu_0 N i r_e^2}{2l_e} \left. \frac{z' - z}{r_e^2 \sqrt{(z - z')^2 + r_e^2}} \right|_{-l_e/2}^{l_e/2} \quad (16)$$

By substitution of the integral limits, the solution for the magnetic field contribution of the solenoid represented in Figure 4.7 is given by:

$$B_s = \frac{\mu_r \mu_0 N i}{2l_e} \left[ \frac{\left(\frac{l_e}{2}\right) - z}{\sqrt{(z - l_e/2)^2 + r_e^2}} + \frac{\left(\frac{l_e}{2}\right) + z}{\sqrt{(z + l_e/2)^2 + r_e^2}} \right] \quad (17)$$

It is important to clarify that the solution obtained in equation (17) corresponds to the magnetic field contribution at any point  $P$  along the  $z$ -axis for a single layer solenoid. However, the electromagnet used in this study is a multilayered solenoid (see Figure 4.8). This means that the copper wire is not only coiled and stacked along the  $z$ -axis, but it is also stacked along the radial axis of the core.

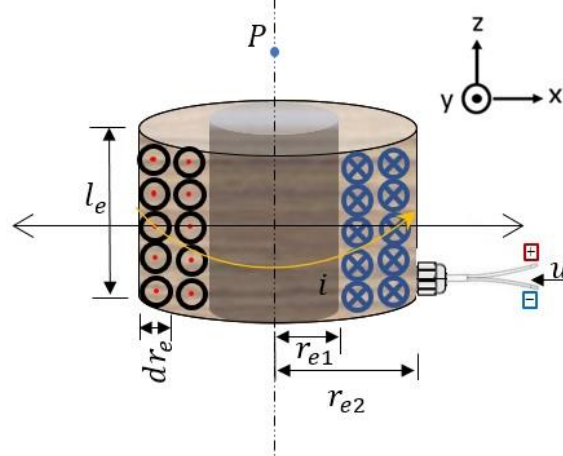


Figure 4.8. Schematic representation of a multilayer solenoid.

To obtain the magnetic field contribution of a finite multilayered solenoid at a point  $P$  on the  $z$ -axis, additional considerations must be taken.

For this, a section of the copper multilayers is randomly taken in the radial axis ( $x$ -axis) between the internal radius ( $r_{e1}$ ) and the external radius ( $r_{e2}$ ). This section is called

$dr_e$  as shown in Figure 4.8. The magnetic field contribution at a point  $P$  on the  $z$ -axis for a section  $dr_e$  could be described as:

$$B = B_s dr_e \quad (18)$$

where:

$B_s$  is the magnetic field contribution of a single layered solenoid, obtained in equation (17).

To obtain the magnetic field contribution of all layers, it is necessary to integrate the entire section occupied by the copper. The expression for this integral is:

$$B = \frac{\mu_r \mu_0 Ni}{2l_e} \int_{r_{e1}}^{r_{e2}} \left( \frac{\left(\frac{l_e}{2}\right) - z}{\sqrt{(z - l_e/2)^2 + r_e^2}} + \frac{\left(\frac{l_e}{2}\right) + z}{\sqrt{(z + l_e/2)^2 + r_e^2}} \right) dr_e \quad (19)$$

The integral limits correspond to the radii  $r_{e1}$  and  $r_{e2}$ .

A standard integral solution could be used to solve each element of equation (19). In this case, equation (19) can be solved by the following standard integral solution:

$$I_{std} = \int_{r_{e1}}^{r_{e2}} \frac{dr_e}{\sqrt{r_e^2 + a^2}} = \left[ \ln \left[ r_e + \sqrt{(r_e^2 + a^2)} \right] \right]_{r_{e1}}^{r_{e2}} \quad (20)$$

The solution of equation (19) is given by:

$$B = \frac{\mu_r \mu_0 Ni}{2l_e(r_{e2} - r_{e1})} \left[ A_1 \ln \left( \frac{r_{e2} + \sqrt{r_{e2}^2 + A_1^2}}{r_{e1} + \sqrt{r_{e1}^2 + A_1^2}} \right) + A_2 \ln \left( \frac{r_{e2} + \sqrt{r_{e2}^2 + A_2^2}}{r_{e1} + \sqrt{r_{e1}^2 + A_2^2}} \right) \right] \quad (21)$$

Where:

$$A_1 = \frac{l_e}{2} - z \quad (22)$$

$$A_2 = \frac{l_e}{2} + z \quad (23)$$

Equation (21) represents the magnetic field contribution at a point P located at any distance along the z-axis of a multilayered solenoid, like the electromagnet used in this study. For this reason, equation (21) will be implemented in the model.

### 4.3.3 Cantilever magnetization block

The magnetic force producing the displacement of the microactuator is directly related to the magnetization of the iron oxide nanoparticles within it. This magnetization is caused by the alignment of their magnetic dipole moments with the external magnetic field ( $B$ ) determined during the last section in equation (21). Magnetic field ( $B$ ) and magnetization ( $M_m$ ) are considered as vectors aligned to the z-axis.

In order to calculate the magnetic force along z-axis, the point P (shown in Figure 4.8) is considered as a magnetic dipole  $\vec{\mu}$ . If the magnetic dipole moment is aligned to the z-axis ( $\vec{\mu} = \mu_z \hat{k}$ ), the dipole will experience a force given by:

$$F = \nabla(\vec{\mu} \cdot \vec{B}) = \nabla(\mu_z B) = \mu_z \left[ \frac{dB}{dz} \right] \hat{k} \quad (24)$$

Where:

$\mu_z$  is the magnetic moment of the magnetic dipole on the z-axis.

Upon differentiating equation (21) and substituting in equation (24), we obtain:



$$\begin{aligned}
F = -\frac{\mu_z \mu_0 \mu_r Ni}{2l_e(r_{e2} - r_{e1})} & \left[ \ln\left(\frac{r_{e2} + C_1}{r_{e1} + C_2}\right) - \ln\left(\frac{r_{e2} + C_3}{r_{e1} + C_4}\right) \right. \\
& + \left( \frac{\left(\frac{l_e}{2} - z\right) \left(\frac{l_e - 2z}{2C_1(r_{e1} + C_2)} - \frac{(l_e - 2z)(r_{e2} + C_1)}{2C_2(r_{e1} + C_2)^2}\right) (r_{e1} + C_2)}{r_{e2} + C_1} \right) \\
& \left. - \left( \frac{(r_{e1} + C_4) \left(\frac{(l_e + 2z)}{2C_3(r_{e1} + C_4)} - \frac{(r_{e2} + C_3)(l_e + 2z)}{2C_4(r_{e1} + C_4)^2}\right) \left(\frac{l_e}{2} + z\right)}{r_{e2} + C_3} \right) \right] \quad (25)
\end{aligned}$$

Where:

$$C_1 = \sqrt{r_{e2}^2 + \left(\frac{l_e}{2} - z\right)^2} \quad (26)$$

$$C_2 = \sqrt{r_{e1}^2 + \left(\frac{l_e}{2} - z\right)^2} \quad (27)$$

$$C_3 = \sqrt{r_{e2}^2 + \left(\frac{l_e}{2} + z\right)^2} \quad (28)$$

$$C_4 = \sqrt{r_{e1}^2 + \left(\frac{l_e}{2} + z\right)^2} \quad (29)$$

Equation (25) describes the magnetic force that only one magnetic dipole aligned to the z-axis will experience when it is located at a point  $P$  from the electromagnet. However, the microactuator is composed by several magnetic dipoles ( $\text{Fe}_2\text{O}_3$  magnetic nanoparticles). Therefore, the term  $\mu_z$  should be replaced by a magnetization term  $M_m$ ; magnetization  $M_m$  is the net magnetic dipole moment of the PVB/ $\text{Fe}_2\text{O}_3$  microactuators. Equation (25) can be rewritten as:

$$\begin{aligned}
F = -\frac{M_m \mu_0 \mu_r Ni}{2l_e(r_{e2} - r_{e1})} & \left[ \ln\left(\frac{r_{e2} + C_1}{r_{e1} + C_2}\right) - \ln\left(\frac{r_{e2} + C_3}{r_{e1} + C_4}\right) \right. \\
& + \left( \frac{\left(\frac{l_e}{2} - z\right) \left(\frac{l_e - 2z}{2C_1(r_{e1} + C_2)} - \frac{(l_e - 2z)(r_{e2} + C_1)}{2C_2(r_{e1} + C_2)^2}\right) (r_{e1} + C_2)}{r_{e2} + C_1} \right) \\
& \left. - \left( \frac{(r_{e1} + C_4) \left(\frac{l_e + 2z}{2C_3(r_{e1} + C_4)} - \frac{(r_{e2} + C_3)(l_e + 2z)}{2C_4(r_{e1} + C_4)^2}\right) \left(\frac{l_e}{2} + z\right)}{r_{e2} + C_3} \right) \right] \quad (30)
\end{aligned}$$

Equation (30) represents the magnetic force that the free end of the microactuator could experience when it is located on the z-axis of the electromagnet. Once having this force, the equation to obtain the static displacement will be proposed.

#### 4.3.4 Nonlinear static displacement block

This section describes the process to obtain the static nonlinear model for the displacement of the microactuator at its free end. All the equations treated here are based on the Euler-Bernoulli beam theory and the nonlinear model for flexible cantilever beams proposed in [192].

The Euler–Bernoulli law states that the bending moment  $M_b$  of a beam is proportional to the change in the curvature produced by the action of a force. Considering Figure 4.9 where  $\theta$  is the angular deformation (slope) at any point  $x$  along the beam measured along its arc length, this law may be written mathematically as follows:

$$\frac{1}{r} = \frac{d\theta_D}{dx_0} = -\frac{M_b}{EI} \quad (31)$$

Where:

$r$  is the radius of the curvature

$\theta_D$  is the angular deformation (slope) at point D

$x_0$  is the arc length of the beam at point D'

$E$  is the modulus of elasticity along the beam

$I$  is the cross-sectional moment of inertia along the length of the beam.

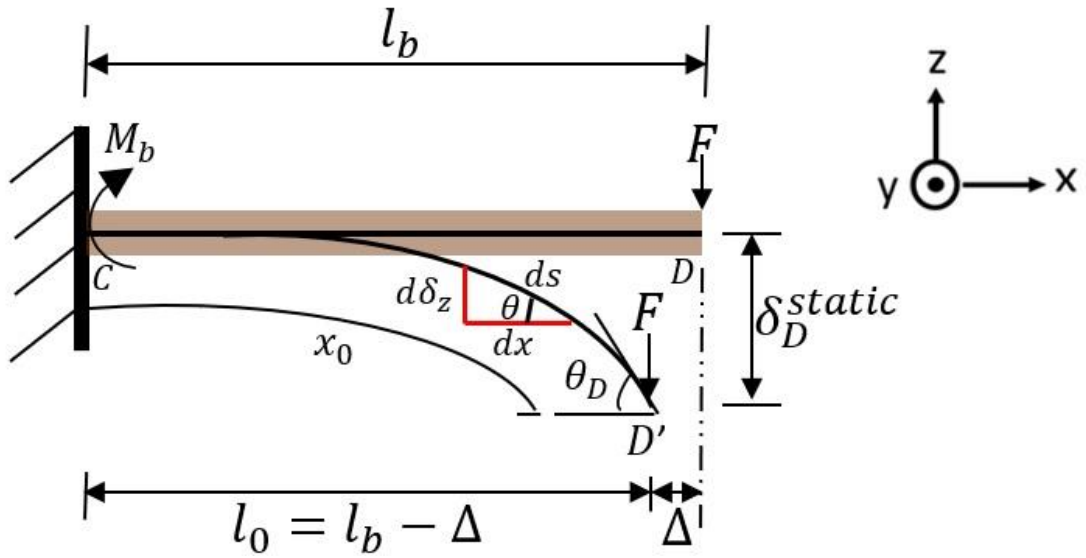


Figure 4.9. Schema of the large deformation (displacement) of the microactuators.

In rectangular  $x, y, z$  coordinates, equation (31) may be written as:

$$\frac{1}{r} = \frac{\delta_z'''}{[1 + (\delta_z')^2]^{3/2}} = -\frac{M_b}{EI} \quad (32)$$

In this case,  $\delta_z$  represents the displacement on the  $z$ -axis at any point  $x$  along the microactuator. Where:

$$\delta_z' = \frac{d\delta_z}{dx} \quad (33)$$

$$\delta_z'' = \frac{d^2\delta_z}{dx^2} \quad (34)$$

By trigonometry:

$$\delta_z' = \tan \theta \quad (35)$$

So,

$$\theta = \tan^{-1} \delta_z' \quad (36)$$

When the deformation of the microactuator is small,  $\delta_z'$  is very small too (compared to 1) and it is usually neglected. So, equation (32) becomes:

$$\frac{1}{r} = \delta_z'' = -\frac{M_b}{EI} \quad (37)$$

Equation (37) is a second order *linear* differential equation and it is the most common application of the Euler-Bernoulli law. However, in the case of this study, deformations are large due to the high flexibility of the PVB/Fe<sub>2</sub>O<sub>3</sub> films. Therefore, it is necessary to deal with equation (32), which is a second order *nonlinear* differential equation.

The integral of equation (32) must be found to obtain the static displacement at the free end ( $\delta_D^{static}$ ) of the microactuator. Although the exact solution of such equation is not presently available, an approximation can be obtained by the analytical method described below.

In order to simplify the integration, a change in variables can be made. Letting  $\delta_z' = p$  and  $\delta_z'' = p'$ , we obtain

$$\frac{p'}{[1 + p^2]^{3/2}} = \lambda(x) \quad (38)$$

Where:

$$\lambda(x) = -\frac{M_b}{EI} \quad (39)$$

By applying statics, the bending moment  $M_b$  was found as:

$$M_b = -Fx \quad (40)$$

Where:

$F$  is the magnetic force obtained from equation (30).

Thus,

$$\lambda(x) = -\frac{M_b}{EI} = \frac{Fx}{EI} \quad (41)$$

Now, equation (38) could be rewritten as follows:

$$\frac{dp/dx}{[1 + p^2]^{3/2}} = \lambda(x) \quad (42)$$

By multiplying both sides of equation (42) by  $dx$  and integrating once, we find

$$\int \frac{dp}{[1 + p^2]^{3/2}} = \int \lambda(x) dx \quad (43)$$

Integration can be done by making the following substitutions:

$$p = \tan \theta \quad (44)$$

$$dp = \sec^2 \theta d\theta \quad (45)$$

By using the beam element shown in red in Figure 4.9 and applying the Pythagorean theorem, we find:

$$(ds)^2 = (dx)^2 + (d\delta_z)^2 \text{ or } ds = [(dx)^2 + (d\delta_z)^2]^{1/2} \quad (46)$$

$$\frac{ds}{dx} = \left[ 1 + \left( \frac{d\delta_z}{dx} \right)^2 \right]^{1/2} = [1 + (\tan \theta)^2]^{1/2} = [1 + p^2]^{1/2} \quad (47)$$

Hence,

$$\cos \theta = \frac{dx}{ds} = \frac{1}{[1 + p^2]^{1/2}} \quad (48)$$

And from equation (44), we find:

$$\sin \theta = p \cos \theta = \frac{p}{[1 + p^2]^{1/2}} \quad (49)$$

By substituting equations (44) and (45) into equation (43) and using equations (48) and (49), we find:

$$\int \frac{\sec^2 \theta \, d\theta}{\left[ 1 + \frac{\sin^2 \theta}{\cos^2 \theta} \right]^{3/2}} = \int \lambda(x) dx \quad (50)$$

By performing trigonometric manipulation, equation (50) reduces to the following equation:

$$\int \cos \theta \, d\theta = \int \lambda(x) dx \quad (51)$$

Integration of equation (51), yields:

$$\sin \theta = \varphi(x) + C \quad (52)$$

where the function  $\varphi(x)$  represents the integration of  $\lambda(x)$  and  $C$  is the constant of integration which can be determined by the boundary conditions of the problem to solve.

$$\int \lambda(x)dx = \varphi(x) + C = \frac{Fx^2}{2EI} + C \quad (53)$$

Equation (52) may be rewritten in terms of  $p$  and  $\delta_z'$  by using equations (49) and (35). Thus,

$$\frac{p}{[1 + p^2]^{1/2}} = \varphi(x) + C \quad (54)$$

$$\frac{\delta_z'}{[1 + (\delta_z')^2]^{1/2}} = \varphi(x) + C \quad (55)$$

By substituting the expression for  $\varphi(x)$  obtained in equation (53) into equation (55), we obtain:

$$\frac{\delta_z'}{[1 + (\delta_z')^2]^{1/2}} = \frac{Fx^2}{2EI} + C \quad (56)$$

In order to determine the boundary conditions to obtain  $C$ , it is important to notice the difference in length  $l_b$  for the non-deformed state of the microactuator and the length  $l_0$  when it is deformed, as shown in Figure 4.9. In this case,  $l_0$  represents the projected length on the  $x$ -axis of the arc formed by the microactuator in the deformed state. So,  $C$  can be

determined by applying the boundary conditions of zero variation of deformation ( $\delta_z' = 0$ ) at  $x = l_0 = l_b - \Delta$ , where  $\Delta$  is the horizontal displacement at the free end (point  $D'$ ). By using these boundary conditions in equation (56), we find

$$C = -\frac{F(l_b - \Delta)^2}{2EI} \quad (57)$$

By substituting equation (57) into equation (56), we obtain

$$\frac{\delta_z'}{[1 + (\delta_z')^2]^{1/2}} = G(x) \quad (58)$$

Where:

$$G(x) = \frac{F}{2EI} [x^2 - (l_b - \Delta)^2] \quad (59)$$

Or

$$G(x) = \frac{F}{2EI} [x^2 - (l_0)^2] \quad (60)$$

And by solving for  $\delta_z'$ :

$$\delta_z'(x) = \frac{G(x)}{(1 - [G(x)]^2)^{1/2}} \quad (61)$$

The large deflection  $\delta_z$  at  $0 \leq x \leq l_0$  may be now obtained by integrating once equation (61) and satisfying the boundary conditions of zero variation of deformation at  $x = l_0$  for the evaluation of the constant of integration. It should be noted that equation (59) is a function of the unknown horizontal displacement  $\Delta$  at the free end of the microactuator. The value of  $\Delta$  may be determined by a trial-and-error procedure from the equation:

$$l_b = \int_0^{l_0} [1 + (\delta_z')^2]^{1/2} dx \quad (62)$$



This procedure involves the assumption of a  $\Delta$  value in equation (60) and its integration in equation (62) should result in the known length  $l_b$  of the microactuator. The procedure may be repeated for various values of  $\Delta$  until the correct length  $l_b$  is obtained. Figure 4.10 shows an algorithm of the procedure to estimate the value of  $\Delta$ .

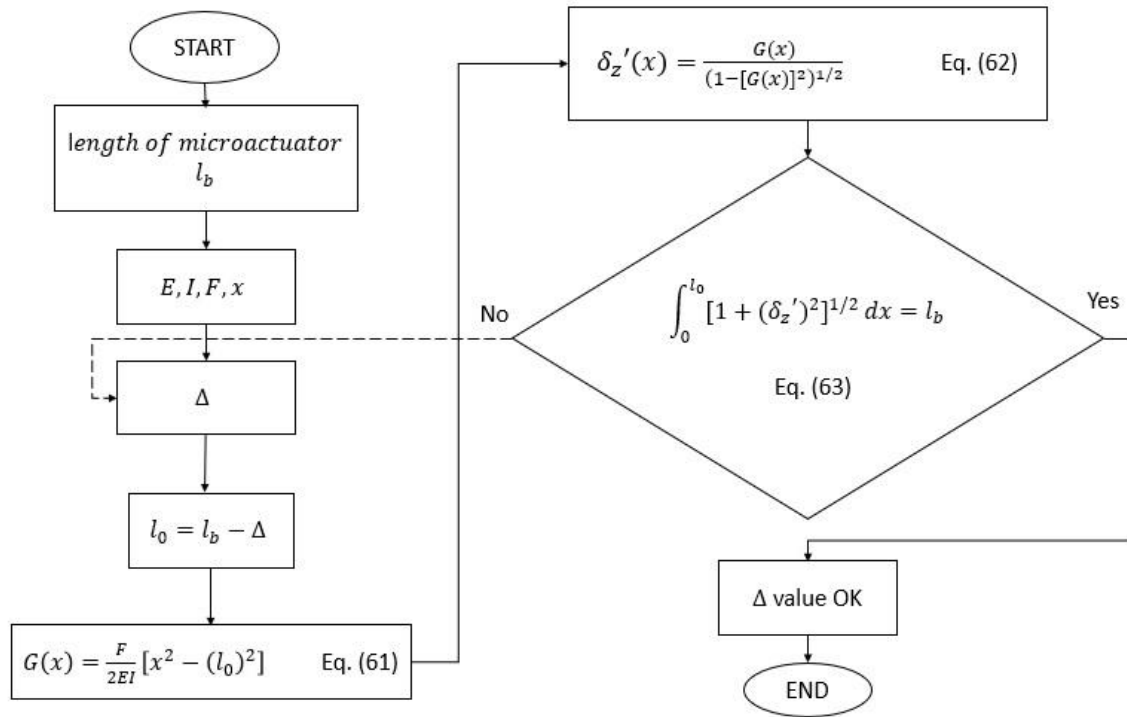


Figure 4.10. Algorithm to estimate the value of  $\Delta$ .

Even if equation (62) aids to assess the displacement ( $\Delta$ ) on the  $x$ -axis, to solve the equation (61) in order to obtain the displacement on the  $z$ -axis ( $\delta_z$ ) is very complex. Current solving methods are available for very limited cases. In this study, the derivation of a pseudolinear equivalent system method is used. This method was chosen due to its flexibility to be used in complex cases, for example, when there are distributed forces along the beam or variations in stiffness along the beam. These considerations can be useful for future improvements of the model.

The derivation of a pseudolinear equivalent system starts from the Euler–Bernoulli law of deformations given by equation (32), which two last terms are:

$$\frac{\delta_z''}{[1 + (\delta_z')^2]^{3/2}} = -\frac{M_b}{EI} \quad (63)$$

By solving equation (63) for  $\delta_z''$  we obtain

$$\delta_z'' = -\frac{M_b}{EI} [1 + (\delta_z')^2]^{3/2} \quad (64)$$

An equivalent moment  $M_e$  may be established as:

$$M_e = -[1 + (\delta_z')^2]^{3/2} M_b \quad (65)$$

By substituting equation (65) into equation (64), we find

$$\delta_z'' = \frac{M_e}{EI} \quad (66)$$

Equation (66) is considered as a pseudolinear differential equation due to its similarity to a linear differential equation (*i.e.* equation (37)) and it represents an equivalent system of constant stiffness  $EI$ . Therefore, it can be solved as a linear differential equation using linear methods of analysis or available formulas from handbooks like the moment-area method [193]. The values of displacement obtained by solving this pseudolinear system are expected to be identical to those of the original nonlinear system.

The moment-area method is useful to solve problems dealing with structures experiencing deformations. According to it, the equation to compute the displacement at the free end of the microactuator (point  $D$  in Figure 4.9) can be written as:

$$\delta_D^{static} = \int_C^{D'} \frac{M_e}{EI} \bar{x} dx \quad (67)$$

The term  $\bar{x}$  corresponds to the  $x$ -coordinate of the centroid of the equivalent moment  $M_e$  diagram (see Figure 4.11). The equivalent moment  $M_e$  in equation (67) should be evaluated at different values of  $x$  from  $C$  to  $D'$ .

The  $x$ -coordinate of the centroid for the  $M_e$  diagram in Figure 4.11 is given by

$$\bar{x} = \frac{2}{3} l_0 \quad (68)$$

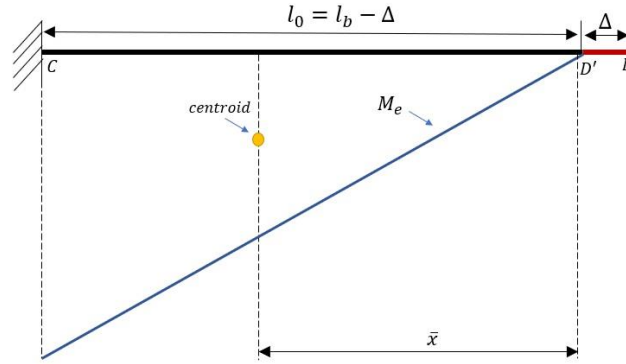


Figure 4.11. Example of a moment diagram for a cantilever beam with an applied force at its free end.

By solving numerically equation (67), the static displacement of the microactuator at its free end can be obtained. However, numerical solutions of equations (59), (61), (62) and (65) shall be previously found in order to solve equation (67).

### 4.3.5 Linear dynamic displacement block

The model that describes the dynamic displacement of the microactuator at its free end ( $\delta_D^{dynamic}$ ) is obtained in this section. Such equation is estimated from the nonlinear static displacement ( $\delta_D^{static}$ ) obtained by equation (67). Figure 4.12 shows a diagram that relates  $\delta_D^{dynamic}$  with  $\delta_D^{static}$ ; this diagram corresponds to the last part of the overall block-structured model presented in Figure 4.3.

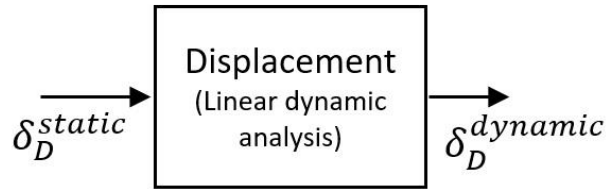


Figure 4.12. Relation between  $\delta_D^{dynamic}$  and  $\delta_D^{static}$ .

While the equation to calculate  $\delta_D^{static}$  was obtained following a series of physical principles, the equation to describe  $\delta_D^{dynamic}$  will be obtained by purely mathematical or behavioral methods. This is because the dynamic behavior of the cantilever is very complex. Thus, once again the diagram that relates  $\delta_D^{dynamic}$  with  $\delta_D^{static}$  is shown in Figure 4.13, where a variable  $g$  (gain) was incorporated inside the block. This variable represents the unknown system reaction to input  $\delta_D^{static}$  that promotes the response  $\delta_D^{dynamic}$ .

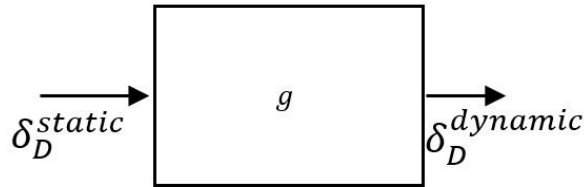


Figure 4.13. Relation between  $\delta_D^{dynamic}$  and  $\delta_D^{static}$  incorporating the term  $g$  (gain).

The relation between  $\delta_D^{dynamic}$  and  $\delta_D^{static}$  along time can be represented by linear differential equations and the final response can be obtained by the convolution integral of them [194], for example:

$$\delta_D^{dynamic}(t) = g(t) * \delta_D^{static}(t) = \int_0^t g(t - \tau_i) \delta_D^{static}(\tau_i) d\tau_i \quad (69)$$

Where

$g(t)$  represents the reaction of the system at the given input  $\delta_D^{static}(\tau)$

$\tau_i$  is an intermediary variable of integration

$(t - \tau_i)$  is the lag between the input and the output times.

Equation (69) can be represented in a transfer function form. A transfer function is expressed as the ratio of the output and the input signals in their Laplace transform. By applying the Laplace transform to the convolution integral we obtain:

$$\mathcal{L}[\delta_D^{dynamic}(t)] = \mathcal{L}[g(t) * \delta_D^{static}(t)] \quad (70)$$

Or

$$\Delta_D^{dynamic}(s) = G(s)\Delta_D^{static}(s) \quad (71)$$

Where

$\Delta_D^{dynamic}(s)$ ,  $G(s)$  and  $\Delta_D^{static}(s)$  are the Laplace transforms of  $\delta_D^{dynamic}(t)$ ,  $g(t)$  and  $\delta_D^{static}(t)$ , respectively.

Therefore, the transfer function is:

$$G(s) = \frac{\Delta_D^{dynamic}(s)}{\Delta_D^{static}(s)} \quad (72)$$

The transfer function in equation (72), in its general case, is represented by a rational fraction of polynomials of the variable  $s$ :

$$G(s) = \frac{b_n s^n + b_{n-1} s^{n-1} + \dots + b_0}{a_d s^d + a_{d-1} s^{d-1} + \dots + a_0} \quad (73)$$

Here,  $n$  and  $d$  are the degrees of the polynomials in the numerator and denominator, respectively. These polynomials are the Laplace transform of the differential parts of the linear differential model. The degree of the denominator  $d$  indicates also the order of the system. Coefficients  $a$  and  $b$  are a set of parameters that describe the behavior of the microactuator. The roots of the numerator are called zeros, while the roots of the denominator are called poles. Roots and poles determine the behavior of the function and they are obtained by factorizing the function.

Equation (73) corresponds to a transfer function of a continuous system. However, in many cases the signals should be processed by a computer and they must be sampled at discrete points (discrete time intervals). A discrete transfer function can be expressed in terms of the  $Z$  transform [195] as:

$$G_T(Z) = \frac{\Delta_D^{dynamic}(Z)}{\Delta_D^{static}(Z)} = \frac{b_0 + b_1Z^{-1} + \dots + b_nZ^{-n}}{a_0 + a_1Z^{-1} + \dots + a_dZ^{-d}} \quad (74)$$

The term  $Z$  is represented in capital letter to make a difference between this one and the term  $z$  used in the magnetic field block section. The concept of  $Z$  transform is the same in comparison to the Laplace transform in continuous systems. In the same manner, the coefficients  $a$  and  $b$ , as well as the poles and zeros, are determinants of the dynamic behavior to the system.

The transfer function of equation (74) will be applied to obtain the dynamic displacement at the free end of the microactuator ( $\delta_D^{dynamic}$ ). However, the parameters such as the coefficients  $a$  and  $b$  as well as the Laplace transform degree ( $n$  and  $d$ ) must be identified. The parameters identification process for the entire model is described in section 4.4.

#### 4.3.6 Summary of equations

The model that describes the dynamic displacement of the microactuator at its free end ( $\delta_D^{dynamic}$ ) related to an applied voltage ( $u$ ) was obtained in the last sections. This model was acquired by following the block diagram shown in Figure 4.3. This diagram is

composed by five blocks, which represent the overall processes involved in the actuation. These blocks were solved independently to obtain an equation for each process. Therefore, the model is represented by equations (75), (76), (79), (84) and (85). The name of each parameter within the equations is summarized in appendix 1.

- Electric circuit block

Current ( $i$ ) in function of the input voltage ( $u$ ) in the time-domain ( $t$ ).

$$u = Ri + L \frac{di}{dt} \quad (75)$$

- The electromagnet block

Magnetic field ( $B$ ) generated by the electromagnet due to a flowing current ( $i$ ) along time ( $t$ ). It is also variable in function of distance ( $z$ ).

$$B = \frac{\mu_r \mu_0 Ni}{2l_e(r_{e2} - r_{e1})} \left[ A_1 \ln \left( \frac{r_{e2} + \sqrt{r_{e2}^2 + A_1^2}}{r_{e1} + \sqrt{r_{e1}^2 + A_1^2}} \right) + A_2 \ln \left( \frac{r_{e2} + \sqrt{r_{e2}^2 + A_2^2}}{r_{e1} + \sqrt{r_{e1}^2 + A_2^2}} \right) \right] \quad (76)$$

Where:

$$A_1 = \frac{l_e}{2} - z \quad (77)$$

$$A_2 = \frac{l_e}{2} + z \quad (78)$$

- Cantilever magnetization block

Magnetic force ( $F$ ) due to the magnetic field ( $B$ ) and the magnetization of the microactuator ( $M_m$ ) along time ( $t$ ).

$$\begin{aligned}
F = -\frac{M_m \mu_0 \mu_r Ni}{2l_e(r_{e2} - r_{e1})} & \left[ \ln\left(\frac{r_{e2} + C_1}{r_{e1} + C_2}\right) - \ln\left(\frac{r_{e2} + C_3}{r_{e1} + C_4}\right) \right. \\
& + \left( \frac{\left(\frac{l_e}{2} - z\right) \left(\frac{l_e - 2z}{2C_1(r_{e1} + C_2)} - \frac{(l_e - 2z)(r_{e2} + C_1)}{2C_2(r_{e1} + C_2)^2}\right) (r_{e1} + C_2)}{r_{e2} + C_1} \right) \\
& \left. - \left( \frac{(r_{e1} + C_4) \left(\frac{(l_e + 2z)}{2C_3(r_{e1} + C_4)} - \frac{(r_{e2} + C_3)(l_e + 2z)}{2C_4(r_{e1} + C_4)^2}\right) \left(\frac{l_e}{2} + z\right)}{r_{e2} + C_3} \right) \right] \quad (79)
\end{aligned}$$

Where:

$$C_1 = \sqrt{r_{e2}^2 + \left(\frac{l_e}{2} - z\right)^2} \quad (80)$$

$$C_2 = \sqrt{r_{e1}^2 + \left(\frac{l_e}{2} - z\right)^2} \quad (81)$$

$$C_3 = \sqrt{r_{e2}^2 + \left(\frac{l_e}{2} + z\right)^2} \quad (82)$$

$$C_4 = \sqrt{r_{e1}^2 + \left(\frac{l_e}{2} + z\right)^2} \quad (83)$$

– Nonlinear static displacement block

Static displacement at the free end of the microactuator ( $\delta_D^{static}$ ).  $M_e$  is in function of the magnetic force  $F$  along time.

$$\delta_D^{static} = \int_C^{D'} \frac{M_e}{EI} \bar{x} dx \quad (84)$$

– Linear dynamic displacement block

Transfer function in discrete time ( $G_T(Z)$ ) to calculate the dynamic displacement at the free end of the microactuator ( $\Delta_D^{dynamic}$ ) in function of the nonlinear static displacement ( $\Delta_D^{static}$ ).



$$G_T(Z) = \frac{\Delta_D^{dynamic}(Z)}{\Delta_D^{static}(Z)} = \frac{b_0 + b_1Z^{-1} + \dots + b_nZ^{-n}}{a_0 + a_1Z^{-1} + \dots + a_dZ^{-d}} \quad (85)$$

The model proposed above depends on different parameters, including geometrical, electrical and mechanical. The following section explains the procedure to identify the value of these parameters.

#### 4.4 PARAMETER IDENTIFICATION

The methods to obtain the parameter values of each equation within the model are addressed in this part of the chapter. All these values are summarized in the appendix 2. The organization of this section follows the block-structured model shown in Figure 4.3.

##### 4.4.1 Electrical circuit block

The electrical parameters needed for the electrical circuit block are the resistance ( $R$ ) and the inductance ( $L$ ) of the electromagnet. Resistance was directly measured by a multimeter and, inductance was calculated from the relation [196]:

$$L = R\tau \quad (86)$$

Where:

$L$  is the inductance of the electromagnet

$R$  is the resistance of the electromagnet

$\tau$  is the inductor time constant.

The inductor time constant ( $\tau$ ) is the time that the electromagnet takes to conduct 63.2% of the maximum current resulting from an applied step voltage. It was obtained experimentally by applying a step voltage of 30 V to the electromagnet.

#### 4.4.2 Magnetic field block

The following parameters are needed to calculate the magnetic field that the electromagnet can supply to a point over the z-axis:

- Geometrical parameters of the electromagnet such as the external diameter ( $r_{e2}$ ), the internal diameter ( $r_{e1}$ ), the length ( $l_e$ ) and the number of turns of copper wire ( $N$ ). Their values are supplied by the manufacturer.
- Magnetic parameters like the magnetic permeability of the core ( $\mu_r$ ) and the magnetic permeability of air ( $\mu_0$ ). The value of  $\mu_r$  is supplied by the manufacturer, while  $\mu_0$  is a physical constant.

Moreover, the parameter  $z$  corresponding to the distance from the central point of the electromagnet to the free end of the cantilever is necessary. However, this parameter is variable along the test as the microactuator approaches to the electromagnet due to magnetic forces.

#### 4.4.3 Cantilever magnetization block

For the magnetization block, the only missing parameter corresponds to the magnetization of the cantilever microactuator  $M_m$ . The approximation of  $M_m$  was performed by following three main steps.

The first step consists of obtaining the magnetic susceptibility ( $\chi_m$ ) of the magnetic hybrid film to be used.  $\chi_m$  can be estimated from the experimental results of the magnetic characterization shown in Chapter 3. Those results were obtained from magnetometry tests in which a magnetic field ( $H$ ) is applied to a sample and the response of magnetization ( $M$ ) of such sample is measured. All results showed a behavior

characteristic of superparamagnetic materials. Generally, for superparamagnetic materials, the relation between  $M$  and  $H$  at low magnetic fields is approximately linear [197]. This behavior can be observed in Figure 4.14. Hence, magnetic susceptibility is considered as the slope of the linear part of the curve and the equation can be written as follows:

$$\chi_m = \frac{\Delta M}{\Delta H} = \frac{M_2 - M_1}{H_2 - H_1} \quad (87)$$

Where:

$\Delta M$  is the difference between two different points of magnetization on the  $y$ -axis

$\Delta H$  is the difference between the corresponding two points of magnetic field strength on the  $x$ -axis.

Units conversion is required as  $\Delta M$  and  $\Delta H$  are in the CGS units. The obtained parameter  $\chi_m$  is in function of the mass, it is usually called mass magnetic susceptibility.

The second step is to obtain the magnetization of the material. As the magnetization is variable in function of the applied magnetic field, equation (88) calculates this magnetization. The result gives a magnetization per unit mass  $M_{mass}$ .

$$M_{mass} = M_0 + \chi_m H \quad (88)$$

Where:

$M_0$  is the initial magnetization per unit mass, considered to be zero

$H$  is the magnetic field strength, considered as  $H = B/\mu_0$ .

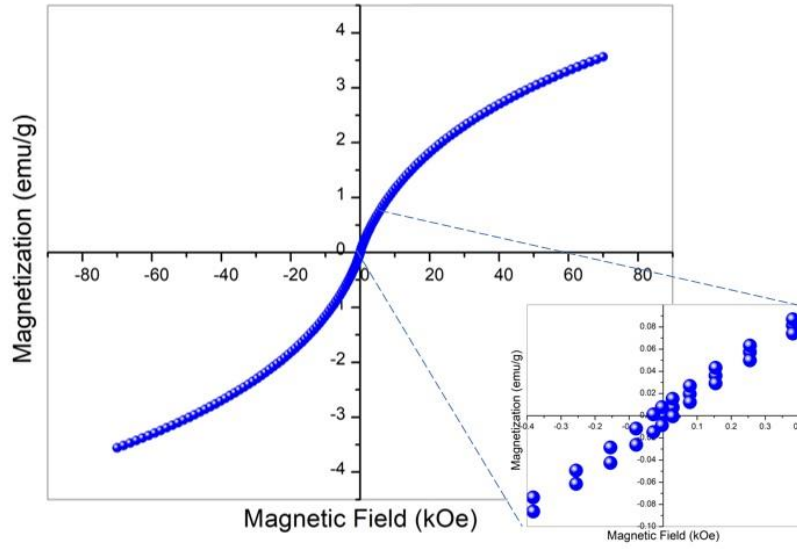


Figure 4.14. Example of test results of magnetization ( $M$ ) versus magnetic field strength ( $H$ ). The zoomed area shows the approximately linear behavior of this kind of responses at low magnetic fields.

Equation (88) can be rewritten in terms of the magnetic field density ( $B$ ) supplied by the electromagnet and described by equation (76):

$$M_{mass} = M_0 + (\chi_m) \left( \frac{B}{\mu_0} \right) \quad (89)$$

The third step is to calculate the magnetization according to the mass of the microactuator. The expression to calculate  $M_m$  is given by:

$$M_m = m * M_{mass} = m \left[ M_0 + \chi_m \left( \frac{B}{\mu_0} \right) \right] \quad (90)$$

Where:

$m$  is the mass of the microactuator measured by a precision balance.

#### 4.4.4 Nonlinear static displacement block

The parameters needed to calculate the nonlinear static displacement of the cantilever are mainly:

- Geometrical parameters such as the length of the microactuator ( $l_b$ ), the width ( $W$ ) and the thickness ( $T$ ).
- Mechanical parameters being the elastic modulus ( $E$ ) and the area moment of inertia ( $I$ ).

Geometrical parameters  $l_b$ ,  $W$  and  $T$  were measured on the microactuators. The elastic modulus ( $E$ ) was acquired from the results of dynamic mechanical analysis (DMA) shown in Chapter 3 from the test at 0.1 Hz and room temperature.

The area moment of inertia  $I$  was estimated by the following equation:

$$I = \frac{WT^3}{l_b} \quad (91)$$

Where:

$W$  is the width of the microactuator

$T$  is the thickness of the microactuator

$l_b$  is the length of the microactuator.

#### 4.4.5 Linear dynamic displacement block

This section addresses the identification of parameters of the transfer function corresponding to equation (85). This parameters identification was conducted by the “System Identification Toolbox” of MATLAB®. In this case, the tool was used to estimate the coefficients  $a$  and  $b$ , as well as the order of the transfer function ( $n$  and  $d$ ). The input

data of this block correspond to the nonlinear static displacement  $\delta_D^{static}$  obtained from equation (84), as shown in Figure 4.12. Output can be any of the dynamic displacement responses obtained experimentally from the step mode test shown in chapter 3. For more details about the procedure to obtain the parameters identification of the linear dynamic displacement block see appendix 3.

In this case, the model of autoregressive with external output (ARX) [198] was used as method to estimate the transfer function in the time domain. For more details about the ARX method see appendix 4. The transfer function in equation (92) was obtained by following the procedure for parameters identification described in appendix 3. This fifth order transfer function was chosen because its solution showed the best agreement with the experimental result used as reference. This transfer function was obtained for a continuous model.

$$G(s) = \frac{25.11 s^4 - 2.387e07 s^3 + 1.657e09 s^2 + 2.469e11 s + 6.98e12}{s^5 + 489.3 s^4 + 9.956e06 s^3 + 1.236e09 s^2 + 7.85e10 s + 6.529e12} \quad (92)$$

The corresponding discrete transfer function expressed in terms of Z transform is:

$$G_T(Z) = \frac{-3.988 Z^4 + 8.974 Z^3 - 2.339 Z^2 - 6.209 Z + 3.564}{Z^5 - 1.209 Z^4 - 1.338 Z^3 + 1.718 Z^2 + 0.4439 Z - 0.613} \quad (93)$$

And the factored form of the discrete transfer function is:

$$G_T(Z) = \frac{-3.9878 (Z^2 - 1.92 Z + 0.9218)(Z - 1.164)(Z + 0.8332)}{(Z^2 - 1.977 Z + 0.9835)(Z - 0.8978)(Z + 0.8332)^2} \quad (94)$$

Transfer function in equation (94) has all the parameters needed to calculate the dynamic displacement of the microactuator. These parameters will be used in the model.

## 4.5 SIMULATION OF THE MODEL

In this section, the dynamic responses of cantilever microactuators composed by PVB/Fe<sub>2</sub>O<sub>3</sub> films are simulated from the model developed along this text and the parameters shown in appendix 2. The validation of this model is conducted by comparisons between the simulated responses and the experimental results. Therefore, validation will be performed for inputs of voltage in step and oscillatory mode, as experiments shown in chapter 3. This validation is only focused on microactuators of the PVB/Fe<sub>2</sub>O<sub>3</sub>\_14%wt Fe sample. Several experiments with this sample were carried out varying the microactuator dimensions and input voltages. The model was also validated for all the experimental repetitions performed for each condition. Results that best fit between model and experiments are presented in this section.

Considering that the maximal used frequency is 50 Hz (0.02 s), the sampling time ( $T_s$ ) used for this simulation is 0.001 s. This sampling time is inside the limits of the processors used in the experimental equipment of this thesis. It was chosen to avoid too high sampling rates that leads to unnecessary and time demanding computations, even too low rates to loss data fidelity.

### 4.5.1 Step response validation

In the step mode test, a step of voltage is applied to the electromagnet resulting in a constant magnetic field. This magnetic field promotes a displacement of the microactuator (see chapter 3 for more details). Two different sizes of the PVB/Fe<sub>2</sub>O<sub>3</sub>\_14%wt Fe microactuator were evaluated. The first size (size 1) has dimensions of 15 mm in length, 2 mm in width and 0.018 mm in thickness. The second size (size 2) has dimensions of 15 mm in length, 4 mm in width and 0.018 mm in thickness. Figure 4.15 summarizes the experimental conditions to be validated by the model.

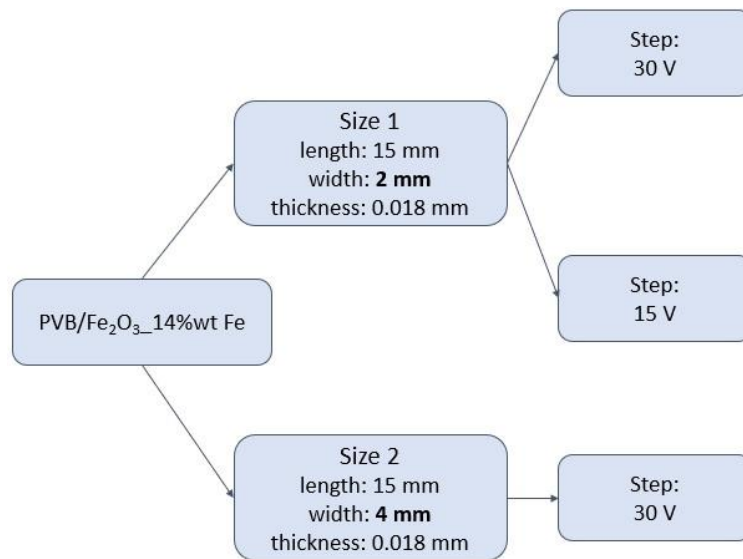


Figure 4.15. Conditions to evaluate by the model in the step mode.

The overall model was implemented in MATLAB by a code (the whole code is in appendix 5). This code is focused on the solution of each block of the model according to the overall block-structured model diagram shown in Figure 4.3.

Figure 4.16 shows an example of the simulated responses for each block of the model. However, the validation of the model will be only focused on the dynamic displacement of the microactuator and its comparison with the respective experimental cases.



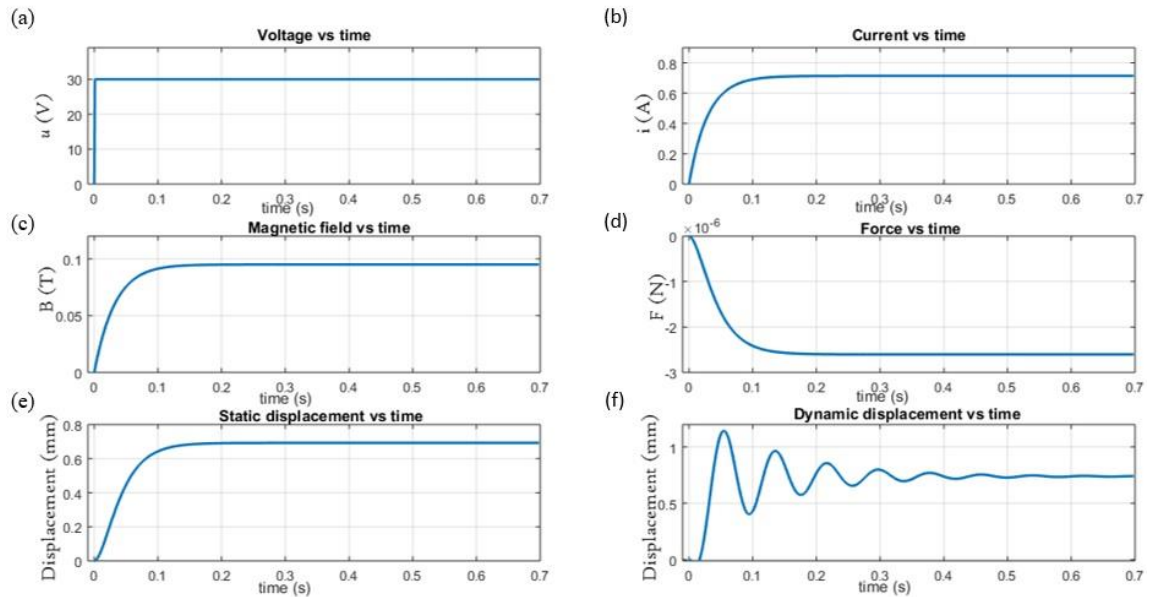


Figure 4.16. Example of the simulated responses for each block of the overall model: (a) applied step voltage of 30 V, (b) current flowing through the electromagnet due to the applied voltage, (c) magnetic field dependent of the current, (d) magnetic force in function of the magnetic field, (e) static displacement of the microactuator free end, and (f) dynamic displacement of the microactuator free end.

Although the validation of the model will be only focused on the dynamic displacement, validations for the intermediary signals of current ( $i$ ) and the magnetic field ( $B$ ) were also made. These intermediary validations were made to discard significant discrepancies between the model and the experimental results at the initial stage. The results for the validation of  $i$  and  $B$  by using a step voltage of 30 V are presented in Figure 4.17. The experimental curve of the current (Figure 4.17a) was acquired by measuring the current of the electromagnet with an oscilloscope. The experimentally recorded curve of the magnetic field (Figure 4.17b) was obtained by placing a gaussmeter at 2 mm from the central axis of the electromagnet, as explained in chapter 3. It is possible to observe good agreement between the experimental data and the model results for both, the current and the magnetic field. The relative error percentage for the comparison between the experimental and simulated current is 1.57% in the steady state region; while the relative error obtained by comparing the experimental and simulated magnetic field is 2.3% in the same region.

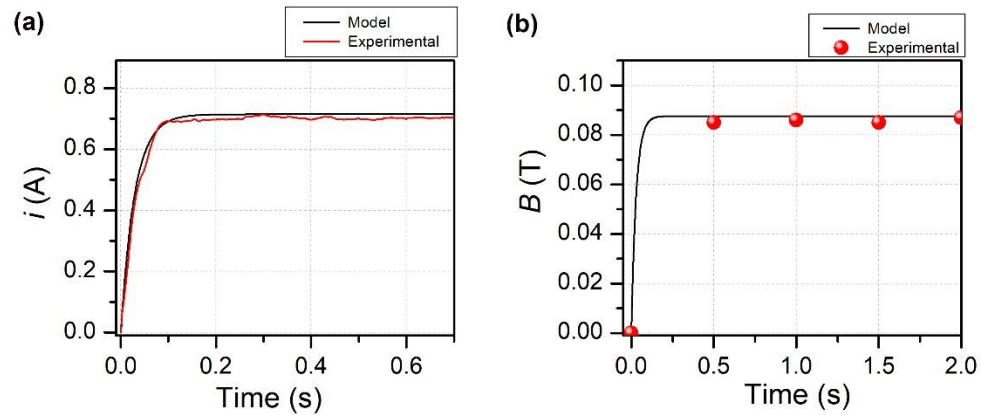


Figure 4.17. Validation of the model for: (a) current and (b) magnetic field, by applying a step voltage of 30 V.

Then, the simulated dynamic displacement was compared with the results obtained from experiments. Figure 4.18 shows the results for the microactuator of the sample PVB/Fe<sub>2</sub>O<sub>3</sub>\_14% wt Fe at the three different conditions tested in the step mode.

Figure 4.18a shows the results of displacement versus time for the microactuator of size 1 when a step of 30 V is applied. The best agreement between the simulated prediction is qualitatively observed in this case. The reason of this good agreement is attributed to the process followed for the identification of the parameters in MATLAB. This process involves the selection of an experimental displacement response that serves as reference to identify the parameters of the transfer function. The experimental response used as reference was the one corresponding to this case. Thus, the best agreement was expected for this case. This transfer function was used for the other cases.

The results of displacement versus time by applying 15 V of step voltage with the same size of microactuator are shown in Figure 4.18b. Here, we also observe a good fit between experimental and model displacements. However, some small differences start to be observed.

Additionally, the validation was made for the microactuator of size 2 when a step of 30 V is applied (Figure 4.18c). Here, a change in width from 2 mm to 4 mm is considered. The

displacement of the simulated response is different compared to the displacement of the experimental response. These differences may be attributed to the dispersion of the magnetic nanoparticles inside the PVB matrix of the microactuator. According to the proposed model, the simulated dynamic displacement is estimated by the assumption of homogeneous dispersion of the magnetic nanoparticles into the PVB matrix; however, the experimental case could be different. Some agglomerated nanoparticles can be into the PVB matrix. Agglomerates can promote nanoparticles-free spaces along the microactuator. These nanoparticles-free spaces can be located at a point near to the free end of the microactuator making it difficult to move. This may be the reason why the displacement on the model is higher compared to the experimental displacement. In fact, it was observed that by doubling the width of the microactuator from 2 mm to 4 mm, the mass is not duplicated as expected. The mass increased from 1.2 mg to only 1.9 mg, which may indicate the need to improve the dispersion of magnetic nanoparticles.

The comparison of the settling displacements for all the experimental cases and their respective simulated results is shown in Table 4.1. This was performed to compute the relative error of the model. From it, it is possible to confirm that the best agreement was achieved for the microactuator of size 1 when a step of 30 V is applied.

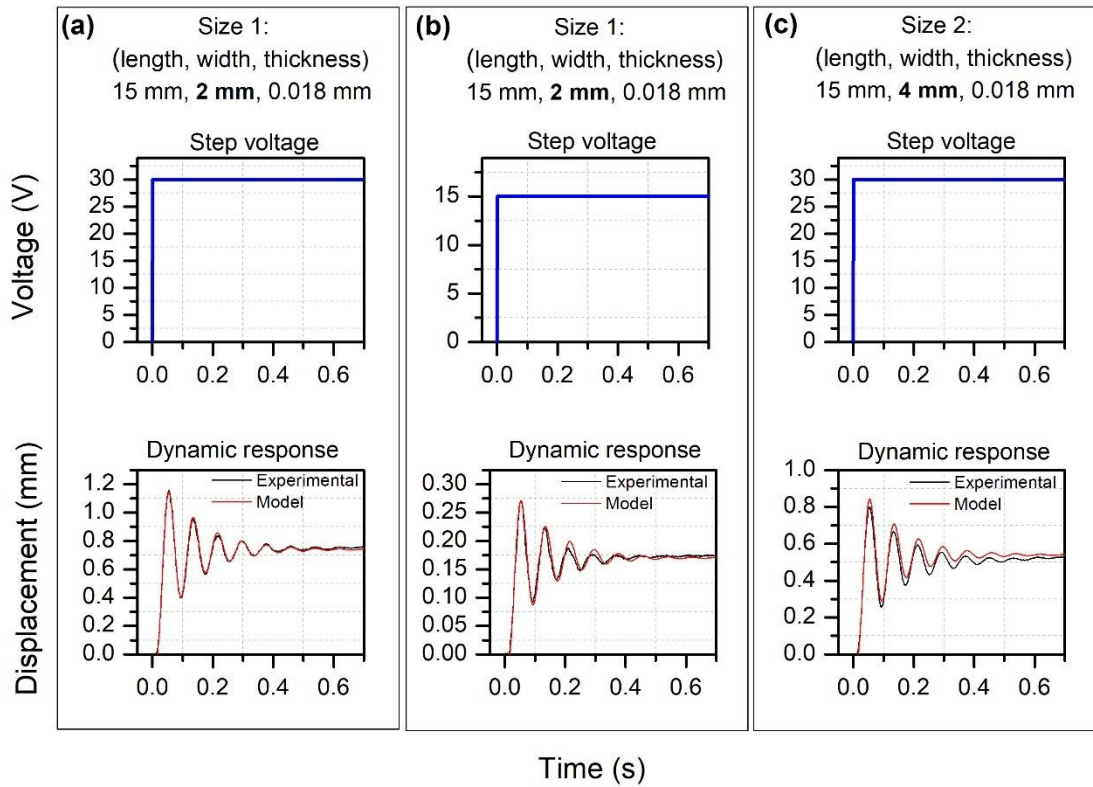


Figure 4.18 Comparison between simulated and experimental dynamic displacements for the microactuator of the sample PVB/Fe<sub>2</sub>O<sub>3</sub>\_14% wt Fe tested at the following conditions: (a) 30 V of step and size 1, (b) 15 V of step and size 1, and (d) 30 V of step and size 2.

Table 4.1. Comparison between experimental and simulated settling displacements.

Step	Size	Experimental	Model	% error
30 V	1	0.753	0.742	1.46
15 V	1	0.174	0.170	2.29
30 V	2	0.525	0.539	2.66

In order to validate the proposed model in the frequency domain, further validations were performed for the oscillatory mode test. This validation is shown in the next section.

#### 4.5.2 Oscillatory response validation

The validation of the model was performed in the frequency domain by taking the experimental results obtained from the oscillatory mode test (chapter 3). This test was

conducted by applying a periodic voltage of controlled amplitude and frequency to the electromagnet. The electromagnet generates a harmonic magnetic field in response, which promotes an oscillatory displacement of the microactuator.

The validation of the model was conducted for the microactuator of the sample PVB/Fe<sub>2</sub>O<sub>3</sub>\_14%wt Fe and its variants of the microactuators dimensions and the amplitude and frequency of the input signals. The experimental conditions to be validated at the oscillatory mode are shown in Figure 4.19.

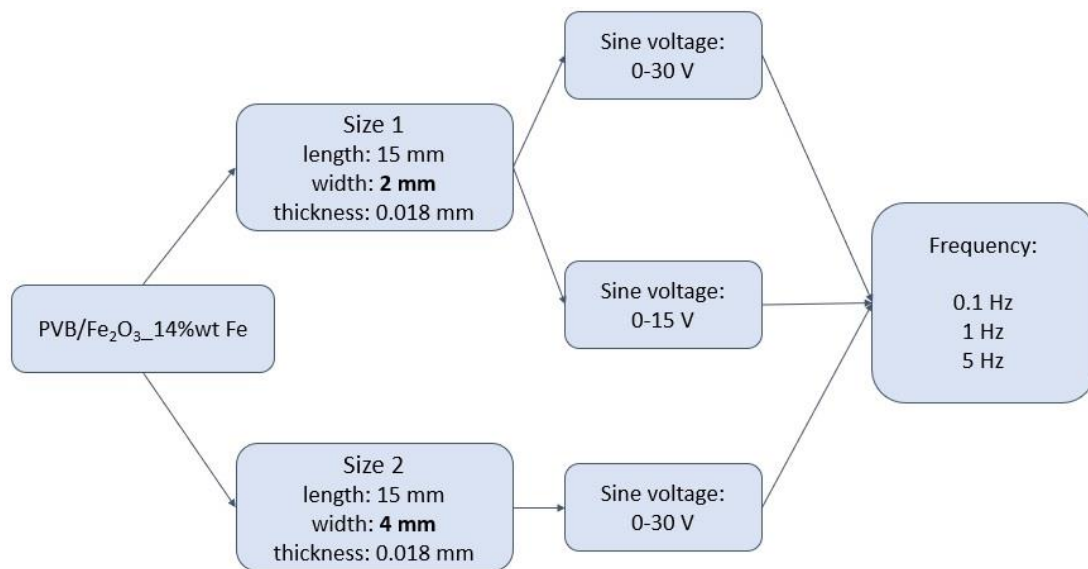


Figure 4.19. Conditions to evaluate by the model in the periodic voltage mode.

Figure 4.20 shows the results corresponding to the case when a sine voltage of 0-30 V is applied and the dimensions of the microactuator is 15 mm in length, 2 mm in width and 0.018 mm in thickness (size 1). In this figure, the results at frequencies of (a) 0.1 Hz, (b) 1 Hz and (c) 5 Hz are illustrated. Due to the computation time, one cycle was taken for the test at 0.1 Hz, while two cycles were taken for the tests at 1 Hz and 5 Hz.

From the plots of displacement versus time and displacement versus voltage at 0.1 Hz shown in Figure 4.20, it was observed that the experimental displacement is higher than the one computed from the model. The maximum displacement achieved for the experimental response is 0.797 mm, while the simulated response exhibits 0.740 mm. This

comparison gives a relative error of 7.15%. This behavior agrees with previous results, which report higher displacements as the rate of deformation is slower [24]. At low deformation rates (such as 0.1 Hz), magnetic dipoles have more time to align with the magnetic field. Also, there is more time to carry out molecular motions of the polymer. Concepts such as relaxation phenomena of the polymers or relaxation of superparamagnetic nanoparticles can be introduced in the model in order to obtain more precise results. The relaxation phenomena of the polymers is useful to identify the times of relaxation related to molecular motions, these motions define the macroscopical behavior of the polymer [23]. Also, the relaxation of superparamagnetic nanoparticles could give useful information of the time they take to be magnetized or demagnetized. These phenomena remain under study and were not included in the model because of their complexity and the lack of a general solution. However deeper mechanical and magnetic experimentation could be performed in order to introduce these concepts.

For the plot of displacement versus voltage at 0.1 Hz shown in the same figure (Figure 4.20), a small hysteresis is observed in the experimental result while hysteresis is not appreciated in the simulated result. This can be caused by the assumption of the model that considers the microactuator as purely elastic, thus neglecting that the mechanical properties of the PVB/Fe<sub>2</sub>O<sub>3</sub> films are viscoelastic. As a reminder of the explained in chapter 3, a viscoelastic material exhibit both viscous and elastic characteristics. Therefore, these materials have an elastic behavior that respond instantaneously to the applied stimulus and return to their original state when the stimulus is removed. However, these materials have also a viscous behavior that dissipates energy when the stimulus is applied and then removed. This dissipation is reflected in a hysteretic performance dependent on the rate of deformation. This rate-dependence is directly related with the relaxation phenomena described in the last paragraph. Thus, the energy dissipation of the viscoelastic material may be examined to improve the model. Additionally, the magnetization and demagnetization dynamics of the magnetic dipoles shall be considered.

In the same plot of displacement versus voltage at 0.1 Hz of Figure 4.20, it is observed that the shape of the experimental curve is very different compared to the shape of the simulated response. This can be also attributed to the aforementioned concepts that are

not considered in the model: the magnetization and demagnetization dynamics of the magnetic dipoles and the rate-dependent viscoelastic properties of the PVB/Fe<sub>2</sub>O<sub>3</sub> films.

However, it is desirable to also consider other concepts such as the dispersion of the magnetic nanoparticles into the polymeric matrix. Moreover, the distribution of the magnetic forces along the microactuator may be considered as the magnetic nanoparticles are also dispersed along the microactuator (see Figure 4.21). These concepts should be deeper analyzed and included as improvements of the model.

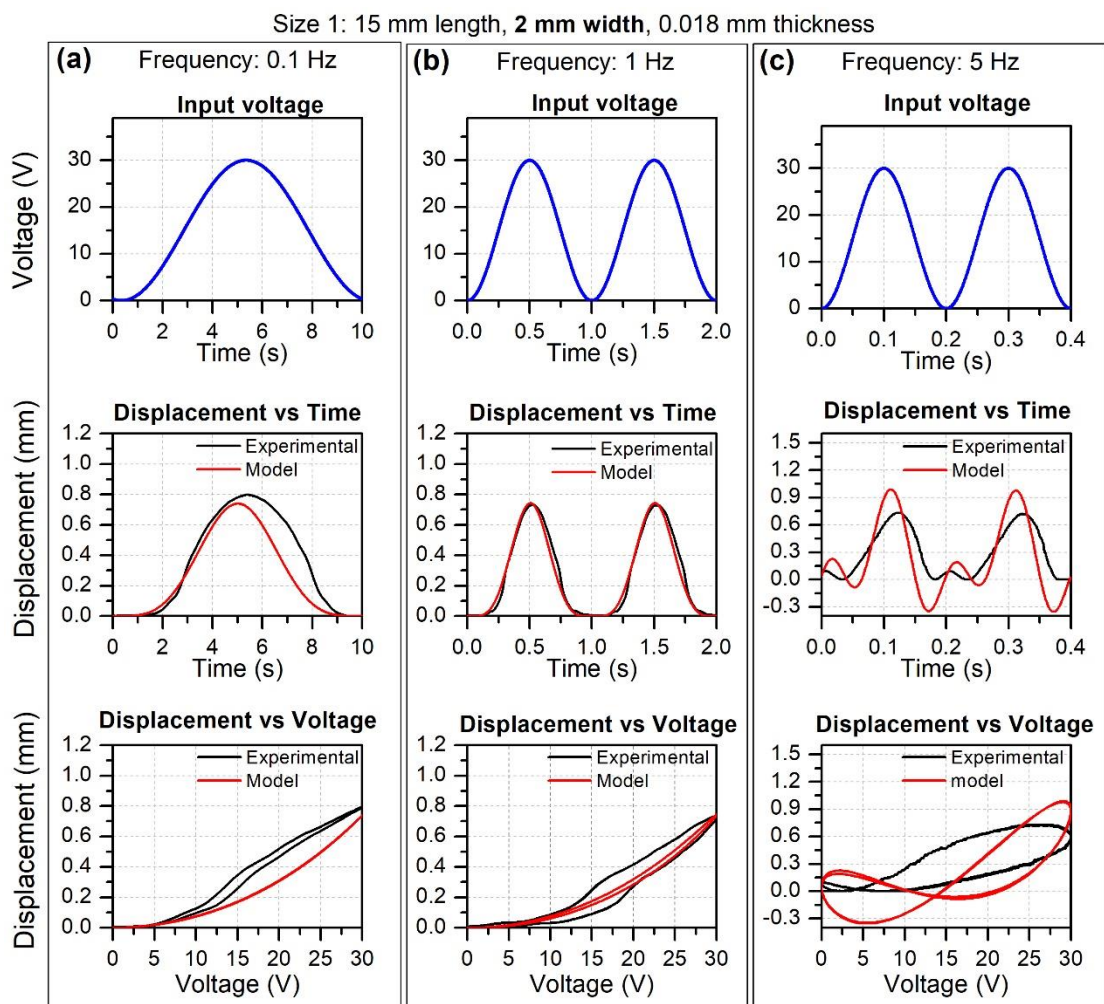


Figure 4.20. Comparison between simulated and experimental dynamic displacements for the PVB/Fe<sub>2</sub>O<sub>3</sub>\_14% wt Fe microactuator, tested in the oscillatory voltage mode. The test was carried out for the microactuator of size 1 by applying a voltage of 0-30 V and frequency of: (a) 0.1 Hz, (b) 1 Hz and (c) 5 Hz.

As the frequency increases to 1 Hz, the maximum displacement obtained from the experimental curve decreases to 0.729 mm. While the simulated maximum displacement is 0.742 mm. The relative error is 1.78%. This can be observed in the plots of displacement versus time and displacement versus voltage in Figure 4.20b. Like the case of 0.1 Hz, it is possible to observe a more pronounced hysteresis for the experimental result in comparison to the simulated result. The hysteretic behavior and its rate dependence can be added to the model by the incorporation of all the previously mentioned concepts.

Figure 4.20c shows the results when the periodic voltage at a frequency of 5 Hz is applied. In this case, a response associated with the presence of additional oscillations was observed. These additional oscillations are related to internal vibrations in the cantilever structure. Internal vibrations appear as the frequency of the cantilever structure approaches to the resonance frequency region. This behavior was observed for both experimental response and simulated responses. Although this last follows some trends of the experimental response, the values are not coincident. Internal vibrations in the simulated response seems to be stronger (higher amplitude) compared to the response of experimental results. As previously mentioned, this can be because the model considers a purely elastic material while the material is viscoelastic. The energy dissipation caused by the viscous behavior of viscoelastic materials works as internal damper that restrict oscillations.



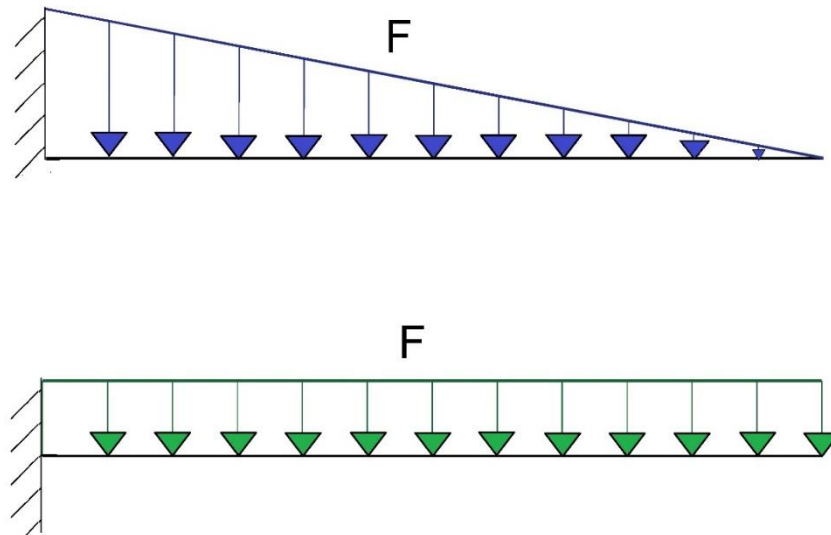


Figure 4.21. Examples of different kind of magnetic force distributions along the cantilever microactuator.

Figure 4.22 shows the response of the microactuator when a voltage of 0-15 V is applied. The dimensions of the microactuator is 15 mm in length, 2 mm in width and 0.018 mm in thickness (size 1). The frequencies of the tests are 0.1 Hz, 1 Hz and 5 Hz. The observed behavior is similar to the one observed when a voltage amplitude of 0-30 V is applied (Figure 4.20) as we are dealing with the same size of microactuator. A maximum displacement of 0.176 mm was observed at 0.1 Hz. This value of maximum displacement is higher than the one observed in the simulated response which is 0.170 mm. At 1 Hz the value of maximum displacement in the experimental response drops to 0.161 mm, while the simulated response remains the same (0.170 mm). The relative error obtained is 3.4% at 0.1 Hz and 5.59% for the test at 1 Hz. Also, the response associated to internal vibrations appears at 5 Hz which is related to the proximity to the resonance frequency. Hence, the analysis made for the case of 0-30 V of sine voltage and same dimensions is applicable to this case.

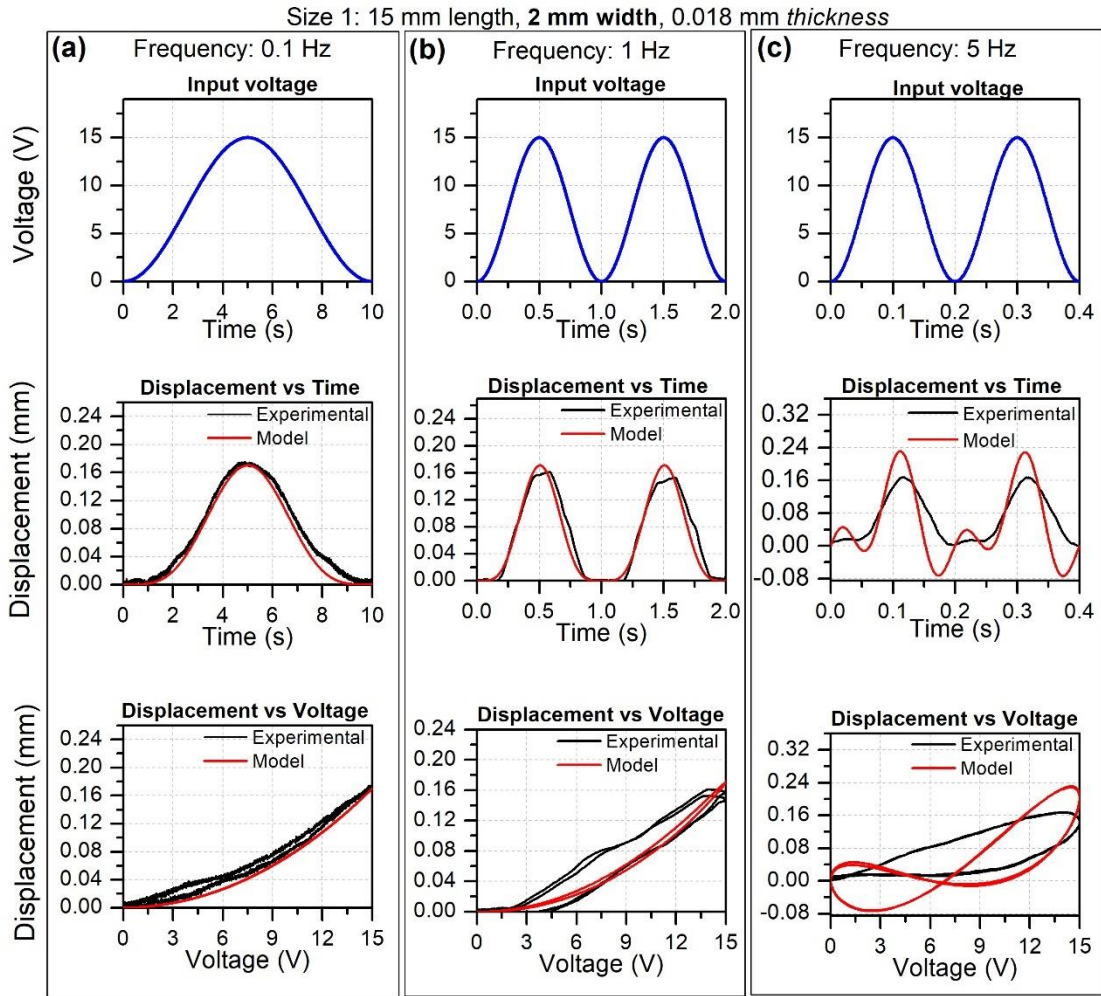


Figure 4.22. Comparison between simulated and experimental dynamic displacements for the microactuator of the sample PVB/Fe<sub>2</sub>O<sub>3</sub>\_14%wt Fe, tested in the oscillatory voltage mode. The tests were carried out for the microactuator of size 1 by applying a sine voltage of 0-15 V and frequencies of: (a) 0.1 Hz, (b) 1 Hz and (c) 5 Hz.

The comparison of the results when a voltage of 0-30 V is applied to a microactuator of dimensions of 15 mm in length, 4 mm in width and 0.018 mm in thickness (size 2) are shown in Figure 4.23. In this case, all the values of displacement estimated by the model are higher than the values obtained experimentally. These results are coincident with the results observed in the step mode test, shown in section 4.5.1. Also, this behavior is attributed to the same reason than the explained in the step mode section; so, the dispersion of the magnetic nanoparticles into the polymer must be improved to avoid significant differences between experimental and simulated results. The relative error was estimated to be 10.88% for 0.1 Hz and 15.31% for 1 Hz. At 5 Hz, it is also possible to observe the

response associated with internal vibrations, which is attributed to the proximity to the resonance frequency region. As in the other cases, the internal vibrations present higher amplitude for the simulated response compared to the experimental response. The analysis of this shall be included in further improvements of the model.

The comparison of the relative errors for the maximum displacements obtained in the periodic voltage mode is shown in Table 4.2. This was performed to for all the experimental cases and their respective simulated results.

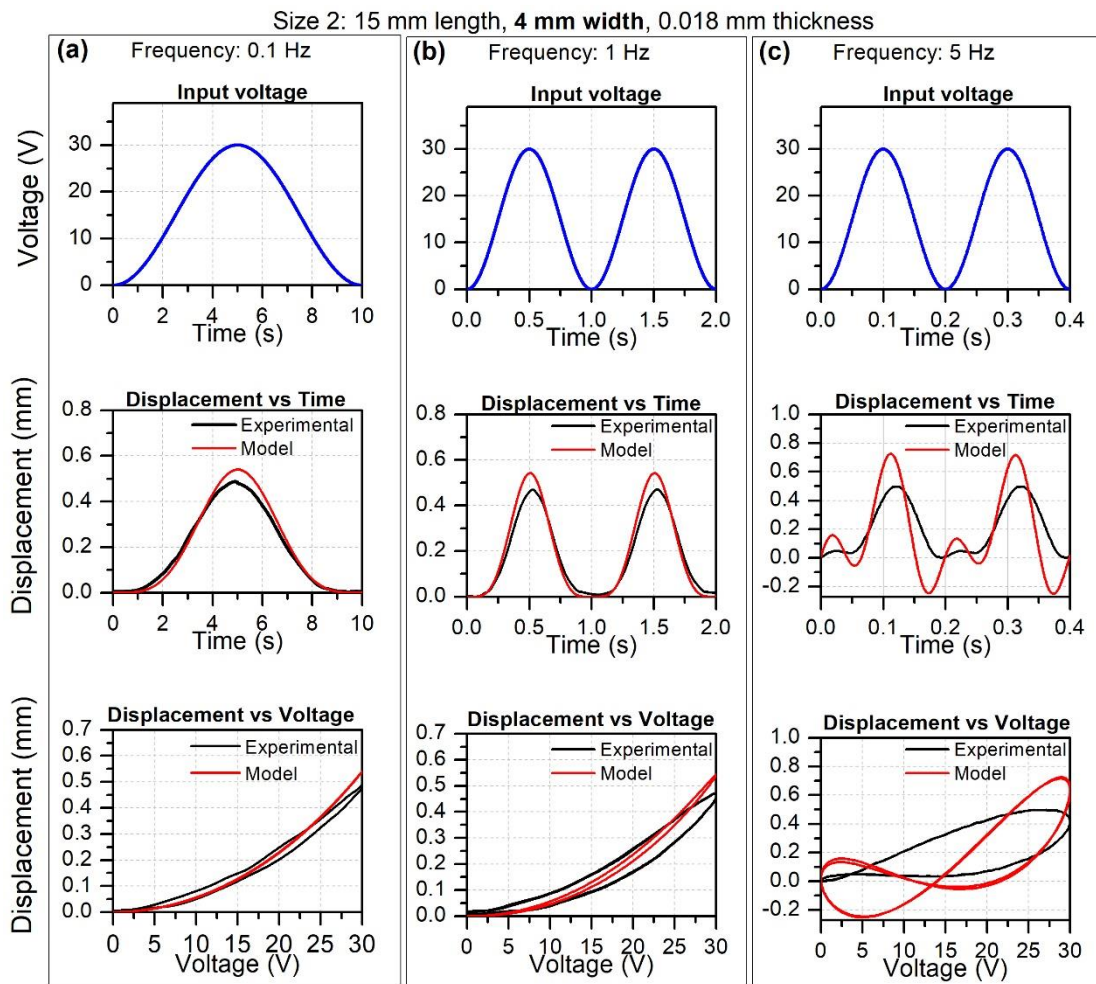


Figure 4.23. Comparison between simulated and experimental dynamic displacements for the microactuator of the sample PVB/Fe<sub>2</sub>O<sub>3</sub>\_14% wt Fe, tested in the oscillatory voltage mode. The tests were carried out for the microactuator of size 2 by applying an amplitude of 0-30 V and frequencies of: (a) 0.1 Hz, (b) 1 Hz and (c) 5 Hz.

Table 4.2. Comparison between experimental and simulated maximum displacements.

Frequency (Hz)	%error		
	Voltage: 0-15V	Voltage: 0-30 V	Voltage: 0-30 V
	Size 1	Size 1	Size 2
0.1	3.4	7.15	10.88
1	5.54	1.78	15.31
5	38.3	35.3	45.58

In order to observe the resonance frequency estimated by the model, the bode diagram of the transfer function (equation (94)) was obtained. This bode diagram is shown in Figure 4.24. The first resonance frequency corresponds to the first peak of the diagram. This resonance frequency is estimated to 12.5 Hz. A second resonance mode (peak) is observed beyond the first one, at 140 Hz. However, this last frequency is far from the scope of the study. At a frequency of 5 Hz, the magnitude of the gain is 4.9 dB which means that the input of the system will be amplified by a factor of 1.6 at its output. This explains the big increment in the amplitude of oscillations at the mentioned frequency for all the cases. The magnitude of the gain at 0.1 Hz and 1 Hz is about zero, which is equivalent to a factor of 1 between the input and the output.

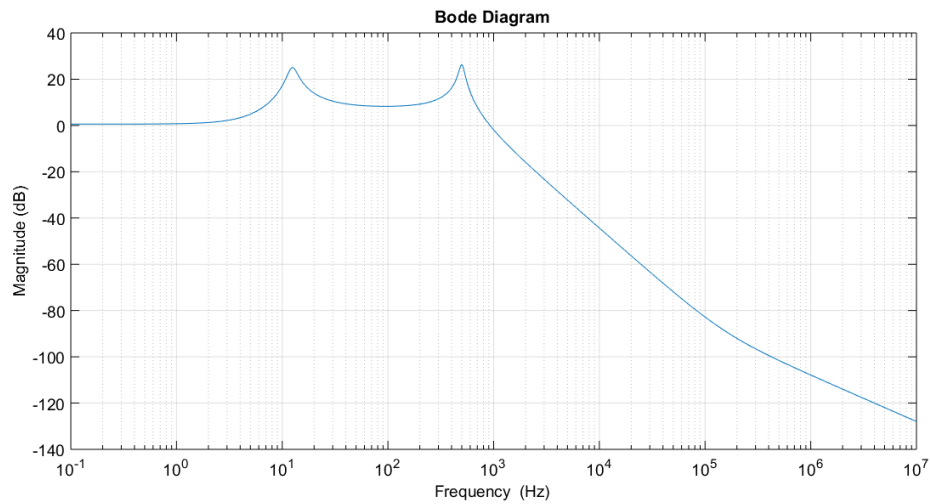


Figure 4.24. Estimated transfer function's bode diagram.

In general, it is possible to conclude that the model is useful to obtain an approximation of the maximum displacement at 0.1 Hz and 1 Hz. The smallest relative error is 1.78% and it was obtained for the microactuator of size 1 when a sine voltage of 0-30 V is applied at a frequency of 1 Hz. However, the relative error is variable for each case. Thus, each particular case should be analyzed according to the expected application. Moreover, further analysis shall be performed to model the hysteresis and the variations promoted by the viscoelastic properties of the material.

#### 4.6 CONCLUDING REMARKS

- A model for the dynamic response of PVB/Fe<sub>2</sub>O<sub>3</sub> films as cantilever microactuators was developed.
- This model was based on physical principles in a block structure.
- The model was evaluated for microactuators of the sample PVB/Fe<sub>2</sub>O<sub>3</sub>\_14% wt Fe at the step mode and oscillatory mode. Also, two different sizes were investigated. The dimensions of the first size (size 1) are 15 mm in length, 2 mm in width and 0.018 mm in thickness. The second size (size 2) has dimensions of 15 mm in length, 4 mm in width and 0.018 mm in thickness.
- The experimental results of the step mode for the microactuator were compared with the simulated results (model results). Results shown a relative error of 1.46% for the microactuator of size 1 by applying 30 V, 2.29% for the microactuator of size 1 at apply 15 V and 2.66% for the microactuator of size 2 at apply 30 V.
- The highest error was obtained for the microactuator of size 2 at a step of 30 V. This is attributed to some agglomerations of magnetic nanoparticles into the PVB matrix. These agglomerations can be in random sections of the microactuator, in consequence, the prediction of the displacement becomes difficult.
- For the microactuator of size 1 in the oscillatory mode, the model is useful to obtain approximations of the maximum displacement achieved at frequencies of 0.1 Hz and 1 Hz; the relative errors are 1.78% and 7.15%, respectively. The smallest relative error (1.78%) was obtained for the microactuator of size 1 when

a sine voltage of 0-30 V is applied at a frequency of 1 Hz. The highest relative errors were obtained for the microactuator of size 2 and it is in concordance with results of the step mode. These errors vary from 10.88% to 15.31% at frequencies of 0.1 Hz and 1 Hz, respectively.

- A response associated with the presence of internal vibrations start to appear at a frequency of 5 Hz for all the cases in the oscillatory mode. These internal vibrations were observed for both, experimental and simulated results. Internal vibrations are related to the proximity to the resonance frequency. However, simulated results exhibit higher amplitudes of vibration compared to the amplitudes obtained in the experimental results.
- According to the bode plot, the resonance frequency of the microactuator is 12.5 Hz.
- Hysteresis in experimental curves is not replicated by simulated curves.
- The model can be improved by adding some considerations such as the viscoelastic properties of the PVB/Fe<sub>2</sub>O<sub>3</sub> films, dynamics of magnetization and demagnetization of the magnetic nanoparticles, interactions between nanoparticles and the polymeric matrix or the distribution of the magnetic forces along the microactuator.
- The aim to include the above-mentioned considerations is mainly to model the hysteretic behavior and other dynamics presented in the experimental results. By modeling this, it is considered that the error values will decrease.

# CONCLUSION AND PERSPECTIVES

The overall objective of this thesis was to study and explore the development of microactuators by using magnetoactive materials. Specifically, the used magnetoactive material was composed by iron oxide nanoparticles synthesized *in situ* and embedded in a polyvinyl butyral matrix (PVB/Fe<sub>2</sub>O<sub>3</sub>). These films are also called magnetic hybrid films.

In order to achieve the overall objective, many activities were performed generating important contributions in the field of magnetoactive polymers as microactuators. The main contributions of this thesis are:

- The exploration of the *in-situ* synthesis of hybrid magnetic films of PVB/Fe<sub>2</sub>O<sub>3</sub> at different nominal concentrations (weight percentage) of iron (Fe). These concentrations were 11% wt, 14% wt and 17% wt.
- The study of the magnetic and mechanical properties of each concentration of the magnetic hybrid films.
- An exhaustive dynamic characterization of the response of magnetic hybrid films of PVB/Fe<sub>2</sub>O<sub>3</sub> as cantilever microactuators when subjected to step and periodic magnetic fields. This characterization was performed for the three different concentrations of magnetic hybrid films. For the microactuator of medium concentration (14%wt Fe), the dynamic characterization was conducted by applying different magnetic field values and by using different sizes of microactuators.
- A mathematical model describing the dynamic response of the PVB/Fe<sub>2</sub>O<sub>3</sub> films as cantilever microactuators. This model has been based on physical concepts and behavioral analysis of the microactuator.

The exploration of the *in-situ* synthesis of magnetic hybrid films of PVB/Fe<sub>2</sub>O<sub>3</sub> at different nominal concentrations of iron gave as a results three magnetic hybrid films with different content of iron oxide nanoparticles. These films shown macroscopical response to magnetic stimuli.

The study of the mechanical properties of the magnetic hybrid films at three different concentrations showed a decrement in the elastic modulus at room temperature as the content of iron oxide nanoparticles increases. Apparently, nanoparticles have a plasticizer effect on the polymeric matrix at room temperature. However, the elastic modulus of these materials was reinforced at higher temperatures in comparison with pristine PVB. Moreover, the glass transition temperature of the PVB increases an average of 5°C with the addition of iron oxide nanoparticles.

Superparamagnetic behavior was obtained for the three different contents of iron oxide nanoparticles. This behavior indicates the presence of magnetic nanoparticles of size under 15 nm into the PVB matrix. The magnetization of the magnetic hybrid films is increased as the iron content increases.

The dynamic behavior of the PVB/Fe<sub>2</sub>O<sub>3</sub> films as cantilever microactuator is underdamped, characteristic of this kind of configuration by applying a step stimulus. The displacement of the microactuator is higher as the iron oxide nanoparticles content increases. The displacement of the microactuator varies directly proportional to the applied magnetic field. If the applied magnetic field is modified, the damping vibrations characteristic of the underdamped response are not modified as long as the iron oxide nanoparticles concentration and the microactuator dimensions remain constant. By doubling the cross section of the microactuator, the displacement decreases approximately 40% for the same applied magnetic field. This decrement is related to the increment of the cross-sectional moment of inertia, which increases the stiffness of the microactuator.

The behavior of the PVB/Fe<sub>2</sub>O<sub>3</sub> films as cantilever microactuator tested with a periodic voltage showed nonlinear and frequency-dependent responses. The highest displacement was achieved at the lowest frequency tested (0.1 Hz) for all the cases. Additionally, the smallest hysteresis loop area was qualitatively observed at this frequency (0.1 Hz), also for all the cases. This kind of responses is attributed to the relaxation time of the PVB matrix and the dynamics of magnetization and demagnetization of the iron oxide nanoparticles. A response associated with internal vibrations starts to be observed at 5 Hz. Low



bandwidth was observed for all the cases. According to the results, the microactuator should operate at frequencies lower than 5 Hz.

The modeling of the dynamic behavior for the microactuator suggests that the relative error is related to the way of dispersion of the iron oxide nanoparticles into the PVB matrix. The proposed model is useful to obtain approximations of the maximum displacement achieved at low frequencies (0.1 Hz and 1 Hz) by applying a periodic stimulus. A response associated with internal vibrations was observed for the simulated results at a frequency of 5 Hz. This response is similar to the behavior obtained for experimental results. The bode plot of the model shown that the resonance frequency is about 12.5 Hz. The model was not able to simulate the hysteresis and more complex shapes of the graphs obtained in the periodic test mode.

Based on the previously mentioned, we can assert that a model of the dynamic behavior of magnetic hybrid films of PVB/Fe<sub>2</sub>O<sub>3</sub> functioning as microactuators was developed and validated. Therefore, the main objective of this thesis has been fulfilled. Future perspectives to be assessed are described below.

- Regarding the properties of the magnetic hybrid films of PVB/Fe<sub>2</sub>O<sub>3</sub>

The improvement of the controlling of the dispersion and size distribution of magnetic nanoparticles into the PVB matrix would be very advantageous for the application of PVB/Fe<sub>2</sub>O<sub>3</sub> films as microactuator. This improvement will facilitate the prediction of their behavior by modeling. Experiments modifying times of stirring or temperatures according to each concentration may be performed. The use of coaters or surface modifiers to enhance the interfacial interaction between iron oxide nanoparticles and the polymeric matrix should be also tested in order to improve their dispersion.

– Regarding the model

The model can be tested for other kind of polymeric matrixes with iron oxide nanoparticles. However, it can be improved by adding the viscoelastic properties of the involved polymer, including its frequency-dependence and relaxation times.

Moreover, the dynamics of magnetization and demagnetization of magnetic nanoparticles can be further analyzed by experimentation or theoretical equations available in literature.

The distribution of magnetic forces along the microactuator can be also considered, by observing that the nanoparticles are distributed along the microactuator.

These considerations may help to model the hysteretic behavior and other dynamics presented in the experimental results as well as to decrease the relative error values.

## REFERENCES

- [1] M.R. Aguilar and J. San Román, "Introduction to Smart Polymers and Their Applications", in *Smart Polymers and their Applications*, Ed. Elsevier, 2014, pp. 1–11.
- [2] H. Meng and G. Li, "A Review of Stimuli-Responsive Shape Memory Polymer Composites", *Polymer*, vol. 54, no. 9, pp. 2199–2221, 2013.
- [3] A. Diermeier, D. Sindesberger and G. Monkman, "Magneto-Active Polymer Actuator", in *Applied Research Conference*, Augsburg, Germany, 2016, pp. 1-4.
- [4] L.F. Campanile and O. Gomis-Bellmunt, "Actuator Principles and Classification", in *Design Rules for Actuators in Active Mechanical Systems*, Ed. Springer-Verlag, London, 2010, pp. 3–28.
- [5] B.C. López-Walle and E. Reyes-Melo, "Characterization and Dynamics of Polymer Microactuators", in *Smart Materials-Based Actuators at the Micro/Nano-Scale: Characterization, Control and Applications*, Ed. Springer New York, 2013, pp. 15–39.
- [6] L.A. Makarova, Y.A. Alekhina, T.S. Rusakova and N.S. Perov, "Tunable Properties of Magnetoactive Elastomers for Biomedical Applications", *Physics Procedia*, vol. 82, December, pp. 38–45, 2016.
- [7] M. Yasui, M. Ikeuchi and K. Ikuta, "Magnetic micro actuator with neutral buoyancy and 3D fabrication of cell size magnetized structure", in *Proceedings IEEE International Conference on Robotics and Automation*, Minnesota, USA, 2012, pp. 745–750.
- [8] J. Zhang, O. Onaizah, K. Middleton, L. You and E. Diller, "Reliable Grasping of Three-Dimensional Untethered Mobile Magnetic Microgripper for Autonomous Pick-and-Place", *IEEE Robotics and Automation Letters*, vol. 2, no. 2, pp. 835–840, 2017.
- [9] M. Świętek, W. Tokarz, J. Tarasiuk, S. Wroński and M. Błazewicz, "Magnetic polymer nanocomposite for medical application", *Acta Physica Polonica A*, vol. 125, no. 4, pp. 891–894, 2014.
- [10] T. Nakahara, J. Suzuki, Y. Hosokawa, F. Shimokawa, H. Kotera and T. Suzuki, "Fabrication of Magnetically Driven Microvalve Arrays Using a Photosensitive Composite", *Magnetochemistry*, vol. 4, no. 7, pp. 1–12, 2018.
- [11] Y.W. Liu, Z. Qing-Feng and L. Run-Wei, "Fabrication, properties and applications of flexible magnetic films", *Chinese Physics B*, vol. 22, no. 12, pp. 1127502 1–14, 2013.
- [12] P. Saxena, J.P. Pelteret and P. Steinmann, "Modelling of iron-filled magneto-active polymers with a dispersed chain-like microstructure", *European Journal of Mechanics-A/Solids*, vol. 50, pp. 132–151, 2015.
- [13] B. Kiefer, K. Haldar and A. Menzel, "Modeling, Simulation and Parameter Identification for Rate-Dependent Magnetoactive Polymer Response", *Proceedings in Applied Mathematics and Mechanics*, vol. 15, no. 1, pp. 395–396, 2015.
- [14] M. Grossard and M. Rakotondrabe, "High Resolution Actuators", *Actuators*, vol. 5, no. 2, pp. 18, act5020018 2016.

- [15] O. Farhan, S. Rakheja and C. Su, "Experimental characterization and modeling of rate-dependent asymmetric hysteresis of magnetostrictive actuators", *Smart Materials and Structures*, vol. 23, no. 3, pp. 035002 1-12, 2014.
- [16] M.J. Dapino, "On Magnetostrictive Materials and Their Use in Smart Material Transducer", *Journal of Structural Engineering and Mechanism*, vol. 17, no. 3, pp. 1–28, 2002.
- [17] J.M. Nealis and R.C. Smith, "Model-Based Robust Control Design for Magnetostrictive Transducers Operating in Hysteretic and Nonlinear Regimes", *IEEE Transactions On Control Systems Technology*, vol. 15, no. 1, pp. 22–39, 2007.
- [18] Q. Liu, H. Li and K.Y. Lam, "Development of a Multiphysics Model to Characterize the Responsive Behavior of Magnetic-Sensitive Hydrogels with Finite Deformation", *Journal of Physical Chemistry B*, vol. 121, no. 22, pp. 5633–5646, 2017.
- [19] M.A. Cantera, M. Behrooz, R.F. Gibson and F. Gordaninejad, "Modeling of magneto-mechanical response of magnetorheological elastomers (MRE) and MRE-based systems: A review", *Smart Materials and Structures*, vol. 26, no. 2, pp. 1–21, 2017.
- [20] P. Saxena, J.P. Pelteret and P. Steinmann, "Modelling of iron-filled magneto-active polymers with a dispersed chain-like microstructure", *European Journal of Mechanics-A/Solids*, vol. 50, pp. 132–151, 2015.
- [21] J.G. Puente-Córdova, "Síntesis y caracterización de un material híbrido de matriz polimérica de polivinil butiral", M.Sc. thesis, Universidad Autónoma de Nuevo León, México, 2013.
- [22] M.E. Reyes-Melo, J.G. Puente-Córdova and B.C. López-Walle, "La carga de espacio en materiales híbridos", *Ingenierías*, vol. 23, no. 67, pp. 38–47, 2015.
- [23] M.E. Reyes-Melo, F.Y. Rentería-Baltiérrez and B.C. López-Walle, "Estudio de la movilidad molecular de PVB mediante análisis mecánico dinámico", *Ingenierías*, vol. 23, no. 67, pp. 38–47, 2015.
- [24] J. Romo-Rico, "Estudio y Control de un Material Híbrido Magnético PVB/Fe<sub>2</sub>O<sub>3</sub> aplicado como Microactuador tipo Cantilever", M.Sc. thesis, Universidad Autónoma de Nuevo León, México, 2018.
- [25] Z. Tong, W. Cheng and S. Jia and X. Chen, "Weak-scattering static diffuser by fast pumping dispersed-nanoparticles in a long distance using microfluidic flows for efficient laser speckle reduction", *Optics Express*, vol. 26, no. 16, pp. 20270, 2018.
- [26] Y. Zhong, S. Lundemo and E.W.H. Jager, "Development of polypyrrole based solid-state on-chip microactuators using photolithography", *Smart Materials and Structures*, vol. 27, no. 7, pp. 074006 1-7, 2018.
- [27] L. Hines, K. Petersen, G. Z. Lum and M. Sitti, "Soft Actuators for Small-Scale Robotics", *Advanced Materials*, vol. 29, no. 13, pp. 1603483, 2017.
- [28] M. Duduta, D. R. Clarke and R. J. Wood, "A high speed soft robot based on dielectric elastomer actuators", in *IEEE International Conference on Robotics and Automation*, Singapore, Singapore, 2017.
- [29] J. Zhang, O. Onaizah, K. Middleton, L. You and E. Diller, "Reliable Grasping of Three-Dimensional Untethered Mobile Magnetic Microgripper for Autonomous Pick-and-Place", *IEEE Robotics and Automation Letters*, vol. 2, no. 2, pp. 835–840, 2017.

- [30] H. Ceylan, I.C. Yasa, O. Yasa, A.F. Tabak, J. Giltinan and M. Sitti, "3D-Printed Biodegradable Microswimmer for Drug Delivery and Targeted Cell Labeling", *bioRxiv*, vol. 1, pp. 379024, 2018.
- [31] F. Carpi and D. De Rossi, "Eyeball pseudo-muscular actuators for an android face", *Proceedings of Society of Photo-Optical Instrumentation Engineers (SPIE)*, vol. 5759, pp. 16, 2005.
- [32] F. Carpi, G. Frediani, S. Turco and R. De Rossi, "Bioinspired tunable lens with muscle-like electroactive elastomers", *Advanced Functional Materials*, vol. 21, no. 21, pp. 4152–4158, 2011.
- [33] M. Rakotondrabe, "Smart materials-based actuators at the micro/nano-scale: Characterization, control, and applications", Ed. Springer, New York, USA, 2013.
- [34] G. Kickelbick, "Introduction to hybrid materials", in *Hybrid Materials: Synthesis, Characterization, and Applications*, Ed. Wiley-VCH, 2007, pp. 1-48.
- [35] S. Pandey and S.B. Mishra, "Sol-gel derived organic-inorganic hybrid materials: Synthesis, characterizations and applications", *Journal of Sol-Gel Science and Technology*, vol. 59, no. 1, pp. 73–94, 2011.
- [36] J. Livage, "Sol-gel synthesis of hybrid materials", *Bulleting of Materials Science*, vol. 22, no. 3, pp. 201–205, 1999.
- [37] G. Schottner, "Hybrid sol-gel-derived polymers: Applications of multifunctional materials", *Chemistry of Materials*, vol. 13, no. 10, pp. 3422–3435, 2001.
- [38] J. Dai, T. Zhang, H. Zhao and T. Fei, "Preparation of organic-inorganic hybrid polymers and their humidity sensing properties", *Sensors and Actuators B: Chemical*, vol. 242, pp. 1108–1114, 2017.
- [39] X. Yu, W. Zhang, P. Zhang and Z. Su, "Fabrication technologies and sensing applications of graphene-based composite films: Advances and challenges", *Biosensors and Bioelectronics*, vol. 89, no. 1, pp. 72–84, 2017.
- [40] S. Beg *et al.*, "Nanoporous metal organic frameworks as hybrid polymer–metal composites for drug delivery and biomedical applications", *Drug Discovery Today*, vol. 22, no. 4, pp. 625–637, 2017.
- [41] N.R. Sinatra, T. Ranzani, J.J. Vlassak, K.K. Parker and R.J. Wood, "Nanofiber-reinforced soft fluidic micro-actuators", *Journal of Micromechanics Microengineering*, vol. 28, no. 8, pp. 084002, 2018.
- [42] M. Rahbar and B.L. Gray, "Maximizing deflection in MEMS and microfluidic actuators fabricated in permanently magnetic composite polymers", in *IEEE 17th International Conference on Nanotechnology*, Philadelphia, USA, 2017.
- [43] S.N.A. Safri, M.T.H. Sultan, M. Jawaid and K. Jayakrishna, "Impact behaviour of hybrid composites for structural applications: A review", *Composites Part B: Engineering*, vol. 133, pp. 112–121, 2018.
- [44] P. Tripathi, V. Kumar Gupta, A. Dixit, R. Kumar Mishra and S. Sharma, "Development and characterization of low cost jute, bagasse and glass fiber reinforced advanced hybrid epoxy composites", *AIMS Materials Science*, vol. 5, no. 2, pp. 320–337, 2018.

- [45] V. Fiore, L. Calabrese, E. Proverbio, R. Passari and A. Valenza, "Salt spray fog ageing of hybrid composite/metal rivet joints for automotive applications", *Composites Part B: Engineering*, vol. 108, pp. 65–74, 2017.
- [46] L. Utzig, C. Karch, J. Rehra, B. Hannemann and S. Schmeer, "Modeling and simulation of the effective strength of hybrid polymer composites reinforced by carbon and steel fibers", *Journal of Materials Science*, vol. 53, no. 1, pp. 667–677, 2018.
- [47] M. Mitra, A. Ghosh, A. Mondal, K. Kargupta, S. Ganguly and D. Banerjee, "Facile synthesis of aluminium doped zinc oxide-polyaniline hybrids for photoluminescence and enhanced visible-light assisted photo-degradation of organic contaminants", *Applied Surface Science*, vol. 402, pp. 418–428, 2017.
- [48] G. Ferik *et al.*, "Monolithic magneto-optical nanocomposites of barium hexaferrite platelets in PMMA", *Science Reports*, vol. 5, no 11395, pp. 1-8, 2015.
- [49] C. Kascholke *et al.*, "Biodegradable and adjustable sol-gel glass based hybrid scaffolds from multi-armed oligomeric building blocks", *Acta Biomaterialia*, vol. 63, pp. 336–349, 2017.
- [50] J.K. Chen and C.J. Chang, "Fabrications and applications of stimulus-responsive polymer films and patterns on surfaces: A review", *Materials (Basel)*, vol. 7, no. 2, pp. 805–875, 2014.
- [51] S. Guragain, B.P. Bastakoti, V. Malgras, K. Nakashima and Y. Yamauchi, "Multi-Stimuli-Responsive Polymeric Materials", *Chemistry-A European Journal*, vol. 21, no. 38, pp. 13164–13174, 2015.
- [52] M. Delcea, H. Möhwald and A.G. Skirtach, "Stimuli-responsive LbL capsules and nanoshells for drug delivery", *Advanced Drug Delivery Reviews*, vol. 63, no. 9, pp. 730–747, 2011.
- [53] E. Cabane, X. Zhang, K. Langowska, C.G. Palivan and W. Meier, "Stimuli-responsive polymers and their applications in nanomedicine", *Biointerphases*, vol. 7, no. 4, pp. 1–27, 2012.
- [54] D. Roy, J.N. Cambre and B.S. Sumerlin, "Future perspectives and recent advances in stimuli-responsive materials", *Progress in Polymer Science*, vol. 35, no. 1–2, pp. 278–301, 2010.
- [55] C. Su, "Environmental implications and applications of engineered nanoscale magnetite and its hybrid nanocomposites: A review of recent literature", *Journal of Hazardous Materials*, vol. 322, pp. 48–84, 2017.
- [56] C. Jo, D. Pugal, I. K. Oh, K.J. Kim and K. Asaka, "Recent advances in ionic polymer-metal composite actuators and their modeling and applications", *Progress in Polymer Science*, vol. 38, no. 7, pp. 1037–1066, 2013.
- [57] T. Hou, T. Zhao, W. Li, F. Li and P. Gai, "A label-free visual platform for self-correcting logic gate construction and sensitive biosensing based on enzyme-mimetic coordination polymer nanoparticles", *Journal of Materials Chemistry B*, vol. 5, no. 24, pp. 4607–4613, 2017.
- [58] G. Rushi, F. Gazala and S. Seema, "Smart Polymers and Their Applications", *Tissue Engineering*, vol. 3, no. 4, pp. 1–27, 2014.
- [59] F. Reyes-Ortega, "pH-responsive polymers: Properties, synthesis and applications", in *Smart Polymers and their Applications*, Ed. Elsevier, 2014, pp. 1–11.

- [60] A. Kawamura and T. Miyata, "Encyclopedia of Polymeric Nanomaterials", Ed. Springer, 2015, pp. 1–9.
- [61] B.P. Bastakoti, S. Guragain, K. Nakashima and Y. Yamauchi, "Stimuli-Induced Core-Corona Inversion of Micelle of Poly (acrylic acid)-block-Poly (N-isopropylacrylamide) and Its Application in Drug Delivery", *Macromolecular Chemistry and Physics*, vol. 216, pp. 287–291, 2015.
- [62] S. Nesrinne and A. Djamel, "Synthesis, characterization and rheological behavior of pH sensitive poly(acrylamide-co-acrylic acid) hydrogels", *Arabian Journal of Chemistry*, vol. 10, no. 4, pp. 539–547, 2017.
- [63] X. Zhang *et al.*, "Recent progress and advances in redox-responsive polymers as controlled delivery nanoplatfoms", *Materials Chemistry Frontiers*, vol. 1, no. 5, pp. 807–822, 2017.
- [64] S. Cerritelli, D. Velluto and J.A. Hubbell, "PEG-SS-PPS: Reduction-sensitive disulfide block copolymer vesicles for intracellular drug delivery", *Biomacromolecules*, vol. 8, no. 6, pp. 1966–1972, 2007.
- [65] K.W. Leong, B.C. Brott and R. Langer, "Bioerodible polyanhydrides as drug-carrier matrices: characterization, degradation, and release characteristics", *Journal of Biomedical Materials Research*, vol. 19, no. 8, pp. 941–955, 1985.
- [66] S. Cohen, T. Yoshioka, M. Lucarelli, L.H. Hwang and R. Langer, "Controlled delivery systems for proteins based on poly(lactic/glycolic acid) microspheres", *Pharmaceutical research*, vol. 8, no. 6, pp. 713–720, 1991.
- [67] M. Huo, J. Yuan, L. Tao and Y. Wei, "Redox-responsive polymers for drug delivery: From molecular design to applications", *Polymer Chemistry*, vol. 5, no. 5, pp. 1519–1528, 2014.
- [68] Y. Chi *et al.*, "Redox-sensitive and hyaluronic acid functionalized liposomes for cytoplasmic drug delivery to osteosarcoma in animal models", *Journal of Controlled Release*, vol. 261, June, pp. 113–125, 2017.
- [69] W. Zhang and C.H. Tung, "Redox-responsive cisplatin nanogels for anticancer drug delivery", *Chemical Communications*, vol. 54, no. 60, pp. 8367–8370, 2018.
- [70] M. Zhao *et al.*, "Redox-responsive nanocapsules for intracellular protein delivery", *Biomaterials*, vol. 32, no. 22, pp. 5223–5230, 2011.
- [71] Z. Yang, Y. Li, J. Gao, Z. Cao, Q. Jiang and J. Liu, "pH and redox dual-responsive multifunctional gene delivery with enhanced capability of transporting DNA into the nucleus", *Colloids Surfaces B Biointerfaces*, vol. 153, pp. 111–122, 2017.
- [72] O. Onaca, R. Enea, D.W. Hughes and W. Meier, "Stimuli-responsive polymersomes as nanocarriers for drug and gene delivery", *Macromolecular Bioscience*, vol. 9, no. 2, pp. 129–139, 2009.
- [73] C. Zhang *et al.*, "Enzyme-responsive peptide dendrimer-gemcitabine conjugate as a controlled-release drug delivery vehicle with enhanced antitumor efficacy", *Acta Biomaterialia*, vol. 55, pp. 153–162, 2017.
- [74] R. Chandrawati, "Enzyme-responsive polymer hydrogels for therapeutic delivery", *Experimental Biology and Medicine*, vol. 241, no. 9, pp. 972–979, 2016.

- [75] J. Rao and A. Khan, "Enzyme sensitive synthetic polymer micelles based on the azobenzene motif", *Journal of the American Chemical Society*, vol. 135, no. 38, pp. 14056–14059, 2013.
- [76] A.J. Harnoy, M. Buzhor, E. Tirosh, R. Shaharabani, R. Beck and R.J. Amir, "Modular Synthetic Approach for Adjusting the Disassembly Rates of Enzyme-Responsive Polymeric Micelles", *Biomacromolecules*, vol. 18, no. 4, pp. 1218–1228, 2017.
- [77] H.R. Culver, J.R. Clegg and N.A. Peppas, "Analyte-Responsive Hydrogels: Intelligent Materials for Biosensing and Drug Delivery", *Accounts of Chemical Research*, vol. 50, no. 2, pp. 170–178, 2017.
- [78] S. Chu, S.L. Sridhar, U. Akalp, S.C. Skaalure, F.J. Vernerey and S.J. Bryant, "Understanding the Spatiotemporal Degradation Behavior of Aggrecanase-Sensitive Poly(ethylene glycol) Hydrogels for use in Cartilage Tissue Engineering", *Tissue Engineering Part A*, vol. 23, pp. 795-810, 2017.
- [79] J.A. Sanz-Herrera, L. Soria, E. Reina-Romo, Y. Torres and A.R. Boccaccini, "Model of dissolution in the framework of tissue engineering and drug delivery", *Biomechanics and Modeling in Mechanobiology*, vol. 17, no. 5, pp. 1331-1341, 2018.
- [80] K. Bauri, M. Nandi and P. De, "Amino acid-derived stimuli-responsive polymers and their applications", *Polymer Chemistry*, vol. 9, no. 11, pp. 1257–1287, 2018.
- [81] M. Karimi *et al.*, "Smart micro/nanoparticles in stimulus-responsive drug/gene delivery systems", *Chemical Society Reviews*, vol. 45, no. 5, pp. 1457-1501, 2016.
- [82] G. Sharifzadeh and H. Hosseinkhani, "Biomolecule-Responsive Hydrogels in Medicine", *Advanced Healthcare Materials*, vol. 6, no. 24, pp. 1–35, 2017.
- [83] Y.J. Kim and Y.T. Matsunaga, "Thermo-responsive polymers and their application as smart biomaterials", *Journal of Materials Chemistry B*, vol. 5, no. 23, pp. 4307–4321, 2017.
- [84] X. Tu *et al.*, "Synthesis and phase transition of poly(N-isopropylacrylamide)-based thermo-sensitive cyclic brush polymer", *Polymers (Basel)*, vol. 9, no. 7, pp. 301 1-13, 2017.
- [85] T. Lorson *et al.*, "Poly(2-oxazoline)s based biomaterials: A comprehensive and critical update", *Biomaterials*, vol. 178, pp. 204–280, 2018.
- [86] L.L. Li, R.Y. Jiang, J.X. Chen, M.Z. Wang and X.W. Ge, "One-step synthesis of self-healable hydrogels by the spontaneous phase separation of linear multi-block copolymers during the emulsion copolymerization", *Chinese Chemical Letters*, vol. 28, no. 4, pp. 868–874, 2017.
- [87] S.M. Modarresi-Saryazdi, V. Haddadi-Asl and M. Salami-Kalajahi, "N,N'-methylenebis(acrylamide)-crosslinked poly(acrylic acid) particles as doxorubicin carriers: A comparison between release behavior of physically loaded drug and conjugated drug via acid-labile hydrazone linkage", *Journal of Biomedical Materials Research*, vol. 106, no. 2, pp. 342-348, 2017.
- [88] M. Behl and A. Lendlein, "Shape-memory polymers", *Materials Today*, vol. 10, no. 4, pp. 20–28, 2007.
- [89] K.E. Smith, M. Garcia, K.M. Dupont, G.B. Higgs, K. Gall and D.L. Safranski, "Shape-memory Polymers for Orthopaedic Soft-Tissue Repair", *Techniques in Orthopaedics*, vol. 32, no. 3, pp. 141–148, 2017.



- [90] X. Zhang, M.A. Geven, D.W. Grijpma, T. Peijs and J.E. Gautrot, "Tunable and processable shape memory composites based on degradable polymers", *Polymer UK*, vol. 122, pp. 323–331, 2017.
- [91] A. Biswas, A.P. Singh, D. Rana, V.K. Aswal and P. Maiti, "Biodegradable toughened nanohybrid shape memory polymer for smart biomedical applications", *Nanoscale*, vol. 10, no. 21, pp. 9917–9934, 2018.
- [92] B. Jin, H. Song, R. Jiang, J. Song, Q. Zhao and T. Xie, "Programming a crystalline shape memory polymer network with thermo- and photo-reversible bonds toward a single-component soft robot", *Science Advances*, vol. 4, no. 1, 2018.
- [93] R. Liu *et al.*, "Shape Memory Polymers for Body Motion Energy Harvesting and Self-Powered Mechanosensing", *Advanced Materials*, vol. 30, no. 8, pp. 1–8, 2018.
- [94] H. Sogawa, K. Terada, T. Masuda and F. Sanda, "Synthesis and properties of amino acid-derived optically active photo-responsive polymers", *Polymer Bulletin*, vol. 63, no. 6, pp. 803–813, 2009.
- [95] E. Burakowska, S.C. Zimmerman and R. Haag, "Photoresponsive crosslinked hyperbranched polyglycerols as smart nanocarriers for guest binding and controlled release", *Small*, vol. 5, no. 19, pp. 2199–2204, 2009.
- [96] T. Ikehara, M. Tanaka, S. Shimada and H. Matsuda, "Optically driven actuator using photo-induced phase-transition polymer", *Sensors Actuators A: Physical*, vol. 96, no. 2–3, pp. 239–243, 2002.
- [97] O. Bertrand and J.F. Gohy, "Photo-responsive polymers: synthesis and applications", *Polymer Chemistry*, vol. 8, no. 1, pp. 52–73, 2017.
- [98] L. Ricotti and T. Fujie, "Thin polymeric films for building biohybrid microrobots", *Bioinspiration and Biomimetics*, vol. 12, no. 2, 2017.
- [99] Y. Bar-Cohen, "Electroactive polymers: current capabilities and challenges", *Smart Structures and Materials*, vol. 4695, pp. 1–7, 2002.
- [100] J Kwang and S. Tadokoro, "Electroactive Polymers for Robotic Applications", Ed. Springer Verlag London, London, UK, 2007.
- [101] Y. Bar-Cohen, K.J. Kim, H.R. Choi and J.D.W. Madden, "Electroactive polymer materials", *Smart Materials and Structures*, vol. 16, no. 2, 2007.
- [102] M. Yoonessi *et al.*, "Transparent large strain thermoplastic polyurethane magneto-active nanocomposites", *ACS Applied Materials & Interfaces*, vol. 7, no. 3, pp. 2686–2693, 2011.
- [103] M. Królewicz and J. Kaleta, "Influence of filler particle distribution on the magnetorheological effect in magnetoactive elastomers", *Proceedings of the 7th International Conference on Mechanics and Materials in Design*, Albufeira, Portugal, 2016, pp. 633–634.
- [104] M. Yoonessi *et al.*, "High-temperature multifunctional magnetoactive nickel graphene polyimide nanocomposites", *Polymer UK*, vol. 54, no. 11, pp. 2776–2784, 2013.
- [105] H. Meng and J. Hu, "A brief review of stimulus-active polymers responsive to thermal, light, magnetic, electric, and water/solvent stimuli", *Journal of Intelligent Material System and Structures*, vol. 21, no. 9, pp. 859–885, 2010.

- [106] M.A. Rafique, E. Kandare and S. Sprenger, "Fiber-reinforced magneto-polymer matrix composites (FR-MPMCs) - A review", *Journal of Materials Research*, vol. 32, no. 6, pp. 1020–1046, 2017.
- [107] V.Q. Nguyen, A.S. Ahmed and R.V. Ramanujan, "Morphing soft magnetic composites", *Advanced Materials*, vol. 24, no. 30, pp. 4041–4054, 2012.
- [108] A. Tayefeh, M. Wiesner, S.A. Mousavi and R. Poursalehi, "Modeling magneto-mechanical behavior of Fe<sub>3</sub>O<sub>4</sub> nanoparticle/polyamide nanocomposite membrane in an external magnetic field", *Journal of Composite Material*, vol. 52, no. 11, 2018.
- [109] D.J. Griffiths, "Introduction to Electrodynamics", Ed. Prentice Hall, Boston, USA, 2017.
- [110] K. Trommer, C. Petzold and B. Morgenstern, "Thin polymer layers with superparamagnetic properties", *Journal of Polymers*, vol. 2015, pp. 1-9, 2015.
- [111] W.D. Callister, "Materials Science and Engineering: An introduction", Ed. John Wiley and Sons, New York, USA, 2001.
- [112] M. Rahbar, "Design, Fabrication and Testing of Magnetic Composite Polymer Actuators Integrated With Microfluidic Devices and Systems", Ph.D. thesis, Simon Fraser University, Canada, 2016.
- [113] A.J. Rondinone, A.C.S. Samia and Z.J. Zhang, "Superparamagnetic relaxation and magnetic anisotropy energy distribution in CoFe<sub>2</sub>O<sub>4</sub> spinel ferrite nanocrystallites", *Journal of Physical Chemistry B*, vol. 103, no. 33, pp. 6876–6880, 1999.
- [114] P. Zajc, J. Kaleta, D. Lewandowski and A. Gasperowicz, "Isotropic magnetorheological elastomers with thermoplastic matrices: Structure, damping properties and testing", *Smart Materials and Structures*, vol. 19, no. 4, 2010.
- [115] K. Kobayashi and K. Ikuta, "Three-dimensional magnetic microstructures fabricated by microstereolithography", *Applied Physics Letters*, vol. 92, no. 26, pp. 2012–2015, 2008.
- [116] A.H. Lu, E.L. Salabas and F. Schüth, "Magnetic nanoparticles: Synthesis, protection, functionalization, and application", *Angewandte Chemie International Edition*, vol. 46, no. 8, pp. 1222–1244, 2007.
- [117] Y. Han, W. Hong and L. E. Faidley, "Rate dependent finite deformation of magneto-active polymers", *Proceedings of the International Society for Optical Engineering (SPIE)*, vol. 7978, pp. 797819 1–11, 2011.
- [118] J.M. Ginder, S. M. Clark, W.F. Schlotter and M.E. Nichols, "Plunger nonferrous ring MR elastomer", *International Journal of Modern Physics B*, vol. 16, no. 17–18, pp. 2412–2418, 2002.
- [119] H. Vatandoost, M. Norouzi, S.M.S. Alehashem and S.K. Smoukov, "A novel phenomenological model for dynamic behavior of magnetorheological elastomers in tension-compression mode", *Smart Materials and Structures*, vol. 26, no. 6, 2017.
- [120] Q. Liu, H. Li and K.Y. Lam, "Transition of magnetic field due to geometry of magneto-active elastomer microactuator with nonlinear deformation", *Journal of Microelectromechanical Systems*, vol. 27, no. 2, pp. 127–136, 2018.
- [121] V.M. Kalita, A.A. Snarskii, D. Zorinets and M. Shamonin, "Single-particle mechanism of magnetostriction in magnetoactive elastomers", *Physical Review E*, vol. 93, no. 6, pp. 1–7, 2016.

- [122] A.M. Biller, O.V. Stolbov and Y.L. Raikher, "Modeling of particle interactions in magnetorheological elastomers", *Journal of Applied Physics*, vol. 116, no. 11, pp. 114901 1-8, 2014.
- [123] M.R. Jolly, J.D. Carlson and B.C. Munoz, "A model of the behavior of magnetorheological materials", *Smart Materials and Structures*, vol. 5, no. 5, pp. 607–614, 1996.
- [124] G.V. Stepanov, D.Y. Borin, Y.L. Raikher, P.V. Melenev and N.S. Perov, "Motion of ferroparticles inside the polymeric matrix in magnetoactive elastomers", *Journal of Physics: Condensed Matter*, vol. 20, no. 20, pp. 1-6, 2008.
- [125] I. Agirre-Olabide, A. Lion and M.J. Elejabarrieta, "A new three-dimensional magneto-viscoelastic model for isotropic magnetorheological elastomers", *Smart Materials and Structures*, vol. 26, no. 3, pp. 1–10, 2017.
- [126] R. Sheridan, J. Roche, S.E. Lofland and P.R. Vonlockette, "Numerical simulation and experimental validation of the large deformation bending and folding behavior of magneto-active elastomer composites", *Smart Materials and Structures*, vol. 23, no. 9, pp. 1-14, 2014.
- [127] A.A. Amiri Moghadam, W. Hong, A. Kouzani, A. Kaynak, R. Zamani and R. Montazami, "Nonlinear dynamic modeling of ionic polymer conductive network composite actuators using rigid finite element method", *Sensors and Actuators A: Physical*, vol. 217, pp. 168–182, 2014.
- [128] S. Lee, H.C. Park and K.J. Kim, "Equivalent modeling for ionic polymer - metal composite actuators based on beam theories", *Smart Materials and Structures*, vol. 14, no. 6, pp. 1363–1368, 2005.
- [129] V. De Luca *et al.*, "Ionic electroactive polymer metal composites: Fabricating, modeling, and applications of postsilicon smart devices", *Journal of Polymer Science Part B: Polymer Physics*, vol. 51, no. 9, pp. 699–734, 2013.
- [130] G. Alici, "An effective modelling approach to estimate nonlinear bending behaviour of cantilever type conducting polymer actuators", *Sensors and Actuators B: Chemical*, vol. 141, no. 1, pp. 284–292, 2009.
- [131] R. Mutlu, G. Alici, X. Xiang and W. Li, "Electro-mechanical modelling and identification of electroactive polymer actuators as smart robotic manipulators", *Mechatronics*, vol. 24, no. 3, pp. 241–251, 2014.
- [132] P. Du, X. Lin and X. Zhang, "A multilayer bending model for conducting polymer actuators", *Sensors and Actuators A: Physical*, vol. 163, no. 1, pp. 240–246, 2010.
- [133] C.H. Nguyen, G. Alici and G. Wallace, "An advanced mathematical model and its experimental verification for trilayer conjugated polymer actuators", *IEEE/ASME Transactions on Mechatronics*, vol. 19, no. 4, pp. 1279–1288, 2014.
- [134] T. Safwat, R. Tosto, M.D. Grissom and C.D. Rahn, "A dynamic model of electrostrictive unimorph actuators for haptic devices", *Proceedings ASME Design Engineering Technical Conference*, vol. 3, pp. 1–9, 2016.
- [135] J. Zha *et al.*, "Superparamagnetic polyimide/ $\gamma$ -Fe<sub>2</sub>O<sub>3</sub> nanocomposite films: Preparation and characterization", *Thin Solid Films*, vol. 516, no. 18, pp. 6315–6320, 2008.

- [136] J. Zhou, R. Li and S. Liu, "Structure and magnetic properties of regenerated cellulose/Fe<sub>3</sub>O<sub>4</sub> nanocomposite films", *Polymer Composites*, vol. 21, no. 7, pp. 449–456, 2013.
- [137] O.S. Rodríguez-Fernández, C.A. Rodríguez-Calzadía, I.G. Yáñez-Flores and S.M. Montemayor, "Preparation and characterization of a magneto-polymeric nanocomposite: Fe<sub>3</sub>O<sub>4</sub> nanoparticles in a grafted, cross-linked and plasticized poly(vinyl chloride) matrix", *Journal of Magnetism and Magnetic Materials*, vol. 320, no. 14, pp. e81-e84, 2008.
- [138] N. Sanaeifar, M. Rabiee, M. Abdolrahim and A. H. Monfared, "A novel glucose biosensor based on immobilization of glucose oxidase in iron oxide nanoparticles/poly(vinyl alcohol) nanocomposite film", in *23rd Iranian Conference on Biomedical Engineering ICBME*, Theran, Iran, 2017.
- [139] C.J. Brinker, "Dip coating", in *Chemical Solution Deposition of Functional Oxide Thin Films*, Ed. Springer, 2013, pp. 233–261.
- [140] L. Wu, J. Zhang, B. Li and A. Wang, "Magnetically driven super durable superhydrophobic polyester materials for oil/water separation", *Polymer Chemistry*, vol. 5, no. 7, pp. 2382–2390, 2014.
- [141] C. Suchomski, C. Reitz, D. Pajic, Z. Jaglicic, I. Djerdj and T. Brezesinski, "Large-pore mesoporous Ho<sub>3</sub>Fe<sub>5</sub>O<sub>12</sub> thin films with a strong room-temperature perpendicular magnetic anisotropy by sol-gel processing", *Chemistry of Materials*, vol. 26, no. 7, pp. 2337–2343, 2014.
- [142] V. Iacovacci *et al.*, "Polydimethylsiloxane films doped with NdFeB powder: magnetic characterization and potential applications in biomedical engineering and microrobotics", *Biomedical Microdevices*, vol. 17, no. 6, pp. 1–7, 2015.
- [143] A. Kumar and K.L. Yadav, "Magnetic, local ferroelectricity and magnetodielectric properties of NiFe<sub>2</sub>O<sub>4</sub>-poly(vinylidene-fluoride)-BaTiO<sub>3</sub> composite film", *Materials Research Express*, vol. 3, no. 4, pp. 1–5, 2016.
- [144] J. Rani, K.L. Yadav and S. Prakash, "Structural and magnetodielectric properties of poly(vinylidene fluoride)-[ 0.8(Bi<sub>0.5</sub>Na<sub>0.5</sub>)TiO<sub>3</sub>-0.2CoFe<sub>2</sub>O<sub>4</sub>] polymer composite films", *Composites Part B: Engineering*, vol. 79, pp. 138–143, 2015.
- [145] F. Ridi, M. Bonini and P. Baglioni, "Magneto-responsive nanocomposites: Preparation and integration of magnetic nanoparticles into films, capsules, and gels", *Advances in Colloid Interface Science*, vol. 207, no. 1, pp. 3–13, 2014.
- [146] J. Kim, S.E. Chung, S.-E. Choi, H. Lee, J. Kim and S. Kwon, "Programming magnetic anisotropy in polymeric microactuators", *Nature Materials*, vol. 10, pp. 747, 2011.
- [147] J. Feng, S. Xuan, L. Ding and X. Gong, "Magnetoactive elastomer/PVDF composite film based magnetically controllable actuator with real-time deformation feedback property", *Composites Part A: Applied Science and Manufacturing*, vol. 103, pp. 25–34, 2017.
- [148] A.K. Dhaliwal and J.N. Hay, "The characterization of polyvinyl butyral by thermal analysis", *Thermochimica Acta*, vol. 391, no. 1–2, pp. 245–255, 2002.
- [149] T.S. Valera and N.R. Demarquette, "Polymer toughening using residue of recycled windshields: PVB film as impact modifier", *European Polymer Journal*, vol. 44, no. 3, pp. 755–768, 2008.

- [150] M. Sônego, L.C. Costa and J.D. Ambrósio, "Flexible thermoplastic composite of Polyvinyl Butyral (PVB) and waste of rigid Polyurethane foam", *Polímeros*, vol. 25, no. 2, pp. 175–180, 2015.
- [151] X. Zhang, H. Hao, Y. Shi and J. Cui, "The mechanical properties of Polyvinyl Butyral (PVB) at high strain rates", *Construction and Building Materials*, vol. 93, pp. 404–415, 2015.
- [152] E. Cascone *et al.*, "Blends of polypropylene with poly(vinyl butyral)", *Journal of Applied Polymer Science*, vol. 82, no. 12, pp. 2934–2946, 2001.
- [153] D. Posavec, A. Dorsch, U. Bogner, G. Bernhardt and S. Nagl, "Polyvinyl butyral nanobeads: Preparation, characterization, biocompatibility and cancer cell uptake", *Microchimica Acta*, vol. 173, no. 3–4, pp. 391–399, 2011.
- [154] J. Puente-Córdova, "Síntesis y caracterización del comportamiento eléctrico de materiales híbridos magnéticos", Ph.D. thesis, Universidad Autónoma de Nuevo León, México, 2017.
- [155] Z. Guo, D. Zhang, S. Wei, Z. Wang and A.B. Karki, "Effects of iron oxide nanoparticles on polyvinyl alcohol: interfacial layer and bulk nanocomposites thin film", *Journal of Nanoparticle Research*, vol. 12, no. 7, pp. 2415–2426, 2010.
- [156] A.S. Teja and P.Y. Koh, "Synthesis, properties, and applications of magnetic iron oxide nanoparticles", *Progress in Crystal Growth and Characterization of Materials*, vol. 55, no. 1–2, pp. 22–45, 2009.
- [157] M. Rahman, S. Bahadar Khan, A. Jamal and M. Faisal, "Iron oxide nanoparticles", *IntechOpen*, vol. 2, pp. 64, 2018.
- [158] S. Laurent *et al.*, "Magnetic Iron Oxide Nanoparticles: Synthesis, Stabilization, Vectorization, Physicochemical Characterizations, and Biological Applications", *Chemical Reviews*, vol. 108, no. 6, pp. 2064–2110, 2008.
- [159] W. Wu, Z. Wu, T. Yu and C. Jiang, "Recent progress on magnetic iron oxide nanoparticles: synthesis, surface functional strategies and biomedical applications", *Science and Technology of Advanced Materials*, vol. 16, pp. 023501 1-43, 2015.
- [160] B.J. Park, J.L. You, H.J. Choi, S.Y. Park and B.Y. Lee, "Synthesis and magnetorheological characterization of magnetite nanoparticle and poly(vinyl butyral) composite", *IEEE Transaction on Magnetics*, vol. 45, no. 6, pp. 2460–2463, 2009.
- [161] H. Akil and M.H. Zamri, "Performance of natural fiber composites under dynamic loading", in *Natural Fibre Composites* Woodhead Publishing, UK, 2014, pp. 323–344.
- [162] W.M. Groenewoud, "Dynamic Mechanical Analysis", in *Characterisation of Polymers by Thermal Analysis*, Ed. Elsevier Science B.V., Amsterdam, 2001, pp. 94–122.
- [163] T. Eliades, S. Zinelis, D.-G. Kim and W. Brantley, "Structure/property relationships in orthodontic polymers", in *Orthodontic Applications of Biomaterials*, Ed. Woodhead Publishing, 2017, pp. 39–59.
- [164] S. Sinha Ray, "Electrical and thermal conductivity of environmentally friendly polymer nanocomposites (EFPNCs) using biodegradable polymer matrices and clay/carbon nanotube (CNT) reinforcements", *Environmentally Friendly Polymer Nanocomposites*, pp. 450–464, 2013.

- [165] S. Ebnesajjad and P.R. Khaladkar, "Failure Analysis", Fluoropolymer Applications in the Chemical Processing Industries, Ed. Elsevier, 2004, pp. 315–357.
- [166] J. Jordan, K.I. Jacob, R. Tannenbaum, M.A. Sharaf and I. Jasiuk, "Experimental trends in polymer nanocomposites — a review", Materials Science and Engineering, vol. 393, no. 1-2, pp. 1–11, 2005.
- [167] L.W. McKeen, "Introduction to Plastics and Polymers", in Permeability Properties of Plastics and Elastomers, Ed. Elsevier, 2016, pp. 21–37.
- [168] X. Ma, Y. Zare and K.Y. Rhee, "A Two-Step Methodology to Study the Influence of Aggregation / Agglomeration of Nanoparticles on Young's Modulus of Polymer Nanocomposites", Nanoscale Research Letters, vol. 12, no. 621, pp. 0–6, 2017.
- [169] S.L. Gómez-Flores, B. López-Walle, E. Reyes-Melo, "Optical and Magnetic Properties of Hybrid Films Composed by Polyvinyl Butyral and Iron Oxide Nanoparticles Synthetized in-situ (PVB/Fe<sub>2</sub>O<sub>3</sub>)", in Proceedings of International Conference and Exhibition on Advanced and Nanomaterials ICANM, Quebec, Canada, 2018, pp. 1-11.
- [170] N. Zhu *et al.*, "Surface Modification of Magnetic Iron Oxide Nanoparticles", Nanomaterials, vol. 8, no. 810, pp. 1–27, 2018.
- [171] J. Yi, M.C. Boyce, G.F. Lee and E. Balizer, "Large deformation rate-dependent stress – strain behavior of polyurea and polyurethanes", Polymer, vol. 47, no. 1, pp. 319–329, 2006.
- [172] L.A. Pothan, Z. Oommen and S. Thomas, "Dynamic mechanical analysis of banana fiber reinforced polyester composites", Composite Science and Technology, vol. 63, no. 2, pp. 283–293, 2003.
- [173] D.J. Griffiths, "Introduction to Electrodynamics", Ed. Prentice Hall, Boston, USA, 1999
- [174] S.A. Hussain-Shah, "Vibrating Sample Magnetometry: Analysis and Construction", Ph.D. Thesis, Syed Babar Ali School of Science and Engineering, Pakistan, 2013.
- [175] T. Thomson, "Magnetic Properties of Metallic Thin Films", in Metallic Films for Electronic, Optical and Magnetic Applications, Ed. Elsevier, New Delhi, India, 2014, pp. 454-546.
- [176] T. Thirugnanasambandan and M. Alagar, "Chem inform abstract: innovation of superparamagnetism in lead nanoparticles innovation of superparamagnetism in lead nanoparticles", Physics and Technical Science, vol. 1, no. 3, pp. 39-45, 2013.
- [177] P. Macioce, "Viscoelastic Damping 101", Sound and Vibration, vol. 37, no. 4, pp. 10, 2003.
- [178] H.H. Law, P.L. Rossiter, L.L. Koss and G.P. Simon, "Mechanisms in damping of mechanical vibration by piezoelectric ceramic-polymer composite materials", Journal of Materials Science, vol. 30, no. 10, pp. 2648–2655, 1995.
- [179] X. Zhou, Y. Sun, Y. Jiang, Y. Liu and G. Zhao, "Effect of magnetic nanoparticles on damping property of nature rubber", Polymer Bulletin, vol. 66, no. 9, pp. 1281–1288, 2011.
- [180] E.I. Rivin and B. Balachandran, "Stiffness and Damping in Mechanical Design", Ed. Marcel Dekker Inc., New York, USA, 2000.

- [181] J. Zou and G. Gu, "Modeling the viscoelastic hysteresis of dielectric elastomer actuators with a modified rate-dependent Prandtl-Ishlinskii model", *Polymers (Basel)*, vol. 10, no. 5, pp. 1–12, 2018.
- [182] E. Reyes-Melo, J. Martinez-Vega, C. Guerrero-Salazar and U. Ortiz-Mendez, "Application of fractional calculus to the modeling of dielectric relaxation phenomena in polymeric materials", *Journal of Applied Polymer Science*, vol. 98, no. 2, pp. 923–935, 2005.
- [183] P. Frübing, D. Blischke, R. Gerhard-Multhaupt and M. Salah Khalil, "Complete relaxation map of polyethylene: filler-induced chemical modifications as dielectric probes", *Journal of Physics D: Applied Physics*, vol. 34, no. 20, pp. 3051–3057, 2001.
- [184] G. Concas, F. Congiu, G. Muscas and D. Peddis, "Determination of blocking temperature in magnetization and mössbauer time scale: a functional form approach", *Journal of Physical Chemistry C*, vol. 121, no. 30, pp. 16541–16548, 2017.
- [185] M. Llamas-Hernández, B. López-Walle, M. Rakotondrabe and E. Reyes-Melo, "Dynamic behavior of magnetic hybrid films of polyvinyl butyral/iron oxide nanoparticles (PVB/Fe<sub>2</sub>O<sub>3</sub>) for their control as microactuators", *Physica B: Condensed Matter*, vol. 549, pp. 113-117, 2017.
- [186] M. Al Janaideh, S. Rakheja and C.Y. Su, "Experimental characterization and modeling of rate-dependent hysteresis of a piezoceramic actuator", *Mechatronics*, vol. 19, no. 5, pp. 656–670, 2009.
- [187] A. York, J. Dunn and S. Seelecke, "Experimental characterization of the hysteretic and rate-dependent electromechanical behavior of dielectric electro-active polymer actuators", *Smart Materials and Structures*, vol. 19, no. 9, pp. 1-9, 2010.
- [188] F. Fujii, K. Tatebatake, K. Morita and T. Shiinoki, "A Bouc–Wen model-based compensation of the frequency-dependent hysteresis of a piezoelectric actuator exhibiting odd harmonic oscillation", *Actuators*, vol. 7, no. 3, pp. 37, 2018.
- [189] G.T. Landi, "Influence of the magnetization damping on dynamic hysteresis loops in single domain particles", *Journal of Applied Physics*, vol. 111, no. 4, pp. 043901 1-13, 2012.
- [190] S. Ozer, H. Zorlu and S. Mete, "System identification application using Hammerstein model", *Sadhana – Academy Proceedings in Engineering Science*, vol. 41, no. 6, pp. 597–605, 2016.
- [191] R.J. Herrick, "DC/AC Circuits and Electronics: Principles & Applications", Ed. Thomson/Delmar Learning, New York, USA, 2003.
- [192] D.G. Fertis, "Nonlinear Structural Engineering: With Unique Theories and Methods to Solve Effectively Complex Nonlinear Problems", Ed. Springer Berlin Heidelberg, Berlin, Germany, 2007.
- [193] B.K. Sarkar, "Strength of Materials", Ed. McGraw-Hill Education, New Delhi, India, 2003.
- [194] J. Humar, "Dynamics of Structures", Ed. CRC Press, London, UK, 2012.
- [195] D. Chinarro, "System Engineering Applied to Fuenmayor Karst Aquifer (San Julián de Banzo, Huesca) and Collins Glacier (King George Island, Antarctica)", Ph.D. thesis, Universidad de Zaragoza, Spain, 2014.
- [196] J. Bird, "Electrical and Electronic Principles and Technology", Ed. Routledge Taylor and Francis Group, New York, USA, 2010.

[197] S.S. Shevkoplyas, A.C. Siegel, R.M. Westervelt, G. Prentiss and G.M. Whitesides, "The force acting on a superparamagnetic bead due to an applied magnetic field", *Lab on a Chip*, vol. 7, pp. 1294–1302, 2007.

[198] S. Rachad, B. Nsiri and B. Bensassi, "System Identification of Inventory System Using ARX and ARMAX Models", *International Journal of Control and Automation*, vol. 8, no. 12, pp. 283–294, 2015.



# Appendix 1

## List of parameters abbreviations

### *Electric circuit block*

$i$	Electrical current
$u$	Input voltage
$u_R$	Voltage in the resistance
$u_L$	Voltage in the inductance
$L$	Inductance of the electromagnet
$R$	Resistance of the electromagnet
$t$	Time
$i_0$	Initial current (at $t = 0$ )
$\tau$	Constant time

### *Electromagnet block*

$B_{loop}$	Magnetic field generated by one loop of copper wire
$r_e$	Radius of one loop
$P$	Randomly taken point on the $z$ -axis used for magnetic analysis
$B_s$	Magnetic field generated by a solenoid of one layer of copper wire loops
$z'$	Random position on the $z$ -axis
$B$	Magnetic field supplied by the electromagnet
$\mu_0$	Magnetic permeability of vacuum
$\mu_r$	Relative magnetic permeability of the iron core
$N$	Number of turns of copper wire of the electromagnet
$r_{e2}$	External radius of the electromagnet
$r_{e1}$	Internal radius of the electromagnet
$l_e$	Length of the electromagnet
$z$	Distance from the reference origin to a point on the $z$ -axis

$I_{std}$  Standard integral form to solve an integral equation

*Cantilever magnetization block*

$F$  Magnetic force

$\mu_z$  Magnetic moment of a magnetic dipole on the z-axis

$M_m$  Magnetization of the microactuator

$M_0$  Initial magnetization of the microactuator

$\chi_m$  Magnetic susceptibility of the magnetic material

$m$  Mass of the microactuator

*Nonlinear static displacement block*

$r$  Radius of the curvature of the deformed microactuator

$\theta$  Angular deformation (slope) at any point along the microactuator

$x_a$  Arc length of the microactuator from the origin to any point along x-axis

$M_b$  Bending moment of the microactuator

$E$  Elastic modulus of the microactuator

$I$  Cross-sectional moment of inertia

$\theta_D$  Angular deformation (slope) at the free end of the microactuator

$x_0$  Arc length of the deformed microactuator from the origin to the free end of the microactuator

$\delta_z$  Displacement on the z-axis at any point  $x$  along the microactuator

$p$  Change of variable to simplify the notation of  $\delta_z'$

$p'$  Change of variable to simplify the notation of  $\delta_z''$

$\lambda$  Change of variable to simplify the notation of  $\frac{Fx}{EI}$

$\varphi$  Result of the integration of  $\lambda(x)$

$\Delta$  Horizontal displacement at the free end of the microactuator

$x$  Distance from the origin to a point on the x-axis

$l_0$  Projected length on the x-axis of the arc formed by the microactuator in its deformed state

$G$	Change of variable to simplify the notation $\frac{F}{2EI}[x^2 - (l_0)^2]$
$M_e$	Equivalent moment. Change of variable to simplify the notation $[1 + (\delta_z')^2]^{3/2} M$
$\delta_D^{static}$	Nonlinear static displacement at the free end of the microactuator
$\bar{x}$	Centroid of the equivalent moment diagram ( $M_e$ diagram) on the $x$ -axis
$W$	Width of the microactuator
$T$	Thickness of the microactuator
$l_b$	Length of the microactuator

*Linear dynamics displacement block*

$\delta_D^{dynamic}$	Displacement at the free end of the microactuator. The displacement here includes the steady-state and the dynamics or transient parts
$g$	Gain of the dynamic system
$t - \tau_i$	Lag between the input and the output of a dynamic system
$\Delta_D^{dynamic}(s)$	Laplace transform of $\delta_D^{dynamic}(t)$
$G(s)$	Laplace transform of $g(t)$
$\Delta_D^{static}(s)$	Laplace transform of $\delta_D^{static}(t)$
$b_n$	Coefficients of the numerator in the transfer function
$a_d$	Coefficients of the denominator in the transfer function
$n$	Order of the numerator in the transfer function
$d$	Order of the denominator in the transfer function
$G_T(Z)$	Discrete transfer function equivalent to the transfer function $G(s)$
$\Delta_D^{dynamic}(Z)$	Discrete time form of $\Delta_D^{dynamic}(s)$
$\Delta_D^{static}(Z)$	Discrete time form of $\Delta_D^{static}(s)$

# Appendix 2

## Parameter values

### *Electric circuit block*

<b>Symbol</b>	<b>Value</b>	<b>Units</b>
$L$	1.21	<i>Henry (H)</i>
$R$	42	Ohm ( $\Omega$ )
$\tau$	0.028	<i>seconds (s)</i>
$i_0$	0	<i>Amperes (A)</i>

### *Electromagnet block*

<b>Symbol</b>	<b>Value</b>	<b>Units</b>
$\mu_0$	$4\pi \times 10^{-7}$	<i>H/m</i>
$\mu_r$	20	<i>Unitless</i>
$N$	320	<i>Unitless</i>
$r_{e2}$	0.014	<i>m</i>
$r_{e1}$	0.007	<i>m</i>
$l_e$	0.024	<i>m</i>
$z$	0.014 (at the starting point)	<i>m</i>

*Magnetization block*

<b>Symbol</b>	<b>Value</b>	<b>Units</b>
$M_0$	0	$Am^2/kg$
$\chi_m$	0.006 Sample: PVB/Fe <sub>2</sub> O <sub>3</sub> _14% Fe	$m^3/kg$
$m_1$	$1.2 \times 10^{-6}$ Sample: PVB/Fe <sub>2</sub> O <sub>3</sub> _14% Fe Geometry: 15 mm length, 2 mm width, 0.018 mm thickness	$kg$
$m_2$	$1.2 \times 10^{-6}$ Sample: PVB/Fe <sub>2</sub> O <sub>3</sub> _14% Fe Geometry: 15 mm length, 4 mm width, 0.018 mm thickness	$kg$

*Displacement (nonlinear static analysis) block*

<b>Symbol</b>	<b>Value</b>	<b>Units</b>
$l_b$	0.015	$m$
$T$	0.002 and 0.004	$m$
$W$	0.018	$m$
$E$	$3.9 \times 10^9$ Sample: PVB/Fe <sub>2</sub> O <sub>3</sub> _14% Fe	$Pa$

*Displacement (linear dynamic analysis) block*

For the continuous time transfer function

<b>Symbol</b>	<b>Value</b>	<b>Units</b>
$b_0$	25.11	<i>Unitless</i>
$b_1$	$-2.387 \times 10^7$	<i>Unitless</i>
$b_2$	$1.657 \times 10^9$	<i>Unitless</i>
$b_3$	$2.469 \times 10^{11}$	<i>Unitless</i>
$b_4$	$6.98 \times 10^7$	<i>Unitless</i>
$a_0$	1	<i>Unitless</i>
$a_1$	489.3	<i>Unitless</i>
$a_2$	$9.956 \times 10^6$	<i>Unitless</i>
$a_3$	$1.236 \times 10^9$	<i>Unitless</i>
$a_4$	$7.85 \times 10^{10}$	<i>Unitless</i>
$a_5$	$6.529 \times 10^{12}$	<i>Unitless</i>
$n$	4	<i>Unitless</i>
$d$	5	<i>Unitless</i>

# Appendix 3

## Identification of transfer function parameters

The identification of parameters for the transfer function that describes the dynamic displacement of the microactuator was conducted by using the “System Identification Toolbox” of MATLAB®. These parameters correspond to the coefficients of such transfer function. The transfer function will approximate the behavior between the input and the output of the block shown in Figure A3. 1. This block is the last one of the overall block-structured model proposed in chapter 4. At this step, the modeling method is considered as a black box model, which ignores physical parameters. The interface of the system identification toolbox of MATLAB is displayed in Figure A3. 2. This interface appears when the MATLAB ident command is executed.

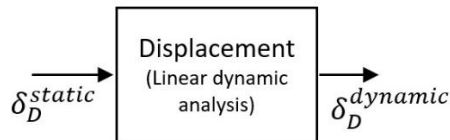


Figure A3. 1. Last block of the overall block-structured model representing the linear dynamics and proposed in chapter 4.

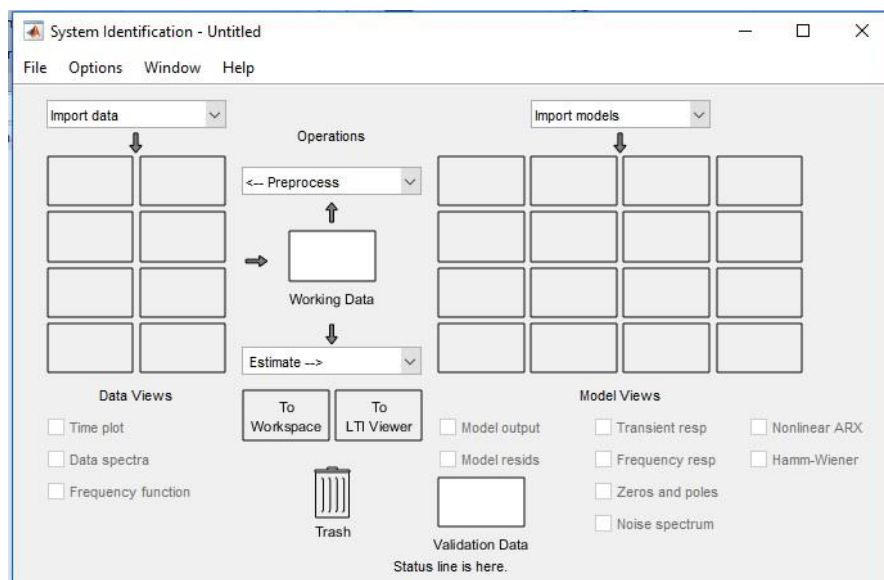


Figure A3. 2. Interface of the System Identification Toolbox of MATLAB.

The principle of the parameters identification for a transfer function is to extract a mathematical model guided by experimental data. Therefore, the first step is the selection of one experimental result in order to use it as reference. In this case, the chosen experimental result corresponds to the condition when 30 V of a step voltage is applied to the PVB/Fe<sub>2</sub>O<sub>3</sub>\_14%wt Fe microactuator with dimensions of 15 mm in length, 2 mm in width and 0.018 mm in thickness. This experimental result will be the output of the block in Figure A3. 1, corresponding to  $\delta_D^{dynamic}$ . After that, the theoretical nonlinear static displacement  $\delta_D^{static}$  is also computed for the same condition.

Next, the theoretical  $\delta_D^{static}$  and the experimental  $\delta_D^{dynamic}$  are imported to the system identification toolbox in the time domain, as shown in Figure A3. 3.

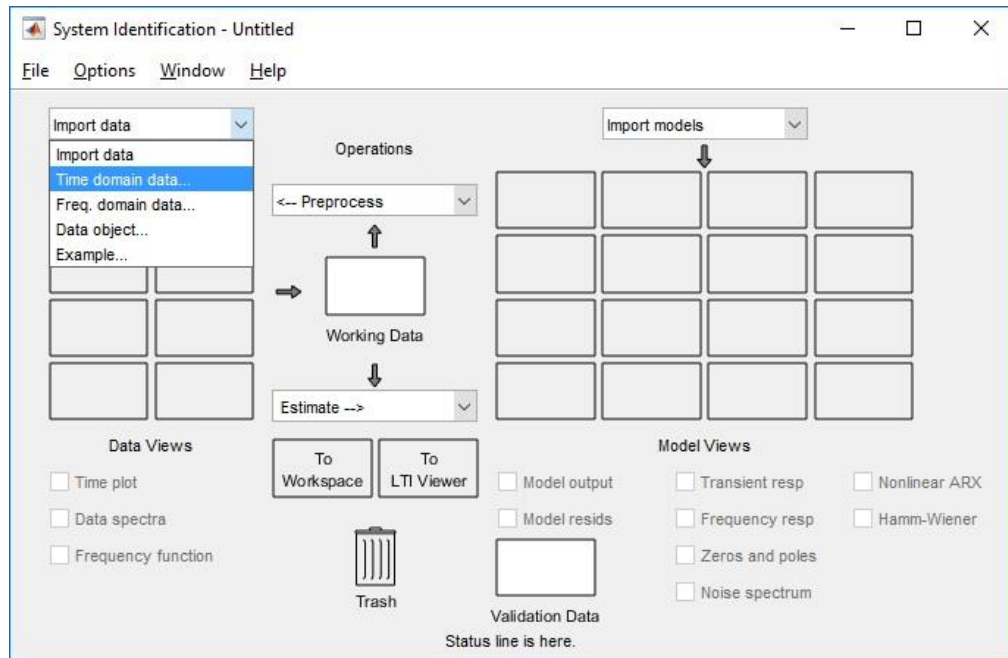


Figure A3. 3. Import data in the time domain.

The term as  $\delta_D^{static}$  is declared as  $D_{static}$  while the term  $\delta_D^{dynamic}$  is declared as  $D_{dynamic}$  to be in agreement with MATLAB nomenclature.  $D_{static}$  and  $D_{dynamic}$  are the input and output of the dynamic system, respectively. This is illustrated in Figure A3. 4. The starting time and the sampling time shall be also stated. The starting time and the sampling time are 0 and 0.001 (in seconds), respectively, as shown in the same figure.



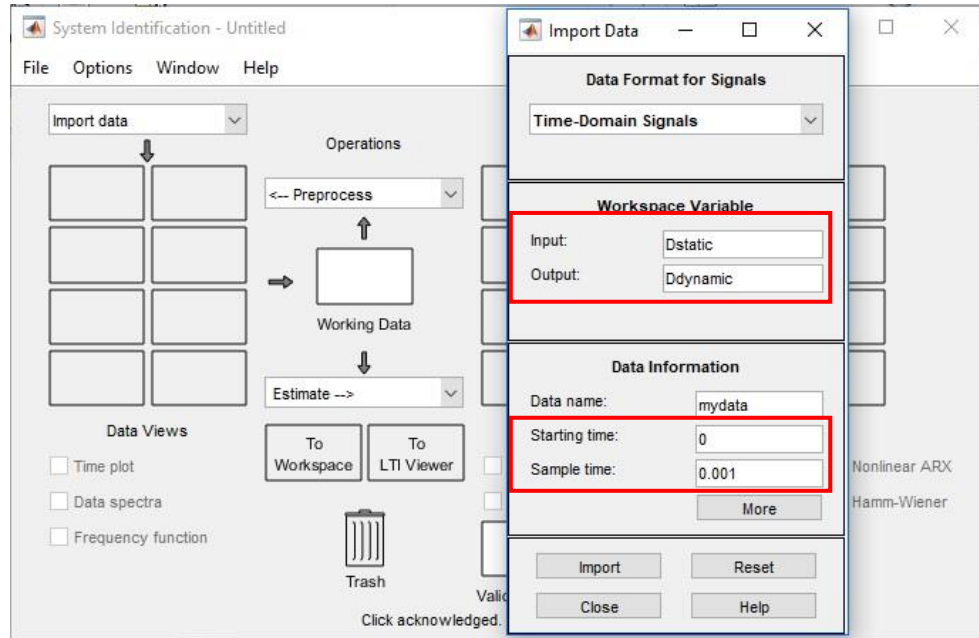


Figure A3. 4. Declaration of input, output, starting time and sampling time.

The input and output data of the dynamic system has been declared and their behavior can be observed as in Figure A3. 5. For MATLAB,  $u1$  corresponds to the input (nonlinear static displacement  $\delta_D^{static}$ ) and  $y1$  is the output (linear dynamic displacement  $\delta_D^{dynamic}$ ) of the system.

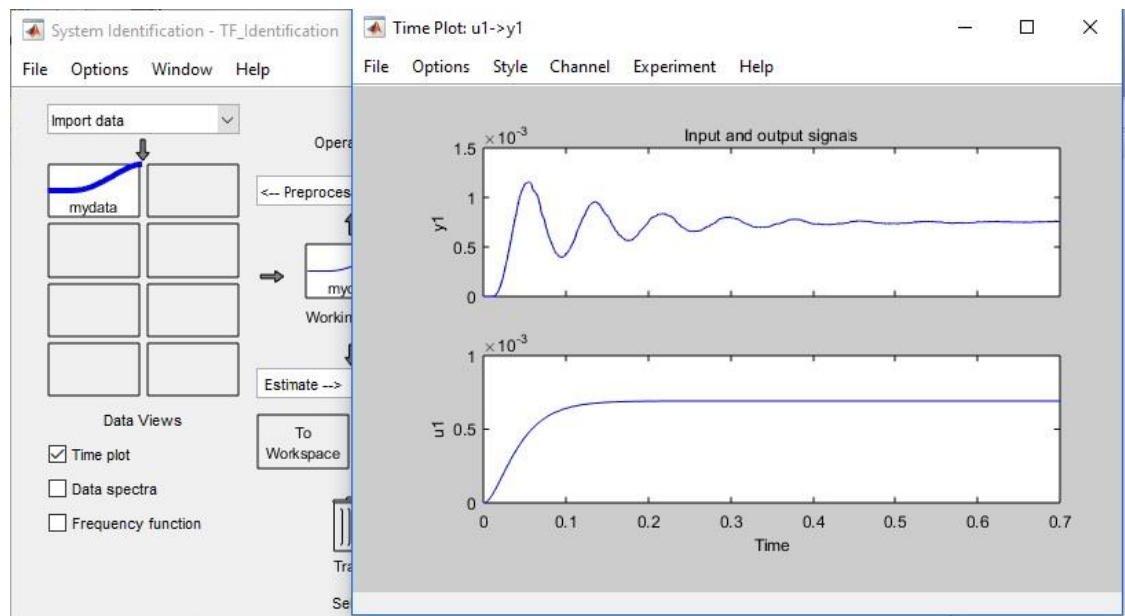


Figure A3. 5. Input and output behavior of the dynamic system. The input ( $u1$ ) corresponds to the static displacement, while the output ( $y1$ ) is the experimental dynamic displacement.

The estimation of the model can be performed by clicking the box “Estimate” as shown in Figure A3. 6. A set of candidate models are displayed. All these models can be proved one by one to choose the best fit with the experimental response. In this case, the selected option was “Polynomial Models”.

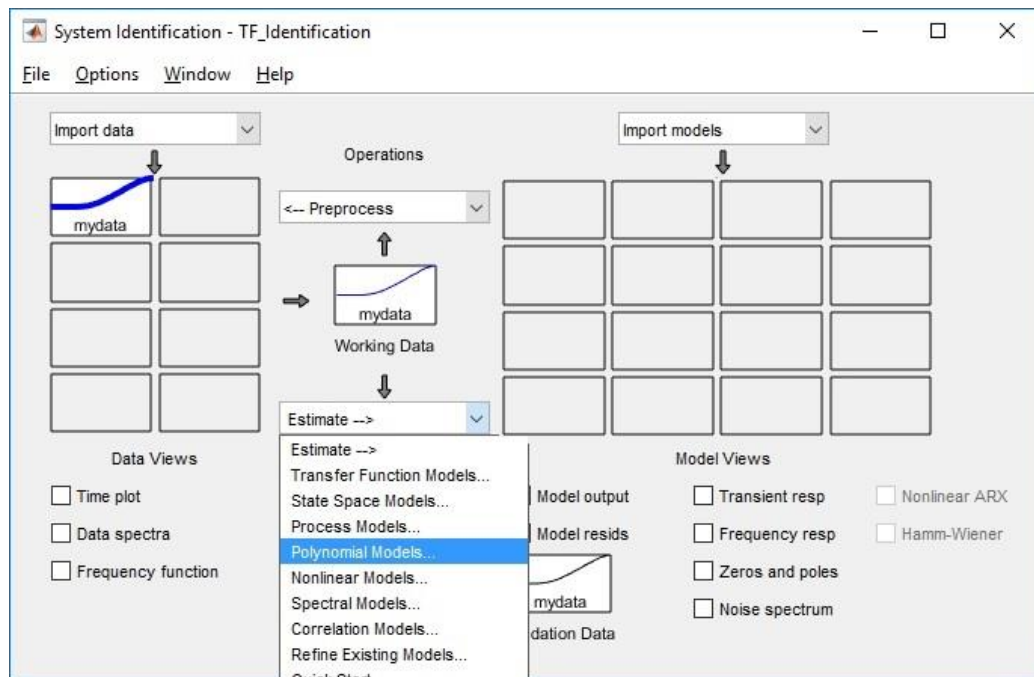


Figure A3. 6. The model was estimated as a polynomial model.

Polynomial models relate linearly the output with the input. In MATLAB, there are different options of polynomial model structures, such as Autoregressive with exogenous input (ARX), Autoregressive Moving Average with exogenous input (ARMAX), Output Error (OE) or Box-Jenkins (BJ) (see Figure A3. 7). The difference between these structures is the method used to estimate the model. The four polynomial model structures were tested. The ARX model structure was chosen because it showed the best fitting with the experimental response.

Afterwards, it is possible to select the orders of the ARX polynomials. The chosen orders are 441, which means the numerator polynomial degree is 4, the denominator polynomial degree is 4, and the delay between the input and output is 1 sampling period. This delay is mandatory because the way we measured the input and the output data had one sampling period difference. The order of the system is defined by the denominator polynomial

degree. Figure A3. 8 displays the selection of the orders and the corresponding equation of an ARX model. The agreement between the estimated model and the experimental dynamic response is demonstrated in Figure A3. 9.

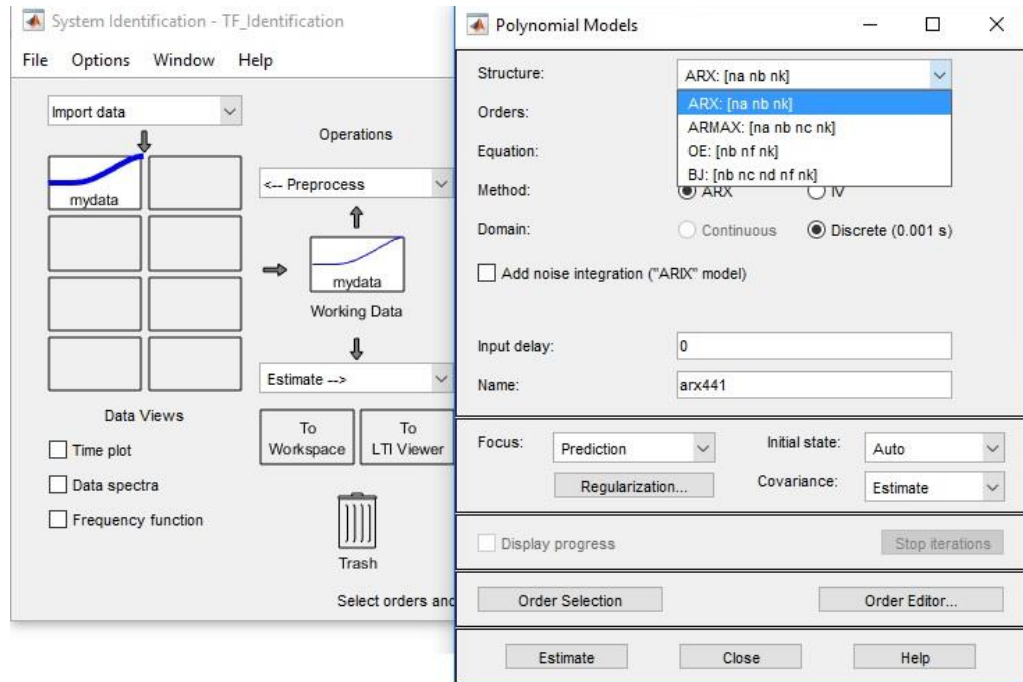


Figure A3. 7. Different polynomial model structures.

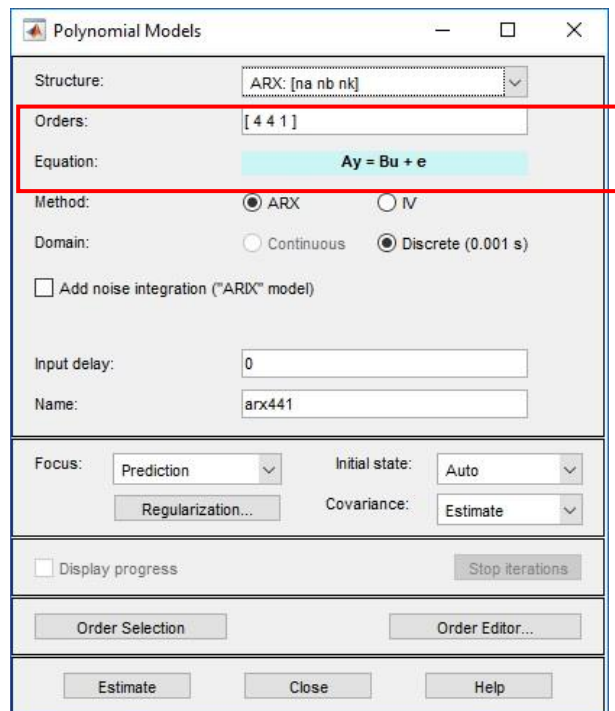


Figure A3. 8. Chosen orders of the ARX model.

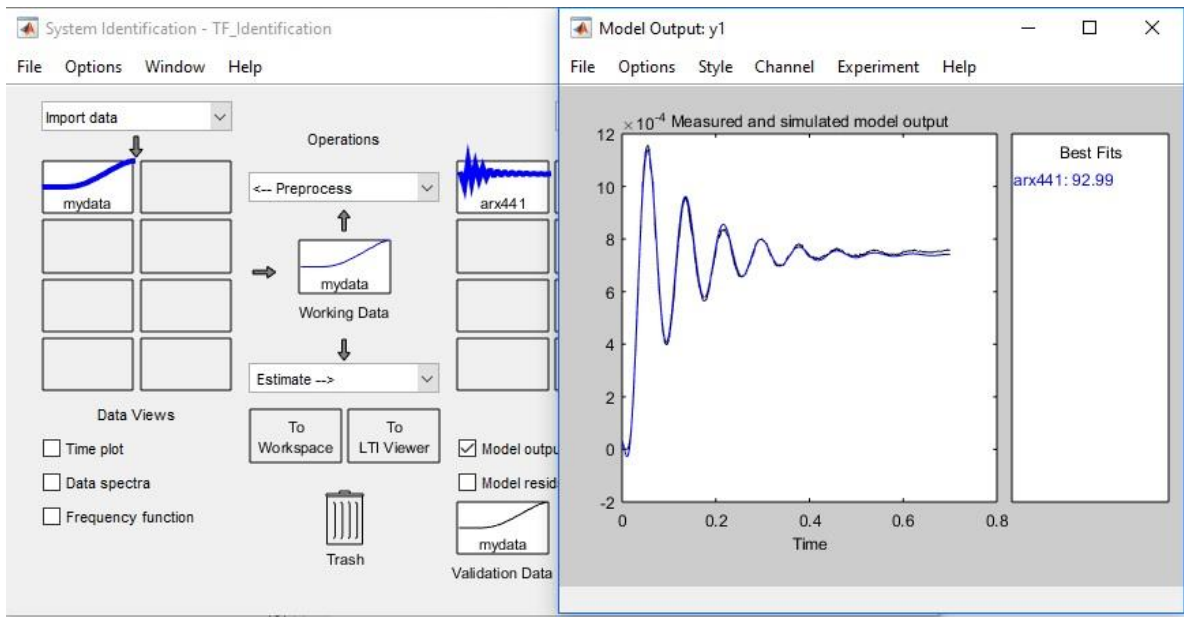


Figure A3. 9. Agreement between model and experimental responses.

After that, the selected model is sent to the workspace of MATLAB by drag and drop the arx441 icon to the block marked in red, as shown in Figure A3. 10.

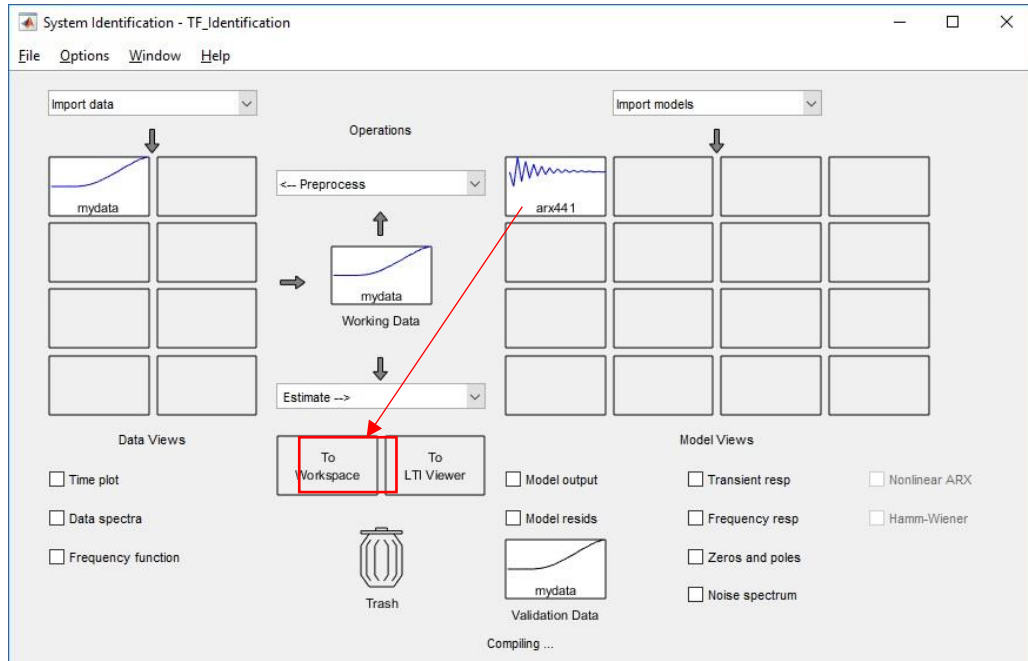


Figure A3. 10. The model is sent to the workspace of MATLAB.

Then, the discrete time transfer function and all its parameters can be obtained in the workspace of MATLAB by some commands. This is illustrated in Figure A3. 11.

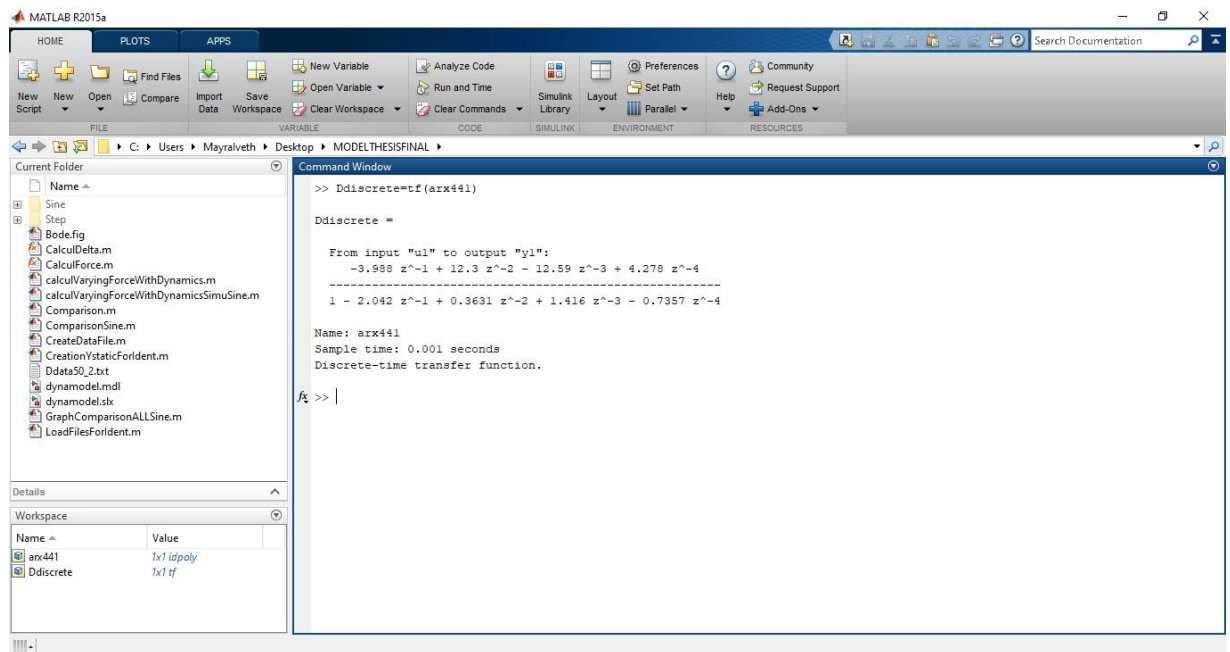


Figure A3. 11. Discrete transfer function from the selected polynomial model.

Finally, the parameters obtained for the transfer function are saved in a file. This file will be reused for validation of the overall model at different experimental conditions. Note that this procedure will lead to a discrete transfer function. By using the MATLAB d2c command and the zero-order hold (ZOH) method, we can obtain the related continuous domain transfer function. The ZOH interpolation method increases the model order that has real negative poles. Thus, the obtained transfer function is of fifth order, as shown in Figure A3. 12.

```
>> Ddiscrete=tf(arx441);
D=d2c(Ddiscrete, 'zoh')

D =

From input "u1" to output "y1":
  25.11 s^4 - 2.387e07 s^3 + 1.657e09 s^2 + 2.469e11 s + 6.98e12
-----
s^5 + 489.3 s^4 + 9.956e06 s^3 + 1.236e09 s^2 + 7.85e10 s + 6.529e12

Continuous-time transfer function.
```

Figure A3. 12. Obtained continuous time transfer function.

# Appendix 4

## Autoregressive with exogenous input (ARX) model

The autoregressive with exogenous input (ARX) model structure is considered as one of the simplest ways to represent dynamic systems. An ARX model describes the output of a dynamic system as the sum of the previous input and output observations (regression) plus an equation of error. The equation of error corresponds to exogenous variables outside the process to model, such as noise or any other external disturbance [198]. The schematic representation of an ARX model for a single input single output dynamic system (SISO system) is shown in Figure A4. 1.

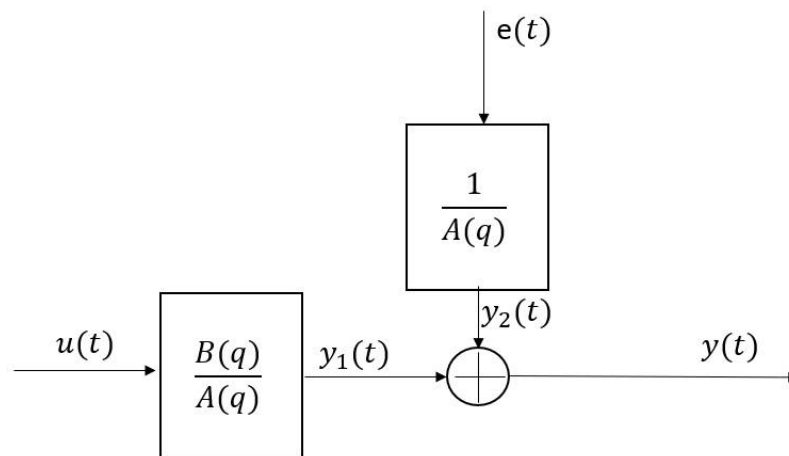


Figure A4. 1. Interpretation of ARX models. Dynamic system with input  $u(t)$ , error  $e(t)$  and output  $y(t)$ .

From this figure, it is possible to observe that the relation between the output  $y_1(t)$  and the input  $u(t)$  is determined by a transfer function  $B(q)/A(q)$ . The error of the process  $e(t)$  is related with its output  $y_2(t)$  by the transfer function  $1/A(q)$ . Thus, the observed output will be described by

$$y(t) = y_1(t) + y_2(t) \quad (95)$$

The polynomial representation is given as follows:

$$A(q)y(t) = B(q)u(t - n_k) + e(t) \quad (96)$$

Or

$$y(t) = \frac{B(q)}{A(q)}u(t - n_k) + \frac{1}{A(q)}e(t) \quad (97)$$

where  $n_k$  is the delay time between  $y(t)$  and  $u(t)$ ,  $t$  is the time and  $q$  is the delay operator.

$A(q)$  and  $B(q)$  are polynomials given by:

$$A(q) = 1 + a_1q^{-1} + \dots + a_nq^{-n} \quad (98)$$

$$B(q) = b_1q^{-1} + \dots + b_dq^{-d} \quad (99)$$

where  $a_n$  and  $b_d$  are the model parameters. Also,  $n$  and  $d$  indicate, respectively, the orders of the polynomials of the input  $A(q)$  and the output  $B(q)$ , respectively.

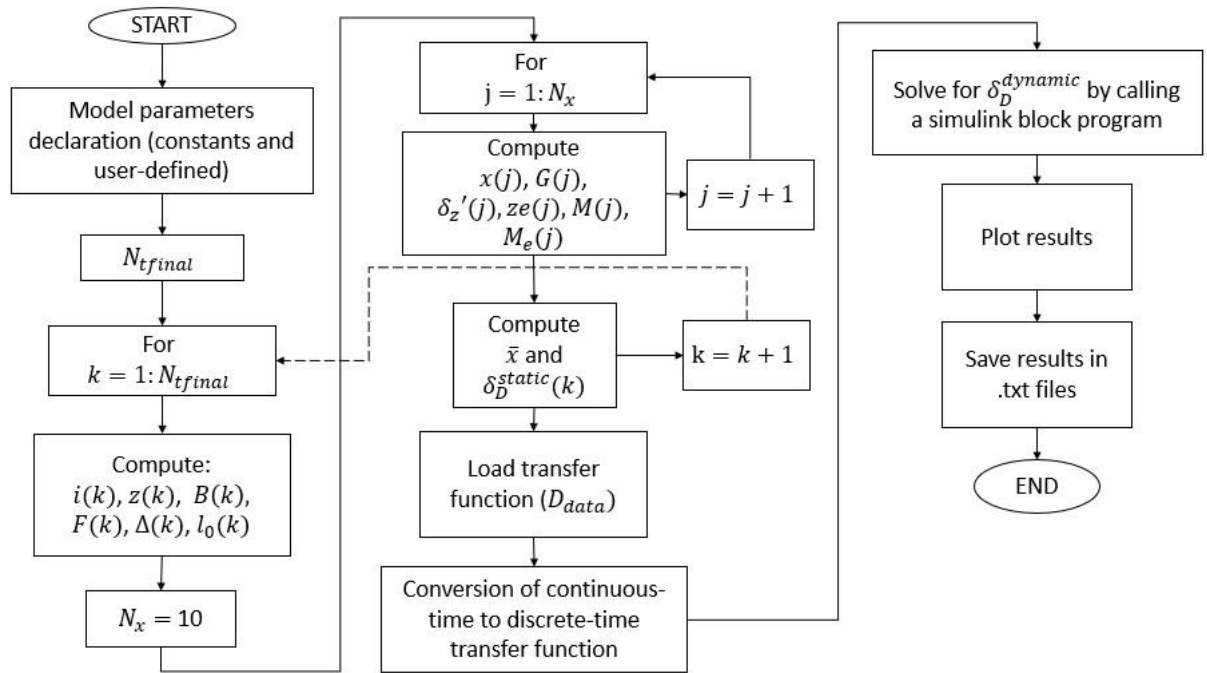
$A(q)$  and  $B(q)$  are estimated by the least squares identification method.

Reference: L. Ljung, "System identification toolbox", The MATLAB user's guide, 1988 (1<sup>st</sup> edition).

# Appendix 5

## Flowchart and code of overall model

### Flowchart of the overall model



### Code of the step mode test

```

clear all
clc

lb=15e-3;           %length of the microactuator l_b
E=3.9E9;           %elastic modulus
W=2e-3;            %width of the microactuator
T=0.018e-3;        %thickness of the microactuator
I=(W*(T^3))/12;    %area moment of inertia
EI=E*I;            %stiffness

R=42;              %Resistance of the electromagnet
L=1.21;            %Inductance of the electromagnet

tfinal=0.7;        %total execution time
Ts=1e-3;           %sampling time
  
```



```

Ntfinal=tfinal/Ts;

% initial values

Distance=0.014;           %initial distance from the electromagnet to the
                           free end of the microactuator
Dstaticdef=0;             %initial static deformation (as a constant)
t(1)=0;                   %initial time
u(1)=0;                   %initial voltage
i(1)=0;                   %initial current
B(1)=0;                   %initial magnetic field
F(1)=0;                   %initial magnetic force
Dstatic(1)=0;             %initial static deformation (as a variable
vector)

for k=2:Ntfinal

    t(k)=(k-1)*Ts;

    u(k)=30;               %Step voltage
    i(k)=(Ts/(R*Ts+L))* (u(k)+(L/Ts)*i(k-1)); %current along time

    z=Distance-Dstaticdef; %update value of z (distance of the free
                           end of the microactuator to the
                           electromagnet
    [B(k),F(k)]=CalculForce(i(k),z); %call function to calculate
                                     magnetic force CalculForce.m
    Delta=CalculDelta(F(k,EI,lb); %compute displacement on x-axis Δ
    CalculDelta.m
    l0=lb-Delta;           %compute the projection of the length
                           after displacement
    Nx=10;

    %initial conditions to calculate the nonlinear static displacement:

    x(1)=0;
    G(1)=(F(k)/(2*EI))*(((x(1))^2)-(L0^2));
    dD(1)=G(1)/((1-(G(1)^2))^(1/2));
    ze(1)=((1+(dD(1)^2))^(3/2));
    Mx(1)=-F(k)*x(1);
    Me(1)=ze(1)*Mx(1);
    dMe1(1)=0;
    pas=l0/Nx;

    for j=2:Nx
        x(j)=pas*(j-1); %x value along l0
        G(j)=(F(k)/(2*EI))*(((x(j))^2)-(l0^2)); %compute G(x)
        dD(j)=G(j)/((1-(G(j)^2))^(1/2)); %compute δ'_z
        ze(j)=((1+(dD(j)^2))^(3/2)); %compute ze
        Mx(j)=-F(k)*x(j); %compute M(x)
        Me(j)=ze(j)*Mx(j); %compute Me
    End

    dMe1=(1/2)*(l0-0)*Me(j)*((2/3)*(l0-0)); %compute x̄

```

```

        Dstatic(k)=(1/EI)*(dMe1);           %compute  $\delta_D^{static}$ 
        Dstaticdef=Dstatic(k);           %change of variable for
manipulations

end

% Dynamic model
load Ddata.txt           %load file with the transfer function parameters
num=Ddata(1,:);         %coefficients of numerator
den=Ddata(2,:);         %coefficients of denominator

Dc=tf(num,den);         %Transfer function from numerator and
denominator
D=c2d(Dc,Ts);          %Continuous time to discrete time transfer
function

tic
sim('dynamodel.mdl')   %Call for the Simulink block program
toc

%Plot results

subplot(3,2,1)
plot(t,u)
grid
title('Voltage vs time')
xlabel('time (s)')
ylabel('u(V)')

subplot(3,2,2)
plot(t,i)
grid
title('Current vs time')
xlabel('time (s)')
ylabel('i(A)')

subplot(3,2,3)
plot(t,B)
grid
title('Magnetic field vs time')
xlabel('time (s)')
ylabel('B(T)')

subplot(3,2,4)
plot(t,F)
grid
title('Force vs time')
xlabel('time (s)')
ylabel('F(N)')

subplot(3,2,5)
plot(t(1:length(Dstatic)),Dstatic)
grid
title('Static displacement vs Time')
xlabel('Time (s)')

```

```

ylabel('Displacement (m)')

subplot(3,2,6)
plot(t(1:length(Dstatic)),Ddynamic(1:length(Dstatic)))
grid
title('Dynamic displacement vs Time')
xlabel('time (s)')
ylabel('Displacement (m)')

%Save results
save DdynamicStep_30V.txt Ddynamic -ascii
save DstaticStep_30V.txt Dstatic -ascii

```

---

### Function: CalculForce.m

```

function [B,F]=CalculForce(i,z)

%Electromagnet constants
le=0.024; %length of the electromagnet
N=320; %number of turns of copper wire
ur=20; %relative permeability of the core;
u0=(4*pi)*(10^-7); %permeability of vacuum
re1=0.007; %internal radius of the electromagnet core
re2=0.014; %external radius of the electromagnet core

%Magnetization constants
m=1.2e-6; %total mass of the microactuator
H1=154.13304*((10^3)/(4*pi)); %magnetic field of magnetometry
H2=255.08698*((10^3)/(4*pi)); %magnetic field of magnetometry
M1=0.03612; %corresponding magnetization at H1 taken from magnetometry
M2=0.0573; %corresponding magnetization at H2 taken from magnetometry
Xm=(M2-M1)/(H2-H1); %magnetic susceptibility

M0=0; %initial magnetization

A1=((le/2)-z); %Segment of equation to obtain magnetic field B
A2=((le/2)+z); %Segment of equation to obtain magnetic field B
A3=log((re2+((re2^2)+(A1^2))^(1/2))/(re1+((re1^2)+(A1^2))^(1/2)));
%Segment of equation to obtain B
A4=log((re2+((re2^2)+(A2^2))^(1/2))/(re1+((re1^2)+(A2^2))^(1/2)));
%Segment of equation to obtain B
A5=((u0*ur*N*i)/(2*le*(re2-re1)) %Segment of equation to obtain B);
B=A5*((A1*A3)+(A2*A4)); %Magnetic field density supplied by the
electromagnet

%Magnetization
M=M0+((Xm)*(B/(u0))); %Magnetization per unit mass
Mm=m*Me; %Magnetization according to the mass of the microactuator

```

```

%force computation
F=(Mm*N*i*u0*ur*(log((re2 + ((le/2 - z)^2 + re2^2)^(1/2))/(re1 + ((le/2 - z)^2 + re1^2)^(1/2))) - log((re2 + ((le/2 + z)^2 + re2^2)^(1/2))/(re1 + ((le/2 + z)^2 + re1^2)^(1/2)))) + ((le/2 - z)*((le - 2*z)/(2*((le/2 - z)^2 + re2^2)^(1/2))*re1 + ((le/2 - z)^2 + re1^2)^(1/2))) - ((le - 2*z)*re2 + ((le/2 - z)^2 + re2^2)^(1/2))/(2*((le/2 - z)^2 + re1^2)^(1/2))*re1 + ((le/2 - z)^2 + re1^2)^(1/2))^2))*re1 + ((le/2 - z)^2 + re1^2)^(1/2))/(re2 + ((le/2 - z)^2 + re2^2)^(1/2)) - ((re1 + ((le/2 + z)^2 + re1^2)^(1/2))*((le + 2*z)/(2*((le/2 + z)^2 + re2^2)^(1/2))*re1 + ((le/2 + z)^2 + re1^2)^(1/2))) - ((re2 + ((le/2 + z)^2 + re2^2)^(1/2))*((le + 2*z)/(2*((le/2 + z)^2 + re1^2)^(1/2))*re1 + ((le/2 + z)^2 + re1^2)^(1/2)))^2))*re1 + ((le/2 + z)^2 + re1^2)^(1/2))/(re2 + ((le/2 + z)^2 + re2^2)^(1/2))))/(2*le*(re1 - re2));

```

```
end
```

---



---

### Function: CalculDelta.m

```

function Delta=CalculDelta(F,EI,lb)

syms d xs;

gammaD = (F/(2*EI))*((xs^2) - ((lb-d)^2)); %Compute G(x)
fgammaD = gammaD/((1 - (gammaD^2))^0.5) ; %Compute δ'_z
fxs = (1 + (fgammaD^2))^0.5; %Function to integrate

Eq = int(fxs, xs, 0, lb - d) == lb; %Integration of fxs must be
equal to lb
Delta = solve(Eq, d); %Delta Δ is the numerical solution of
Eq with respect to d

End

```

---



---

### Code of the periodic mode test

```

clear all
clc

lb=15e-3; %length of the microactuator l_b
E=3.9E9; %elastic modulus
W=2e-3; %width of the microactuator
T=0.018e-3; %thickness of the microactuator
I=(W*(T^3))/12; %area moment of inertia
EI=E*I; %stiffness

R=42; %Resistance of the electromagnet
L=1.21; %Inductance of the electromagnet

```

```

tfinal=10;          %total execution time, depends on the frequency and the
                    %number of cycles to evaluate
Ts=1e-3;           %sampling time

Ntfinal=tfinal/Ts;

% initial values

Distance=0.014;    %initial distance from the electromagnet to the
                    %free end of the microactuator
Dstaticdef=0;      %initial static deformation (as a constant)
t(1)=0;            %initial time
u(1)=0;            %initial voltage
i(1)=0;            %initial current
B(1)=0;            %initial magnetic field
F(1)=0;            %initial magnetic force
Dstatic(1)=0;      %initial static deformation (as a variable
                    %vector)

am=30;             %amplitude of the periodic voltage
f=0.1;             %frequency of the periodic voltage

for k=2:Ntfinal

    t(k)=(k-1)*Ts;

    u(k)=(sqrt(am))*sin(2*pi*(f/2)*t(k)).^2;    %Periodic voltage
                                                %function
    i(k)=(Ts/(R*Ts+L))*(u(k)+(L/Ts)*i(k-1)); %current along time

    z=Distance-Dstaticdef;    %update value of z (distance of the free
                                %end of the microactuator to the
                                %electromagnet
    [B(k),F(k)]=CalculForce(i(k),z);    %call function to calculate
                                        %magnetic force CalculForce.m
    Delta=CalculDelta(F(k),EI,lb);    %compute displacement on x-axis Δ
                                        %CalculDelta.m
    l0=lb-Delta;                    %compute the projection of the length
                                    %after displacement

    Nx=10;

    %initial conditions to calculate the nonlinear static displacement:

    x(1)=0;
    G(1)=(F(k)/(2*EI))*((x(1))^2)-(L0^2);
    dD(1)=G(1)/((1-(G(1)^2))^(1/2));
    ze(1)=(1+(dD(1)^2))^(3/2);
    Mx(1)=-F(k)*x(1);
    Me(1)=ze(1)*Mx(1);
    dMe1(1)=0;
    pas=l0/Nx;

    for i=2:Nx
        x(j)=pas*(j-1);    %x value along l0
    end
end

```

```

        G(j)=(F(k)/(2*EI))*((x(j))^2)-(l0^2); %compute G(x)
        dD(j)=G(j)/((1-(G(j)^2))^(1/2)); %compute  $\delta'_z$ 
        ze(j)=((1+(dD(j)^2))^(3/2)); %compute ze
        Mx(j)=-F(k)*x(j); %compute M(x)
        Me(j)=ze(j)*Mx(j); %compute  $M_e$ 
    End

    dMe1=(1/2)*(l0-0)*Me(j)*((2/3)*(l0-0)); %compute  $\bar{x}$ 
    Dstatic(k)=(1/EI)*(dMe1); %compute  $\delta_D^{static}$ 
    Dstaticdef=Dstatic(k); %change of variable for
manipulations

end

% Dynamic model
load Ddata.txt %load file with the transfer function parameters
num=Ddata(1,:); %coefficients of numerator
den=Ddata(2,:); %coefficients of denominator

Dc=tf(num,den); %Transfer function from numerator and
denominator
D=c2d(Dc,Ts); %Continuous time to discrete time transfer
function

tic
sim('dynamodel.mdl') %Call for the Simulink block program
toc

%Plot results

subplot(3,2,1)
plot(t,u)
grid
title('Voltage vs time')
xlabel('time (s)')
ylabel('u(V)')

subplot(3,2,2)
plot(t,i)
grid
title('Current vs time')
xlabel('time (s)')
ylabel('i(A)')

subplot(3,2,3)
plot(t,B)
grid
title('Magnetic field vs time')
xlabel('time (s)')
ylabel('B(T)')

subplot(3,2,4)
plot(t,F)
grid
title('Force vs time')

```

```

xlabel('time (s)')
ylabel('F(N)')

subplot(3,2,5)
plot(t(1:length(Dstatic)),Dstatic)
grid
title('Static displacement vs Time')
xlabel('Time (s)')
ylabel('Displacement(m)')

subplot(3,2,6)
plot(t(1:length(Dstatic)),Ddynamic(1:length(Dstatic)))
grid
title('Dynamic displacement vs Time')
xlabel('time (s)')
ylabel('Displacement(m)')

%Save results
save DdynamicStep_30V.txt Ddynamic -ascii
save DstaticStep_30V.txt Dstatic -ascii

```

-----  
-----

Functions *CalculForce.m* and *CalculDelta.m* are the same as those applying for the step voltage mode test.

# Mayra Iveth Llamas Hernández



(+521) (81) 84668119



mi.llamashr@gmail.com



Guadalupe, Nuevo León, México



[www.linkedin.com/in/millamas](http://www.linkedin.com/in/millamas)

## Skills

## Languages

Spanish   
English   
French 

## Technical knowledge

- Expertise in materials science and their relationship structure-properties.
- Knowledge in electronic circuits and programming of microcontrollers.
- Modeling of mechatronic systems.
- Finite element analysis simulations.
- Electronics laboratory equipment.
- Materials testing laboratory equipment.

## Computer skills

Matlab/Simulink



Origin Pro



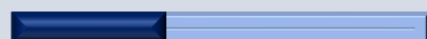
Comsol multiphysics



Solidworks



LabVIEW



## Personal skills

- Analytics
- Creative
- Team player
- Leadership
- Adaptable
- Project management

## Professional profile

Engineer with experience in the modeling and characterization of polymeric nanocomposites for technological devices. Experienced leading projects as well as collaborating as a team member. Knowledge in industrial and academic settings. Quickly adaptable to diverse work environments and multidisciplinary projects.

## Academic background

### 2015 - 2019

- Ph.D. in materials engineering and Ph.D. in automation  
Dual-degree modality between Universidad Autónoma de Nuevo León (Mexico) and Université Bourgogne Franche-Comté (France)  
Research in the modeling of a polymer with iron oxide nanoparticles (magnetoactive polymer) for their application as microactuator.

### 2010-2012

- M.Sc. in mechanical engineering with specialization in materials  
Universidad Autónoma de Nuevo León  
Academic exchange (August 2011 – January 2012) at the École Polytechnique, Université de Montréal, Canada with professor Pierre Carreau  
Research in the improvement of the mechanical and electronic properties of polymers by adding graphene nanoplates.

### 2005-2010

- Mechatronics engineer  
Universidad Autónoma de Nuevo León

## Employment experience

### 2017

Substitute professor for the lectures “industrial maintenance” and “ceramics and glass” for the industrial design engineering students. Escuela Politécnica de Apodaca, Nuevo León, México.

### 2012-2015

- Oil & Gas project engineer at FRISA FORJADOS S.A.
- Chosen to participate in the first generation of the “Young talent development” program
  - In charge of complete oil and gas project for high impact customers
  - Elaboration of metallurgical analysis (simulation and characterization), decreasing operating costs
  - Interaction directly with customers for technical discussions.



## Scientific publications and congresses participation

- Llamas-Hernández, Mayra; López- Walle, Beatriz; Rakotondrabe, Micky; Reyes-Melo, Edgar, “Dynamic behavior of magnetic hybrid films of polyvinylbutyral/iron oxide nanoparticles (PVB/Fe<sub>2</sub>O<sub>3</sub>) for their control as microactuators”. Physica B, 2018.  
<https://doi.org/10.1016/j.physb.2017.10.095>
- Llamas MI, Guerrero CA, Reyes ME, Luna JF “Comportamiento Elástico y Morfológico de Compuestos Polipropileno-Grafeno”. Revista Ingenierías UANL, 2015.  
<https://dialnet.unirioja.es/servlet/articulo?codigo=5247960>
- Participation in the congress of hysteresis modeling and micromagnetics, Barcelona, Spain. (May 2017)
- Participation in the congress of international materials research, Cancún, Mexico (August 2013)
- Invited speaker at the rheology group seminar in the department of chemical engineering, École Polytechnique, Montréal, Canada. (December 2011)

## Trainings attended

- Effective Negotiating  
KARRAS, 2015
- Leadership  
CDG Consultorías, 2014
- Líderes Socialmente Responsables  
SELIDER ABP, 2013
- Green Belt and Six Sigma  
Frisa Forjados, 2013
- Comunicación para lograr Resultados Efectivos C.A.R.E.  
Frisa Forjados, 2013